Fe/MgO catalysts for the hydrogenation of nitriles

Bond, G.

Award date:
1992

Awarding institution:
University of Bath

Fe / MgO CATALYSTS

FOR THE

HYDROGENATION OF NITRILES

BY

G. BOND, B. Sc

Thesis submitted for the Degree of

Doctor of Philosophy

University of Bath 1992

ProQuest LLC
789 East Eisenhower Parkway
P.O. Box 1346
Ann Arbor, MI 48106-1346

ABSTRACT

Iron catalysts are frequently used in industry as hydrogenation catalysts. The catalyst usually takes the form of an unsupported catalyst to which is added a variety of promoters.

This work describes the preparation of some iron supported on magnesium oxide catalysts. Catalysts with iron loadings in the range 1-30 mol% have been prepared by both impregnation and coprecipitation techniques. The phases present in the starting precipitates, calcined precursors and the reduced catalyst have been determined by X-ray diffraction and Mössbauer spectroscopy. Other methods of characterisation used include gas adsorption studies (N_2 and CO), selective oxidation using nitrous oxide and an infrared study of adsorbed probe molecules (CO and NO).

The activity and selectivity of the catalysts for the hydrogenation of nitriles has been studied, using nitriles with carbon chain lengths varying between 2 and 12 carbon atoms. The investigations have been studied using both flow and static reactors.

An attempt to study the interaction of ethanenitrile and propanenitrile with the catalysts using infrared spectroscopy has also been carried out.

ACKNOWLEDGEMENTS

I am indebted to my supervisor Prof. F. S. Stone for his encouragement and guidance throughout this work. I would like to thank all the technical staff without whose help this work could not have progressed. A special thanks is due to Dr. K. Molloy for his help with the Mössbauer spectroscopy. I am also grateful to all the people at ICI wilton who have been involved in the work, in the form of practical assistance and useful discussion.

I would like to thank SERC and ICI Chemicals and Polymers division for funding this work.

Many thanks to many dear friends within the departments for sharing some of the lighter moments.

I would like to pay a special tribute to my mother for her support throughout my academic studies.

TO

My wife and my mother - whose sacrifices

go untold

CONTENTS

Chapter 1

Introduction

"Reading maketh a full man; conference a ready man; and writing an exact man"

Francis Bacon 1561-1626

1.1. General Introduction

The aim of the research described in this thesis was to investigate MgO-supported iron catalysts and to examine whether they could be used for selective hydrogenation of nitriles to primary amines. The interest of ICI in this reaction stems from their long-established position as a producer of nylon-6,6. In the production of Nylon 6,6 the C_6 dinitrile, adiponitrile (ADN) is hydrogenated to the corresponding primary amine 1,6-hexamethylenediamine (HMD) using an unsupported cobalt, nickel or iron catalyst (1).

The theme of using iron supported on magnesium oxide as the catalyst for nitrile hydrogenation was fivefold:

(i) Iron was chosen as the active metal as it was already proven as an active metal for the hydrogenation of nitriles with a high selectivity to primary amines.

(ii) MgO is easily prepared in a high surface area form, this being one of the basic requirements for a catalyst support.

(iii) MgO has been shown to be capable of stabilising small iron particles (2,3). The mechanism of this stabilisation will be discussed in greater detail at a later stage.

(iv) MgO has been shown to be capable of the heterolytic activation of hydrogen ($H_2 \longrightarrow H^+ + H^-$), (4-6); in this activated form hydrogen is more active towards hydrogenation. Therefore MgO provides the potential for a reverse spillover of active hydrogen to the metal, resulting in a more active catalyst.

(v) The formation of secondary and tertiary amines proceeds via a condensation reaction, this is believed to be catalysed by acid sites on the catalyst (7). The use of a basic support such as MgO may result in a more selective catalyst.

1.2. Definition of Catalysis

Catalysis is the key to chemical transformations in a majority of chemical industries which produce billions of pounds worth of products annually. Sulphuric acid, ammonia, nitric acid, alcohols, butadiene, aromatic hydrocarbons, synthetic rubber, plastics and many other products are now produced wholly, or almost wholly, by catalytic processes. Moreover, important new catalytic processes, some of which provide products previously unknown, are being introduced with increasing frequency. In this chemical age, catalysis may be said to be man's most important tool.

Changes in reaction rate produced by a catalyst are positive, corresponding to acceleration. By increasing the rate of a required reaction relative to unwanted reactions, the formation of a desired product can be maximised compared with undesired by-products. The acceleration of a selected reaction is one of the most important features of catalysis. Moreover, by increasing the rate of a normally undetectably slow reaction to values that can be observed, a catalyst can, for all practical purposes actually initiate a previously unobserved reaction. It was the observed increase in rate produced by additions of trace amounts of substances that were not consumed

in the reaction, which prompted the famous Swedish scientist Berzelius to write:

"I shall therefore call it the catalytic power of substances and the decomposition by means of this power catalysis, just as we use the word analysis to denote the separation of the component parts of bodies by means of ordinary chemical forces. The catalytic power actually means that substances are able to awake affinities which are asleep at this temperature by their mere presence and not by their own affinity."

Today the usually accepted definition of a catalyst is that it is a substance which increases the rate at which a chemical system approaches equilibrium, without being consumed in the process. Catalysis is the phenomenon of a catalyst in action.

1.3 Iron Catalysts

Iron is the most abundant metal after aluminium and the fourth most abundant element in the earth's crust. Therefore it is relatively inexpensive and hence is attractive as a catalytic material providing it has the desired activity.

Iron catalysts find widespread application in a number of processes being practised on an industrial scale. The ammonia synthesis and Fischer-Tropsch synthesis are essentially based on metallic iron catalysts. In the oxidised state iron catalysts have proved to be effective in the water-gas shift reaction, the dehydrogenation of ethylbenzene and in the

removal of sulphur-containing compounds.

1.3.1 Ammonia Synthesis

The first observation of ammonia synthesis over an iron catalyst was made by Perman (8) in 1905. Perman carried out his reaction at 1073 K and atmospheric pressure. The modern ammonia synthesis plant operates under vastly different conditions to those of Perman, namely much lower temperature and much higher pressure. Typical operating conditions are 150-350 atm and 670 K.

The literature concerning ammonia synthesis is vast and well beyond the scope of this thesis; authoritative accounts may be found in a number of reviews on the subject (9-11).

The industrial iron catalyst for ammonia synthesis is generally prepared by fusion of premixed iron(II)/iron(III) oxide, potassium nitrate and alumina at temperatures exceeding 1873 K. During the fusion process alumina dissolves into magnetite (Fe_3O_4). The doubly promoted iron catalysts contain typically 0.6 - 2.0 wt% of Al_2O_3 and 0.3 - 1.5 wt% K_2O. The reduction of the resultant iron oxide to the catalytically active metallic phase is carried out above 623 K, in a flow of H_2 or N_2/H_2. In addition to Al_2O_3 and K_2O, CaO, MgO, TiO_2 or SiO_2 may be present.

1.3.2. Fischer-Tropsch Synthesis

Fischer-Tropsch synthesis is the catalytic conversion of CO/H_2 synthesis gas to predominantly linear alkanes and alkenes by a surface polymerisation which gives rise to a characteristic Schulz-Flory product distribution (12). The seventies saw an increased interest in the reaction and a number of review papers exist on the subject(13,14). The choice of process variables largely influences the product spectrum obtained. A high wax selectivity is usually realised in isothermal fixed and slurry bed reactors at temperatures of about 523 K. On the other hand, fluidised bed reactors operated at higher temperatures (up to 633 K) produce mainly hydrocarbons of low molecular weight. Technical Fischer-Tropsch catalysts developed for the fixed bed reactors are prepared by precipitation techniques. A solution of water-glass is added to a slurry of iron oxide, precipitated by contacting a solution of iron nitrate with a sodium carbonate solution. To obtain the large metallic surface area required for the active catalyst, subsequent reduction with hydrogen, carbon monoxide or a mixture of both is performed at between 450 and 550 K. The reduction pretreatment delicately determines the final selectivity performance. In the fluidised bed reactor the fused ammonia synthesis catalyst is generally used.

1.3.3. Water-gas Shift Reaction

The water-gas shift reaction, ie the reaction of steam with carbon monoxide producing hydrogen and carbon dioxide, is an important step in many industrial processes. Examples are the ammonia synthesis, gasification of coal and the production of hydrogen for eg coal liquefaction, the hydrotreating of heavier petroleum and shale oil liquids and the hydrogenation of fatty oils. The catalyst used for the water gas shift reaction is generally unsupported iron oxide which is stabilised by about 14 wt % of Cr_2O_3 to prevent reduction and loss of surface area. This so-called high temperature shift (HTS) catalyst, utilised at temperatures from 590 to 720 K, can tolerate small quantities of sulphur, in contrast to the very sulphur sensitive low temperature shift (LTS) catalyst which is copper-based. The reduction pretreatment of the HTS catalyst leading to the formation of Fe_3O_4, which is considered to be the active component, is carried out at temperatures between 520 and 670 K (15).

1.4. Supported Iron Catalysts

The general aim when producing a supported metal catalyst is to achieve a high dispersion of the active metal on a high area support. This results in the formation of a catalyst which has a large active surface area for a relatively small amount of metal. This is particularly important when the active metal

is expensive, as in the case of platinum, for example. As discussed previously iron is relatively inexpensive and most commercial catalysts use iron in an unsupported form. However, the literature contains reports of iron supported on a wide range of support materials, including niobia (16), titania (17,18), carbon (19,20), zeolites (21) as well as the more traditional supports silica (22-26), alumina (22,27-30) and magnesia (2,3,28,31-36).

1.4.1. Reduction of Supported Iron Catalysts

In contrast to eg. copper oxide and nickel oxide, the reduction of iron oxide calls for a low ratio of the partial pressures of water vapour to hydrogen (37). Water vapour is tenaciously adsorbed by the usual support materials, and since its transport out of the carrier is a relatively slow process, reduction of supported iron oxide is difficult. The rate of reduction also depends upon the size and mutual contact area of the iron moieties in the catalyst precursors, on the interaction with the support and on the pore structure.

The equilibria between Fe_2O_3, Fe_3O_4, FeO and metallic iron for unsupported iron has been discussed by Kock (38). FeO is only stable above 843 K; at lower temperatures Fe_3O_4 is reduced to metallic iron. Reduction of Fe_2O_3 to Fe_3O_4 proceeds at a ratio of partial pressures of water and hydrogen of about 10^5, while reduction to metallic iron calls for ratios of 10^{-5} at 300 K to 0.01 at about 500 K.

Another complication with supported catalysts is that

iron can react to form stable compounds with the support. With silica, alumina, magnesia and carbon Fe(II)SiO_3, Fe(II)Al_2O_4, $MgFe_2O_4$ and iron carbides can result, respectively. Furthermore experiments on iron single crystals by Vink et al. (39) have established that the removal of the last monolayer of oxygen from Fe(100) surface with hydrogen does not proceed measurably. This contrasts with the more closely packed Fe(110), which can be readily freed from adsorbed oxygen by hydrogen reduction. Electron microscopy (37) has shown that large iron particles have a shape bounded almost completely by {110} surfaces. Only at edges and corners are other crystallographic planes present. Small iron particles by contrast will contain a substantial fraction of crystallographic planes in their surface other than the {110} surface. The consequence of this is that after hydrogen reduction an appreciable part of the surface will still be covered by a monolayer of oxygen.

1.4.1.1. Fe/MgO Catalysts

The reduction behaviour of iron catalyst precursors prepared by the impregnation of magnesium hydroxycarbonate (MHC) with iron(III) nitrate has been studied by Boudart et al. (2). Topsøe et al. (3) have compared the synthesis and reduction of catalyst precursors from the impregnation of MHC and from the coprecipitation of the magnesium and iron(III) nitrates with ammonium hydroxide. The schematic models for the genesis of both MHC impregnated and coprecipitated catalysts as

GENESIS OF CATALYSTS

Catalyst produced by impregnating of magnesium hydroxycarbonate

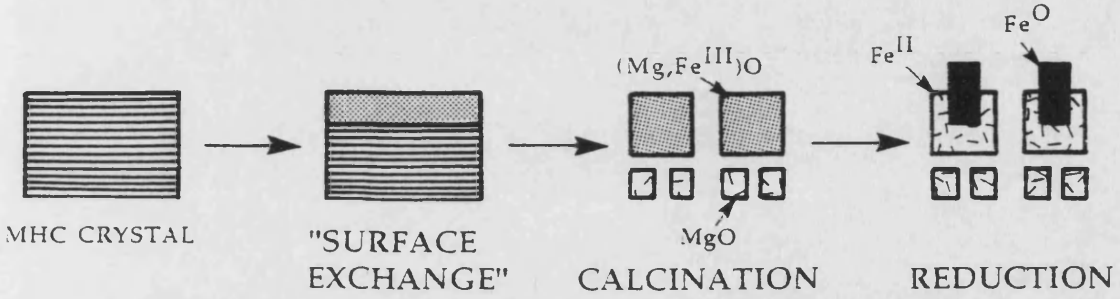

Catalyst produced by coprecipitation

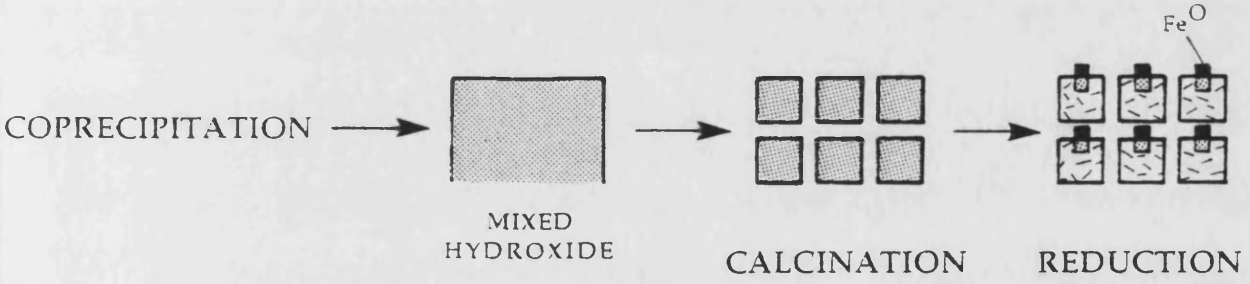

Figure 1.1. Schematic models for the genesis of impregnated and coprecipitated catalysts as proposed by Topsoe *et al.* (3).

described by Topsøe et al (3) are shown in Figure 1.1. Magnesium oxide has been shown to be capable of stabilising small iron particles, whether produced by impregnation or coprecipitation. Topsøe et al. (3) have suggested that the more homogeneous mixed hydroxide produced via coprecipitation leads to smaller iron particles compared to the impregnation of MHC which results in high surface concentrations of iron and hence larger metallic iron crystallites in the reduced catalyst.

X-ray diffraction and electron microscopy indicate that the Fe^{2+} is not homogeneously dispersed, but has the tendency to form clusters, the concentration of Fe^{2+} in these clusters being virtually independent of the iron loading. Iron has a well-known tendency to sinter (40) and therefore it seems unlikely that small metallic iron particles could be produced without the presence of a strong iron-support interaction. The nature of the Fe-MgO interaction, however, clusters the Fe^{2+}, thereby isolating the resulting metallic iron particles formed upon further reduction (2). This clustering may account for the fact that the fraction of metallic iron formed varies only slightly with loading.

The reduction in a CO atmosphere of precursors produced from the impregnation of MHC with iron(III) nitrate has been studied by Kock et al. (28). However, their results do not agree with those of Boudart et al. (2) in that the fraction of metallic iron produced on reduction was found to be dependent on the loading.

1.4.1.2. Fe/Al_2O_3 Catalysts

The reduction of alumina supported catalysts containing α-Fe_2O_3 and FeOOH has been studied by several authors (27,28). There is agreement that the reduction in hydrogen at temperatures in the region of 673 K proceeds as shown below

$$\begin{matrix}\alpha\text{-}Fe_2O_3 \\ FeOOH\end{matrix} \longrightarrow Fe_3O_4 \longrightarrow FeO \longrightarrow \alpha\text{-}Fe$$

As stated prevoiusly, in the reduction of unsupported iron catalysts FeO is not observed at temperatures below 843 K. Hence the formation of FeO in the alumina supported catalysts is indication of a strong interaction with the support. The formation of this stabilised FeO phase has the effect of reducing the thermodynamic driving force for reduction beyond this phase,and hence reduction to metallic iron is difficult.

The formation of $FeAl_2O_4$ has been reported in Fe/Al_2O_3 catalyst. Reduction of this phase to metallic iron requires high temperatures, hence the production of metallic iron is more difficult.

1.4.1.3. Fe/SiO_2 Catalysts

One of the most striking features of the reduction of silica supported iron catalysts is that a magnetite phase is not observed.

Two different oxide structures containing Fe^{2+} have however been observed by Yuen et al. (25), on the basis of two doublets in the Mössbauer spectrum. One doublet is claimed to be due to Fe^{2+} strongly interacting with the support in sites

of low coordination with oxygen (eg.,fourfold). It is suggested that these iron cations are present as thin "rafts" on the silica support. The other doublet is claimed to arise from Fe^{2+} in small iron oxide particles and these exhibit a high coordination with oxygen (eg., sixfold). These particles are also believed to be in intimate contact with the silica support as explained by their stability against reduction. As the reduction temperature is increased, Fe^{2+} cations in high coordination are converted into cations in low coordination as shown by the schematic representation in Figure 1.2.

Wielers et al. (22) only observed one Fe^{2+} doublet in the Mössbauer spectrum of their reduced Fe/SiO_2 catalyst. These authors claim that Fe^{2+} cations react to form iron(II) silicate, which accounts for the slow reduction to the metallic state. The reduction of iron(II) silicate to metallic iron requires a $p(H_2O)/p(H_2)$ ratio three orders of magnitude lower than that required for the reduction of Fe_2O_3 (41).

An infrared study of CO adsorption by the above authors indicated that after reduction at 723 K the catalyst exhibited bulk characteristics consistent with the presence of metallic iron (Mössbauer spectroscopy) but no absorption bands due to CO adsorbed on metallic iron. The authors therefore proposed that the iron silicate forms an encapsulating layer around the metallic iron. At higher reduction temperatures metallic iron was observed as a surface species, but this was accompanied by the sintering of the iron particles. Figure 1.3 shows a schematic representation of the reduction process for iron/silica catalyst as described by Wielers et al. (22).

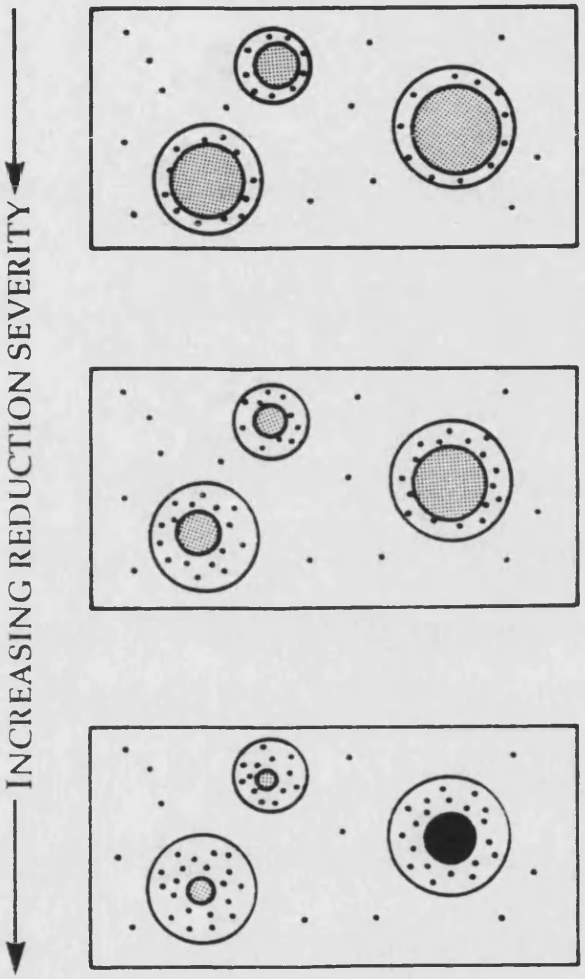

Figure 1.2 Schematic model of Fe/SiO_2 at increasing reduction severity as proposed by Yuen *et al.* (25).
Stippled, dotted and black regions represent outer-double Fe^{2+}, inner-double Fe^{2+}, and metallic iron respectively.

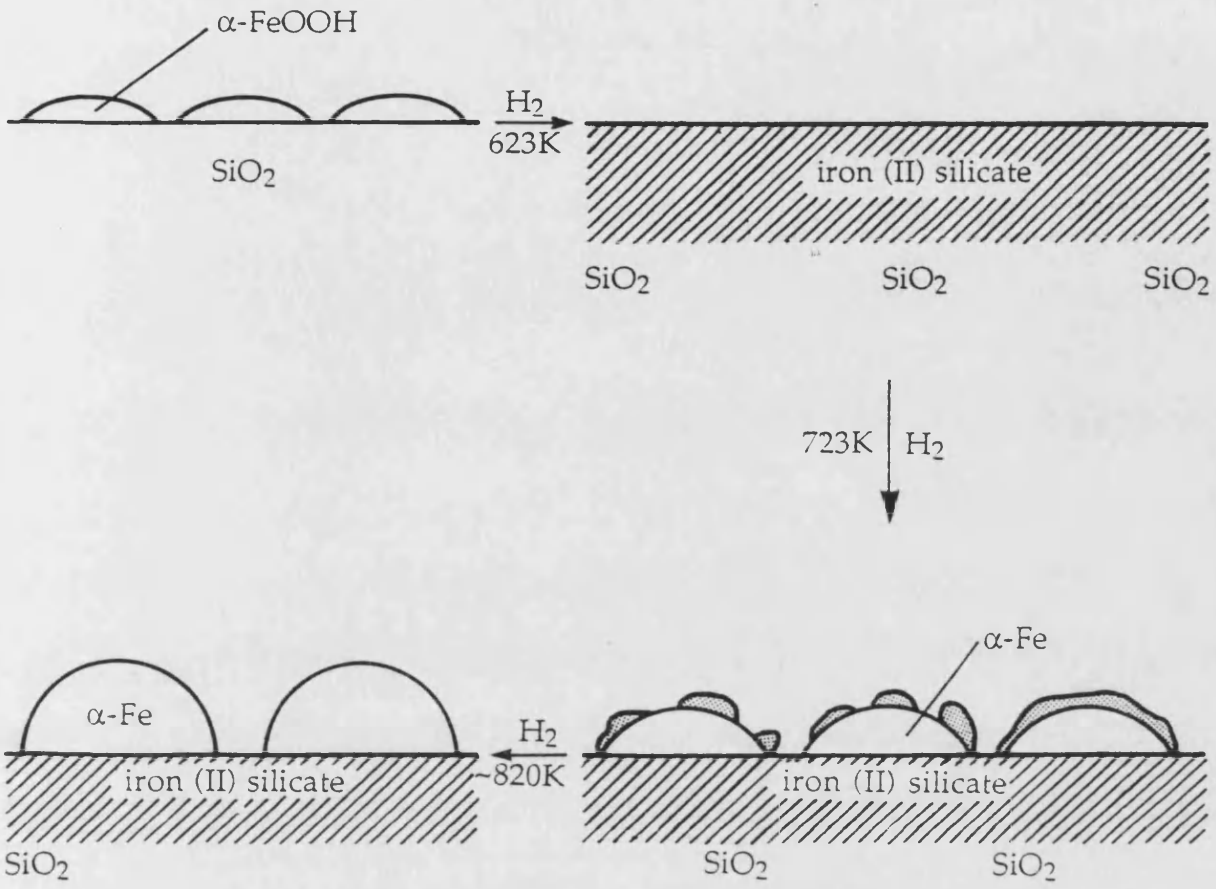

Figure 1.3. Schematic model of Fe/SiO_2 at increasing reduction severity as proposed by Wielers *et al.* (22).

The encapsulation of the metallic iron in silica-supported catalysts may explain some of the chemisorptive and catalytic properties of Fe/SiO_2 catalysts, eg small extents of hydrogen chemisorption at room temperature and the markedly lower Fischer-Tropsch activity of silica-supported iron catalysts compared to alumina-supported catalysts (22).

1.5. Production of Nitriles

In this section an account will be given of routes for the industrial production of nitriles. However, not every synthetic route resulting in the formation of a nitrile need be covered. The ones of most relevance to this thesis are those which lead to 1,4-dicyanobutane, adiponitrile $NC(CH_2)_4CN$. Four routes have been developed for the large scale manufacture of adiponitrile and these will be discussed here.

1.5.1. Dehydrative Amination of Adipic Acid

This process is carried out by ICI, Rhône-Poulenc, and Monsanto, the reaction has been studied on the laboratory scale during the course of this work (42). The reaction is carried out in the presence of excess ammonia at a temperature of 350°C in the presence of a boron phosphate catalyst.

The first step is

$$RCO_2H + NH_3 \rightleftarrows RCONH_2 + H_2O$$

which is approximately thermally neutral, but the second step

$$RCONH_2 \rightleftarrows RCN + H_2O$$

is endothermic and absorbs 84.4 kJ mol^{-1}, i.e. ΔH = +168.8 kJ mol^{-1} for the dinitrile, adiponitrile.

Since adipic acid is bifunctional the process can be depicted as shown in Figure 1.4. The phosphate catalyst (designated X_2P-OH) probably enters into the reaction as shown below

1. $X_2P\text{-}OH + NH_3 \rightleftharpoons X_2P\text{-}NH_2 + H_2O$

2. $X_2P\text{-}NH_2 + RCOOH \rightleftharpoons RCONHPX_2 + H_2O$

2A. $X_2P\text{-}OH + RCONH_2 \rightleftharpoons RCONHPX_2 + H_2O$

3. $RCONHPX_2 \rightleftharpoons RCN + X_2P\text{-}OH$

1.5.2. Indirect Hydrocyanation of Butadiene via the 1,4-Dichlorobutene Intermediate

Butadiene hydrocyanation can take place indirectly via chlorination of butadiene, as shown by the reactions in Figure 1.5. This route has been developed by the Dupont Company (43). The chlorination is carried out in the gas phase at 200 - 300°C without a catalyst. A mixture of 3,4-dichloro-1-butene and cis and trans 1,4-dichlorobutene is obtained, the selectivity being approximately 96 %. Thereafter, the dichlorobutenes are reacted in the liquid phase at 80°C with HCN or an alkali cyanide to butene dinitriles. The formation of 3,4-dicyano-1-butene is not disadvantageous as an allyl rearrangement takes place under the hydrocyanation conditions, in the presence of the copper-cyano complex. Thus a mixture of the cis/trans isomers of 1,4-dicyano-2-butene is obtained with approximately 95 %

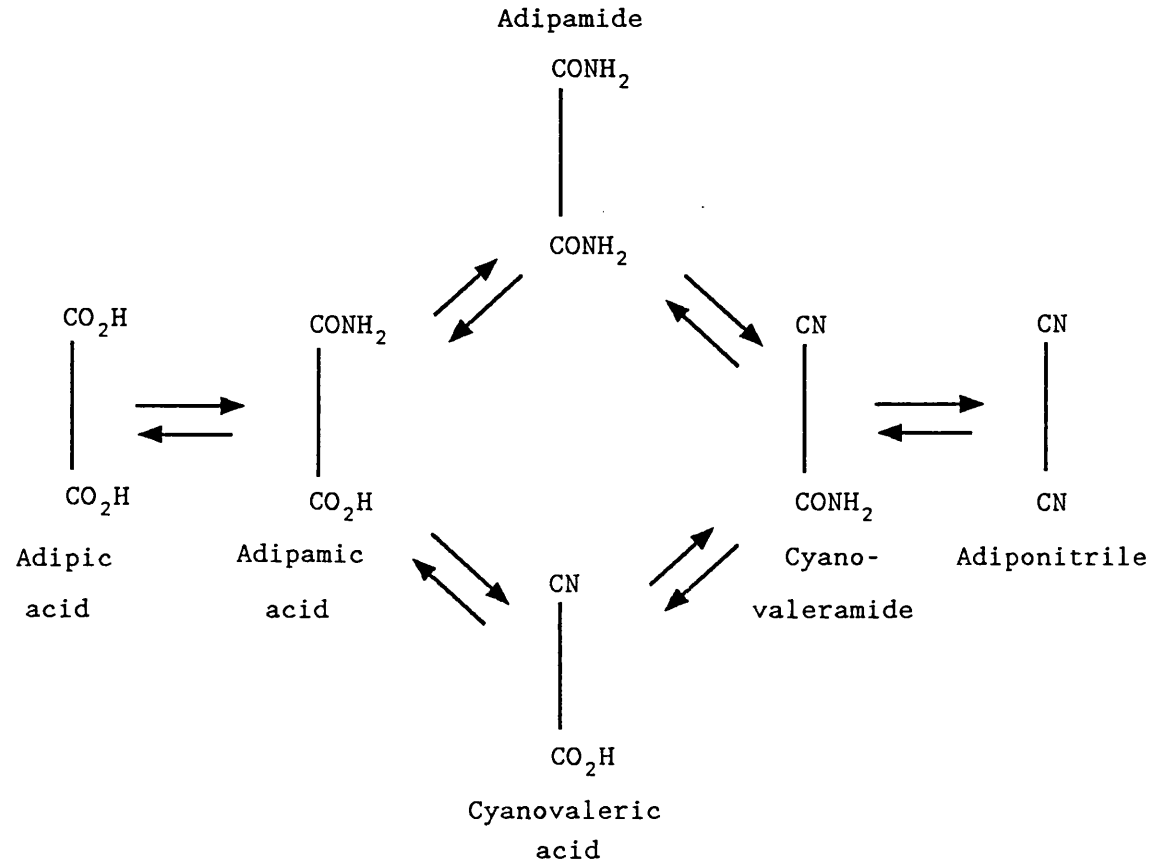

Vertical bar represents $-(CH_2)_4-$

Figure 1.4 Reaction Scheme showing Intermediates in Dehydrative Amination of Adipic Acid to form Adiponitrile.

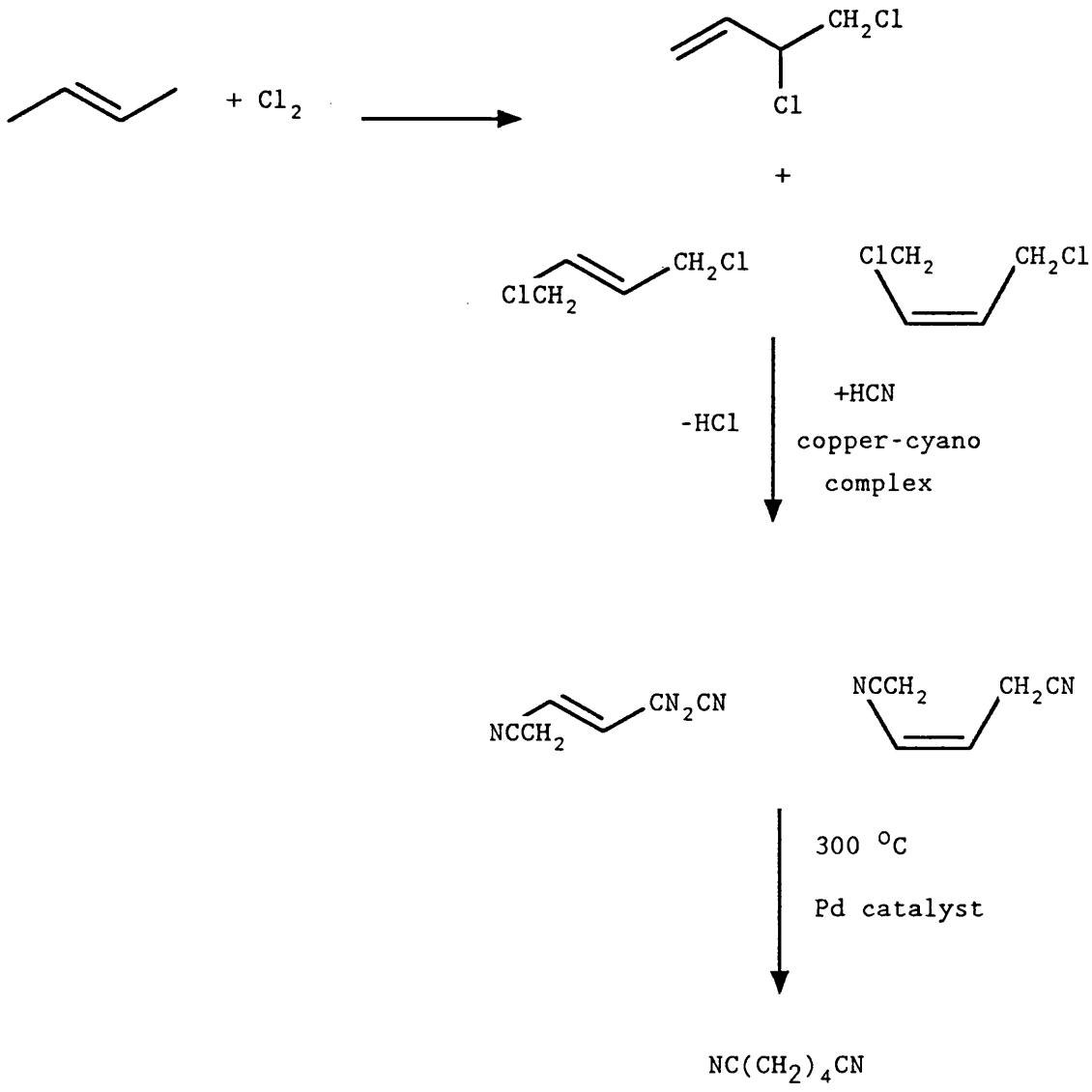

Figure 1.5 Reaction sequence for the production of adiponitrile via the the hydrocyanation of butadiene.

The encapsulation of the metallic iron in silica-supported catalysts may explain some of the chemisorptive and catalytic properties of Fe/SiO_2 catalysts, eg small extents of hydrogen chemisorption at room temperature and the markedly lower Fischer-Tropsch activity of silica-supported iron catalysts compared to alumina-supported catalysts (22).

1.5. Production of Nitriles

In this section an account will be given of routes for the industrial production of nitriles. However, not every synthetic route resulting in the formation of a nitrile need be covered. The ones of most relevance to this thesis are those which lead to 1,4-dicyanobutane, adiponitrile $NC(CH_2)_4CN$. Four routes have been developed for the large scale manufacture of adiponitrile and these will be discussed here.

1.5.1. Dehydrative Amination of Adipic Acid

This process is carried out by ICI, Rhône-Poulenc, and Monsanto, the reaction has been studied on the laboratory scale during the course of this work (42). The reaction is carried out in the presence of excess ammonia at a temperature of 350°C in the presence of a boron phosphate catalyst.

The first step is

$$RCO_2H + NH_3 \rightleftarrows RCONH_2 + H_2O$$

which is approximately thermally neutral, but the second step

$$RCONH_2 \rightleftarrows RCN + H_2O$$

is endothermic and absorbs 84.4 kJ mol^{-1}, i.e. ΔH = +168.8 kJ mol^{-1} for the dinitrile, adiponitrile.

Since adipic acid is bifunctional the process can be depicted as shown in Figure 1.4. The phosphate catalyst (designated X_2P-OH) probably enters into the reaction as shown below

1. $X_2P\text{-}OH + NH_3 \rightleftharpoons X_2P\text{-}NH_2 + H_2O$

2. $X_2P\text{-}NH_2 + RCOOH \rightleftharpoons RCONHPX_2 + H_2O$

2A. $X_2P\text{-}OH + RCONH_2 \rightleftharpoons RCONHPX_2 + H_2O$

3. $RCONHPX_2 \rightleftharpoons RCN + X_2P\text{-}OH$

1.5.2. Indirect Hydrocyanation of Butadiene via the 1,4-Dichlorobutene Intermediate

Butadiene hydrocyanation can take place indirectly via chlorination of butadiene, as shown by the reactions in Figure 1.5. This route has been developed by the Dupont Company (43). The chlorination is carried out in the gas phase at 200 - 300°C without a catalyst. A mixture of 3,4-dichloro-1-butene and cis and trans 1,4-dichlorobutene is obtained, the selectivity being approximately 96 %. Thereafter, the dichlorobutenes are reacted in the liquid phase at 80°C with HCN or an alkali cyanide to butene dinitriles. The formation of 3,4-dicyano-1-butene is not disadvantageous as an allyl rearrangement takes place under the hydrocyanation conditions, in the presence of the copper-cyano complex. Thus a mixture of the cis/trans isomers of 1,4-dicyano-2-butene is obtained with approximately 95 %

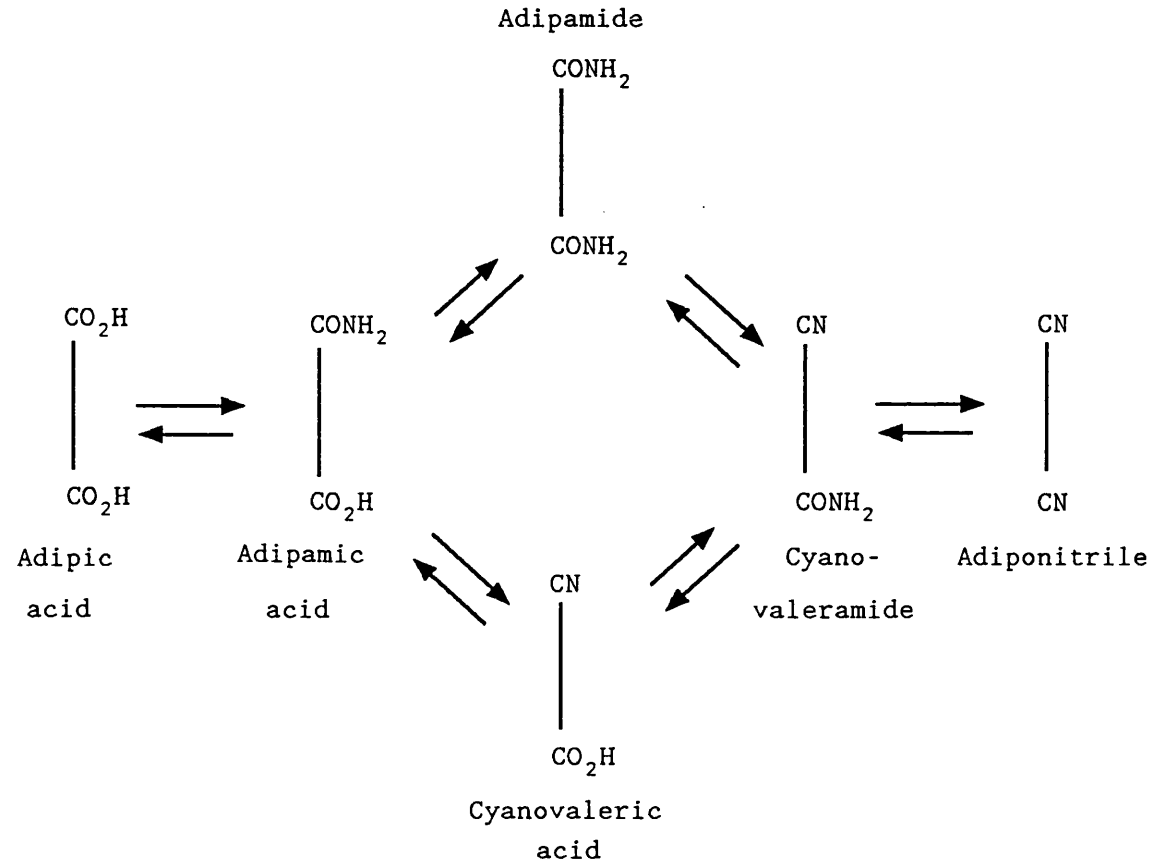

Vertical bar represents $-(CH_2)_4-$

Figure 1.4 Reaction Scheme showing Intermediates in Dehydrative Amination of Adipic Acid to form Adiponitrile.

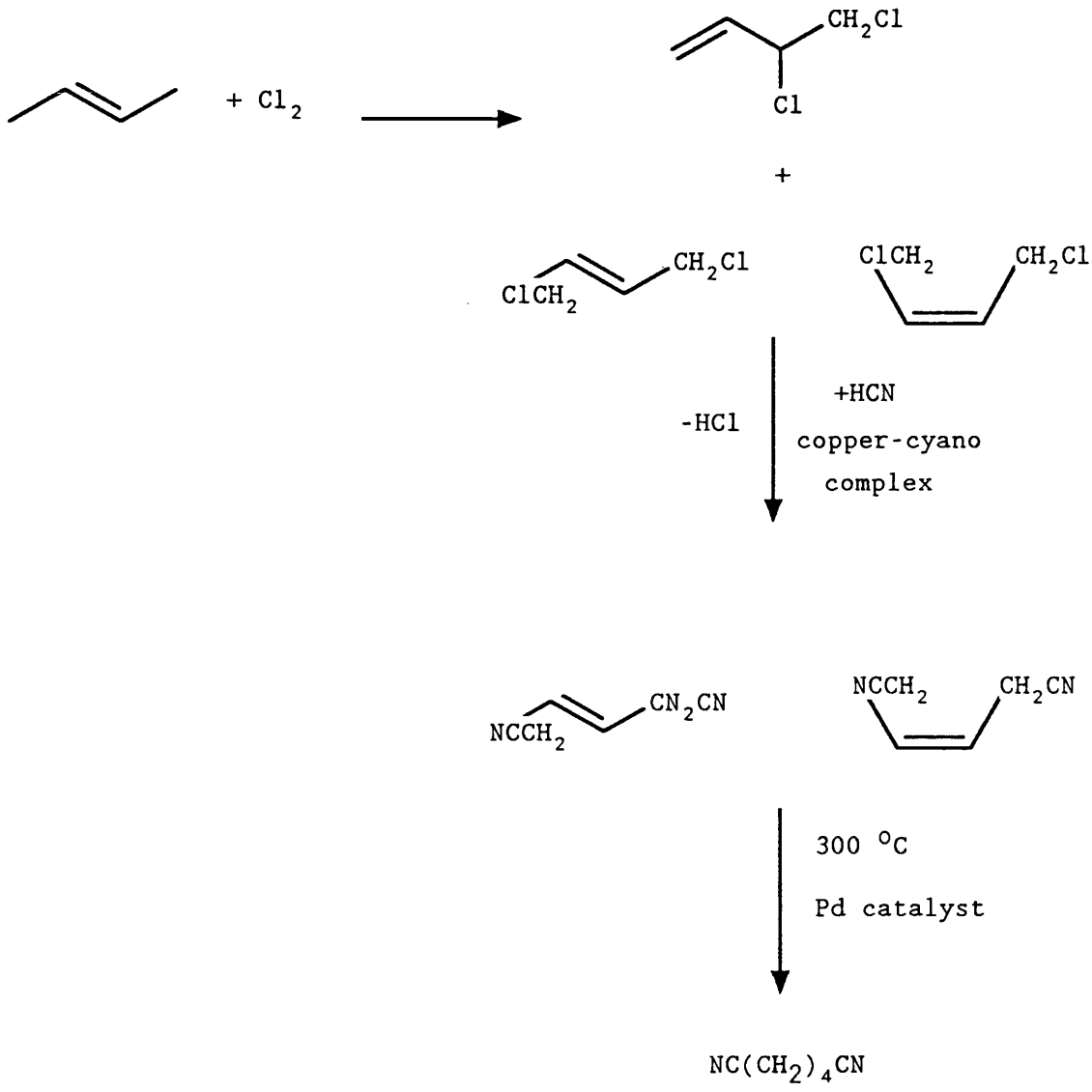

Figure 1.5 Reaction sequence for the production of adiponitrile via the the hydrocyanation of butadiene.

selectivity. The mixture can then be hydrogenated to adiponitrile at 300°C in the gas phase using a Pd catalyst with 95-97 % selectivity.

1.5.3. Direct Hydrocyanation of Butadiene with HCN

The direct hydrocyanation was also developed by DuPont. The reaction takes place at normal pressure and 30 - 150°C in the liquid phase using a solvent such as tetrahydrofuran. Ni^0-complexes with phosphine or phosphite ligands and metal salt promoters, eg zinc or aluminium chlorides are suitable catalysts. The net reaction is said to lead to adiponitrile in high selectivity.

1.5.4. Hydrodimerisation of Acrylonitrile

This method is known as the Monsanto electro-hydrodimerisation process. It is based on the hydrogenative dimerisation of acrylonitrile to adiponitrile as shown below.

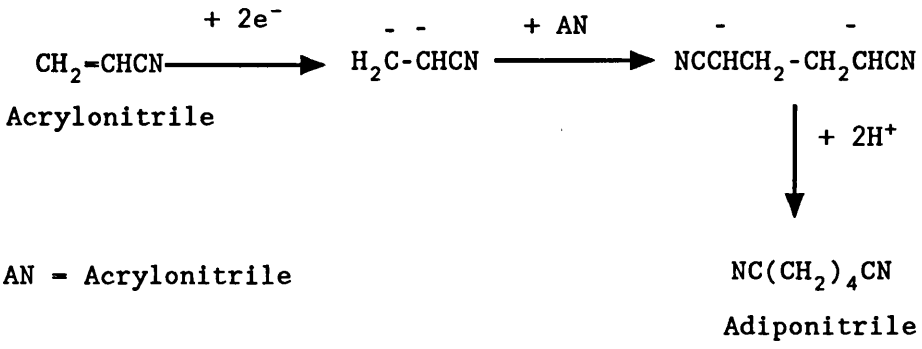

A finely divided two-phase emulsion is rapidly pumped through the cathode anode system. The aqueous phase contains the conducting salt and a small amount of acrylonitrile (

determined by its solubility), whilst the organic phase consists of acrylonitrile and adiponitrile. The more facile transfer of acrylonitrile from the emulsified organic phase to the aqueous phase counteracts the drop in the concentration of the acrylonitrile. The materials used for the anode and cathode are iron and cadmium, respectively.

The conducting salt, a tetraalkylammonium salt, screens so completely with its hydrophobic alkyl groups that no water electrolysis with hydrogen formation can occur. This prevents the hydrogenation of the acrylonitrile and only the organophilic acrylonitrile can be dimerised at the cathode. After passing through the electrolysis cell, part of the organic phase, the non-reacted acrylonitrile and adiponitrile is separated by distillation. The adiponitrile selectivity amounts to approximately 90 %, by products being propionitrile and biscyanoethyl ether.

1.6. Production of Amines

There are two main processes carried out industrially for the production of amines, namely the hydrogenation of nitriles and dehydroamination of alcohols.

1.6.1. Nitrile Hydrogenation

The hydrogenation of nitriles is an important method for the industrial preparation of diverse amines. It is usually carried out in the liquid phase at elevated hydrogen pressures

in the presence of various metallic catalysts. The hydrogenation of adiponitrile and nitriles of fatty acids leading to the corresponding primary, secondary or tertiary amines are among the most important reactions of this type.

In contrast to other hydrogenations which usually proceed relatively simply, in the hydrogenation of nitriles a mixture of compounds is formed, consisting mostly of primary, secondary and tertiary amines. The catalyst represents the most important factor determining the composition of the reaction product: a suitable choice of catalyst can enable one to carry out the hydrogenation with a high selectivity to primary amines, or with an increased selectivity to secondary and tertiary amines.

The majority of data on nitrile hydrogenation has been published in the patent literature. The effect of catalyst type and reaction conditions adopted in the hydrogenation of nitriles has been reviewed by Volf and Pašek (44).

1.6.1.1 Reaction Scheme in the Formation of Primary, Secondary and Tertiary Amines

A mixture of primary, secondary and tertiary amines is usually formed when nitriles are hydrogenated in the presence of metallic catalysts. In the 1920's, a number of investigators tried to explain the formation of secondary amines(45-47). In 1923, Braun et al. (48) published the results of liquid phase hydrogenation of a number of nitriles catalysed by nickel. According to the reaction scheme proposed by these authors, secondary amines are formed as follows. In the first stage the

nitrile is hydrogenated to aldimine, which yields the primary amine upon further hydrogenation.. A 1-aminodialkylamine is

$$RC{\equiv}N \xrightarrow{+H_2} RCH{=}NH \xrightarrow{+H_2} RCH_2NH_2$$

then formed by the reaction between the aldimine and the primary amine. The 1-aminodialkylamine can lose ammonia to

$$RCH_2NH_2 + RCH{=}NH \longrightarrow \underset{\displaystyle NH_2}{\overset{\displaystyle |}{RCH}}\text{-}NH\text{-}CH_2R$$

yield an alkylidenealkylamine which is in turn hydrogenated to a secondary amine. Braun et al. (48) consider that the

$$\underset{\displaystyle NH_2}{\overset{\displaystyle |}{RCH}}\text{-}NH\text{-}CH_2R \xrightarrow{-NH_3} RCH{=}N\text{-}CH_2R \xrightarrow{+H_2} RCH_2NHCH_2R$$

secondary amine can also be formed by the hydrogenolysis of the 1-aminodialkylamine. The experimental fact established by these

$$\underset{\displaystyle NH_2}{\overset{\displaystyle |}{RCH}}\text{-}NH\text{-}CH_2R \xrightarrow{+H_2} RCH_2NHCH_2R + NH_3$$

authors, that the content of secondary amines increases with the nitrile concentration in hydrogenations carried out in a solvent is in accord with the scheme proposed for the formation of secondary amines.

Braun's scheme was later verified by a number of investigators (49-52). Greenfield (53) presented a similar scheme for the formation of tertiary amines, and maintained that they are formed analogously by the reaction between the aldimine and the secondary amine. According to this author,

$$RCH{=}NH + (RCH_2)_2NH \longrightarrow \underset{\displaystyle NH_2}{\overset{\displaystyle |}{RCH}}\text{-}N\begin{matrix}\diagup CH_2R \\ \diagdown CH_2R\end{matrix}$$

tertiary amines are formed by hydrogenolysis of substituted 1-aminotrialkylamines. According to Wheeler (54), tertiary

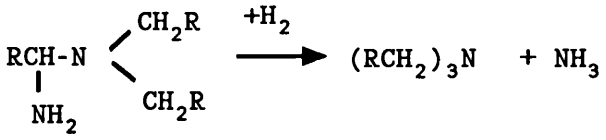

amines could be formed via an intermediate enamine originating (similarly to imines) by elimination of ammonia from the 1-aminotrialkylamine and the tertiary amine could be formed by

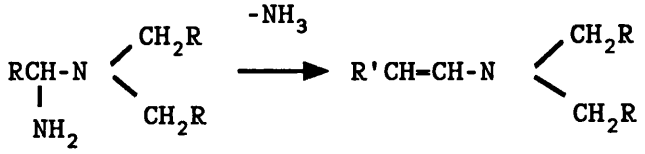

hydrogenation of the enamine

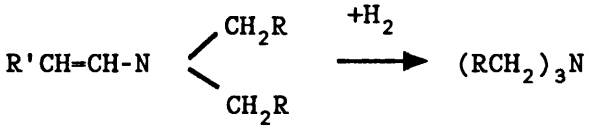

1.6.1.2. Hydrogenation of Adiponitrile

Adiponitrile is hydrogenated to hexamethylenediamine (HMD) using an iron catalyst at 100-180°C and 300-350 bar (1)

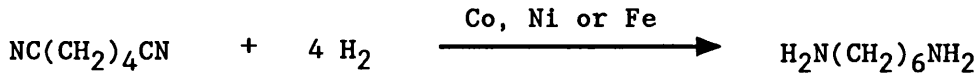

$\Delta H = -314$ kJ mol^{-1}

1.6.2. Dehydroamination of Alcohols

The dehydroamination of alcohols has been reviewed by Baiker and Kijenski (55). The catalysts commonly used include nickel, copper and cobalt. The reaction is normally carried out at 150-250°C at pressures of up to 300 bar.

HMD is manufactured by Celanese (USA) using this method, as shown below. Caprolactone is first hydrogenated to

1,6-hexanediol. The reaction conditions are 250°C and 280 bar. Adipic acid or hydroxycaproic acid may also be used as starting materials for the production of 1,6-hexanediol. Hexanediol is then aminated at 200 °C and 230 bar, with ammonia in the presence of Raney-nickel, to HMD.

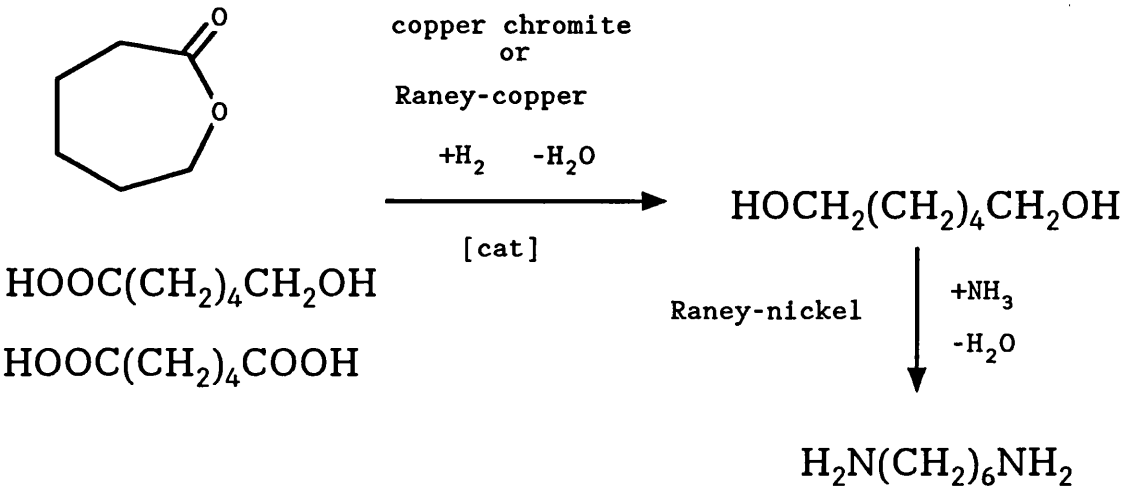

1.7. Nylon Production

Polyamides or nylons are polycondensation products of diamines with dicarboxylic acids or aminocarboxylic acids as well as being polymerisation products based on lactams.

Polyamides are designated using a code, according to which one figure represents synthesis from a single bifunctional compound (aminocarboxylic acid or lactam). Two figures signify synthesis from two components (diamine and dicarboxylic acid). The digits themselves represent the number of carbon atoms in the components. The codes and starting materials for industrially significant polyamides are contained in Table 1.1.

Table 1.1 Code and Starting Materials for Industrially Significant Polyamides

Nylon Code	Starting Materials	Formula
6	ϵ-Caprolactam	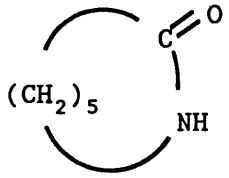
6,6	Hexamethylenediamine Adipic Acid	$H_2N(CH_2)_6NH_2$ $HOOC(CH_2)_4COOH$
6,10	Hexamethylenediamine Sebacic Acid	$H_2N(CH_2)_6NH_2$ $HOOC(CH_2)_8COOH$
6,12	Hexamethylenediamine 1,12-Dodecanedioic Acid	$H_2N(CH_2)_6NH_2$ $HOOC(CH_2)_{10}COOH$
11	ϵ-Aminoundecanoic Acid	$H_2N(CH_2)_{10}COOH$
12	Lauryl Lactam	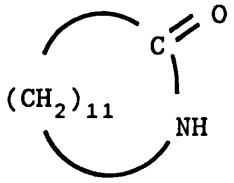

1.7.1. Nylon 6,6

Nylon 6,6 was first discovered by Carothers (56) in 1933 and first produced by DuPont on an industrial scale in 1939.

A schematic diagram showing the steps involved in the production of nylon 6,6 is shown in Figure 1.6. Adipic acid is produced via the oxidative cleavage of cyclohexane (57). Cyclohexane is oxidised to a mixture of cyclohexanol and cyclohexanone at 125-165°C and 8-15 bar pressure in the liquid phase using either a Mn- or Co-naphthenate catalyst. The ketone-alcohol mixture is then oxidised to adipic acid. Two processes are currently in use, one involves oxidation using HNO_3 and an ammonium metavanadate/ copper nitrate catalyst, the other uses air and a copper manganese acetate catalyst. The adipic acid is converted to adiponitrile, which is then hydrogenated to HMD. Finally HMD is polymerised with further adipic acid to form nylon 6,6

Hexamethylenediammonium adipate (nylon 6,6 salt) is made by mixing stiochiometric proportions of HMD and adipic acid in water. The salt solution is adjusted to the proper pH (7.6) and concentration prior to the polymerisation process. A 9.5 % aq solution of the salt has a pH of 7.6. When the crystalline salt is desired, methanol is used as the solvent, this is used because the salt is only 0.4 % soluble at 25°C. The salt of nylon 6,6 forms white diamond-shaped monoclinic crystals melting at 190-191°C.

Conversion of the salt to polymer involves heating to a temperature at which the condensation of $-NH_2$ and $-CO_2H$ groups

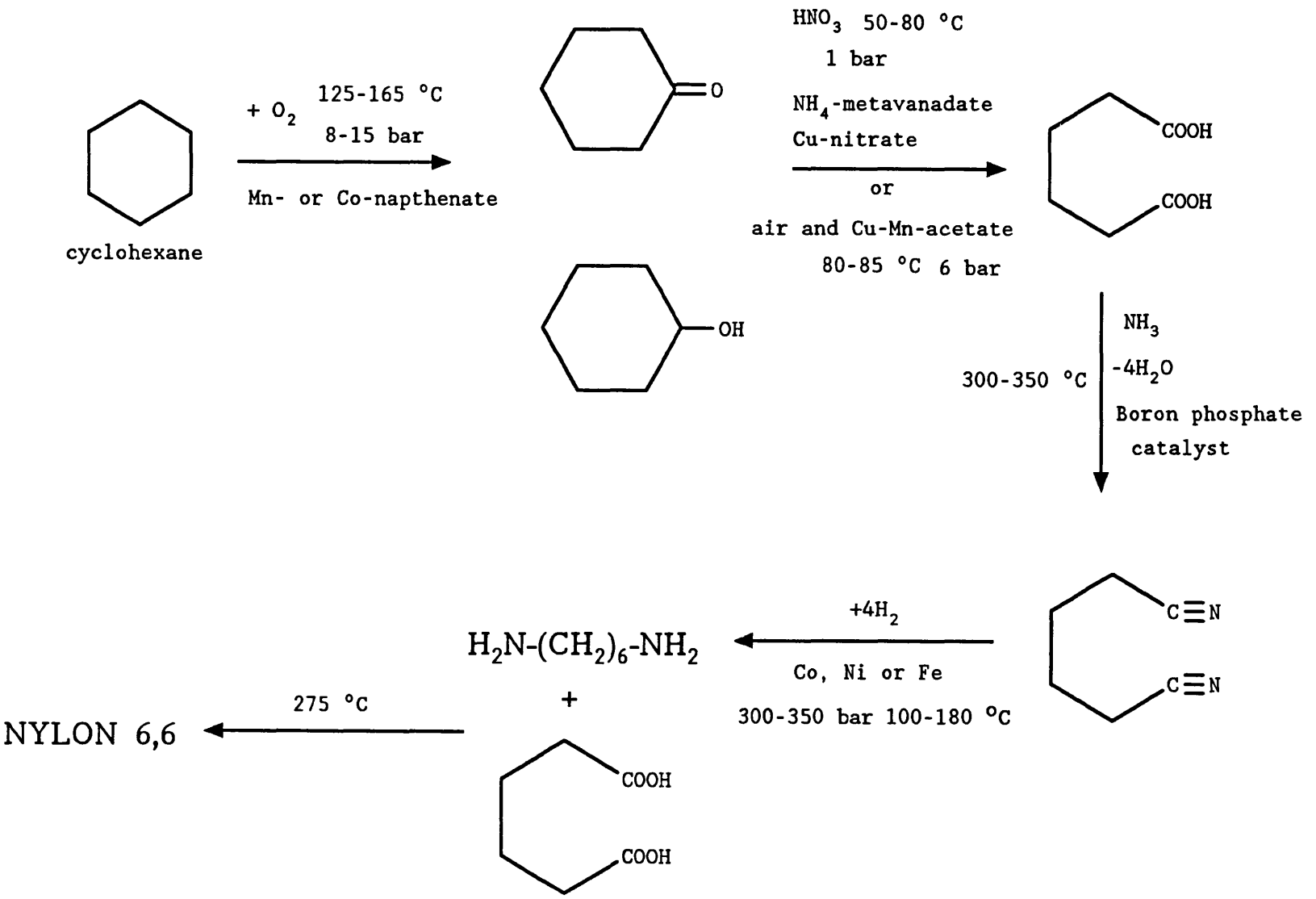
cyclohexane
+ O_2
125-165 °C
8-15 bar
Mn- or Co-napthenate
O
OH
HNO_3 50-80 °C
1 bar
NH_4-metavanadate
Cu-nitrate
or
air and Cu-Mn-acetate
80-85 °C 6 bar
COOH
COOH
NH_3
$-4H_2O$
300-350 °C
Boron phosphate
catalyst
C≡N
C≡N
+$4H_2$
Co, Ni or Fe
300-350 bar 100-180 °C
$H_2N-(CH_2)_6-NH_2$
+
COOH
COOH
275 °C
NYLON 6,6

occurs, releasing water and forming -CONH- linkages. The operation must prevent loss of the amine component of the salt when the stream is released during heating so that proper reactant balance is maintained and sufficiently high molecular weights are attained. Commercial polymerisation of nylon 6,6 is controlled by temperature and equilibrium water concentration in the melt. In practice it has been found to be convenient to control the average chain length by addition of small amounts of monofunctional reactants (eg 0.2-1.5 % acetic acid) which react with the $-NH_2$ groups and prevent further growth at these ends. The number average molecular weight is given by $M_n = 2x10^6/([-CO_2H]+[-NH_2]+[\text{stabiliser}])$. The equilibrium number average molecular weight of nylon 6,6 containing 0.75 % acetic acid stabiliser at 275 ^oC under 1 atm of steam is approximately 14,000. The world wide production in 1976 amounted to 2.7 million tonnes, 90 % of which was used in the manufacture of fibres 10 % for thermoplastic moulding materials.

2.1. The Preparation of Fe / MgO Catalysts

2.1.1. Nomenclature

An important factor in describing supported metal catalysts is the metal loading. Different workers adopt different definitions of metal loading and therefore it is essential that a clear definition is given. The iron loadings of the catalysts studied in this work are expressed as atom % Fe i.e. atom fraction $\frac{Fe}{Fe + Mg} \times 100$.

A similar method of nomenclature to that of Topsøe et al (3) has been adopted to describe catalysts prepared by different methods. Catalysts prepared from the impregnation of magnesium hydroxycarbonate are denoted as IP x% where x denotes the iron loading as described previously. Catalysts prepared by coprecipitation using either OH^- or CO_3^{2-} as the precipitating ion are denoted as OH x% or CCP x% respectively. A catalyst derived from the iron hydrotalcite, pyroaurite, is referred to as HT1.

2.1.2. Preparation of catalyst precursors

Supported iron catalysts have been prepared using magnesium oxide as a support material. Various techniques were employed in the preparation of the catalyst precursors which had loadings in the range 5-30 %. Accurate loadings have been determined using Atomic Absorption Spectroscopy (AAS). One

exception was a catalyst sample prepared using enriched ^{57}Fe with a 1% loading. This was a special sample prepared for Mössbauer spectroscopy studies to enable information to be gained on the iron species present in catalysts with low loadings. Catalysts of low loading do not lend themselves to investigation by techniques such as X-ray diffraction or UV-visible spectroscopy, but by using enriched ^{57}Fe it is possible to make a study using Mössbauer spectroscopy.

Table (2.1) lists the source and nominal purity of the starting materials used.

(a) Ammonium carbonate precipitated precursors

A mixture of 1 M $Fe(NO_3)_3$ and 1 M $Mg(NO_3)_2$ solutions in varying mole ratios was heated in a stirred vessel to a temperature of 358-363 K. 1.0 M $(NH_3)_2CO_3$ was added dropwise from a burette until an excess of the precipitating agent was present. The resulting precipitate was washed with distilled water and filtered. The solid was then dried at 373 K prior to being calcined at 773 K in air. This resulted in the production of the catalyst precursor.

(b) Ammonium hydroxide precipitated precursors

Mixtures of 1 M $Fe(NO_3)_3$ and $Mg(NO_3)_2$ solutions in varying mole ratios were added dropwise to a stirred vessel containing ammonia solution at 303 K. The pH of the reaction mixture in the reaction vessel was monitored using a pH meter.

Table 2.1 Nominal Purities and Suppliers of the Materials used in the Preparation of the Catalysts

Substance	Supplier	Purity / %
Iron (III) nitrate $Fe(NO_3)_3 .9H_2O$	BDH	98
Magnesium nitrate $Mg(NO_3)_2 .6H_2O$	BDH	99
Ammonium carbonate $NH_4HCO_3.NH_2COONH_4$	BDH	95.3
Magnesium carbonate basic, heavy	Fluka	
Ammonia Solution 0.88 specific gravity	Fisons	35 % NH_3
Enriched ^{57}Fe	UKAEA (Harwell)	95.7 % ^{57}Fe

The pH within the vessel was maintained at pH 11 by further additions of ammonia solution. The resulting precipitate was washed, dried and calcined as described previously. The catalyst prepared using the sample of enriched ^{57}Fe was prepared using this method

(c) Precursors derived from the hydrotalcite structure

Catalyst precursors have been prepared from the iron hydrotalcite, pyroaurite $Mg_6Fe_2(OH)_{16}CO_3$, using a method previously described (58). The starting precipitate was formed by combining two solutions. Solution 1 consisted of 300 cm^3 1 M $Mg(NO_3)_2$ and 100 cm^3 1 M $Fe(NO_3)_3$, solution 2 400 cm^3 0.125 M $(NH_4)_2CO_3$. Solution 1 and 2 were simultaneously pumped using a peristaltic pump at a rate of 70 cm^3 h^{-1} into a stirred reaction vessel, the temperature of which was kept constant at 323 K. During the reaction the pH in the reaction vessel was monitored using a pH meter and maintained at pH 9.8 by the addition of NH_4OH. The resulting precipitate was washed, filtered and dried in air prior to being calcined in the manner described above.

(d) Preparation of catalyst precursors by impregnation

The precursors were prepared by the method described by Boudart et al (2). A slurry of 10 g of magnesium carbonate (hydrated basic heavy) in 160 ml of distilled water was stirred with a mechanical stirrer and heated to 340 K. Then 160 ml of

aqueous ferric nitrate solution preheated to 340 K was added rapidly to the slurry. The molality of the solution was the only variable changed in preparing catalysts with different iron loadings. After stirring for 30 minutes at 340 K, the slurry was washed and dried under vacuum at 360 K for 12 hours. This was then calcined as described previously to produce the catalyst precursor.

2.1.3. Activation of the Catalyst Precursors

In order for the catalyst precursors to become active as catalysts it was first necessary to obtain some of the iron in the Fe^0 oxidation state. This reduction was carried out in a static system using hydrogen as the reducing agent. A similar heating program to that of Boudart et al.(2) was adopted. The heating program consisted of heating the catalyst in hydrogen at a pressure of 30 Torr for a period of 24 hours at 553 K, 24 hours at 623 K, and 24 hours at 693 K. The water vapour produced during the reduction process was frozen out using a 77 K cold trap. This reduction procedure was used as the standard procedure for catalyst activation unless otherwise stated.

It has been shown by several authors that it is not possible to obtain total reduction of the iron containing species to the Fe^0 oxidation state. The extent of reduction has been monitored using the gravimetric and volumetric systems described in Section 2.2. The gravimetric system measured the weight lost by the sample during the reduction process and

related this to the loss of oxygen from the iron containing species. In the volumetric system the reduction was carried out in a section of known volume and the hydrogen uptake was monitored by the pressure transducer.

2.2. Adsorption Apparatus

Two sets of equipment have been used to make adsorption measurements carried out at the University of Bath; both high vacuum frames were made of glass. One relied on measuring the volume of gas adsorbed and will be referred to as the volumetric system. The second incorporated a vacuum microbalance for making measurements of the mass of gas adsorbed and this will be referred to as the gravimetric system.

2.2.1. The Volumetric System

The volumetric frame is illustrated in Fig 2.1 and was a slightly modified version of the apparatus constructed by Rennison (59). The frame was constructed from Pyrex glass and was evacuated using a rotary oil pump and water-cooled mercury diffusion pump protected by a liquid nitrogen cold trap. Using this pumping system pressures of 3 $x10^{-6}$ Torr were obtainable within the frame. The system incorporated four electrical pressure measuring devices and a McLeod gauge. Two of the former were of the Pirani type (G 6B DO24-11-000) (P1,P2), measuring pressures in the range 1 atmosphere to 1 $x10^{-3}$ Torr.

DP = Mercury Diffusion Pump

CT = Liquid Nitrogen Cold Trap

RP = Oil Rotary Pump

M_1 = McLeod Gauge (10^{-3} - 10^{-6} Torr)

M_2 = McLeod Gauge (10^{-1} - 10^{-4} Torr)

M_3 = Mercury Manometer

GB = Gas Burette

P_1 = Pirani Gauge

P_2 = Pirani Gauge

P_3 = Penning Gauge

P_4 = Pressure Transducer (0 - 50 Torr)

PT = Pressure Transducer (0 - 5

MB = Vacuum Microbalance

SB = Sample Bulb

 = Ground Glass Tap

 = Young's Greasless Tap

Key for Figures 2.1 and 2.2

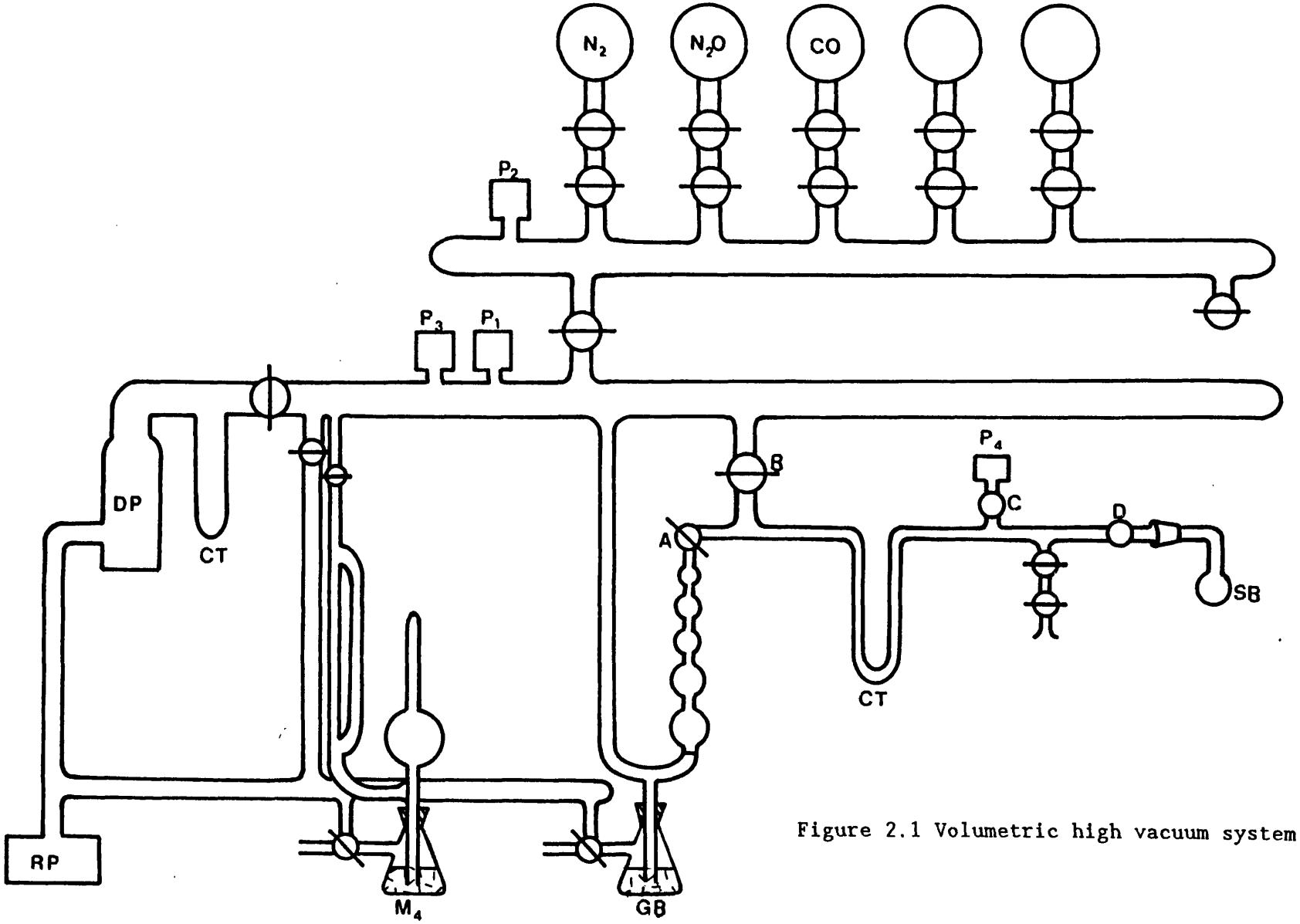

Figure 2.1 Volumetric high vacuum system

The third was a Penning gauge model 6 (P3) with an operating range of 1 $x10^{-3}$ to 1 $x10^{-6}$ Torr. The fourth was a pressure transducer (Bell and Howell BHL-4105-00) (P4) with a linear operating range of 0-50 Torr. This transducer was connected to a digital voltmeter. When calibrated this provided a more accurate means of measuring the pressure within the frame than the analogue reading provided by the transducer alone.

The volumes of the individual bulbs of the gas burette (GB) were calibrated by removing this section of the frame, filling with mercury to the corresponding marks and weighing. This gave an accurate calibration of the gas burette. The burette could then be used to calculate the volume contained within the section ABC and the volume of the sample bulb; this was carried out with the trap area at 77 K.

2.2.2. The Gravimetric System

The gravimetric frame is shown in Fig 2.2 and was originally purpose built for adsorption studies of cyano compounds by Lockyer (60). This frame was constructed of Pyrex glass and contained a number of features which were not used during the present work. For the studies to be described, the system can be considered to consist of two sections. The first is a gas handling section consisting of a rotary oil pump and water-cooled mercury diffusion pump. The hot mercury in the diffusion pump was protected from oxidising vapours by an in-line cold trap (CT1). This allowed pressures in the range of

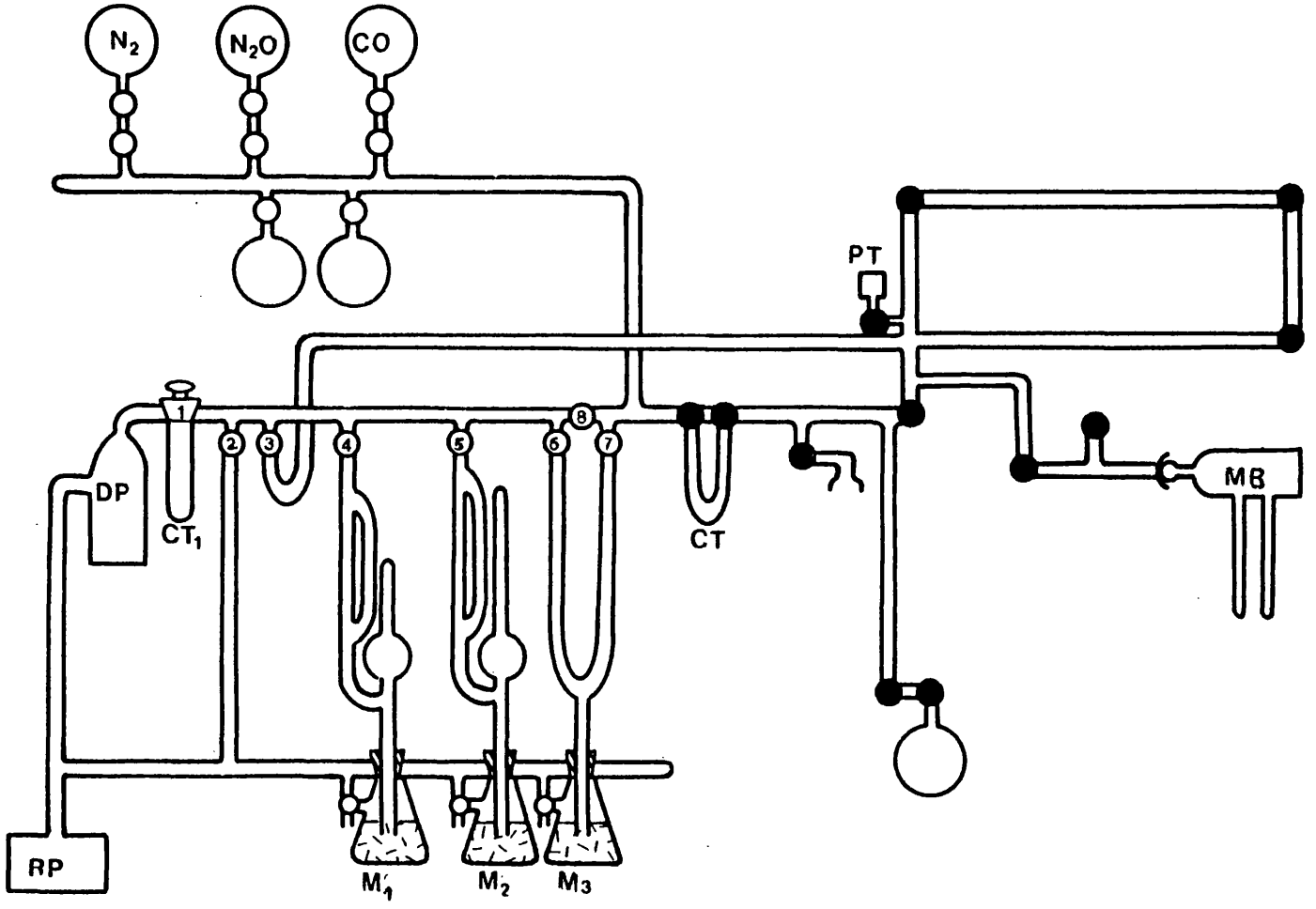

Figure 2.2 gravimetric high vacuum system

2 x10^{-6} Torr to be obtained. Also contained in this section were two McLeod gauges (M1 and M2). These had ranges from 10^{-1} to 10^{-4} Torr and 10^{-3} to 10^{-6} Torr respectively. A mercury manometer (M3) was also included in order to measure higher pressures encountered during adsorption experiments. The taps in this section were conventional ground glass taps sealed with Apiezon N grease. A gas inlet was also incorporated into the system through which the gas storage bulbs could be filled.

The second section housed the microbalance. This was a standard C.I. Electronics MK II balance contained in a Pyrex vacuum jacket. It was connected to the vacuum frame via a greaseless joint sealed with a Viton O-ring. In this section Young's greaseless taps were used throughout to prevent sample contamination by grease. The microbalance head was protected from vibrations, caused by the rotary pump, by supporting it in foam rubber padded clamps.

The balance operated by generating a current directly proportional to the weight of the sample. This provided an electrical output to a pen recorder. The current was generated when the microbalance arm moved, since it carried an aperture which permitted light from an internal source to impinge on a pair of photocells. Movement of the arm caused a change in the relative illumination of these cells causing an excess current to flow across an electrical bridge. When amplified this current restored the beam to its equilibrium position. The balance head was contained in a black cardboard sleeve which protected the photocells from exposure to external light and thus prevented signal interference. The sample was contained in

a bucket constructed from aluminium foil attached to the microbalance head via a long suspension fibre. The sample bucket was contained in a silica hangdown tube connected to the microbalance jacket via a greaseless joint. The temperature of the sample was measured using a chromel-alumel thermocouple whose junction was situated adjacent to the sample bucket.

The microbalance was capable of measuring weight changes in the range 25 μg - 100 mg, over five sensitivity ranges. The output from the balance was plotted as a function of time on a Gould Bryans flat bed chart recorder (series 270). Only the less sensitive ranges were usable in the work carried out due to the large weight changes incurred during the reduction process. The microbalance was calibrated by adding weights of known mass and measuring the deflection on the chart recorder.

2.3. Total Surface Area and Pore Size Distributions using Nitrogen Adsorption Isotherms

2.3.1. Theory

The total surface areas of catalysts studied were determined by physical adsorption using the BET equation.

$$\frac{P}{V(P_0-P)} = \frac{1}{V_m c} + \frac{(C-1)P}{V_m c P_0} \qquad (2\text{-}1)$$

where V is the total volume adsorbed at pressure P, P_0 is the saturation vapour pressure of the adsorbate, V_m is the volume of gas needed to form a monolayer, and c is a constant. The most common adsorbate used is nitrogen and this has been

used throughout this work, although other gases may be used in the determination of surface areas.

A plot of $\frac{P}{v(P_0-P)}$ vs $\frac{P}{P_0}$ for values of P/P_0 between 0.05 and 0.35 should give a straight line of slope $\frac{(C-1)}{V_mC}$ and intercept of $\frac{1}{V_mC}$. Hence

$$V_m = \frac{1}{\text{slope + intercept}} \qquad (2\text{-}2)$$

The volume of the monolayer is then corrected to STP and the number of nitrogen molecules contained within calculated. The effective area occupied by each adsorbed nitrogen molecule can be calculated from the density of liquid nitrogen (0.81 gcm^{-3}) on the basis of a model of close-packed spheres. The value so obtained is 16.2×10^{-20} m^2. Hence the area of the monolayer can be calculated, dividing by the mass of catalyst yields the specific surface area of the catalyst.

Increasing the pressure in incremental steps to the saturation pressure yields a complete adsorption isotherm. The desorption isotherm is produced via the stepwise reduction in pressure while monitoring volumes and equilibrium pressures. In the case of porous solids the adsorption and desorption isotherms do not coincide, i.e. there is hysteresis. The origin of adsorption hysteresis is still much debated, this topic has been covered in some detail by Gregg and Sing (61).

The Kelvin equation for the adsorption side is given by

$$\ln \frac{P_a}{P_s} = - \frac{2\gamma V \cos\theta}{RTr_k} \qquad (2\text{-}3)$$

where P_a, P_s, γ and V are the observed equilibrium pressure on adsorption, the saturated vapour pressure, the surface tension

and molar volume of the liquid adsorbed, θ is the wetting angle, and r_k is the radius of the cylindrical pore. At P_s, however, the wetting is complete, consequently, for the desorption branch cosθ=1. This explains why P_d the equilibrium pressure on desorption is less than P_a for a given amount adsorbed. It also follows that the desorption branch corresponds to the true capillary condensation equilibrium. Hence the desorption branch is most commonly used in the determination of pore structure . Therefore equation (2-3) becomes

$$r_p = \frac{2\gamma V}{RT \ln (P_o/P_s)} + t \qquad (2\text{-}4)$$

The majority of models for pore structure analysis are based on either parallel plates (62) or cylinders (63), although the analysis can be made without assuming a pore shape (64). This method, while having been shown to be adequate for many purposes, does also have limitations.

2.3.2. Experimental Determination of Surface Area and Pore Size Distribution

Total surface area and pore size measurements have been obtained from nitrogen adsorption and desorption isotherms obtained at 77 K. The total surface area measurements were obtained from adsorption isotherms using both the volumetric and gravimetric systems described in Section 2.2. Pore size distributions were measured from adsorption and desorption isotherms obtained at ICI Wilton using a Digisorb instrument (Micromeritics Instrument Corporation).

(a) Volumetric Frame

A sample weighing ≈0.5g was installed in the volumetric system shown in Fig. 2.1 and outgassed in vacuo at 393 K overnight. With tap D closed nitrogen (white-spot) was admitted into the gas burette. Tap A was closed and section ABCD was re-evacuated. The N_2 pressure in the burette was measured using a cathetometer. Tap B was then closed and taps A and D opened to admit N_2 to the sample. The system was allowed to reach equilibrium (approx 30 mins), after which the pressure was remeasured. The mercury level within the gas burette was then raised systematically one bulb at a time, thereby reducing the volume of the system and therefore increasing the equilibrium pressure, and in this way the adsorption isotherm was obtained. The surface area was obtained from the data as described previously.

(b) Gravimetric Frame

A sample weighing ≈0.2 g was mounted on the microbalance and outgassed in vacuo at 393 K overnight. The sample was cooled using liquid N_2,taps A and I(Fig. 2.2) were closed and the sample was exposed to N_2 from the storage bulb. The adsorption process was monitored using the microbalance. When the system had reached equilibrium, i.e. no further deviation of the recorder pen, the nitrogen pressure was increased incrementally and the new adsorption equilibrium was determined. Successive admissions enabled the isotherm to be measured. The nitrogen pressure was measured using the mercury manometer, the levels being read using a cathetometer.

(c) Digisorb apparatus

The Digisorb apparatus (Fig. 2.3) consisted of Monel metal multivalve manifold system interconnecting five samples for analysis and five samples for outgassing, a vacuum system, a pressure measuring system and a PDP-8/m computer coupled with a PET microcomputer.

The vacuum system consisted of a mechanical forepump, a diffusion pump, a cold trap, and a sorption pump. The forepump and diffusion pump produced an ultimate vacuum of 10^{-6} Torr, the purpose of the cold trap being to trap troublesome gases and vapours. The function of the sorption pump was to remove any material outgassed from the reference side of the pressure heads and to maintain a good reference vacuum.

The pressures within the manifold were measured by two differential capacitance-type pressure sensors; one side of each was maintained at a high vacuum and was termed the reference side. These sensors consisted of tightly stretched metal diaphragms placed between two stationary reference electrodes. Pressure differentials deflected the diaphragms resulting in a change in the electronic capacitance. The pressure sensors had ranges of 0-1000 Torr with an accuracy of 0.1 Torr.

The samples were outgassed at 398 K,and the sample bulbs were then filled with helium, prior to being transferred to the analysis section of the instrument. The helium was not adsorbed at room temperature and helped to prevent the samples from being recontaminated with atmospheric gases during the transfer to the analysis section. It was at this stage that the sample

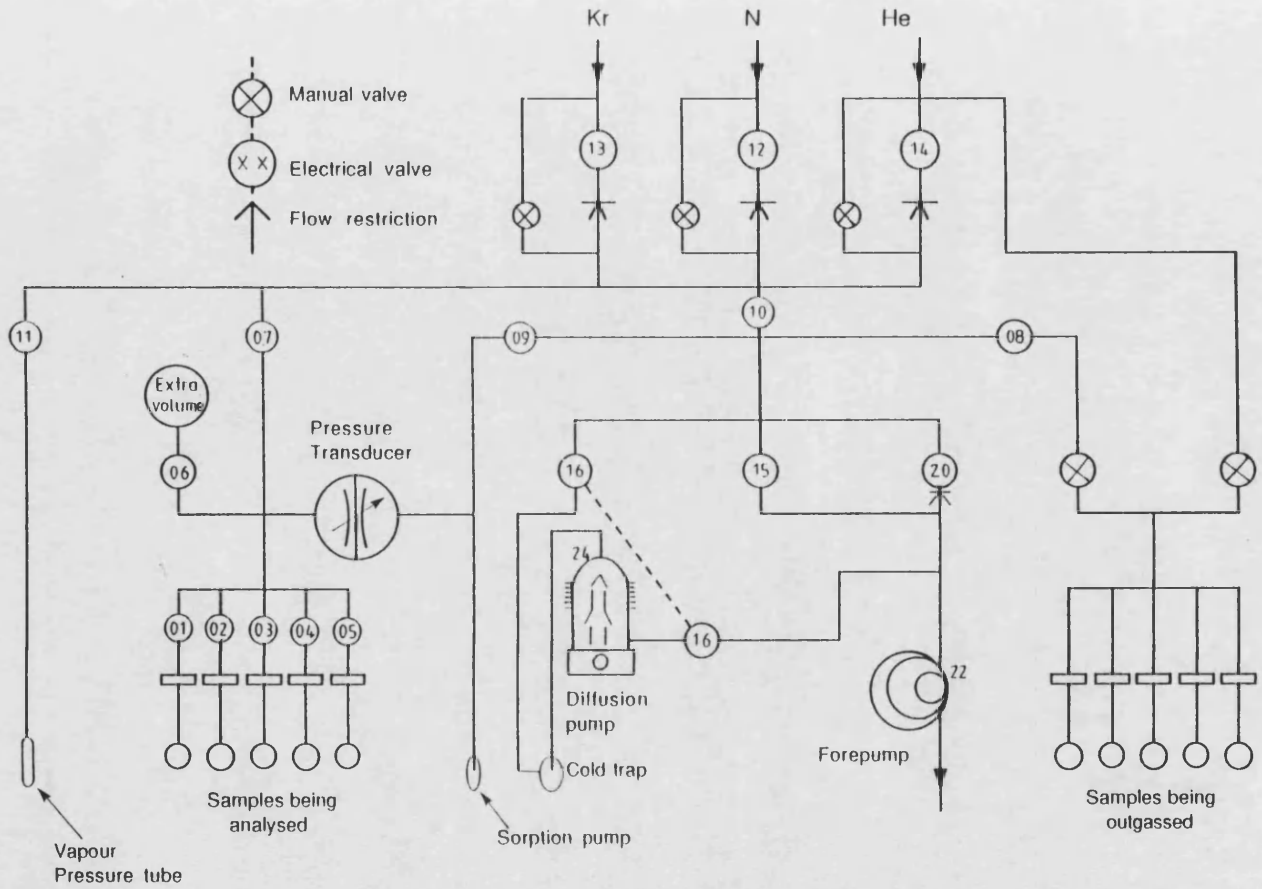

NOTE: The cold trap, sorption pump, vapor pressure tube and samples being analyzed are immersed in the Dewar flask of liquid nitrogen during the analysis

Figure 2.3 Scematic diagram of the Digisorb apparatus

weight was recorded.

Once the sample vessels had been connected to the analysis section they were evacuated. The instrument automatically checked the leak or outgassing rate. If the rate of pressure increase was less than 0.03 Torr min^{-1}, the instrument proceeded with the adsorption routine. If the rate exceeded this value then the samples were evacuated further and the leak rate was measured again. If still unsatisfactory a leak check was performed and those samples which failed this were excluded from further analysis. For those samples which outgassed without leaks, the instrument then expanded helium from the distribution manifold into the evacuated sample. Both before and after the expansion the pressure was measured. The manifold volume was known, and as the amount of helium adsorbed was negligible, the free sample space ("dead space ") was computed from the ideal gas equation.

The nitrogen adsorption was carried out with the sample at 77 K. The adsorption or desorption proceeded in a closed system at an ever decreasing rate towards equilibrium. In practice, equilibrium may be established in a matter of minutes or it may require hours. The Digisorb assumed equilibrium to have been attained when seven consecutive measurements, each taken at 6 second intervals, differed from the mean by 0.1% or less. The instrument made 21 incremental additions of nitrogen to produce an adsorption isotherm with 21 points, three of which were used to calculate the BET surface area. The desorption isotherm was produced by reducing the equilibrium pressure in 21 stages giving a desorption isotherm with 21

points

The instrument also determined the saturation pressure of the adsorbate, in this case nitrogen. This was achieved by condensing nitrogen in a small glass tube which was immersed in the sample Dewar and measuring its vapour pressure. The saturation pressure was monitored at 2 hour intervals during the analysis, the value being stored and used in the calculation of the relative pressure.

2.4. The Determination of Iron Surface Area and Dispersion

2.4.1. Introduction

The quantitative characterisation of the exposed reactive surface is a matter of obvious importance in the study of catalytic reactions on supported metals. Since most supported metals exist as a large number of non identical sub micron particles, the problem of surface area determination is much more difficult than for materials with macroscopic dimensions. Terms such as particle size distribution or dispersion are somewhat ambiguous when applied to a system of particles which can be inhomogeneous in both size and shape. The problem is compounded by the fact that different experimental techniques are sensitive to different parts of a given particle size distribution and as a result, two or more methods can easily give vastly different results.

It is the aim of this section to discuss the use of chemisorption techniques in the determination of the reactive surface area and dispersion of the iron in the catalysts. Much of the pioneering work with regard to low temperature chemisorption of a variety of gases on different commercial catalysts has been performed by Brunauer, Emmett and coworkers (H_2 (64), O_2, CO, CO_2, Ar, CH_4, NO, N_2O, NH_3 and C_4H_{10} (65-69). In more recent times CO chemisorption has been used by Boudart et al.(2) and this technique may now be regarded as the standard method for the determination of iron surface areas. Hence in this work we have chosen to use carbon monoxide chemisorption, as this is undoubtedly the most frequently applied technique to measure metallic iron surface areas of supported catalysts. Complementary measurements have also been made using nitrous oxide decomposition which has received considerably less attention in the determination of iron surface areas.

2.4.2. Carbon Monoxide Chemisorption

Carbon monoxide adsorption measurements have been made both gravimetrically and volumetrically using the apparatus described previously.

The technique required the determination of two isotherms at 195 K. The sample, having undergone the activation procedure described in Section 2.13, was allowed to cool to ambient temperature during which the hydrogen was evacuated. Although it is essential to remove any adsorbed hydrogen from the sample

prior to admitting any CO it must be noted that the evacuation of catalysts of this nature at elevated temperatures has been shown to result in the reoxidation of the metallic iron with water molecules formed by condensation of hydroxyl groups from the support(34) $Fe^0 + H_2O \longrightarrow Fe^{2+}O + H_2$. The sample was cooled to 195 K using a dry ice/acetone slurry. Carbon monoxide was admitted to the sample and the pressure was increased incrementally while monitoring the CO uptake by the sample. The sample was then evacuated for a minimum of 30 minutes, while the sample was maintained at 195 K. After the evacuation was completed CO was again admitted to the sample and a second isotherm determined.

The first isotherm corresponded to the amount of CO both chemisorbed and physisorbed. Evacuation had the effect of removing the physically adsorbed CO but not that which had been chemisorbed. Hence the second isotherm corresponded only to the adsorption of physically adsorbed CO. Subtracting the second isotherm gives the volume of CO chemisorbed on the surface Fe^0 and possibly the surface Fe^{2+} atoms.

Throughout this work CO isotherms have been measured at 195 K. In line with other workers (2), this temperature was chosen in preference to 77 K since the chemisorption of CO has been shown to be too slow to be fully completed at 77 K (69). On the other hand volumetric gas adsorption measurements have been carried out at temperatures as high as 407 K (70). Under these conditions extensive iron pentacarbonyl formation can be expected to occur. Hence temperatures of 195 K or lower should be used for surface area determination as at higher

temperatures Ostwald ripening of iron particles by volatile iron pentacarbonyl particles could occur.

2.4.2.1. Carbon Monoxide Adsorption Stoichiometry

The strong bond between CO and metallic iron suggests that the chemisorption at low temperature proceeds to full monolayer coverage. As a working hypothesis Brunauer and Emmett (68) assumed that one CO molecule chemisorbs on each surface atom and that atoms with incomplete coordination but below the topmost layer of atoms will not chemisorb a CO molecule. However, the most closely packed plane on Fe, the (110) plane, was assumed to chemisorb one CO molecule for every two surface atoms due to steric effects. Westrik and Zwietering (71) on the other hand, postulated that one CO molecule would chemisorb on two surface atoms for the (100) plane and three surface atoms for the (110) plane.

An extensive investigation of Fe/MgO catalysts has been published (2). The authors applied CO chemisorption, magnetic susceptibility and transmission electron microscopy. The agreement between the values determined from the latter two methods conclude that the CO chemisorption technique, assuming an Fe/CO = 2 adsorption geometry is applicable over a wide particle size range. The study of Jung et al (72) confirmed the agreement between the Langevin particle size estimations from magnetic susceptibility on the one hand, and the CO uptake at 195 K on the other. Further support was advanced by Bianchi et

al (73), who also found excellent correspondence between results from X-ray line broadening transmission electron microscopy and those obtained with CO chemisorption at 199 K. As a result a Fe/CO = 2 adsorption geometry has been assumed throughout this work.

2.4.3. Nitrous Oxide Decomposition

Selective oxidation using nitrous oxide in the determination of the active area in copper based catalysts is a well documented technique (74-76). However, until recently little attention has been given to this technique in the determination of the active area in iron-based catalysts.

Nitrous oxide interacts with the surface in the following manner $N_2O \longrightarrow N_2 + O_{ads}$. The adsorbed oxygen has the effect of oxidising the uppermost layers of the iron atoms. The depth of this oxidation is a matter of some contention and is probably dependent upon the conditions under which the experiment is carried out.

During the present work nitrous oxide decompositions have been carried out at ambient temperature and a nitrous oxide pressure of 20 Torr. After dosing the nitrous oxide the system was allowed to equilibrate for a period of 16 hours. The experiments were carried out making the assumption that at ambient temperature N_2O and N_2 do not adsorb to a significant extent on the catalyst surface. Studies of this type have been made using both the gravimetric and volumetric apparatus

described in Section 2.2. The gravimetric experiments allowed the number of surface iron atoms present to be derived directly from the mass of oxygen adsorbed as a result of the decomposition. The volumetric experiments were carried out with taps A and B in Fig. 2.1 closed. Hence the sample was enclosed within a system of known volume. After the system had been allowed to equilibrate for the desired time, the remaining N_2O was frozen out using a liquid nitrogen trap. The N_2 pressure within the section could then be measured using the pressure transducer. From the N_2 pressure it was possible to calculate the number of moles of N_2O decomposed and hence the number of surface iron atoms in the catalyst sample.

The number of surface iron atoms have been related to a surface area in $m^2\ g^{-1}$ assuming the iron surface atom density is 1.2×10^{19} atoms m^{-2}.

2.5. X-ray Diffraction

2.5.1. X-ray Diffraction Techniques

X-ray diffraction experiments when reduced to the basic essentials require an X-ray source, the sample under investigation and a detector to pick up the diffracted X-rays. It is variations in these basic essentials which govern the different X-ray techniques:

(a) radiation - monochromatic or variable

(b) sample - single crystal, powder or solid piece

(c) detector - radiation counter or photographic film

The different X-ray techniques are summarised in Fig.2.4

2.5.2. The use of the X-ray Diffractometer for Qualitative Analysis

The technique adopted in the present work was diffractometry. The principle of the powder diffractometer is shown in Fig.2.5. A monochromatic beam of X-rays strike a finely powdered sample that ideally has crystals randomly arranged in every possible orientation. In such a powder sample the various lattice planes are also present in every possible orientation. For each set of planes, therefore, at least some crystals must be orientated at the Bragg angle, θ, to the incident beam and thus, diffraction occurs for these crystals and planes. The diffracted beam that results appears to be emitted from the sample as cones of radiation, as shown in Fig.2.6, each cone is in fact a large number of closely spaced diffracted beams. The angle between diffracted and undiffracted beams is 2θ and the angle of the cone is 4θ. Each set of planes gives its own cone of radiation. The diffracted beam is detected using a proportional scintillation counter or Geiger counter coupled to a chart recorder. The detector scans over a specified range of 2θ at a constant velocity. The typical range of 2θ scanned is 5^{o} to 80^{o}.

(a) radiation - monochromatic or variable

(b) sample - single crystal, powder or solid piece

(c) detector - radiation counter or photographic film

The different X-ray techniques are summarised in Fig.2.4

2.5.2. The use of the X-ray Diffractometer for Qualitative Analysis

The technique adopted in the present work was diffractometry. The principle of the powder diffractometer is shown in Fig.2.5. A monochromatic beam of X-rays strike a finely powdered sample that ideally has crystals randomly arranged in every possible orientation. In such a powder sample the various lattice planes are also present in every possible orientation. For each set of planes, therefore, at least some crystals must be orientated at the Bragg angle, θ, to the incident beam and thus, diffraction occurs for these crystals and planes. The diffracted beam that results appears to be emitted from the sample as cones of radiation, as shown in Fig.2.6, each cone is in fact a large number of closely spaced diffracted beams. The angle between diffracted and undiffracted beams is 2θ and the angle of the cone is 4θ. Each set of planes gives its own cone of radiation. The diffracted beam is detected using a proportional scintillation counter or Geiger counter coupled to a chart recorder. The detector scans over a specified range of 2θ at a constant velocity. The typical range of 2θ scaned is 5^{o} to 80^{o}.

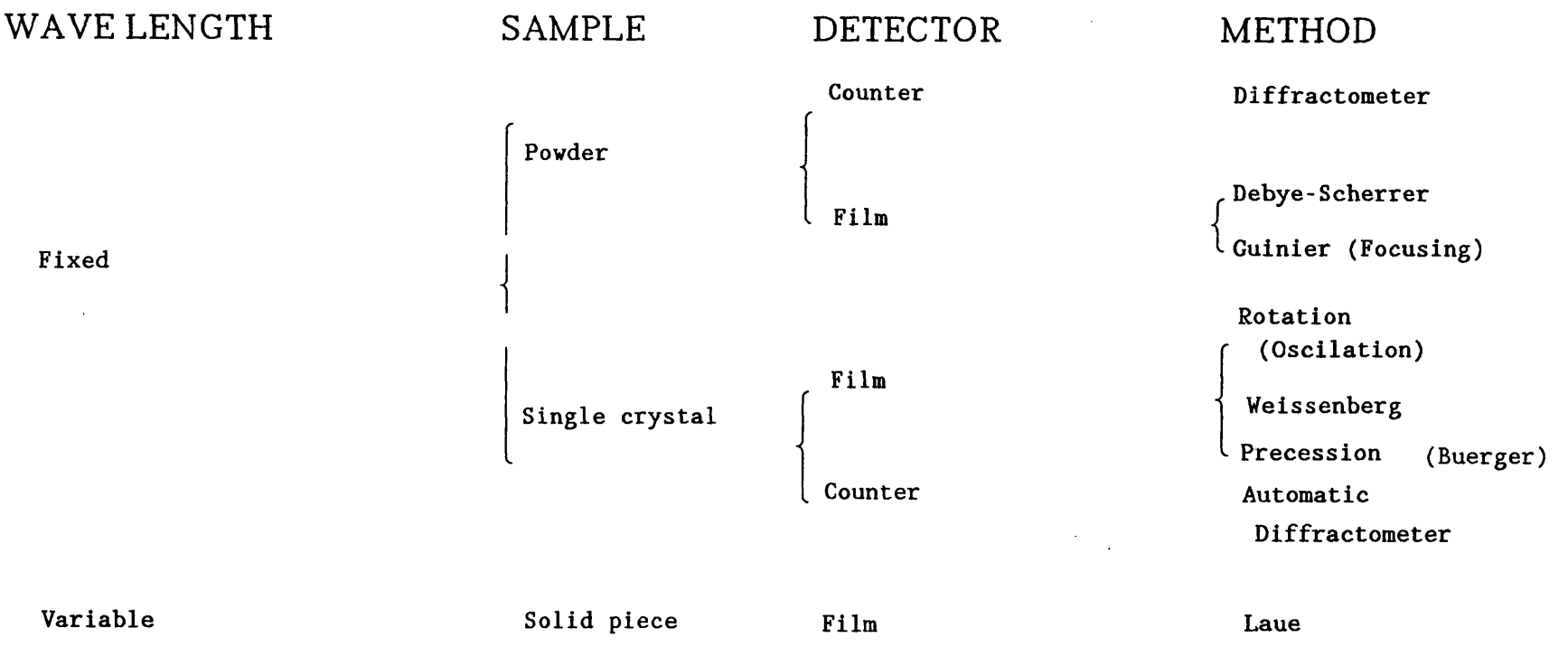

Figure 2.4 The different X-ray diffraction techniques

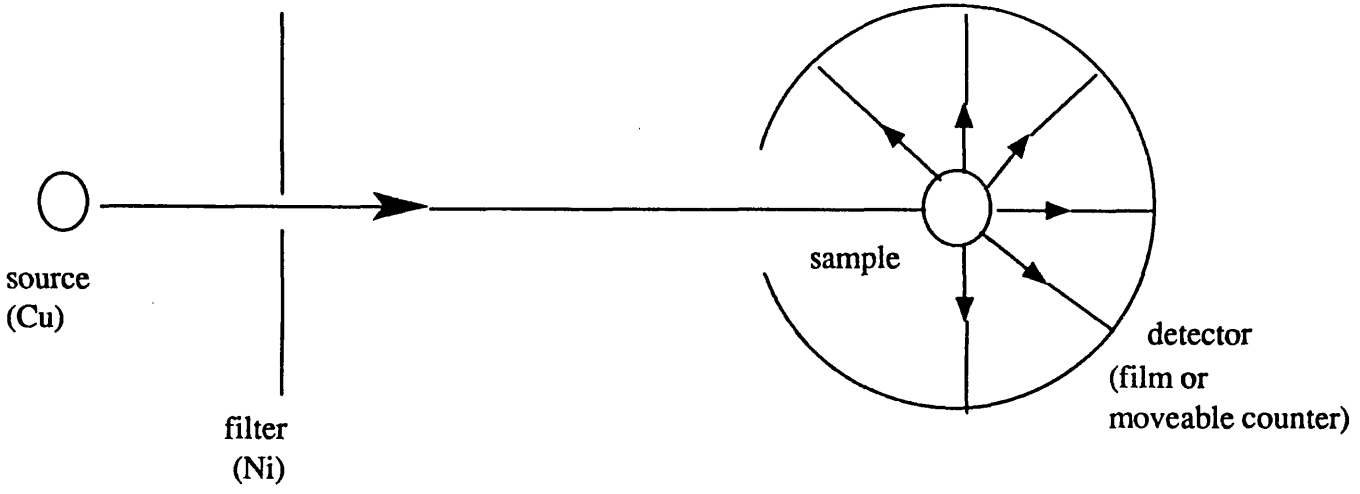

Figure 2..5 Experimental arrangement used in X-ray powder diffraction

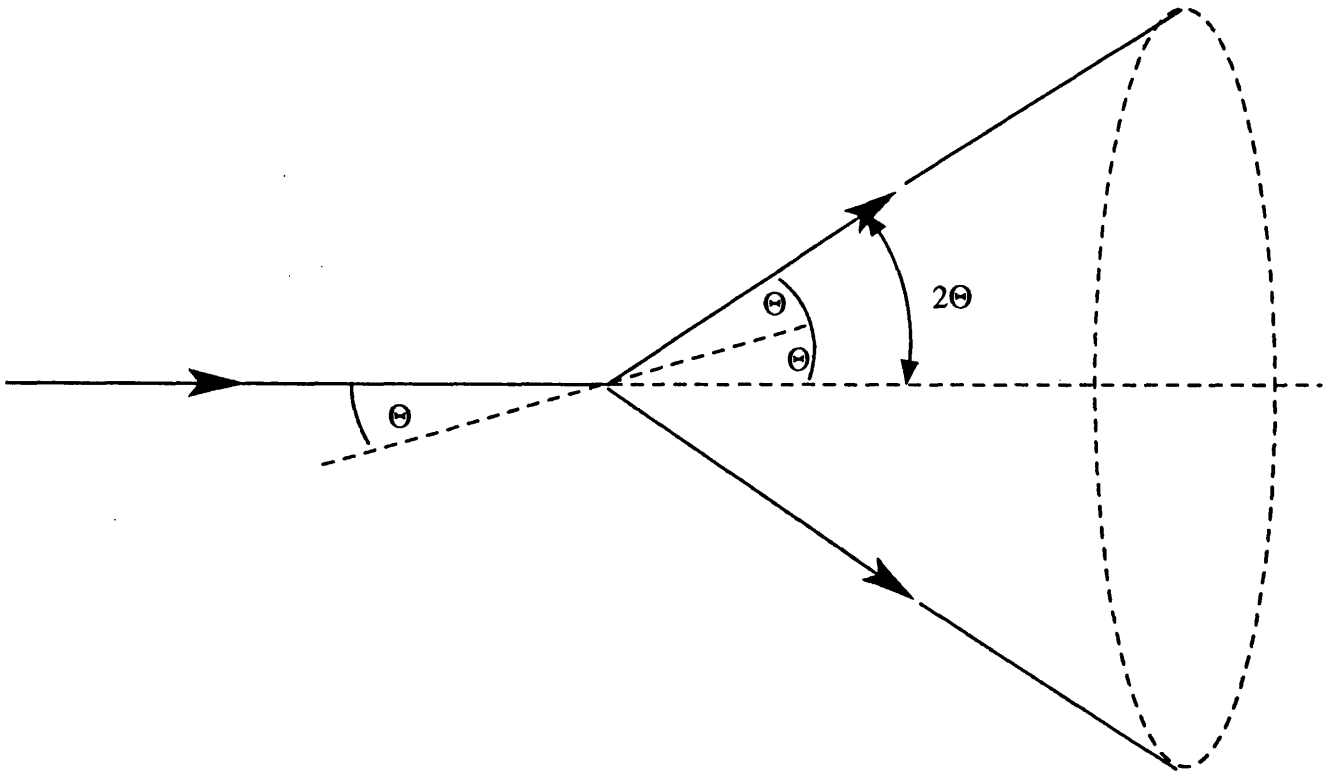

Figure 2.6 The formation of a cone of diffracted radiation

in X-ray powder diffraction.

From the chart recorder trace it is possible to calculate the d-spacings for peak positions using the Bragg equation

$$\theta_{hkl} = \mathrm{Sin}^{-1}\left[\frac{n\lambda}{2d_{hkl}}\right] \qquad (2\text{-}5)$$

where h, k and l are the Miller indices of the diffracting planes, n is an integer (in X-ray diffraction the value of n is often set equal to unity; if so, the indices h, k and l may contain a common factor) and λ is the X-ray wavelength. The trace also provides information concerning the intensities of the diffracted beams through measurment of the peak height or, for more accurate work, peak areas.

The normal practice in using powder patterns for identification purposes is to pay most attention to the d-spacings but at the same time to check that intensities are roughly correct. For the identification of unknown crystalline materials, an invaluable reference is the powder diffraction file (Joint Committe on Powder Diffraction Standards, Swarthmore, USA)

2.5.3. Instrumentation for the production of Diffractograms

X-ray powder diffractograms have been obtained from the starting precipitates, catalyst precursors and samples which had been reduced but passivated prior to the recording of the diffractogram. The aim was to identify the various phases present.

In the early part of the work diffractograms were

obtained using the following instrumentation:

Philips PW 1730/10 4KW X-ray generator

Philips PW 2273/20 long fine focus X-ray tube

Philips PW 1050/25 vertical diffractometer goniometer

Philips PW 4620 rate meter, single chanel analyser

Philips Xe proportional counter

Philips PM 8000 chart recorder

The instruments were operated under the following conditions:

divergent slit	1°
receiving slit	0.2 mm
diffraction slit	1°
scanning speed	1° min^{-1}
chart speed	1 cm min^{-1}
time constant	4 seconds

Later in the research the instrumentation was up-graded to the following:

Philips 1820/00 computer controlled vertical diffractometer goniometer

Philips proportional control PW 1711/10 with graphite monochromator and automatic divergence slit assembly

Philips PW 170 diffractometr control

Philips PM 8203 chart recorder

The phases present in the samples were identified by calculating the d-spacings from the peak positions using the method described previously.

2.6. X-ray Diffraction Line Broadening

Under the ideal conditions of diffraction of a strictly parallel and monochromatic beam of X-rays, the Bragg equation predicts diffraction of a given wavelength by crystal planes of spacing d only at a discrete angle. However, in practice, these ideal conditions never exist. Departures from ideality cause a varying degree of diffraction to occur over a range of angles near θ, resulting in a broadening of the diffraction lines recorded by the diffractometer chart. Thus X-ray line broadening can provide information about the degree of perfection. In particular it can be used as a very valuable method for the determination of the size of crystalline particles in the range 100-3 nm . Below 3 nm the line is very broad and tends to become lost.

2.6.1. Factors Causing Line Broadening

The main factors which can contribute to line broadening are:

(a) instrumental broadening

(b) small crystallite size

(c) strain

(d) structural faults

(a) Instrumental broadening

Any X-ray diffraction line will have a minimum breadth determined by the geometry of the apparatus and the experimental conditions. The instrumental factors causing line broadening are (i) width of the X-ray source, (ii) flat rather than curved sample surface, (iii) vertical divergence, (iv) width of the recieving slit and (v) penetration of the sample by the beam. This last factor, although usually studied together with pure instrumental factors , is clearly dependent upon the nature of the specimen. Thus, when absorption in the sample is low , diffraction takes place not only in the surface layer but also in the interior of the sample giving rise to broadening (77). Alexander (78) provided a detailed theoretical treatment of line broadening due to penetration of the sample by the X-ray beam. No further discussion of this will be given here, as in practical work an overall correction for instrumental broadening is made.

(b) Small crystallite size

In the derivation of Bragg's law it is assumed that the diffracting crystal has an infinite dimension (compared with the X-ray wavelenth), ie that there are an infinite number of repeating structure units in the crystal. Under this condition and for a crystal showing ideal perfection, the diffraction of a strictly monochromatic and paralell beam of x-rays will only occur at discrete θ angles.

However, if the linear dimensions of the crystal are finite, there will be be relaxation of Bragg's condition in the sense that diffraction will occur although with decreasing amplitude, over an angular interval ± $\Delta\theta$ on both sides of the Bragg angle. This will have the effect of broadening the diffraction lines. This becomes noticeable when the individual crystals are smaller than 100 nm. The line breadth can be related to the crystal size using the Scherrer equation (79)

where β is the line breadth (in radians), K is a constant

$$\beta = \frac{K \lambda}{D \cos \theta} \qquad (2.6)$$

known as the shape factor, λ is the wavelength of the incident radiation, and D is the relevant crystallite dimension (thickness of the crystal in a direction normal to the diffracting planes).

The shape factor or Scherrer constant K has a constant value of 1.0747 for spherical crystallites, but for other crystal shapes K takes different values according to the index of reflecting planes.

(c) Strain

If the crystal is larger than 1 μm, diffraction may still take place over a considerable range if the crystal is otherwise imperfect. Thus, in a distorted crystal the interplanar spacing d will not be constant throughout, and different parts of the crystal will diffract at different angles. If the maximum strain in the crystal is ϵ, the spacing will vary from $d(1+\epsilon)$ to $d(1-\epsilon)$, and θ will vary over a range

equal to $2\epsilon d(\delta\theta/\delta d)$, this can be differentiated to give $2\epsilon \tan\theta$. The deviation of the rays is 2θ, hence the angular range over which reflection is appreciable will be $2 \times 2\epsilon \tan\theta$ that is

$$\beta = 4\epsilon \tan\theta \qquad (2.7)$$

In cases of broadening from this cause Stokes and Wilison (80) have defined "an apparent strain", η, by

$$\eta = \beta \cot\theta \qquad (2.8)$$

Thus the apparent strain is four times the maximum strain.

(d) Structural faults

In certain crystals the atomic arrangement is such that the unit cells are all of the same size and shape, but differ in the disposition of atoms within them. Common cases are superlattices and stacking irregularities. If there were no relation between the different arrangements of atoms, a crystal consisting of domains in which arrangements were different would behave simply as if each domain were a separate crystallite. Usually, however, the atomic arrangements, though different are related, and all domains will scatter in phase for certain reflections, but out of phase or with a random relationship for other reflections. The crystals are thus "large" for reflections in which domains cooperate, but "small" for reflections in which they do not. The consequence is that whilst some diffraction are sharp others display considerable broadening.

2.6.2. Definition of Line Breadth

Two different definitions of line breadth are in usual practice in X-ray line broadening analysis, half peak breadth and intergral breadth. The half peak breadth is the distance between the two points on the line profile at which the intensity is half the maximum. Thus, if I_o is the maximum value of $I(\theta)$, and θ' and θ'' are the values of θ for which $I(\theta) = \frac{1}{2} I_o$, the $\frac{1}{2}$ peak breadth $\beta_{\frac{1}{2}}$, is defined as the factor 2 arises

$$\beta_{\frac{1}{2}} = 2(\theta'' - \theta') \qquad (2.9)$$

as diffraction angles are usually measured as 2θ. The intergral breadth β is defined as the breadth of a rectangle that has the same height, and the same area, as the diffraction peak. That is

$$\beta = \frac{\int I(\theta) d\theta}{I_o} \qquad (2.10)$$

In practice the half peak breadth is easier to measure, and more amenable to practical work. However, the integral breadth is a more precise parameter, and it is easier to handle in theoretical analyses.

2.6.3. Determination of the Pure Diffraction Broadening of the α Fe (110) reflection

The (110) reflection has been used to determine the size of iron crystallites in the various catalyst samples. As it has not been possible to perform in situ X-ray experiments, the samples were first passivated using nitrous oxide as described

in Section 2.4.3.. Experiments performed by other workers (2) have shown that crystallite sizes obtained from passivated samples were in good agreement with those obtained from in situ measurements.

Both the "old" and the "up-dated" X-ray diffractometers were used in the X-ray line broadening experiments. The experimental conditions were modified in order to enlarge the size of the peaks. The operating conditions for the older equipment were modified as follows:

scanning speed ¼° min^{-1}

chart speed 25 mm min^{-1}

time constant 10 sec

In the case of the up-dated equipment the following operating conditions were used:

scanning speed 0.008° sec^{-1}

chart speed 5 cm per degree

Each diffraction peak consists of two superimpossed peaks arising from the Cu K_α radiation consisting of two wavelengths. The α_1-α_2 doublet has been resolved using the method proposed by Dumond and Kirkpatrick (81). This method, which was found to give better results than the method of Rachinger (82), can be understood by refering to Fig. 2.7. Let F(x) be the function representing the observed line profile. Let f(x) be the function representing the contribution to F(x) made by the α_1 line. If the relative maximum intensities of the $\alpha_1$and α_2 lines are assumed to be in the ratio 2:1,(80) then the contribution to F(x) made by the α_2 line will be (½)f(x-δ), where δ is the angular separation between the α_1 and α_2 maxima. It follows

that for any value of x $F(x) = f(x) + (\frac{1}{2})f(x-\delta)$, where F(x) is experimentally given and f(x) is to be found. To compute f(x) Dumond and Kirkpatrick proceeded as follows. From the experimentally known function F(x) subtract the known function $(\frac{1}{2})F(x-\delta)$

$$F(x) - (\frac{1}{2})F(x-\delta) = f(x) + (\frac{1}{2})f(x-\delta) - (\frac{1}{2})f(x-\delta) + (\frac{1}{4})fx-2\delta)$$

To this in turn add the known function $(\frac{1}{4})F(x-2\delta)$

$$F(x) - (\frac{1}{2})F(x-\delta) + (\frac{1}{4})F(x-2\delta) = f(x) - (\frac{1}{4})f(x-2\delta) + (\frac{1}{4})f(x-2\delta) + (\frac{1}{8})f(x-3)$$

If this process is continued indefinitely the result will be

$$F(x) - (\frac{1}{2})F(x-\delta) + (\frac{1}{4})F(x-2\delta) - (\frac{1}{8})F(x-3\delta) + ... = f(x)$$

The error due to neglecting the last term will soon vanish due to the rapidly decreasing coefficients and to the diminution in $f(x-n\delta)$ as n becomes large. In practice the decomposition was very rapidly effected graphically by the following procedure. The curve (x) representing the observed line was constructed. Equally spaced vertical ordinates with the spacing δ were erected as shown in Fig.2.7. The value of the ordinate F_4 (say) was corrected by subtracting from it half the value of F_3, then adding a quarter of F_2, subtracting an eighth of F_1, etc, until the amounts to be added or subtracted from F_4 became negligible.

Having resolved the K_α doublet, it was necessary to separate instrumental broadening and broadening due to the sample . The latter is often refered to as the intrinsic broadening, or pure diffraction broadening. The two most

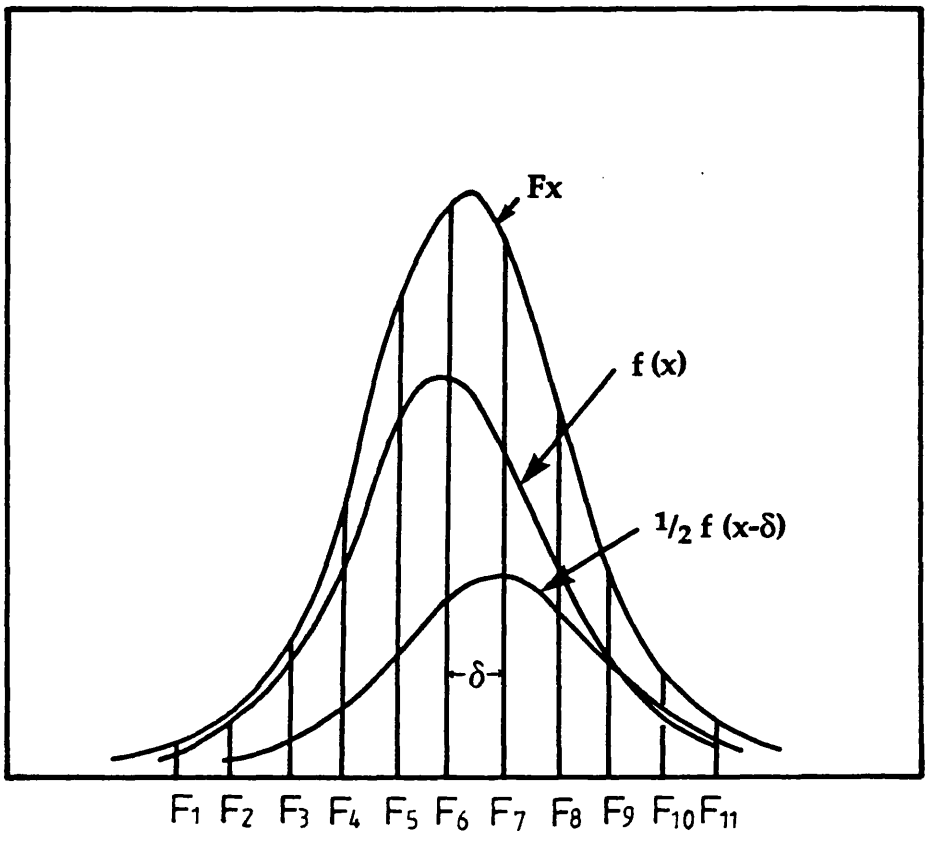

Figure 2.7 Diagram ilustrating the resolution of the Cu Kα doublet

commonly assumed line shapes are Gaussian

$$I(s) = I_p(s) \exp(-K^2s^2) \qquad (2.11)$$

and Cauchy

$$I(s) = I_p(s) / (1+K^2s^2) \qquad (2.12)$$

where I_p is the intensity at maximum height and k is a numerical constant. If B, and β, and b are respectively the total, intrinsic, and instrumental line breadths, then it can be shown that for all Gaussian profiles

$$B^2 = b^2 + \beta^2 \qquad (2.13)$$

whilst for all Cauchy profiles

$$B = b + \beta \qquad (2.14)$$

The better one of the two to use depends on whether a Gaussian or a Cauchy function gives a better approximation to the line shapes. Schoening (83) points out that broadening produced by small particle size tends to produce a Cauchy profile and that by strain broadening a Gaussian shape. However, very often the actual profiles do not fit either function very well and, moreover, the profile of the pure instrumental broadening may not have the same shape as that due to intrinsic broadening. These difficulties were overcome by Jones (84) who devised a method based on the direct comparison of broadened and sharp lines produced under the same experimental conditions. He expressed his results in the form of a relation between b/B and β/B, as shown in Fig. 2.8 . The plot in this figure has been used to derive the pure line breadth β. The value for the instrumental broadening b was obtained from a sample of iron powder (Koch Light laboratories 95% pure) which was heated in hydrogen at 723 K to ensure the sample was well sintered.

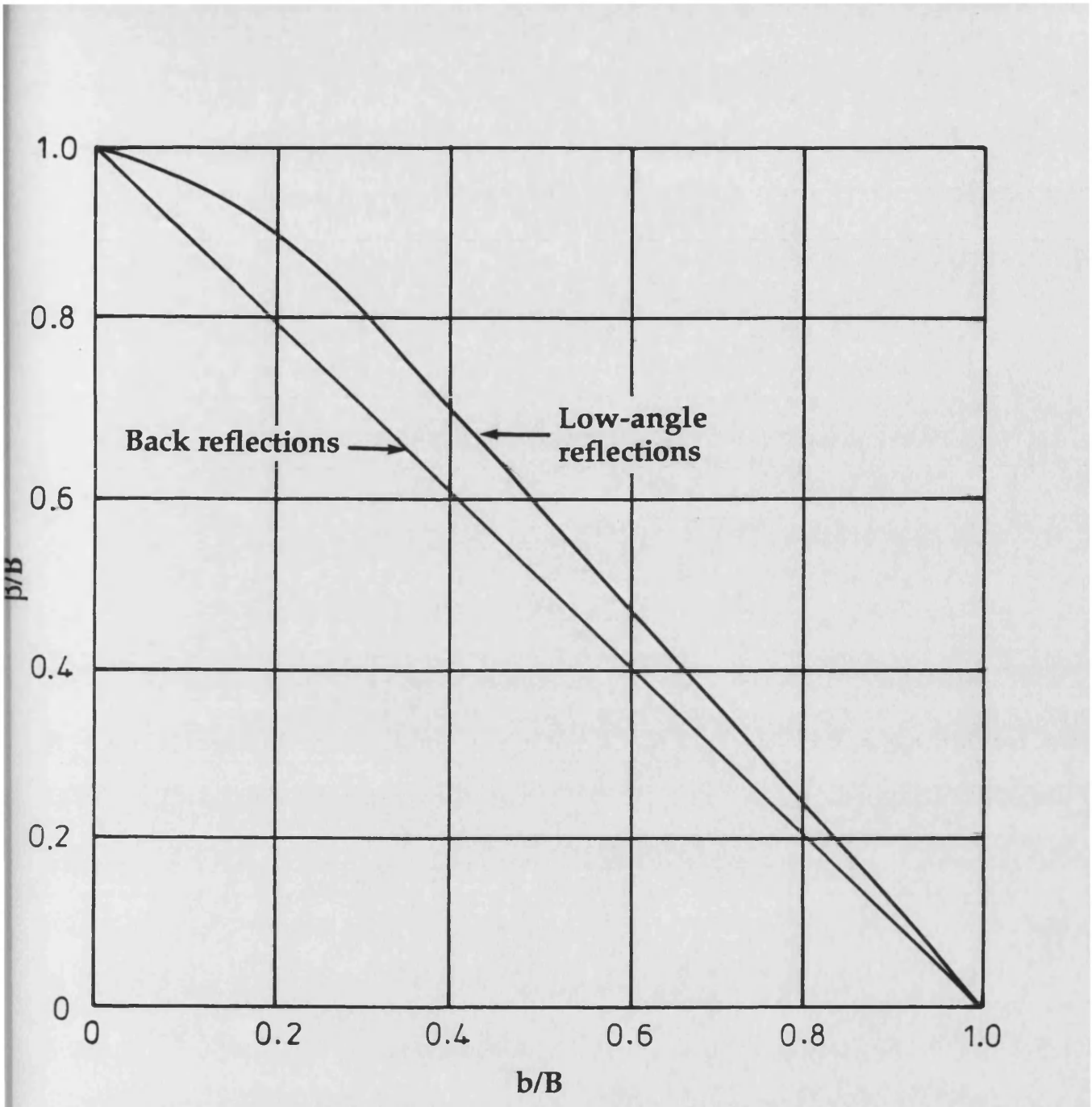

Figure 2.8 Curves for correcting X-ray diffractometer line breadths for instrumental broadening

2.7. Mössbauer Spectroscopy

Mössbauer spectroscopy is concerned with transitions between energy levels within the nuclei of atoms. About a third of the known elements, principally the heavier ones, when formed by the radioactive decay of an isotope of the same or a different element, are initially produced in an excited nuclear state; after a very short delay, of the order of microseconds, the excited nucleus reverts to the ground state and emits energy of a very high frequency, usually in the γ- ray region of the spectrum. It is the study of this γ-ray emission and subsequent reabsorption which constitutes Mössbauer spectroscopy.

2.7.1. Principles of Mössbauer Spectroscopy

The principles of Mössbauer spectroscopy will be discussed using the iron nucleus as an example. The isotope ^{57}Fe is conveniently produced by the decay of radioactive ^{57}Co, which is a relatively long-lived species, having a half-life of 270 days. A simplified energy level diagram for the process is shown below, where following electron capture the cobalt

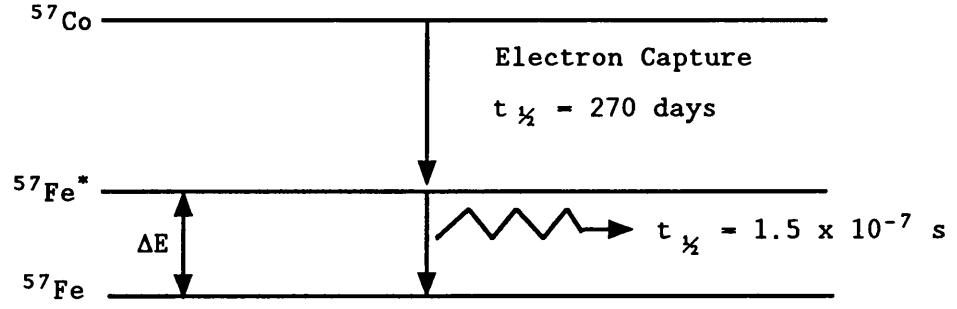

nucleus is seen to produce ^{57}Fe in an excited energy state Fe^*.

Fe^* very rapidly drops to the ground state Fe, the energy change involved being $\Delta E = 2.30 \times 10^{-15}$ J (per nucleus). The frequency of the emitted γ-ray is thus $\upsilon = \Delta E/h = 3.5 \times 10^{18}$ Hz.

If a photon emitted by an excited ^{57}Fe nucleus encounters a ^{57}Fe nucleus in the ground state, it may be expected that this second nucleus would be raised to the excited level by the phenomenon of resonance absorption. This is not necessarily so. From the Heisenberg Uncertainty Principle the linewidth Γ is inversely proportional to τ the life time of the excited state.

$$\Gamma = (2\pi\tau)^{-1} \qquad (2.15)$$

The life-time of the excited state of the ^{57}Fe nucleus under consideration is 97.7 ns, so the linewidth is 1.63×10^6 Hz. The linewidth is thus an extremely small compared to the frequency, so only a small proportional difference in frequency between the absorbing and emitting nucleus will cause the photon to fail to be absorbed. One possible cause for such a difference is the motion of the emitting nucleus. If this nucleus is in the vapour phase or in solution, so that it is free to move the momentum of the emitting photon is sufficient to cause the nucleus to recoil. Thus not all of the energy of the nuclear transition appears as energy of the photon; E_o^2/mc^2 is lost as recoil energy, where E_o is the energy of the nuclear transition, m is the mass of the nucleus, and c is the velocity of light. For ^{57}Fe the recoil energy is 6.24×10^{-22}J (per nucleus), sufficient to cause a decrease of 9.45×10^{11} Hz in the frequency of the γ-radiation. This shift is much greater than the linewidth, so the condition for absorption is not fulfilled. For a resonant absorption of γ-radiation to be

observed, the emitting and absorbing nuclei must both be held firmly in a crystal lattice, so that the effective mass m is that of the crystal as a whole, or, at least a substantial part of it. The importance of this was first realised by Mössbauer, so the phenomenon of recoilless emission and absorption of γ-radiation is termed the Mössbauer effect.

Even if recoil effects are eliminated by embedding the nuclei in a crystal lattice, the photon emitted by one ^{57}Fe nucleus cannot be absorbed by another if the energy gap between ground and excited states is different for the two nuclei. Such a difference may be produced by differences in the electronic states of the two ^{57}Fe atoms. The s orbitals of atoms have the distinctive characteristic that they penetrate through the other orbitals right to the nucleus, whatever their principal quantum number. The 4s valency orbital of ^{57}Fe thus affects the nucleus, and the extent to which this orbital is filled modifies the energy levels within the nucleus. The modification is proportionally very small, the difference in energies of the nuclear transition for $^{57}Fe^{2+}$ and $^{57}Fe^{3+}$ being only 4 $x10^{-8}$ eV, corresponding to a difference in frequency of around 10^7 Hz. This difference is called the isomer shift. The magnitude of the isomer shift thus gives a measure of the relative degree of occupation of the 4s level. To observe the isomer shift, it is necessary to scan through a frequency range of about 10^7 Hz centred on a frequency of 3.48 $x10^{18}$ Hz. This is achieved by making use of the Doppler effect.

2.7.2. Information Obtainable From Mössbauer Spectroscopy

The main features of a Mössbauer spectrum are;

(a) Isomer shift

(b) Quadrupole splitting

(c) Magnetic hyperfine interaction

These parameters have been used to derive information concerning the iron containing species present in the catalyst samples.

The nuclear transitions for magnetic hyperfine splitting of ^{57}Fe as found in metallic iron and for combined magnetic hyperfine and quadrupole splitting as found in α-Fe_2O_3 are shown in Fig.(2.9)

(a) Isomer shift

The isomer shift, or chemical shift as it is also called, is reported with respect to metallic iron standard and has units of cm s^{-1}. The main factor affecting the magnitude of the chemical shift is the electron density at the nucleus concerned and since p,d, etc orbitals have zero density at the nucleus, it is therefore the s orbital density which is important. Observation of shifts therefore allows measurement of relative s electron density which, in turn, gives an estimate of the bond character of atoms or ions chemically attached to the Mössbauer nucleus.

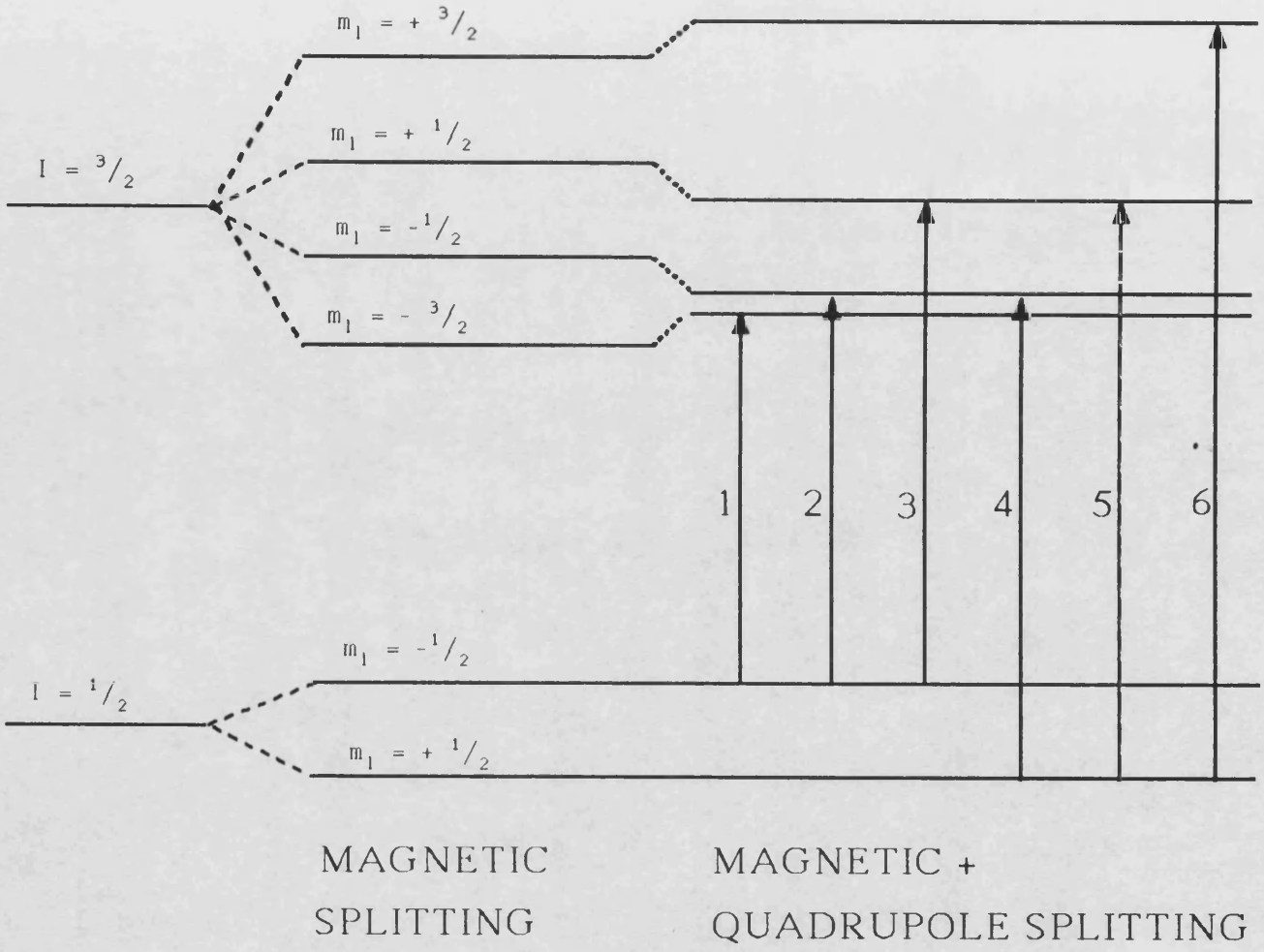

Figure 2.9 The nuclear transitions for magnetic hyperfine splitting of ^{57}Fe as found in metallic Fe and for the combined magnetic hyperfine and quadrupole splitting as found in α-Fe_2O_3

(b) Quadrupole coupling

Nuclei with a spin quantum number greater than ½ have an electric quadrupole moment that may be positive or negative corresponding to the distortion of the nucleus from spherical symmetry. If the electric field set up by the environment of the nucleus lacks spherical symmetry, the quadrupole is aligned in one set of possible orientations to the field, so that a set of energy levels is established. For a nucleus of spin quantum number $^3/_2$, such as the first excited state of ^{57}Fe in an electric field of axial symmetry, the nuclear quadrupole moment can couple with or against the field giving a pair of energy levels. The ground state ^{57}Fe nucleus has a spin quantum number ½ and so does not have a quadrupole moment. Thus the transition from the excited to the ground state of ^{57}Fe gives a doublet in the Mössbauer spectrum if the ^{57}Fe nucleus is in a local electric field gradient. The magnitude of the splitting is related to the nuclear quadrupole moment by the equation

$$\Delta = e\,Q\,q \qquad (2.16)$$

where Δ is the splitting in units J, eQ is the quadrupole moment in units C m^2, and q is the electric field gradient in V m^{-2}. If the electric field gradient lacks axial symmetry, a further factor describing the asymmetry is required

$$\Delta = \frac{e\,Q\,q\,(1 + \eta^2/3)^{\frac{1}{2}}}{2} \qquad (2.17)$$

where η is a measure of the asymmetry.

The field gradient causing quadrupole splitting may be due either to charges on adjacent ions, either on adjacent

sites in the crystal lattice or as ligands, or due to the electrons of the atom itself if one of the orbitals is incompletely filled. The existence of quadrupole splitting thus affords useful evidence as to the molecular structure.

(c) Magnetic hyperfine interaction

Nuclei, being in effect tiny magnets are orientated by magnetic fields. Only certain angles of orientation are permitted as a consequence of the quantisation of energy, so a nucleus of spin quantum number I has (2I + 1) magnetic levels. The energy gaps between these levels are such as to cause noticeable splitting in the Mössbauer spectra and this effect is known as magnetic hyperfine interaction. The magnetic field responsible for this interaction is not observed for all paramagnetic species, since the electrons usually exchange spins so rapidly that the time averaged effect is zero. Magnetic hyperfine interaction is observed only for ferromagnetic materials or for samples in which paramagnetic ions are held well separated from each other in a dilute solid solution in a diamagnetic matrix.

2.7.3. Experimental Procedure

Mössbauer spectra were recorded at ambient temperature using a constant acceleration Mössbauer spectrometer (Cryophysics) fitted with a 10 mCi ^{57}Co in Rh source (Amersham International). Samples were loaded into the glass sample cell

which had been constructed from Pyrex with thin walls so as to minimise the shielding effect produced by the walls of the sample cell. The cell was fitted with a greased glass tap which allowed it to be disconnected from the volumetric vacuum frame without exposure of the sample to the atmosphere. This was necessary as insitu Mössbauer measurements could not be made

Mössbauer spectra have been obtained for two samples, these were CCP30 and sample prepared from enriched ^{57}Fe with a low iron loading. Initially spectra were recorded of the precursors and then at various stages of reduction.

2.8. Infrared Spectroscopy

Infrared spectroscopy is the most widely used technique for studying the gas-solid interface. The reason for this certainly lies in the fact that its experimental requirements have been modest in comparison with many other spectroscopic techniques.

2.8.1. Infrared Spectroscopy of Adsorbed Molecules

A large variety of problems related to the nature of adsorption processes have been studied by infrared spectroscopy. In an "ideal" case one may expect to obtain three types of information from spectroscopic experiments:

a) The identity of active sites on catalytic surfaces

b) The identity of chemisorbed species which act as intermediates in catalytic reactions

c) The nature of the interaction between an active site and an adsorbed molecule

The nature of active sites on catalyst surfaces are frequently determined by infrared spectroscopy. This can be achieved by the adsorption of the reactants for a given reaction and observing the surface species which are formed. However, this not always easily achieved due to the complex nature of the system. In such cases it is common to use probe molecules to determine the active sites on the catalyst surface. Commonly used probe molecules include acetic acid and carbon dioxide (85) which may be used to probe basic sites on catalyst surfaces, while pyridine (86,87) is frequently used to probe acidic sites, but by far the most commonly used probe molecules are carbon monoxide and nitric oxide. These molecules have been used extensively in this work to characterise the catalysts.

2.8.1.2 The Chemisorption of CO and NO

The first model for the adsorption of CO was proposed the Blyholder (88) this can be summarised by Figure 2.10 which shows the relevant orbitals involved in bonding. The orbitals of CO and NO are very similar. NO has one more electron that occupies an antibonding π^*orbital. Both molecules form σ-bonds with the atoms or ions at the catalyst surface through their lone pair of electrons of C or N (5s-orbital). Moreover, the electrons from the surface can flow back to the antibonding π^* orbital of the molecule; this being known as π back donation.

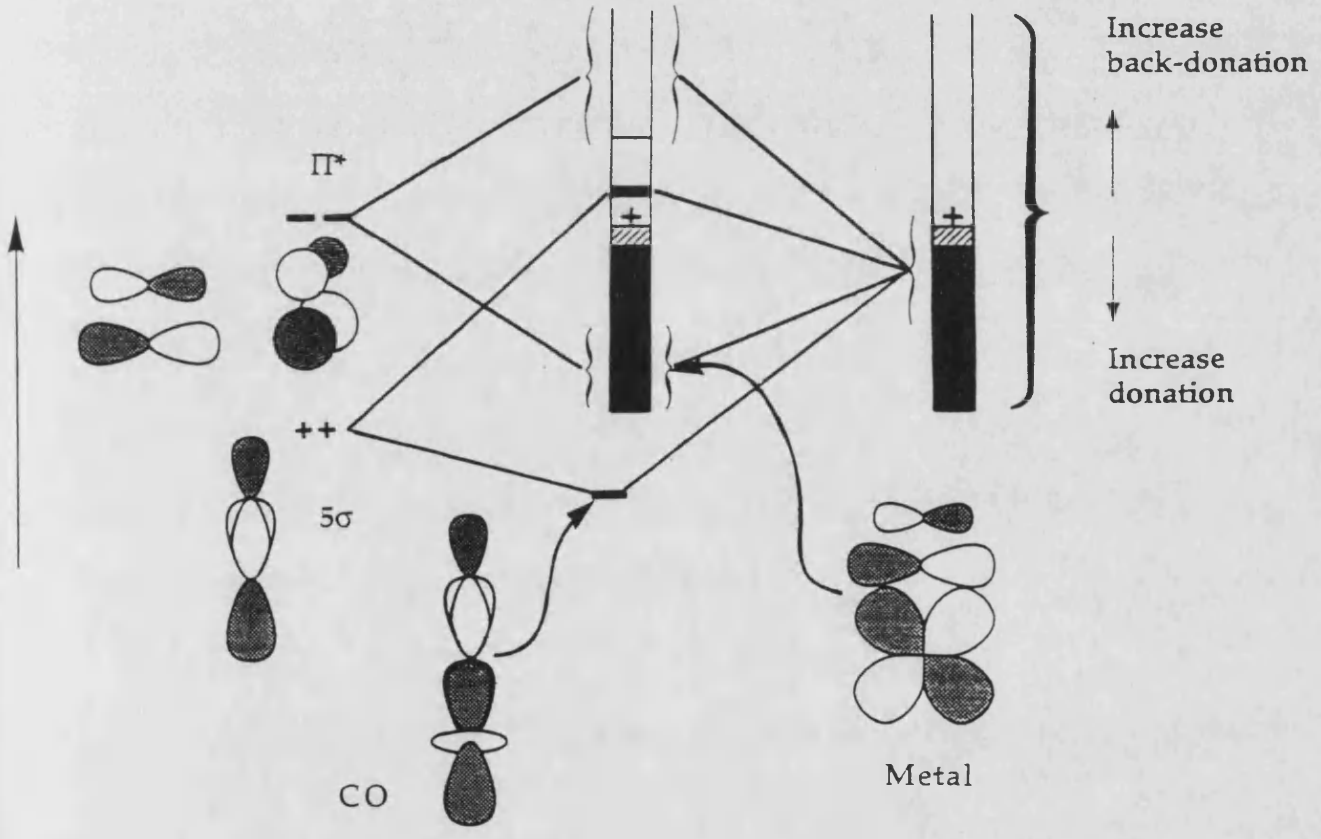

Figure 2.10 Orbital correlation diagram for CO adsorbed on a transition metal surface

These two opposing electron interactions determine the C-O and N-O bond strength and hence the CO and NO stretching frequency, namely the σ-donation (high frequency shift) and the p back donation from the adsorption site into the π^* antibonding orbital (low frequency shift).

In contrast to CO, however, there is already an electron in the π^* orbital in the neutral NO molecule. This electron can easily be transferred to a neutral or ionic site, nominally producing NO^+, and the transfer out of the antibonding π^* orbitals accordingly strengthens the N-O bond and raises the infrared stretching frequency. According to this picture NO adsorbs more strongly than CO on transition metals and metal oxides, and in some instances the data suggests that NO reacts at comparably lower temperatures than O_2 and leads to surface oxidation at temperatures slightly below room temperature, thus giving rise to the appearance of N_2 or N_2O in the gas phase.

2.8.2. The Infrared Spectrophotometer

Infrared spectra were recorded using a Perkin-Elmer 983 i.r. spectrophotometer interfaced to a Perkin-Elmer 3600 data station. The spectrophotometer was operated in the double beam mode to record spectra in the range 4000-180 cm^{-1}. The frequency accuracy of the instrument was as follows:

± 2 cm^{-1} 4000-2000 cm^{-1}

± 1 cm^{-1} 2000-180 cm^{-1}

The frequency reproducibility was 0.005 cm^{-1}, whilst resolution to 0.5 cm^{-1} was obtainable. All spectra were stored on floppy discs using the data station; later they were

manipulated in order to be reproduced in a more useful form.

2.8.3. The Infrared Cells and Vacuum Frame

Infrared spectra were recorded using a purpose built vacuum frame. The vacuum frame, i.r. cell and spectrophotometer were aligned in such a manner that the spectra could be recorded without detaching the cell from the vacuum frame.

The vacuum frame was evacuated using an oil rotary pump and water cooled mercury diffusion pump protected by a liquid nitrogen cold trap. The frame incorporated a McLeod gauge and an ionisation gauge (AEI Metrovac type Vc9) which were used to judge the quality of the vacuum in the frame. A mercury manometer was used to measure the equilibrium pressure of dosed adsorbates. The frame also incorporated storage bulbs, gas inlet connections and a cold trap.

The ambient temperature infrared cell Fig. 2.11 was constructed so that the sample in the form of a thin compressed disc could be supported in the i.r. beam of the spectrometer whilst in vacuo. Since it was necessary to pretreat the sample at high temperatures, the cell was designed so that the disc could be moved between the i.r. beam and furnace without interrupting the vacuum. The sample holder consisted of a silica glass rod with a pair of silica hooks at one end, the opposite end of the rod being connected to a Pyrex tube (A). This tube was inserted into a precision bore tube (B). A vacuum seal was made between these using four Viton O-rings (C), this

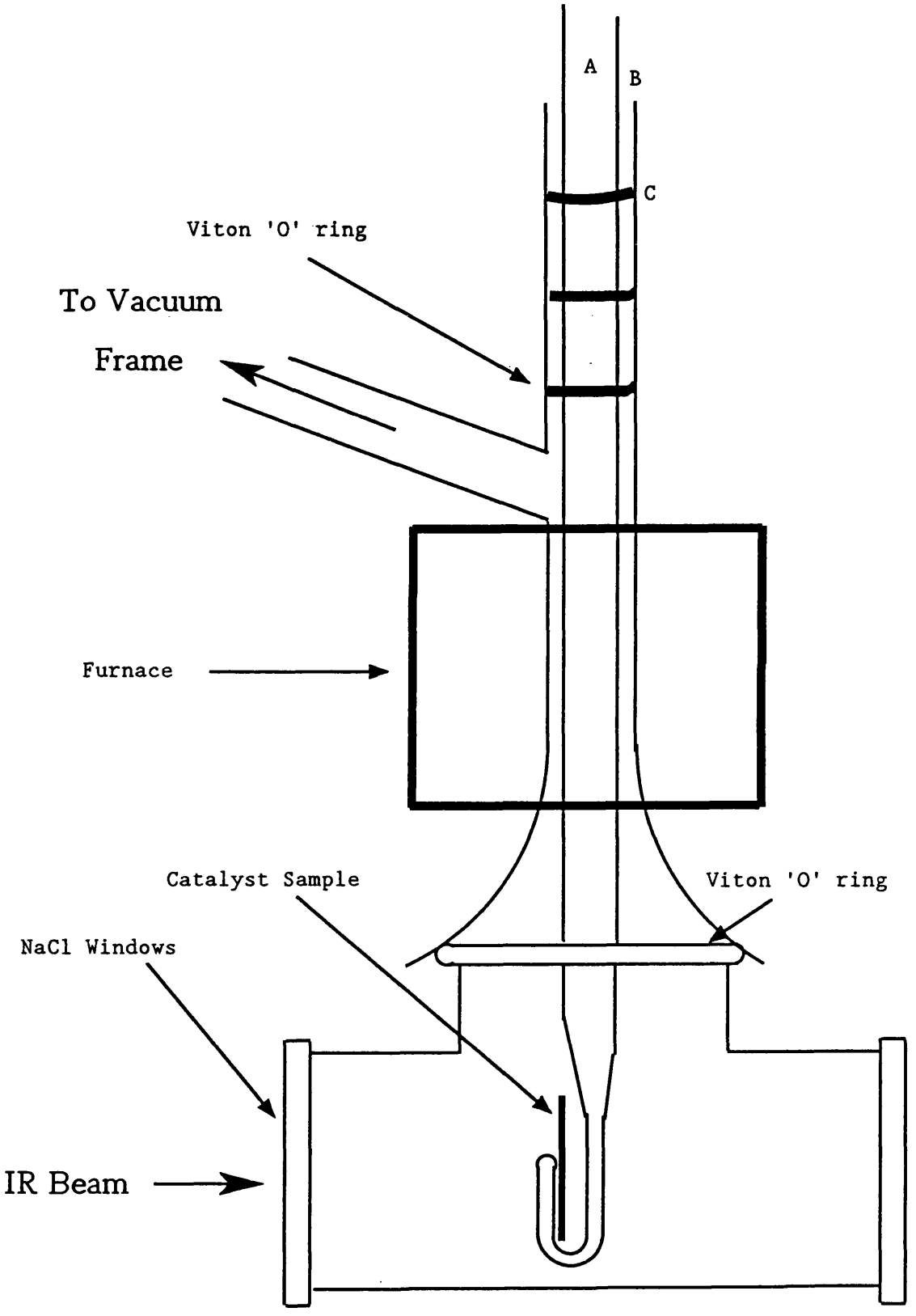

Figure 2.11 Ambient temperature infrared cell

made it possible to slide the inner tube up and down so that the attached sample could be moved into the furnace or the i.r. beam. The furnace consisted of a heating coil wound around a silica tube which enabled temperatures up to 1073 K to be obtained. The heater was controlled by a 8 amp Variac and the temperature of the sample was monitored using a chromel-alumel thermocouple whose junction was positioned along side the sample disc. The cell was connected to the vacuum frame via a glass sidearm and removable glass connecting tube. All joints were sealed with Viton O-rings. The window section consisted of a 7.5 cm long Pyrex tube sealed at both ends with 5 cm diameter sodium chloride windows. The windows were fixed to the glass tube using a silicone rubber compound (R.S. Components Ltd).

The window section was attached to the remainder of the cell via a greaseless O-ring joint and was therefore fully removable. This allowed sample discs to be quickly installed and removed from the silica holder.

An i.r. cell which enabled the sample to be cooled to subambient temperatures was also constructed (Fig.2.12). Thus surface species which would normally be removed by evacuation of the gas phase at ambient temperature could be observed. This is useful as the absorption bands of the gas phase frequently obscure absorption bands due to adsorbed species, and the low-temperature cell enables the latter to be selectively observed. The catalyst disc was contained within a sample holder (A) made from gold foil. This gave the sample sufficient support so that it could be slid from the furnace area into the i.r beam. Gold was chosen for this purpose because of its good

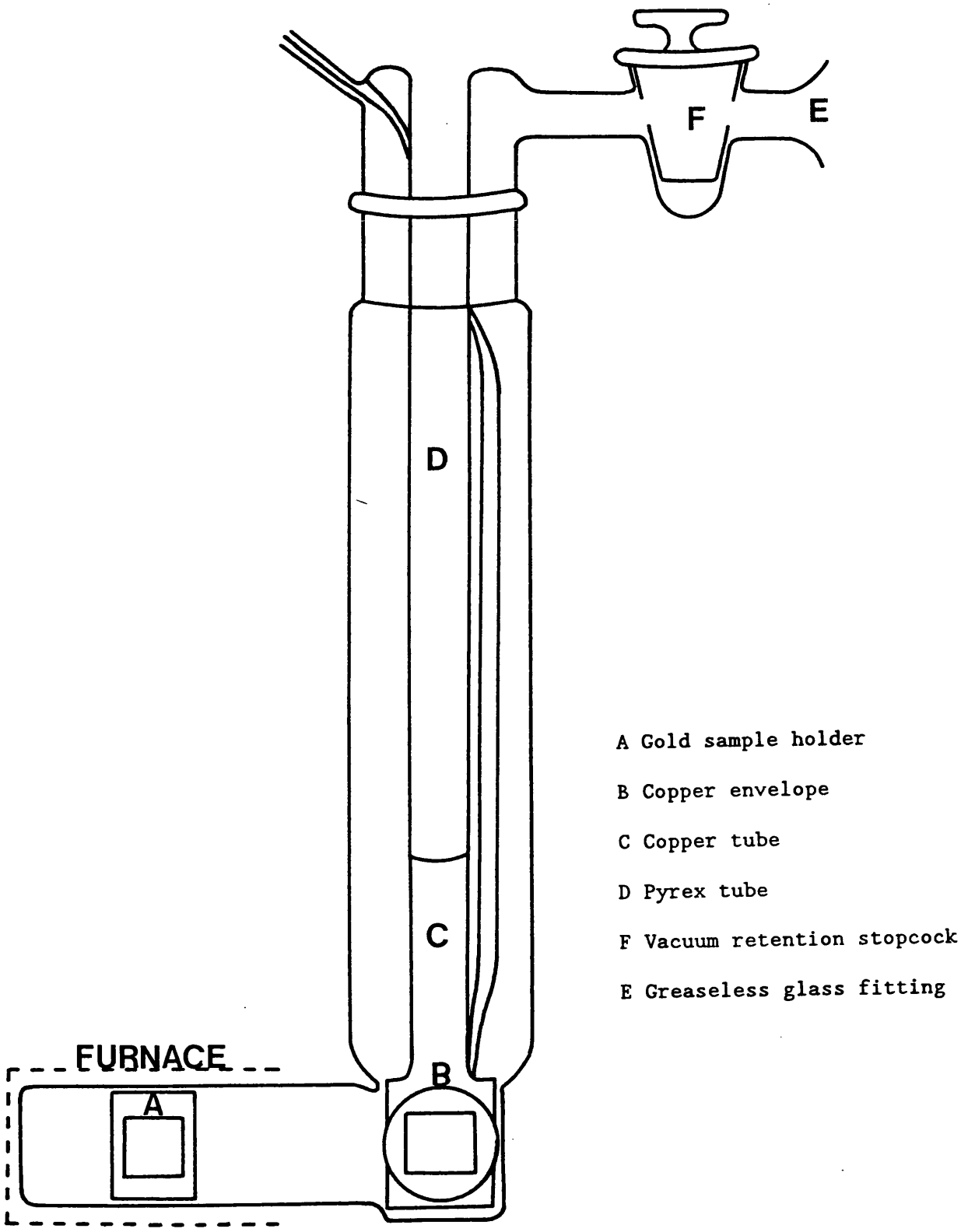

Figure 2.12 Diagram of the low temperature infrared cell

conductive properties and its catalytic inertness. Whilst in the i.r beam the sample and holder were enclosed within a three-sided envelope (B) made from copper, this was joined to a length of copper tube (C) connected via a glass/metal joint to a section of Pyrex tube (D). Tubes C and D were filled with liquid nitrogen in order to lower the temperature of the sample. The body of the cell was constructed from Pyrex and was connected to the vacuum frame via a greaseless joint (E). A vacuum retention stopcock (F) was fitted which allowed the cell to be isolated while the sample holder was moved between the furnace area and the i.r. beam. This was performed by tilting the whole cell and required the cell to be disconnected from the frame. The cell was fitted with two 2.5 cm diameter sodium chloride windows attached by the same method as in the other cell. Two chromel-alumel thermocouples were fitted which enabled the temperature of the sample to be monitored whilst in the i.r. beam and also in the furnace area.

2.8.5. Preparation of Samples for Infrared Spectroscopy

Powdered samples of 5% Fe/MgO and MgO were compressed into self supporting discs. These were made as thin as possible to maximise their transparency towards the i.r. radiation. They were prepared by evenly sprinkling 55 mg of the sample over one face of a 28.5 mm diameter die (Beckmann RIIC Ltd) contained in a die holder. A second die was placed over the sample trapping the powder between two mirror polished die faces. A pressure of

4-5 tons per square inch was applied with a hydraulic press and maintained for several minutes. The space surrounding the dies was evacuated using a rotary pump. This prevented the sample discs from sticking to the die faces. The resultant discs were very fragile but when handled with care were sufficiently strong to resist the mechanical and thermal shocks encountered during the subsequent adsorption studies.

2.9. Catalyst Testing

The catalysts produced have been tested using a high pressure autoclave reactor Fig.2.13 and a flow reactor operating at atmospheric pressure Fig. 2.15. The tests carried out using the autoclave reactor were performed at ICI Wilton. The autoclave reactor was used mainly to hydrogenate propanenitrile although some experiments were performed with hexanenitrile and dodecanenitrile. In the case of the flow reactor ethanenitrile was predominantly used as the reactant nitrile.

2.9.1. High Pressure Autoclave Reactor

2.9.1.1. Operation of the Autoclave Reactor

Prior to loading the catalyst in the reactor it was first necessary to activate the passivated samples of catalyst. This was performed in the flow system shown in Figure 2.14. The passivated catalyst was heated to 300°C in a stream of hydrogen

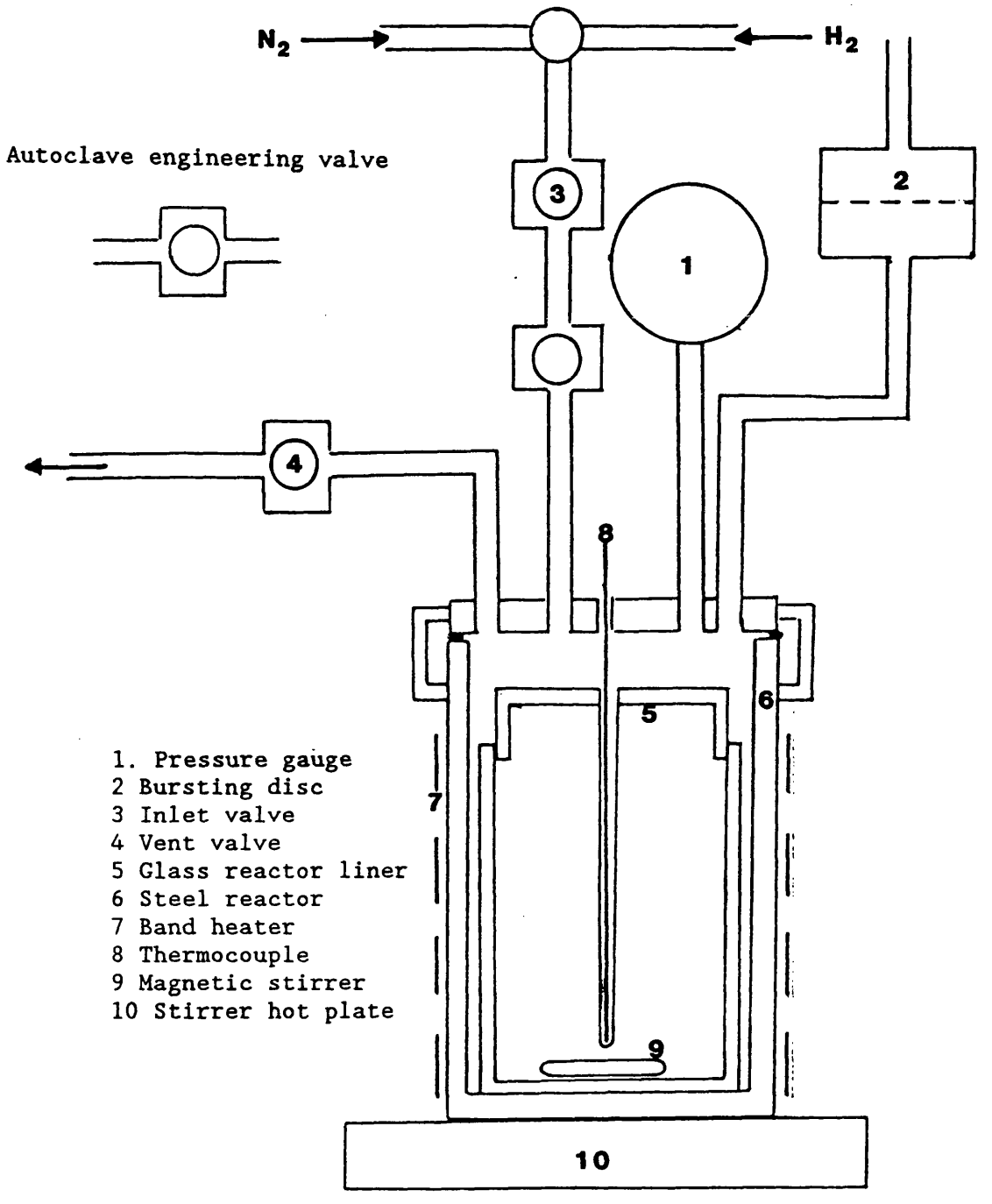

Figure 2.13 Diagram of the Autoclave Reactor used for Nitrile Hydrogenation.

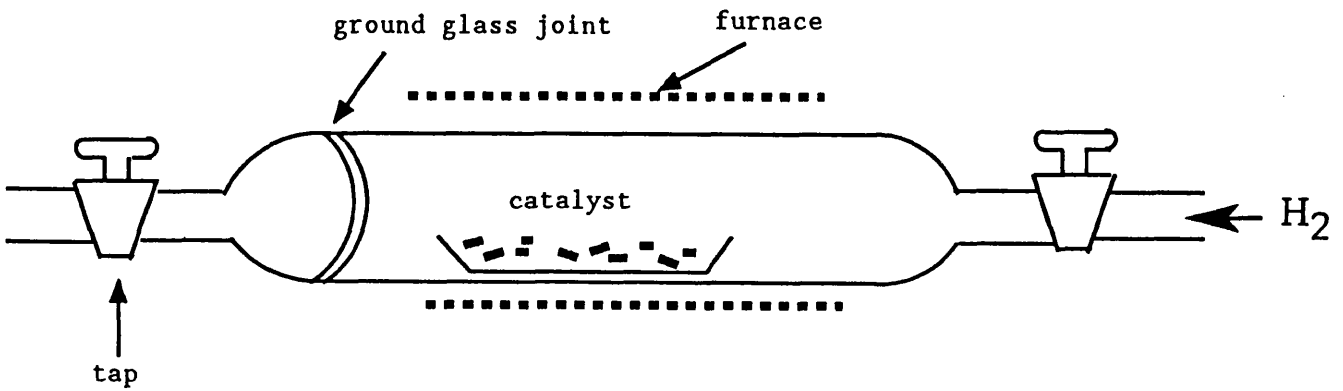

Figure 2.14 Apparatus used for flow reduction of the catalyst before testing in the autoclave reactor

(BOC high purity) flowing at 6.5 l h^{-1} for a period of 16 hours. The activation tube was then removed from the furnace maintaining the flow of hydrogen over the catalyst. The vent end of the tube was then sealed prior to the closure of tap A. This resulted in a slight positive pressure of hydrogen being established within the tube, which aided in preventing the sample from being contaminated by atmospheric gases during the transfer to the glove box. The glove box was purged with nitrogen Once the oxygen level within the glove box as monitored by an oxygen monitor had reached zero % the catalyst was discharged from the activation tube.

After weighing, the catalyst, along with 10 cm^3 of reactant nitrile was loaded into the glass reaction liner. The liner was then sealed prior to being removed from the glove box and was then placed inside the reactor body. It was essential that the seals on the liner were removed before attachment of the reactor body to the upper portion of the reactor. In order that the amount of air entering liner was kept to a minimum, the seals were only removed when in close proximity to the upper portion of the reactor. This process was carried out with a downward flow of nitrogen from the inlet port in a further attempt to reduce the amount of air entering the reaction liner. Once in place the nitrogen was flushed from the system using hydrogen. Unfortunately this loading procedure resulted in some of the nitrile being lost. After several minutes the vent valve was closed, and the reactor pressurised to 200 psig with hydrogen. The system was then pressure tested prior to commencing heating.

Heat was supplied by a band heater situated around the outside of the reactor body. The outer wall of the reactor was maintained at 210°C using a temperature controller (Gulton West). A thermocouple pocket fitted with a chromel-alumel thermocouple extending within the reactor body allowed the temperature during the reaction to be monitored. Using this mode of temperature control it was not possible to maintain a constant temperature within the reactor. Temperature fluctuations of 10 °C were not uncommon during the course of a reaction.

The reaction was allowed to proceed for a period of 1150 ± 50 mins, with the hydrogen pressure being monitored at regular intervals. Agitation of the reaction mixture was provided throughout the reaction by a magnetic stirrer.

The analysis of the final composition of the liquid phase and in some cases the gas phase was made using gas liquid chromatography (GLC).

2.9.1.2. Product Analysis

Analysis of the liquid product was performed by GLC using a Perkin-Elmer 8310 gas liquid chromatograph fitted with a flame ionisation detector (FID) coupled to a V.G. Minichrome computerised data handling system. The operating conditions for the various nitriles are summarised in Table 2.2. Calibrations were carried out for the reactant nitrile,and for primary, secondary and tertiary amines. The response factors relative to

Table 2.2 Operating conditions used for the analysis of the products produced from nitrile hydrogenation

Reactant: Propanenitrile
Internal Standard: N-propanol
Column: $^1/_4$ ", 4 m , 20 % Ucon 50 HB + 4% KOH
Column Temperature: 190°C isothermal
Detector Temperature: 250°C
Injector Temperature: 250°C
Carrier Gas: Nitrogen 22 psi
Hydrogen Pressure: 16 psi
Air Pressure: 22 psi
Reactant: Hexanenitrile
Internal Standard: N-propanol
Column and operating conditions as above
Reactant: Dodecanenitrile
Internal standard: Hexanenitrile
solvent: N-propanol
Column and operating conditions as above

an appropriate internal standard (IS) were calculated using the formula

$$\text{response factor} = \frac{\text{mass of conponent}}{\text{mass of IS}} \times \frac{\text{area of IS peak}}{\text{area of component peak}} \quad (2.18)$$

In the case of the dodecanenitrile only the nitrile and the primary amine were calibrated due to the lack of availability of the higher amines.

The final composition of the gas phase from the hydrogenation of propanenitrile was determined, in order to establish if there was any hydrogenolysis of the reactant taking place. A sample of the gas phase was obtained by the attachment of a 100 ml gas syringe to the vent line. Once the reactor had been allowed to cool to ambient temperature, the vent valve was opened and a sample of the venting gas was drawn into the syringe which was then sealed. Analysis of the sample of the gas phase was then performed using GLC, using a system already commissioned to perform analysis of C_1-C_4 hydrocarbons.

2.9.2. Catalyst Testing using an Atmospheric Pressure Flow Reactor

2.9.2.1. The Flow Reactor

The flow reactor (Fig. 2.15) was designed to operate at atmospheric pressure and was of a simple design. The gas saturator, reactor tube and sampling valve were all constructed from pyrex connected by ¼ " nylon tubing. The reactor was not constructed from stainless steel as is the normal practice because amines are known to adsorb on the walls of stainless

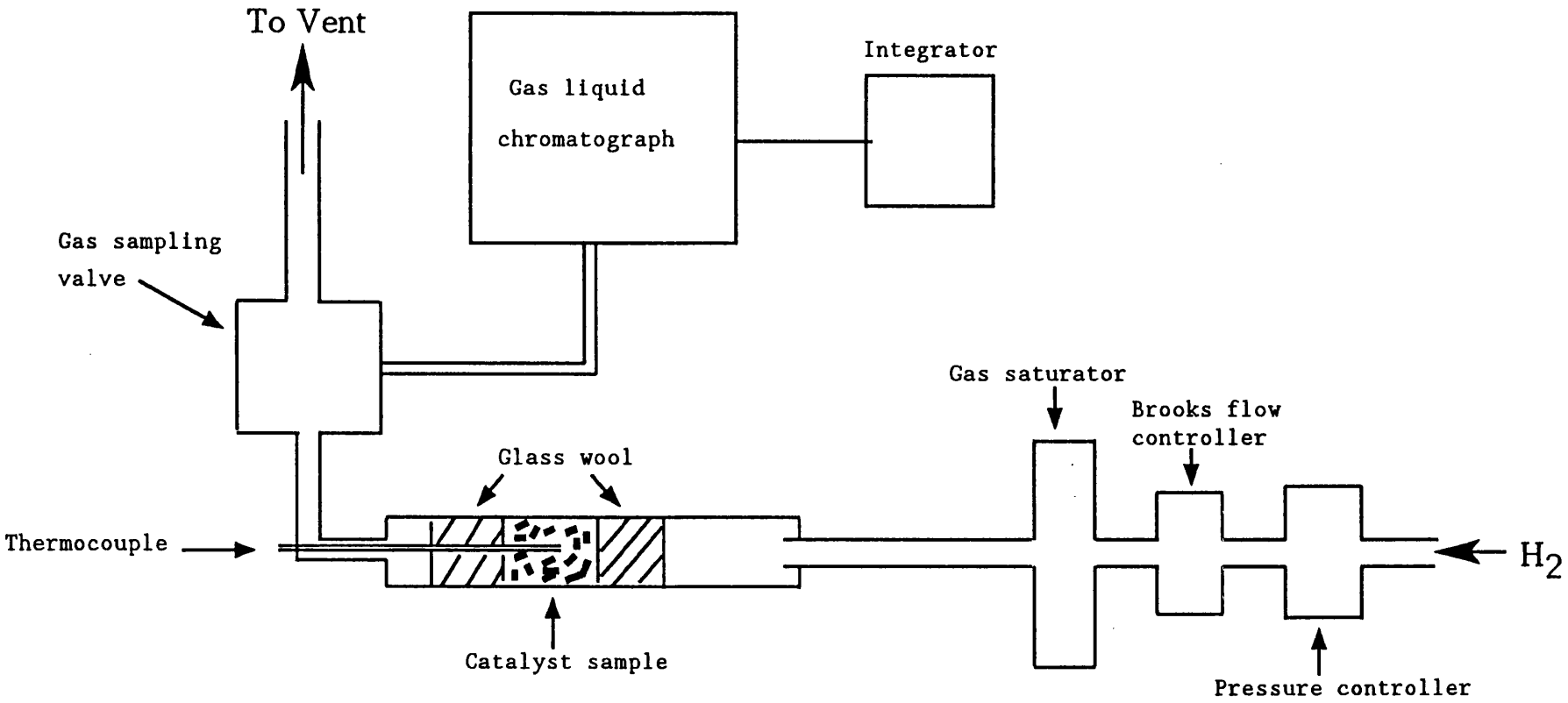

Figure 2.15 Schematic diagram of the flow reactor used in the hydrogenation of ethanenitrile

steel tubing and this can substantially affect the results.

The incoming hydrogen passed through the gas saturator and then through the catalyst bed contained within the reactor tube. The hydrogen flow rate was controlled using a pressure controller and a Brooks mass flow controller. Heat was supplied to the reactor from a tube furnace controlled by a 8 amp Variac. The temperature within the catalyst bed was monitored by a chromel-alumel thermocouple inserted into the thermocouple pocket which extended into the centre of the catalyst bed. The exit gas passed through the sample valve to vent. The sample valve permitted 0.1 ml of exit gas to be injected into the helium carrier gas line of the gas liquid chromatograph (Pye 104). The chromatograph was fitted with a thermal conductivity detector (TCD) allowing the analysis of both organic and inorganic substances. The column used for the chromatographic separation of the products and the operating conditions employed are summarised in Table 2.3. The output from the TCD was fed to an integrator (Spectra Physics SP470).

Calibration of the detector was carried out by injecting 0.1 µl of mixture of various compositions of the reactant nitrile and the corresponding primary, secondary and tertiary amines. Hence plots of peak area vs concentration were obtained for the various compounds.

2.9.2.2. Procedure for Catalyst Testing

The majority of the flow experiments were carried out using ethanenitrile(acetonitrile) as the reactant nitrile,

Table 2.3 Operating conditions used for the gas chromatograph in the flow reactor

Column :	1/4 " 3m 20%Ucon 50 HB
Carrier gas :	Helium / 25 ml min^{-1}
Detector :	TCD / bridge current 100 mA
Detector Temperature :	100 °C
Column Temperature :	90 °C

although some experiments were carried out using propanenitrile for comparison. The passivated catalyst (0.5 g) was loaded into the reactor tube and secured at both ends by glass wool. The system was flushed with hydrogen prior to commencing heating. The reactivation was carried out in a stream of hydrogen for a period of 16 hours. Once in the active state the temperature was lowered to 508 K and the hydrogen was diverted through the gas saturator. The saturator was maintained at a temperature of 273 K and the hydrogen flow rate set to 19.3 ± 0.5 ml min^{-1}. The reaction was monitored until the conversion of the reactant nitrile had attained a steady state. The following experiments were then carried out:

(i) variation of the space velocity in order to determine the rate of reaction;

(ii) variation of temperature in order to determine the activation energy for ethanenitrile hydrogenation;

(iii) variation of ethanenitrile concentration in order to determine the order of reaction with respect to ethanenitrile

(iv) variation of hydrogen concentration in order to determine the order of reaction with respect to hydrogen.

Variation of Space Velocity

The space velocity S_V is defined as

$$S_v = \frac{Q_o}{V} \qquad (2.19)$$

where V is the volume of the catalyst bed and Q_o is the volumetric feed rate, was varied by varying the rate of hydrogen through the gas saturator which was maintained at 273

K. The flow rate was raised and the system allowed to equilibrate prior to analysing the composition of the reactor exit gas; the result recorded was an average of a number of separate analyses. The flow rate was increased in a number of incremental stages up to 60 ml min^{-1} as measured by a bubble flow meter connected to the vent line. The flow rate was then decreased to determine if any deactivation had occurred during the course of the study.

Variation of Temperature

Again the gas saturator was maintained at 273 K, the hydrogen flow rate was set to 19.3 ml min^{-1} and the reactor temperature set to 508 K. The reactor temperature was randomly raised and lowered around this point. The system was allowed to stabilise between each variation in reactor temperature and the composition of the exit stream from the reactor was analysed. Finally the reactor was returned to its original temperature to determine the extent of catalyst deactivation during the course of the experiment.

Variation of Ethanenitrile Concentration

The hydrogen flow rate was maintained at 19.3 ml min^{-1} and the temperature kept constant at 508 K for catalyst OH5 and 483 K for catalyst HT1. The nitrile concentration was varied by varying the temperature of the gas saturator between 273 K and 285 K. This resulted in the partial pressure of ethanenitrile varying between 25 Torr and 47 Torr. As pure hydrogen was used as carrier, the hydrogen/ethanenitrile ratio varied from 29:1 to 15:1. This must be borne in mind when analysing the results

Variation of Hydrogen Concentration

The variation in hydrogen concentration was achieved by using hydrogen/helium mixtures of varying composition. These were produced using a separate piece of apparatus which had the facility for gas mixing. The gas mixture was then piped to the flow reactor. The hydrogen/helium flow rate was maintained constant at 19.3 ml min^{-1} and the reactor was kept at 483 K during the experiment. The composition of the exit gas from the reactor was monitored for different H_2:He ratios.

Chapter 3

Results

"Dans les champs de l'observation le hasard ne favorise que les espirits prepares."

Where observation is concerned, chance favours only the prepared mind.

Louis Pasteur 1822-1895

3.1. Analysis of the Starting Precipitates

3.1.1. Determination of Iron Content

Accurate determinations of iron loadings made by A.A.S. are recorded in Table 3.1

3.1.2. Analysis of the Starting Precipitates

3.1.2.1. Analysis of the Carbonate Coprecipitated Precipitates

The initial solution containing $Mg(NO_3)_2$ and $Fe(NO_3)_3$ had a pH value of approximately 2. Initial addition of $(NH_4)_2CO_3$ resulted in the iron being preferentially precipitated. The nature of this initial iron-containing species was not determined. As more precipitating agent was added the pH of the reaction mixture rose to a value of pH 8, and only at this stage did the magnesium ions start to be precipitated. It was found that in order to precipitate all of the magnesium it was necessary to add a large excess of precipitating agent. In Fig. 3.1, diffractograms D and E refer to precipitates with 5 and 30% iron loadings respectively which have been obtained in this way.

Table 3.1 Iron loadings calculated from atomic absorption measurements.

CATALYST	IRON LOADING / MOLE %
CCP5	4.8
CCP10	10.0
CCP20	18.9
CCP30	30.8
OH5	4.8
OH10	9.5
OH20	18.5
OH30	29.2
IP5	4.9
IP10	10.0
IP20	19.8
IP30	29.9
HT1	22.6

3.1.2.2. Analysis of the Hydroxide precipitated precipitates

Addition of the solution containing $Mg(NO_3)_2$ and $Fe(NO_3)_3$ to ammonia solution resulted in the simultaneous precipitation of magnesium and iron ions providing the pH was maintained at pH 11. The X-ray diffractograms of the dried precipitates are shown in Fig. 3.2. Diffractograms B,C,D and E represent materials with iron contents of 5, 10, 20 and 30% respectively, whilst diffractogram A is that of $Mg(OH)_2$. The position of the lines, d-spacings and their assignments are contained in Table 3.2 for the 5% and 30% loaded materials. It can be seen that the iron containing phase is pyroaurite, the structure of which is shown in Figure 3.3.

3.1.2.3. Analysis of the iron impregnated magnesium hydroxycarbonate

The X-ray diffractograms of the dried materials with 5% and 30% iron loadings are shown in Fig. 3.1 as B and C respectively. The diffractograms are very similar to those produced via the coprecipitation method using $(NH_4)_2CO_3$ as the precipitant.

3.2. Analysis of the Catalyst Precursors

Examples of the X-ray diffractograms obtained from the calcined materials are shown in Figure 3.4. The diffractograms

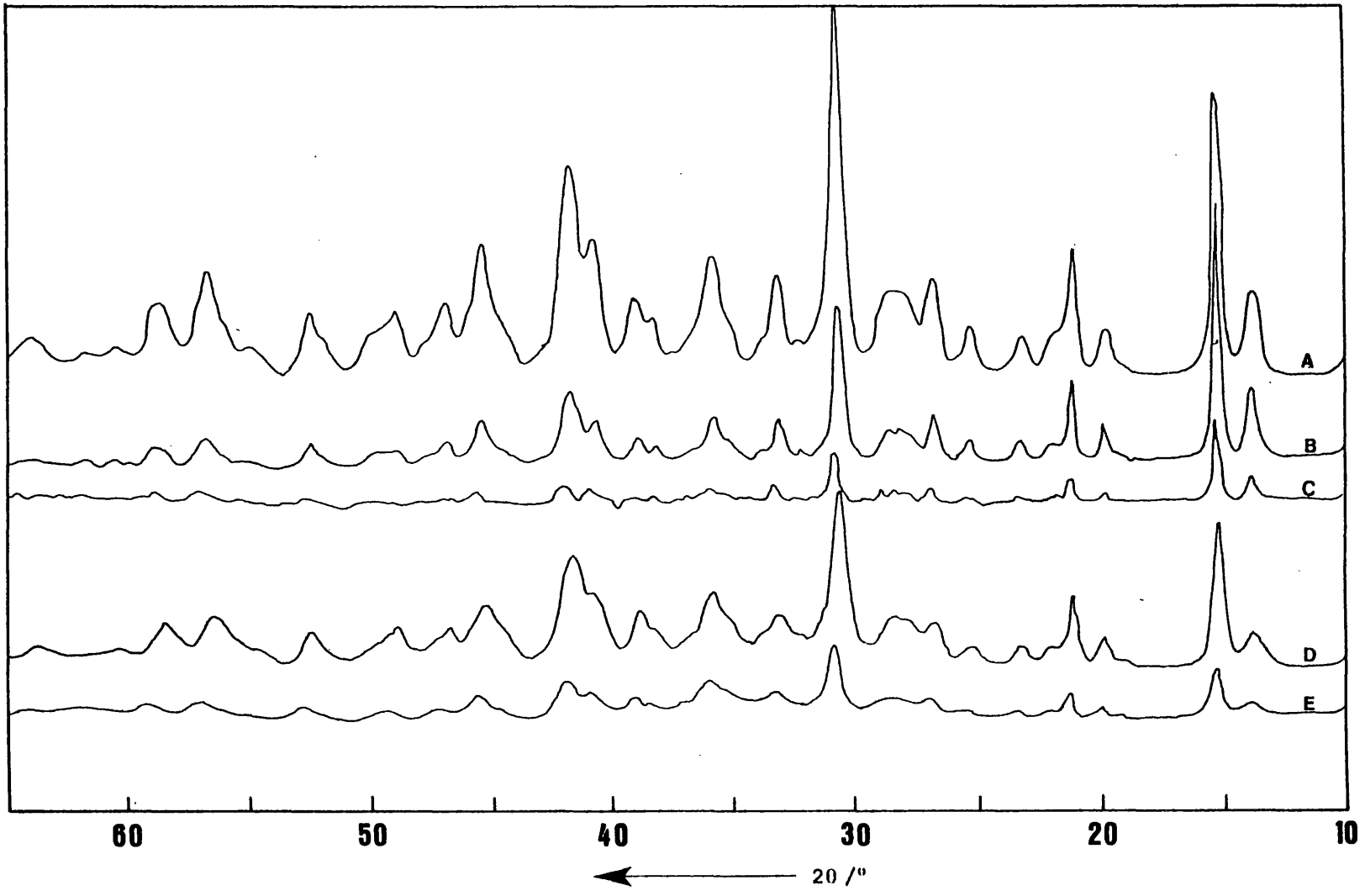

Figure 3.1 Examples of the X-ray diffractograms obtained from carbonate coprecipitated and impregnated starting materials

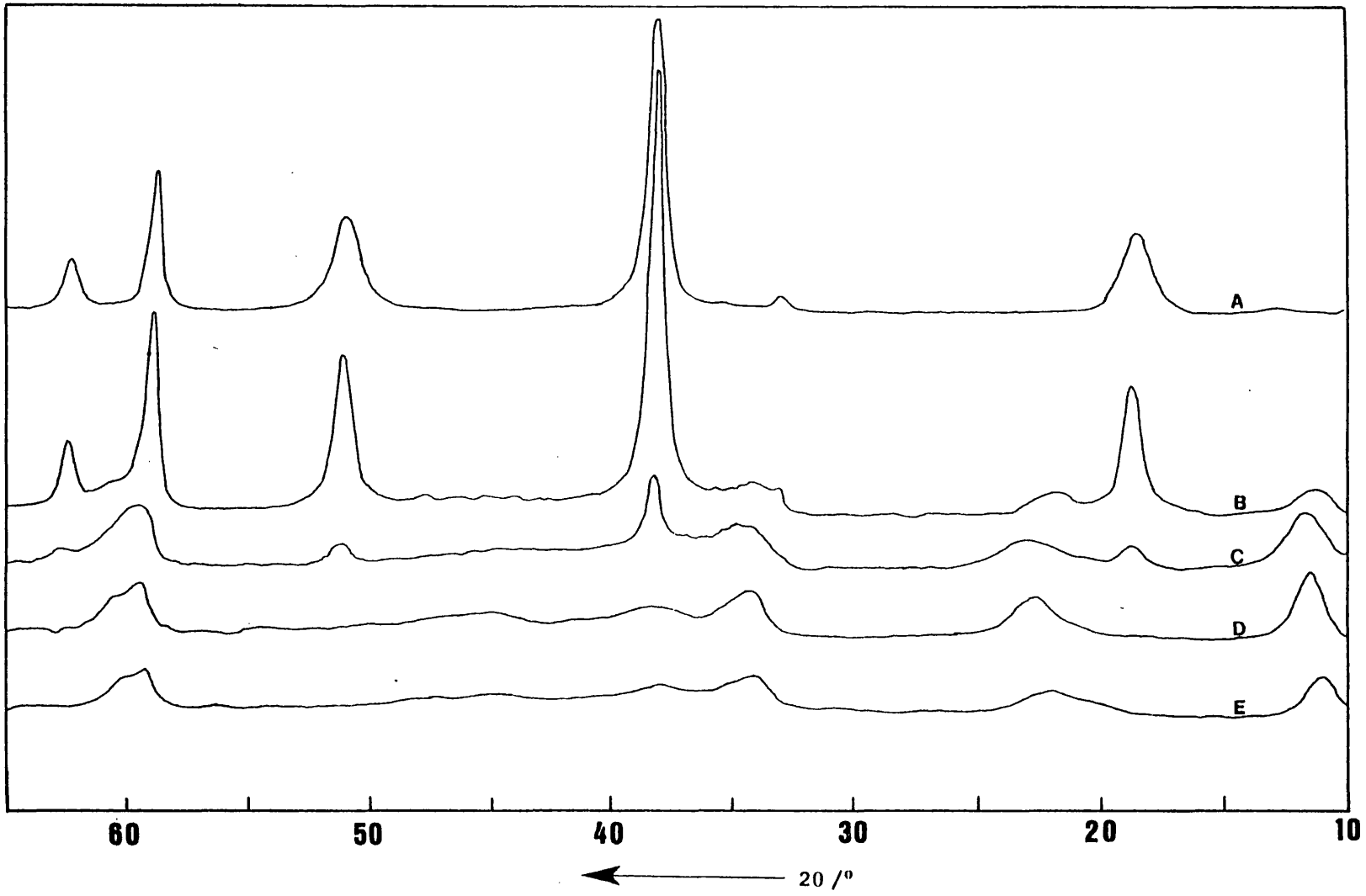

Figure 3.2 X-ray diffractograms of the hydroxide coprecipitated starting materials.

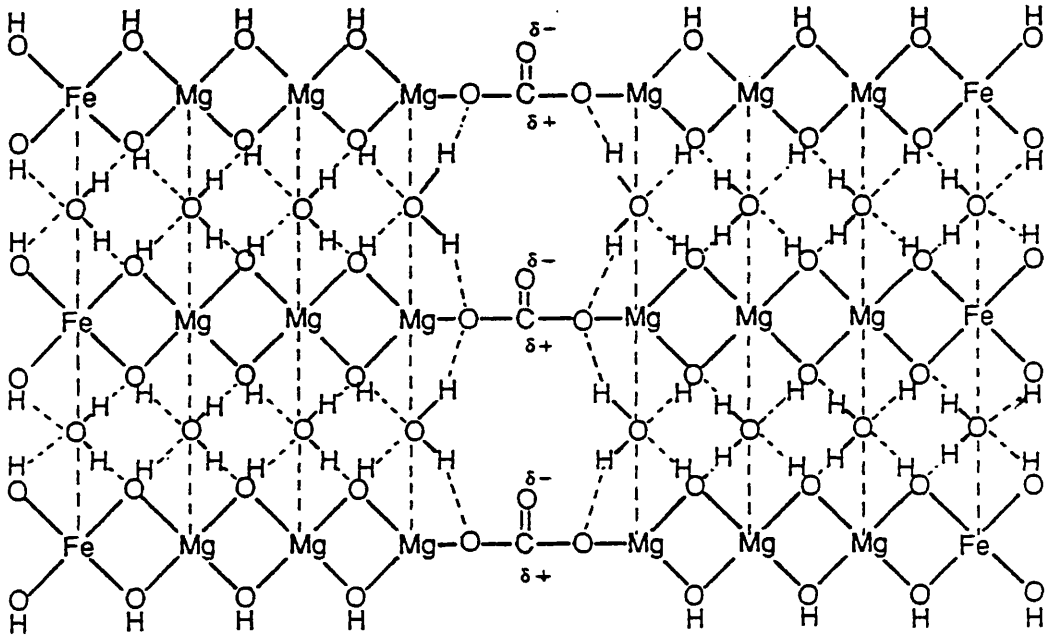

Figure 3.3 The pyroaurite structure.

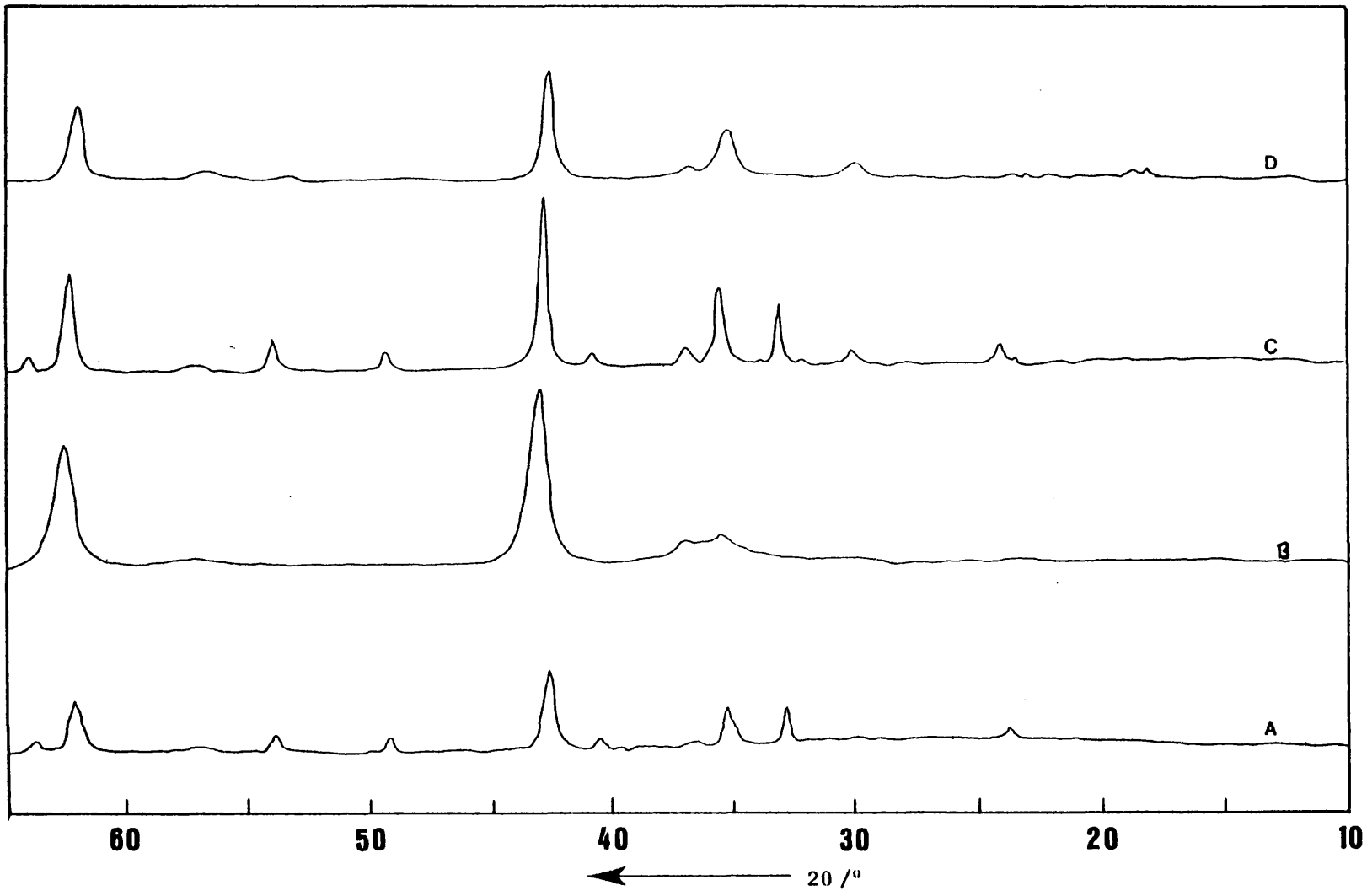

Figure 3.4 Examples of the X-ray diffractograms obtained from the catalyst precursors prepared by the various methods adopted.

Table 3.2 X-ray diffraction line positions and assignments for the hydroxide coprecipitated materials

OH5		
Position/2θ	d-spacing/Å	Assignment
11.4	7.26	pyro (003)
18.8	4.72	bruc (011)
21.9	4.058	pyro (006)
33.0	2.714	
34.2	2.622	pyro (012)
38.15	2.359	bruc (101)/pyro (015)
51.05	1.789	bruc (102)
58.8	1.570	bruc (110)
62.3	1.490	bruc (111)
OH30		
11.25	7.865	pyro (003)
22.5	3.951	pyro (006)
34.2	2.622	pyro (012)
38.0	2.368	bruc (101)
58.55	1.576	bruc (110)
59.4	1.556	pyro (110)

* pyro = pyroaurite

bruc = brucite

A, B, C and D correspond to the precursors IP30, OH20, CCP20 and HT1 respectively. The peak positions, d-spacings and their assignments are given in Table 3.3. In order that a comparison can be made between the reflections due to iron oxide in the catalyst precursors with literature values for iron oxides, the main reflections for both α-Fe_2O_3 and γ-Fe_2O_3 are given in Table 3.4

Some diffractograms exhibit peaks at 2θ values 2.96 and 1.612 ^{o} these are due respectively to the 220 and 511 reflections of the spinel magnesioferrite. The presence of the magnesioferrite phase has also been confirmed by Mössbauer spectroscopy (Section 3.5)

3.3. Reduction of the Catalyst Precursors

The reduction of the catalyst precursors using the standard procedure described in Section 2.1.3 resulted in incomplete reduction of the iron-containing species to metallic iron. This is in agreement with the findings of other workers (2,3). The percentage reduction of Fe^{3+} to Fe^{0} obtained for the various catalysts are recorded in Table 3.5. The results presented in this table have been calculated making the assumption that all the Fe^{3+} is reduced to Fe^{2+} prior to the onset of reduction to Fe^{0}. The slight discrepancy in the results obtained using the volumetric system in comparison with those from the gravimetric studies may be a result of the depletion of the hydrogen supply in the volumetric system during periods of the reduction process.

Table 3.3 Assignment of the x-ray reflections for examples of catalyst precursors prepared by different techniques.

IP30		
Position/2θ	d-spacing/Å	Assignment
23.9	3.723	α-Fe_2O_3 (012)
32.9	2.722	α-Fe_2O_3 (104)
35.35	2.539	α-Fe_2O_3 (110)
40.6	2.222	α-Fe_2O_3
42.6	2.122	MgO (200)
49.25	1.850	α-Fe_2O_3 (024)
53.85	1.702	α-Fe_2O_3 (116)
62.15	1.493	MgO (220)
63.8	1.459	α-Fe_2O_3 (300)
OH20		
35.6	2.522	γ-Fe_2O_3 (311)
36.05	2.491	MgO (111)
43.1	2.099	MgO (200)
62.5	1.486	MgO (220)/γFe_2O_3 (440)
CCP20		
24.05	3.700	α-Fe_2O_3 (012)
33.1	2.706	α-Fe_2O_3 (014)
35.55	2.525	α-Fe_2O_3 (110)
36.85	2.439	MgO (111)
40.80	2.212	α-Fe_2O_3 (113)
42.85	2.110	MgO (200)
49.45	1.843	α-Fe_2O_3 (024)
54.05	1.696	α-Fe_2O_3 (116)
62.25	1.491	α-Fe_2O_3 (214)/MgO (220)
64.0	1.455	α-Fe_2O_3 (300)
HT1		
30.15	2.964	γ-Fe_2O_3 (220)
35.35	2.532	γ-Fe_2O_3 (311)
37.05	2.426	MgO (111)
43.0	2.103	MgO (200)
57.0	1.616	γ-Fe_2O_3 (511)
62.45	1.487	γ-Fe_2O_3 (440)/MgO (220)

Table 3.4 The main reflections for γ-Fe_2O_3 and α-Fe_2O_3.

γ-Fe_2O_3		
d-spacing / Å	I/I_1	hkl
2.52	100	(311)
1.48	53	(440)
2.95	34	(220)
1.61	33	(511)
2.08	24	(400)
2.78	19	(221)
α-Fe_2O_3		
2.703	100	(104)
2.519	70	(110)
1.696	36	(116)
3.686	33	(012)
1.843	31	(024)
1.487	22	(214)
1.454	21	(300)

Table 3.5 Fraction of iron reduced to metallic iron as determined using the gravimetric and volumetric systems

Catalyst	Percent Reduction	
	Microbalance System	Volumetric System
	%	%
CCP5	20	22
CCP10	26	25
CCP20	59	54
CCP30	69	65
OH5	27	26
OH10	39	37
OH20	54	51
OH30	57	54
IP5	24	24
IP10	32	31
IP20	37	35
IP30	53	49
HT1	42	40

3.4. Analysis of the Catalysts

3.4.1. Nitrogen adsorption at 77 K

Nitrogen adsorption isotherms recorded on the samples which had been reduced and passivated using N_2O were analysed to give information concerning the total surface area and pore size distribution of the catalysts. Total surface areas calculated via the BET method are recorded in Table 3.6. The areas range from 45 m^2g^{-1} to 107 m^2g^{-1} and the different apparatus used to make the determinations all gave similar results. The results do not appear to show any sign of a trend with either iron loading or method of preparation. Some surface area measurements were also made on the calcined precursors. The areas were found not to differ greatly from the corresponding reduced and passivated material.

Figure 3.5 shows a typical adsorption / desorption isotherm from a sample which had been reduced and passivated. This shows the hysteresis loop which is characteristic of type IV isotherms of mesoporous solids. The pore size distributions were calculated from both the adsorption and desorption branches of the isotherm. The results represented in the form of bar charts (Figures 3.6 - 3.12) obtained from the adsorption branch as opposed to the desorption branch which is now the more common practice. The reason for this will be discussed in Section 4.4.1.

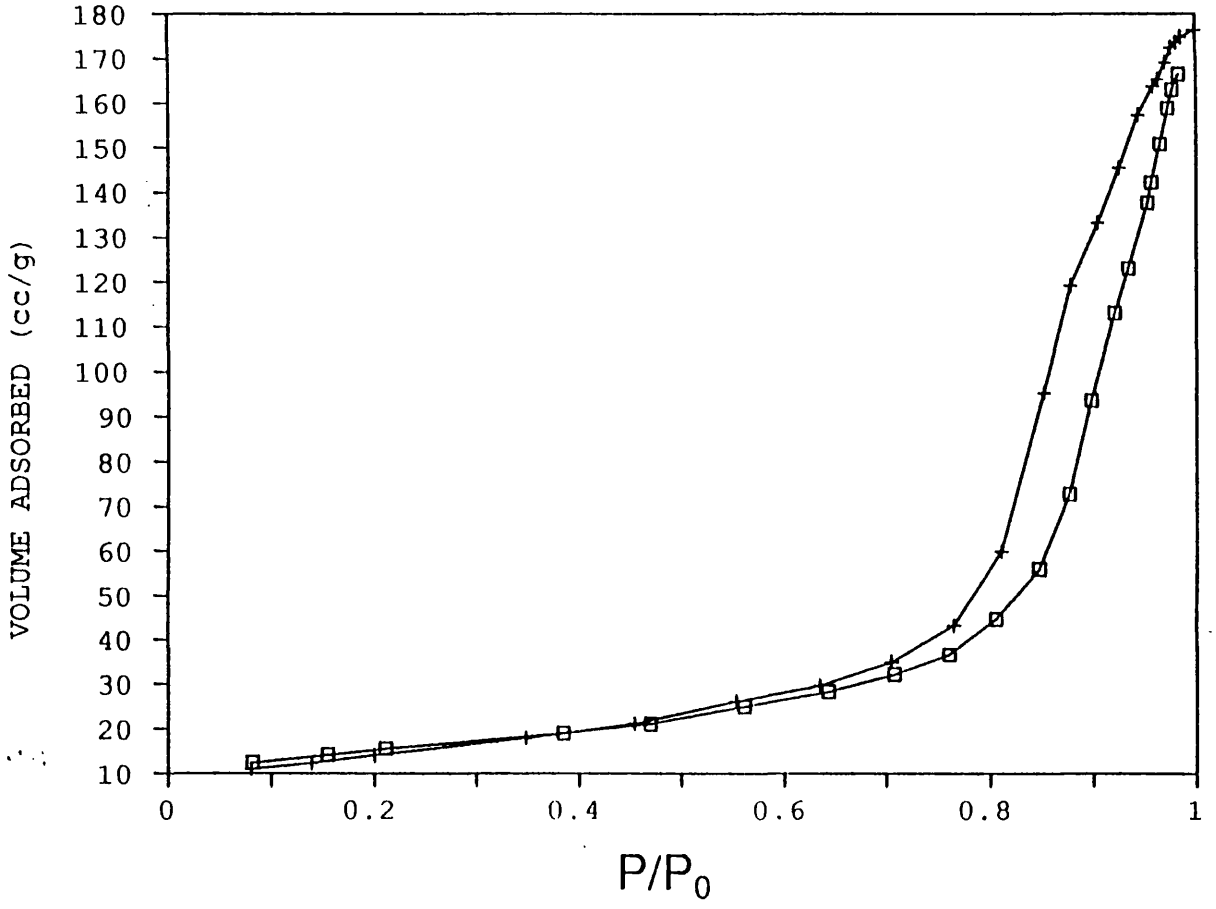

Figure 3.5 Typical Adsorption / Desorption Isotherms

Table 3.6 Total surface areas calculated from nitrogen adsorption isotherms

CATALYST	SURFACE AREA /m^2g^{-1}
CCP5	107
CCP10	58
CCP20	43
CCP30	51
OH5	78
OH10	92
OH20	70
OH30	56
IP5	59
IP10	50
IP20	77
IP30	45
HT1	64

Key for Figures 3.6 - 3.11

Letter	Pore Diameter Range /Å
A	20 - 25
B	25 - 30
C	30 - 35
D	35 - 40
E	40 - 45
F	45 - 50
G	50 - 55
H	55 - 60
I	60 - 65
J	65 - 70
K	70 - 75
L	75 - 80
M	80 - 85
N	85 - 90
O	90 - 95
P	95 - 100
Q	100 - 110
R	110 - 120
S	120 - 130
T	130 - 140
U	140 - 150
V	150 - 160
W	160 - 180
X	180 - 200
Z	200 - 220
a	220 - 240
b	240 - 260
c	260 - 280
d	280 - 300
e	300 - 350
f	350 - 400
g	400 - 450
h	450 - 500
	500 - 600

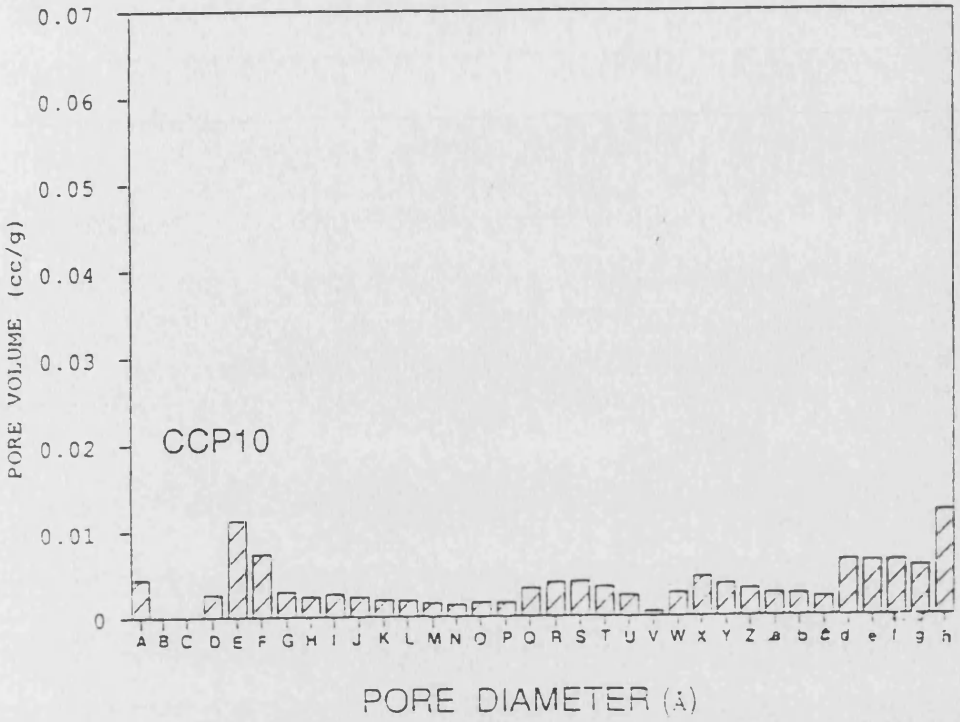

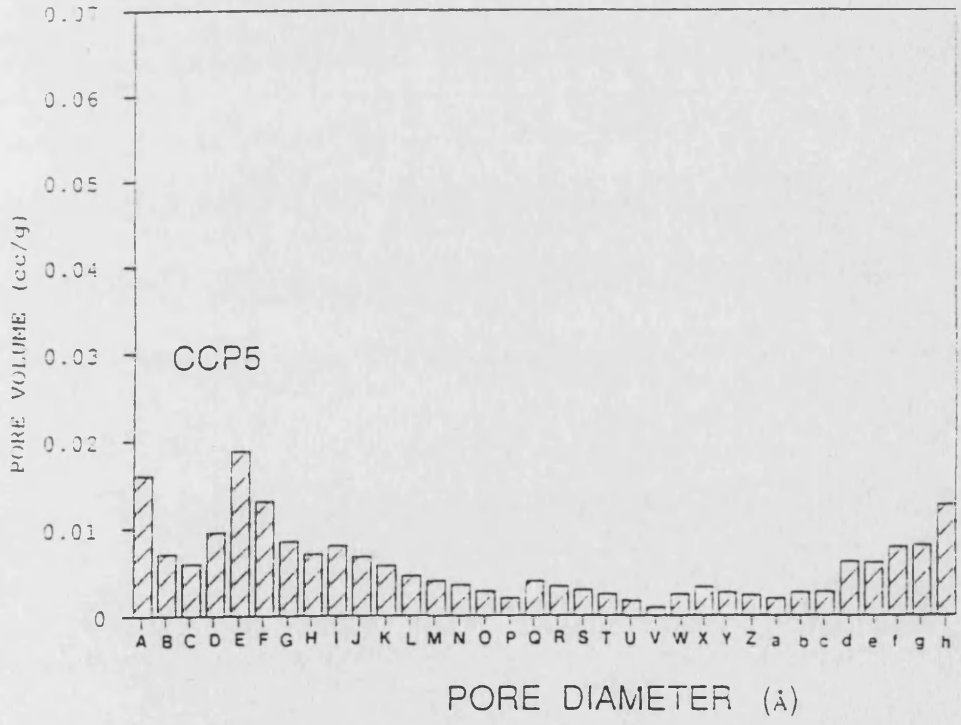

Figure 3.6 Bar charts representing the pore size distributions for catalysts CCP5 and CCP10.

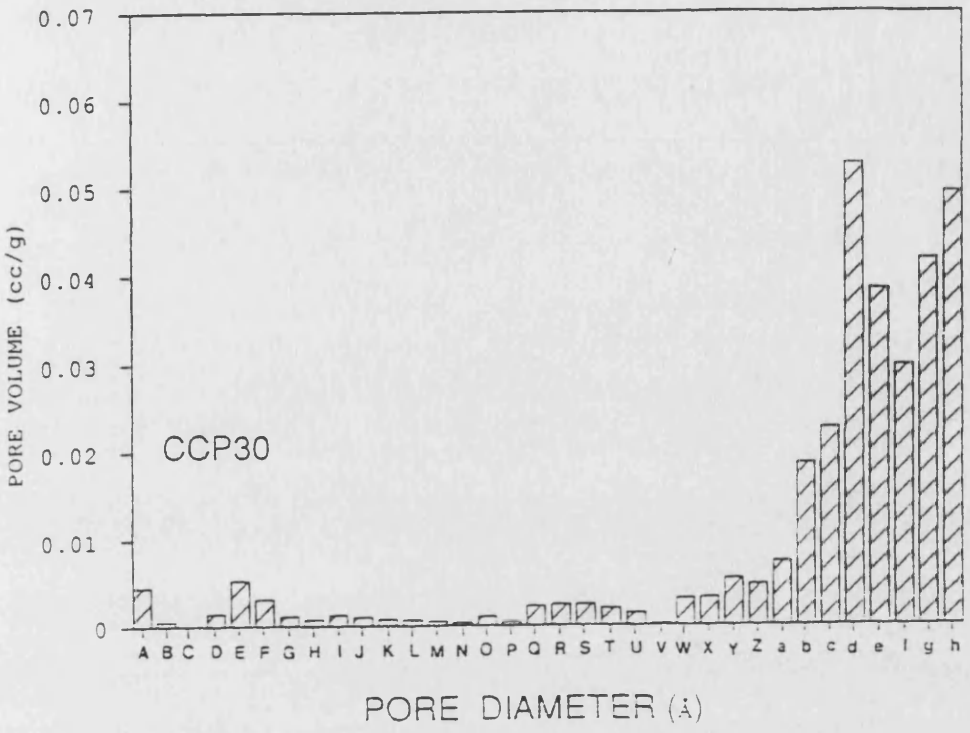

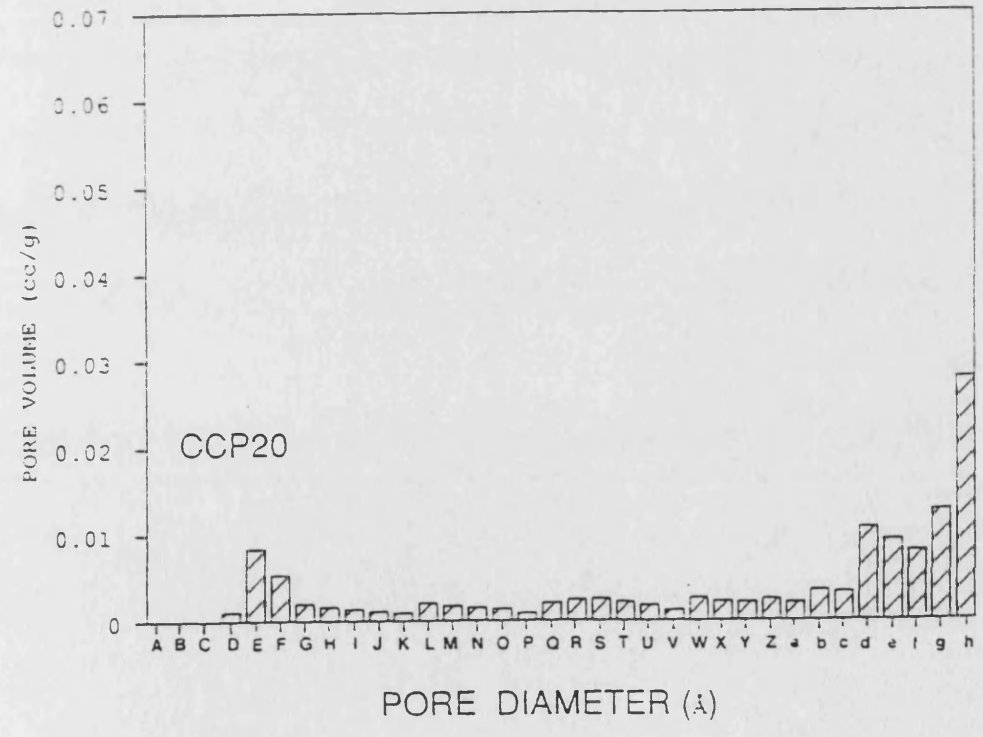

Figure 3.7 Bar charts representing the pore size distributions for catalysts CCP20 and CCP30.

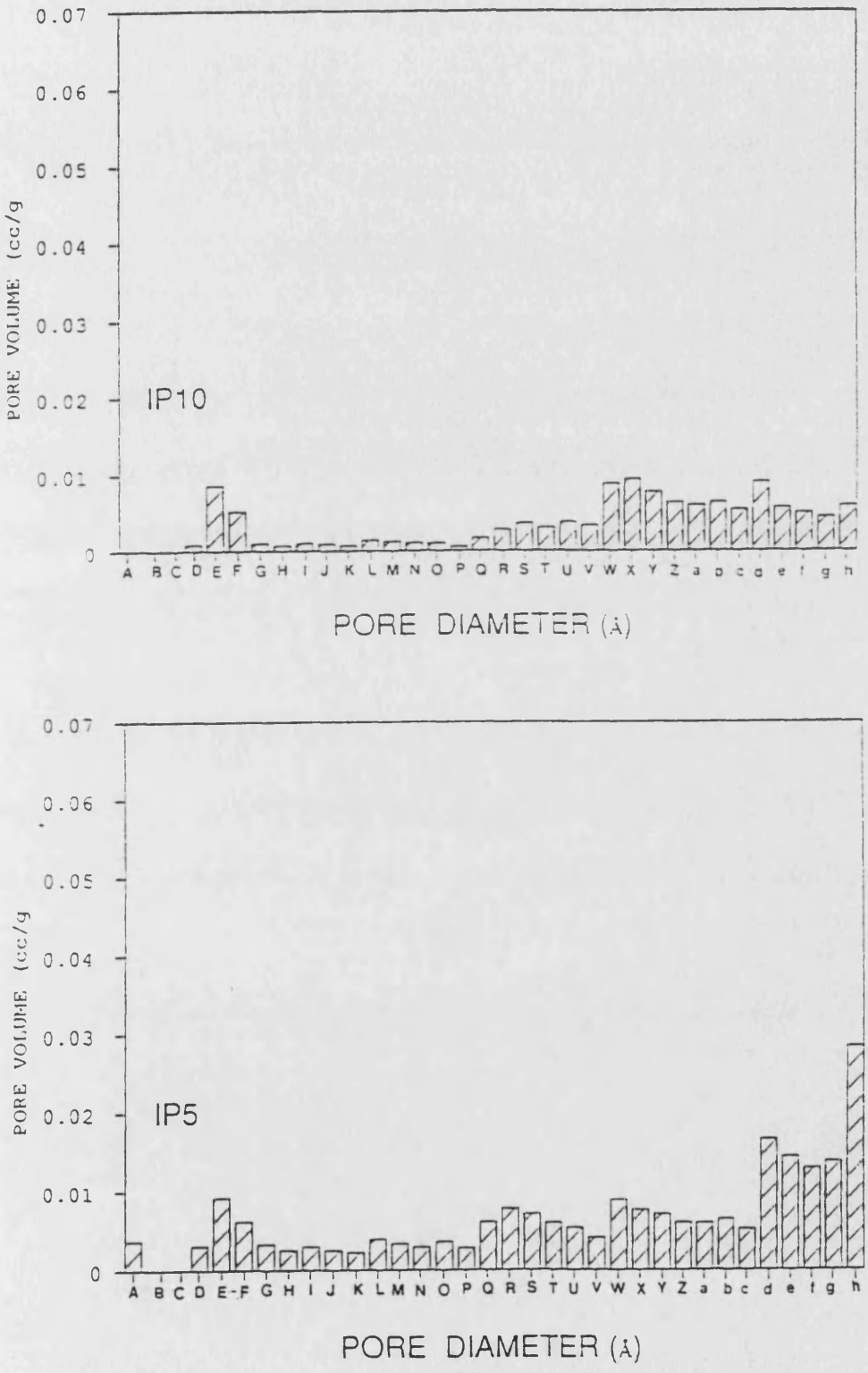

Figure 3.8 Bar charts representing the pore size distributions for catalysts IP5 and IP10.

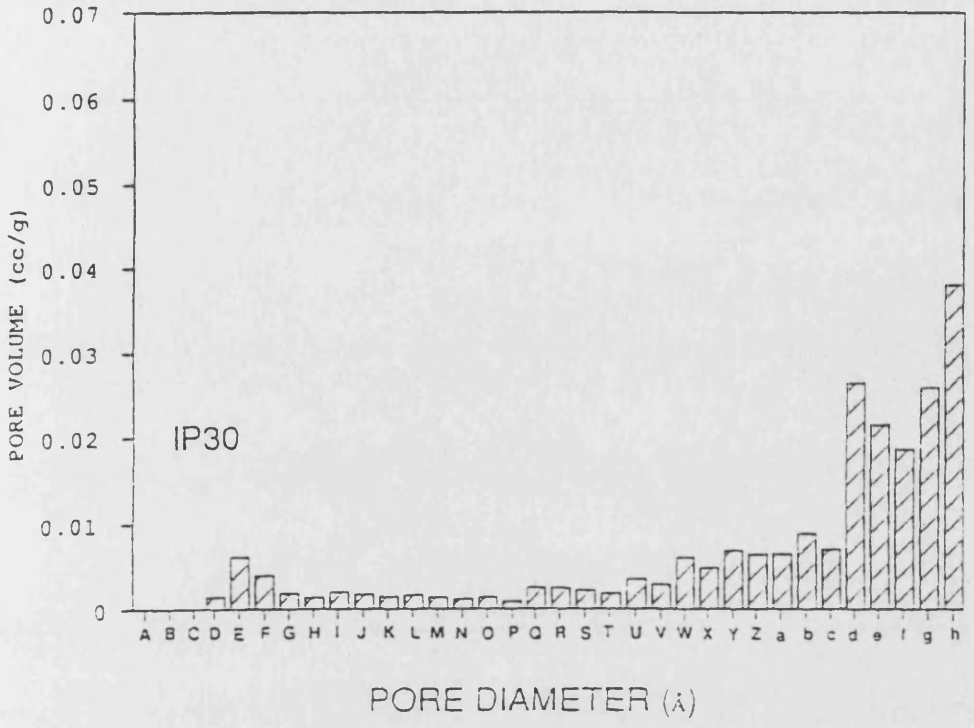

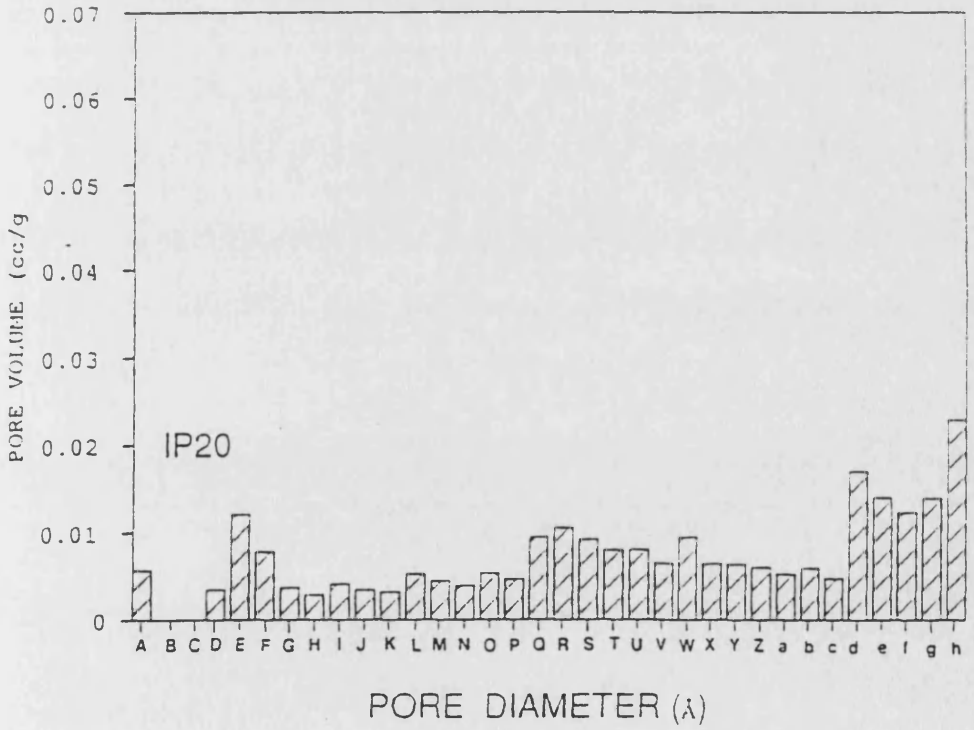

Figure 3.9 Bar charts representing the pore size distributions for catalysts IP20 and IP30.

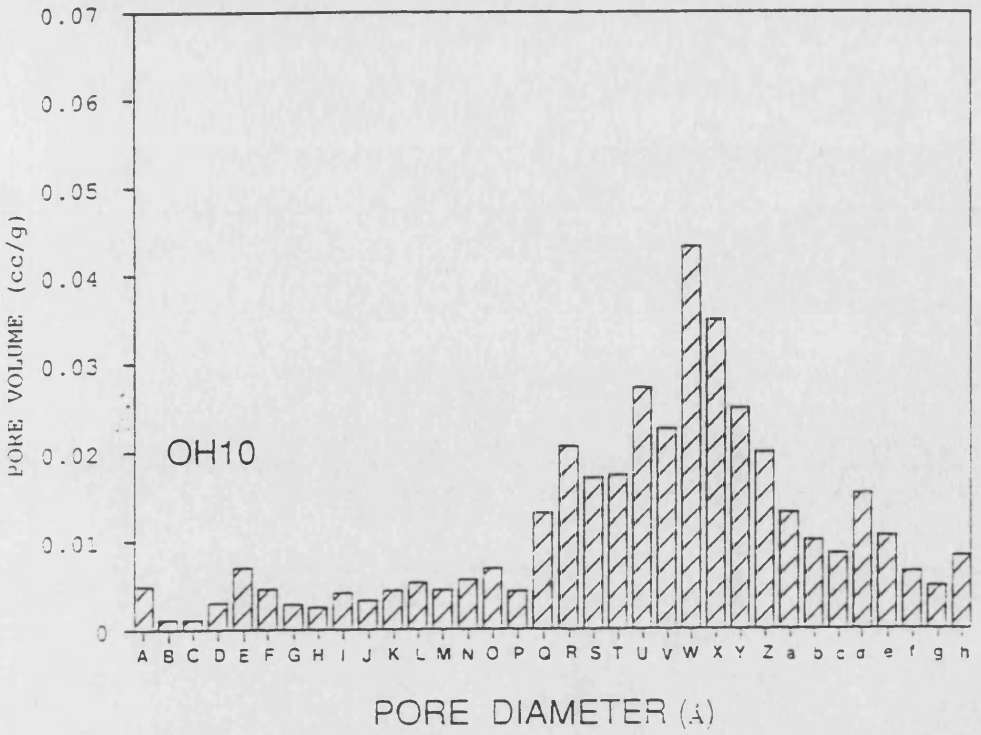

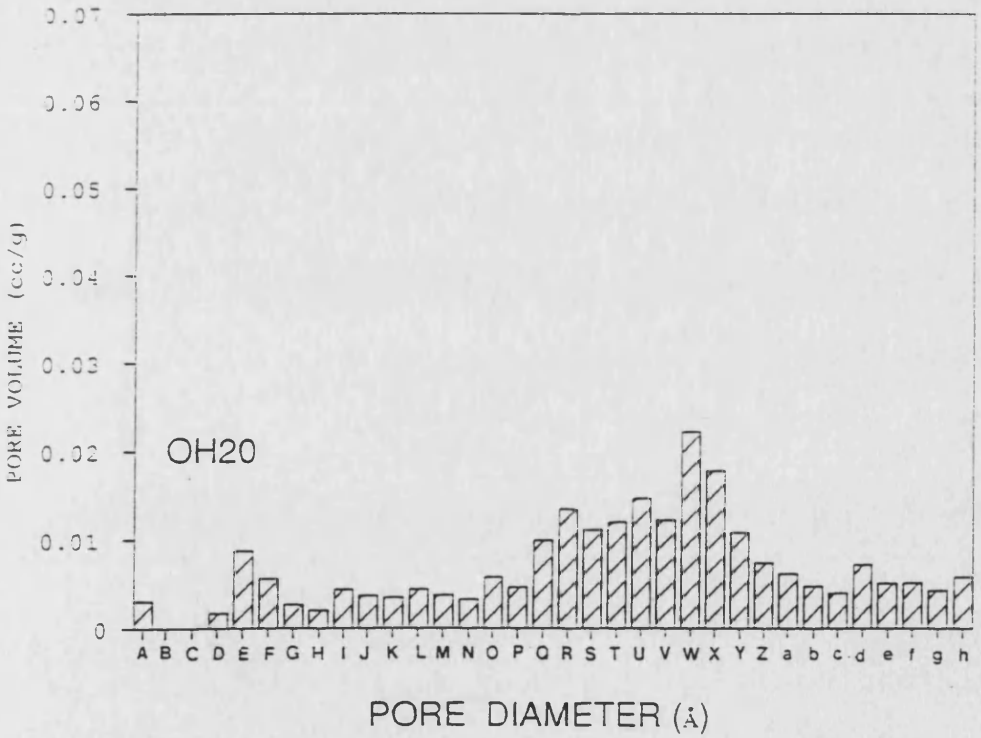

Figure 3.10 Bar charts representing the pore size distributions for catalysts OH10 and OH20.

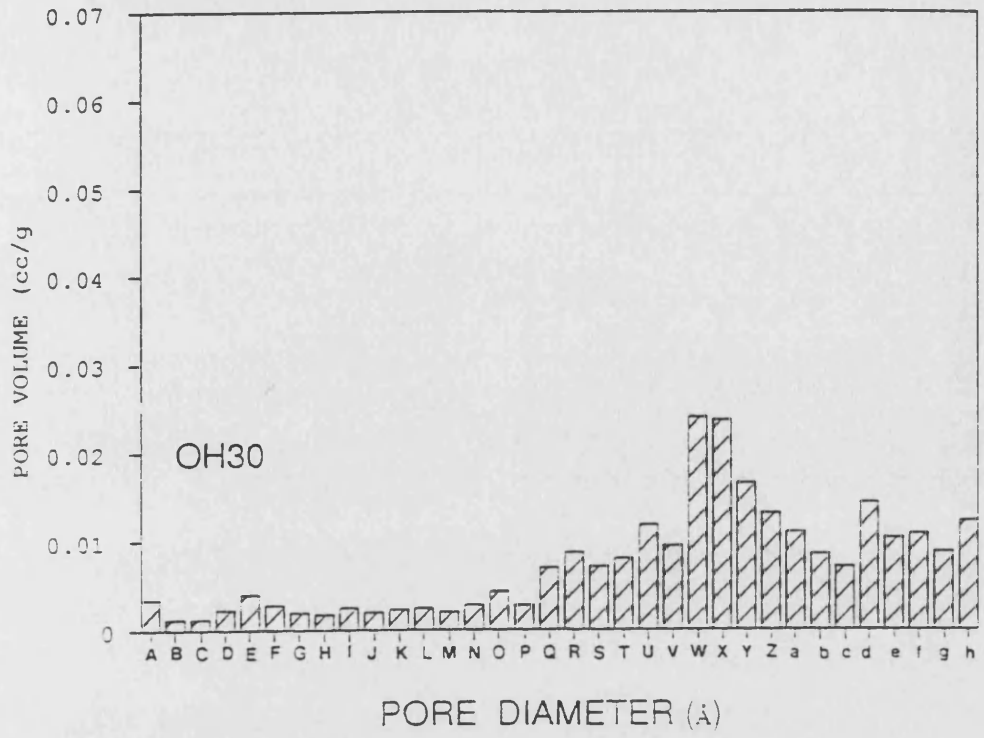

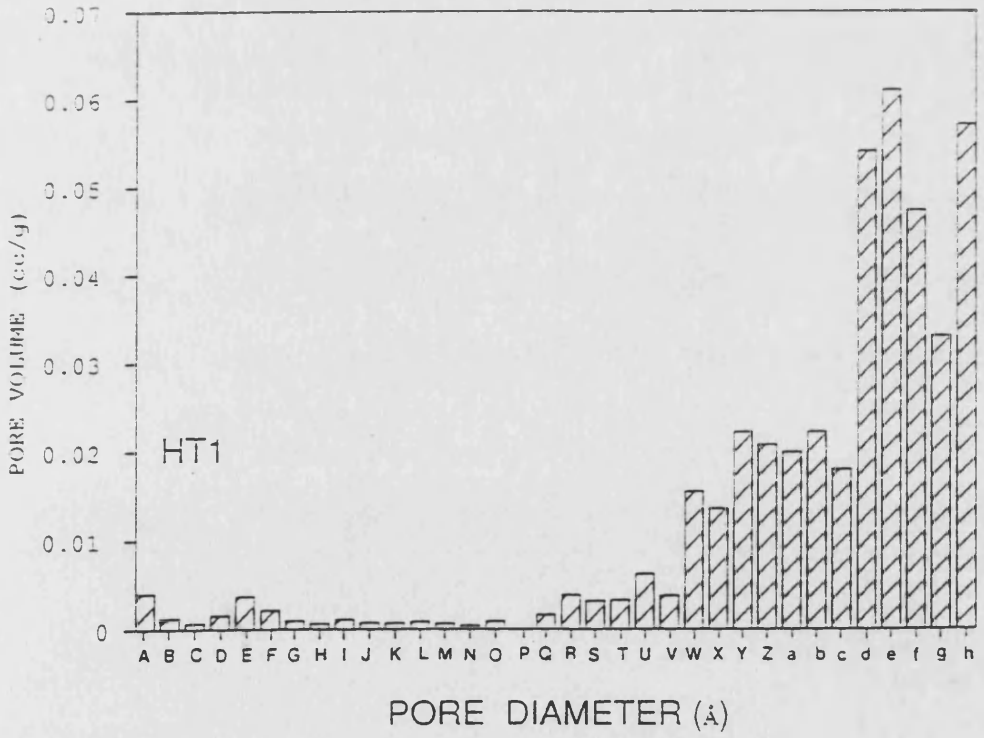

Figure 3.11 Bar charts representing the pore size distributions for catalysts OH30 and HT1.

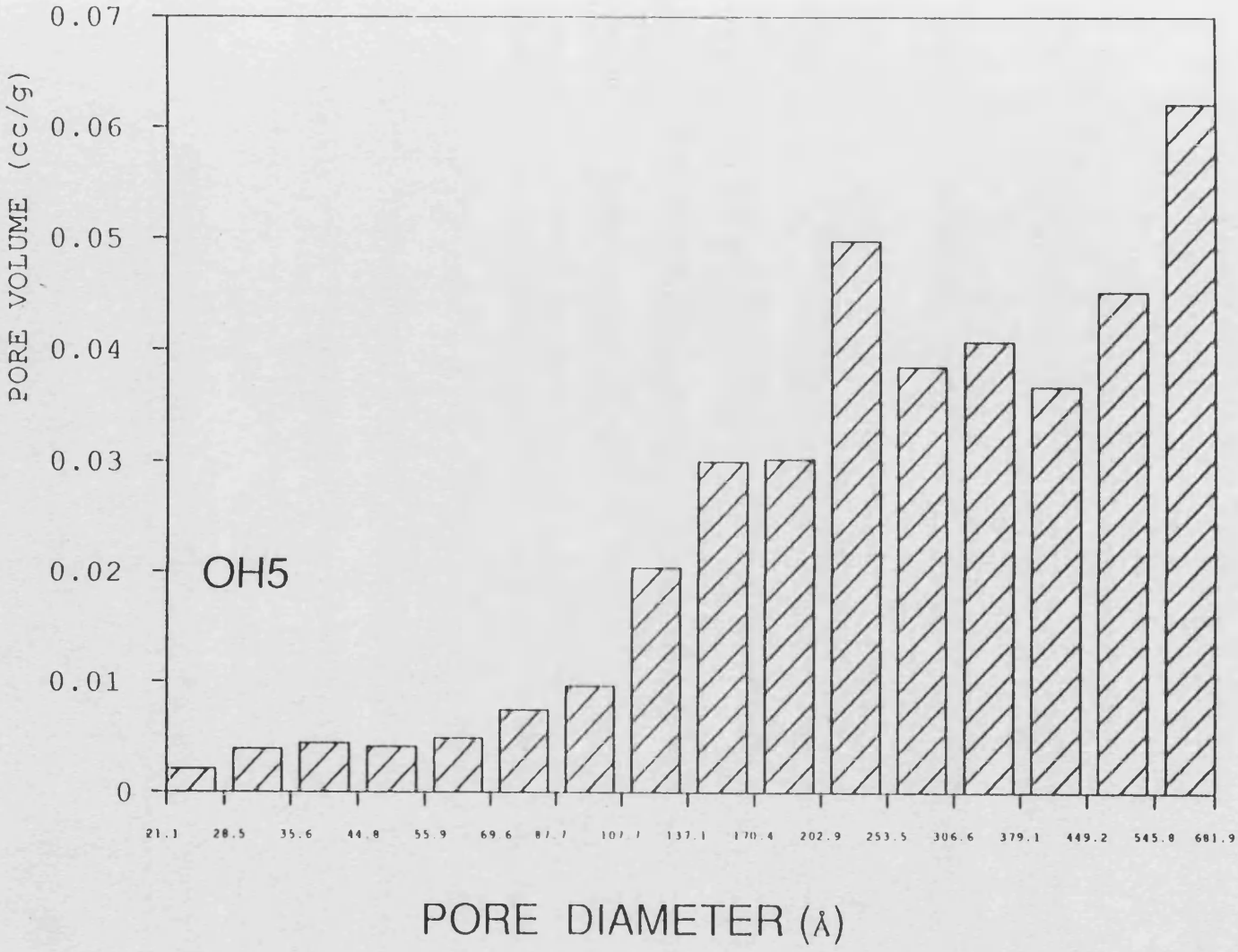

Figure 3.12 Bar chart representing the pore size distribution for catalyst OH5

3.4.2. Determination of Iron Surface Area

Three different methods were used to obtain information on the surface area of iron in the supported iron catalyst. These were (i) chemisorption of carbon monoxide, (ii) reaction of nitrous oxide, and (iii) X-ray line broadening.

3.4.2.1. Carbon Monoxide Isotherms

CO adsorption is the most long-standing of the methods used to estimate the surface area of iron, having been used in the classical work of Brunauer and Emmett (66).

In the present work, isotherms were measured at 195 K using the method described in Section 2.4.2. A first isotherm measures both chemisorbed and physisorbed CO. A second isotherm measures only the reversible physisorbed CO. Figure 3.13 shows the isotherms produced from the adsorption of CO on catalyst HT1, this is typical of the isotherms produced for the all the catalysts used. The amount of CO chemisorbed is obtained by subtraction of the two isotherms in the region where A and B are equal (Fig 3.13).

The CO uptakes (Table 3.8) have been converted to iron surface areas assuming an Fe:CO stoichiometry of 2:1, the reasoning behind this assumption has been discussed in Section 2.4.2.1. An iron surface atom density of 1.2×10^{19} atom m^{-2} is also assumed, this corresponds to the surface atom density of

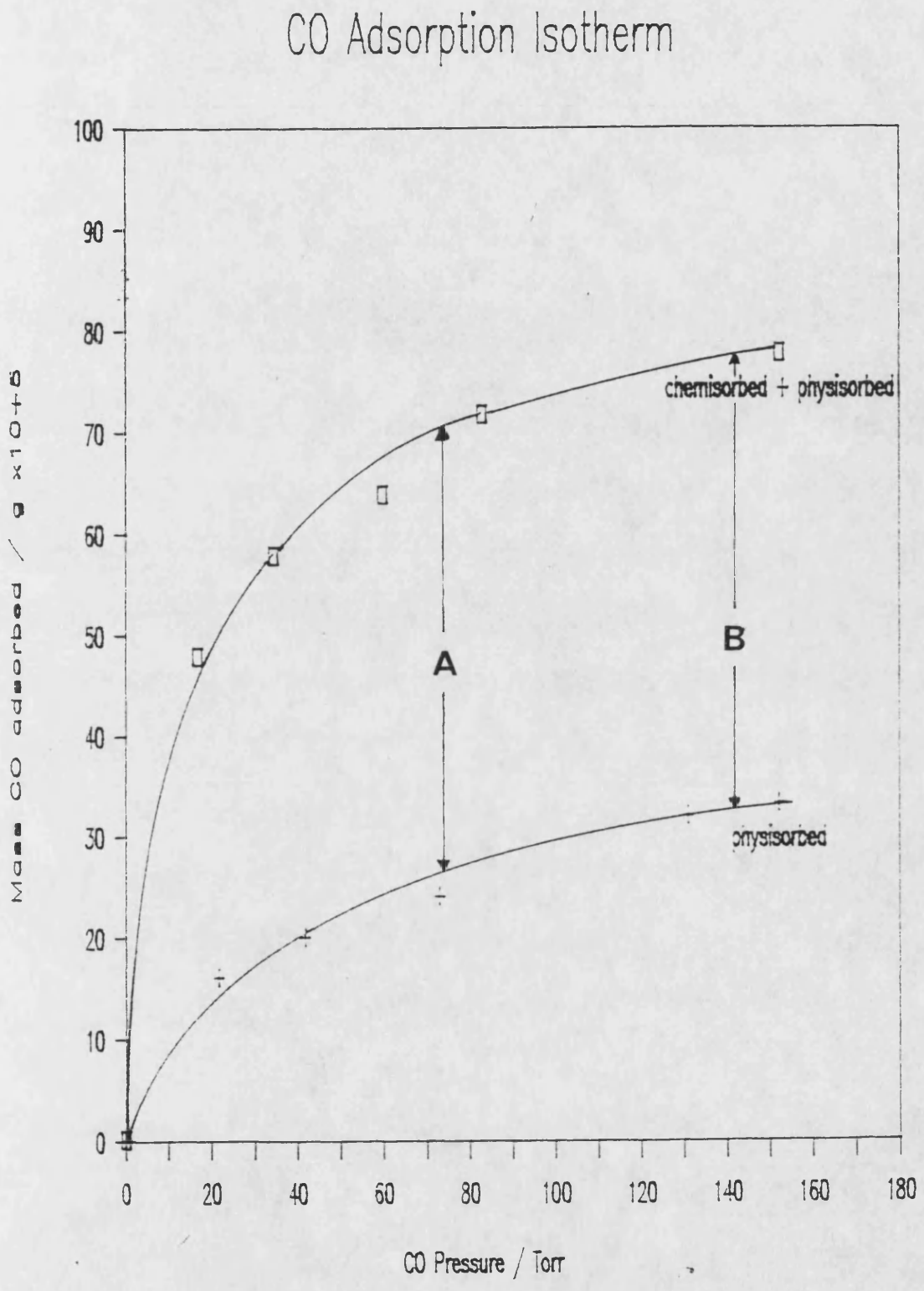

Figure 3.13 Typical carbon monoxide adsorption isotherms.

the (100) face of bcc iron. This has an intermediate value between the more closely packed (110) face and the more open (111) face which have surface atom densities of 1.7×10^{19} and 0.71×10^{19} atoms m^{-2} respectively (89).

3.4.2.2. Nitrous Oxide Decomposition

N_2O decomposition has been advocated as a suitable method for determining iron surface areas by Vogler et al. (90). This has been applied to the catalysts of the present work using procedures described in Section 2.4.3. The measurements have been made using both gravimetric and volumetric techniques; the areas determined by the two methods gave the same values within experimental error, results were reproducible to within ± 6 %. The areas were calculated assuming a Fe^0: N_2O ratio of 1:2.5 (91), and a Fe^0 surface atom density of 1.2×10^{19} atom m^{-2}. Table 3.9 contains the iron surface areas expressed in two forms, as the iron surface area per gram of catalyst and as the iron area per gram of iron. Both terms are commonly used when describing catalysts. The latter is useful as it gives some indication as to the dispersion of the iron in the catalyst

3.4.2.3 The Determination of Iron Surface Areas from X-ray Line Broadening.

X-ray line broadening provides a means, other than chemisorption for the determination of iron surface areas in the catalysts.

Table 3.8 Iron Surface Areas Calculated from CO Chemisorption at 195 K

Catalyst	CO Uptake $\mu mol\ g^{-1}$	Fe Surface Area $/m^2\ g^{-1}_{catalyst}$	Fe Surface Area $/m^2\ g^{-1}_{Fe^0}$
CCP5	28.9	2.9	158.3
CCP10	44.1	4.4	93.1
CCP20	50.2	5.0	26.6
CCP30	53.3	5.3	16.3
OH5	50.0	5.0	202.0
OH10	94.5	9.5	140.3
OH20	100.2	10.1	59.9
OH30	71.5	7.2	27.9
IP5	14.9	1.5	55.9
IP10	21.3	2.1	36.1
IP20	33.8	3.4	27.8
IP30	55.9	5.6	22.9
HT1	74.7	7.5	48.4

Table 3.9 Iron Surface Areas Calculated from N_2O Decomposition

Catalyst	Iron Surface Area $/m^2g^{-1}{}_{catalyst}$	Iron Surface Area $/m^2g^{-1}{}_{Fe^0}$
CCP5	3.1	169.1
CCP10	4.7	99.4
CCP20	5.1	27.2
CCP30	5.7	17.5
OH5	5.1	206.1
OH10	9.8	144.7
OH20	10.2	60.5
OH30	7.0	27.1
IP5	1.3	57.9
IP10	2.5	42.9
IP20	3.1	25.3
IP30	5.5	22.5
HT1	7.4	47.7

The experimental procedure for the determination of the line broadening due only to the size of the iron crystallites has been covered in Section 2.6.3. The results were obtained from the analysis of the Fe (110) reflection. It would of been beneficial to base the results on more than one reflection, unfortunately this did not prove to be possible due to the low intensity of the other iron reflections. All the catalysts were analysed by this particular method, although it did not prove possible to distinguish the Fe (110) reflection from that of the MgO (200) reflection in the catalysts which contained small iron crystallites. The average diameter of the iron crystallites as determined from X-ray line broadening (d) is used to calculate the iron surface area $\sum_{XRD}$, using the equation $\sum_{XRD} = 6/\rho d$ where ρ is the density of iron.

The values obtained for the iron surface areas are contained in Table 3.10. The surface areas are in units of $m^2 g^{-1}_{iron}$ and can be directly compared with results in similar units obtained from nitrous oxide decomposition and CO chemisorption.

3.4.3. Determination of the size of the Iron Crystallites.

3.4.3.1. X-ray Line Broadening

The average size of the iron crystallites (d) were determined from the α-Fe (110) reflection, the results obtained being presented in Table 3.11. For some catalysts containing

Table 3.10 Iron Surface Areas Calculated from X-ray Line Broadening.

Catalyst	$\sum_{XRD}$ / m^2g^{-1}
CCP10	17.6
CCP20	16.9
CCP30	16.7
OH20	19.8
OH30	21.2
IP5	29.9
IP20	16.2
IP30	16.0
HT1	18.4

very small iron crystallites it was not possible to distinguish the iron (110) reflection from the base line and the MgO (200) reflection.

The line broadening due only to the small crystallite size (β) was determined by the method described in Section 2.6.3. Instrumental broadening (b) was determined from a sample of sintered iron powder, and this was found to have a 2θ value of 0.085^{o}.

The average size of the iron crystallites was determined using the Scherrer equation as described in Section 2.6.1. The wavelength of the Cu Kα radiation was taken as 1.5418 Å. A value of 1.0747 was used for the Scherrer constant, which assumes a spherical shape for the iron crystallites.

3.4.3.2. Iron Particle Size Determination from CO Chemisorption.

The size of the iron particles in the reduced catalysts has been determined from the amount of CO chemisorbed and results are presented in Table 3.11 This was achieved using a method described by Boudart et al (2) using the equation $d = \frac{0.85}{D}$ where D is the dispersion. The dispersion is the ratio of surface Fe^{0} atoms to total Fe^{0} atoms. The number of surface Fe^{0} atoms was obtained from the CO chemisorption or N_2O decomposition, whilst the total number of Fe^{0} atoms was obtained knowing the iron loading and the fraction of the iron reduced.

Table 3.11 Iron Crystallite sizes Determined by CO Chemisorption and X-ray Line Broadening.

Catalyst	$d_{chemisorption}$ / nm	d_{XRD} / nm
CCP5	4.8	-
CCP10	8.2	43.4
CCP20	28.6	45.2
CCP30	46.8	45.7
OH5	3.8	-
OH10	5.4	-
OH20	12.7	38.5
OH30	27.3	36.0
IP5	11.4	25.5
IP10	21.2	-
IP20	27.5	47.0
IP30	33.3	47.6
HT1	15.8	41.4

3.5. Mössbauer Spectroscopy

Mössbauer spectra have been obtained for two samples these were CCP30 and a sample with a low iron loading. The spectra were recorded at ambient temperature using the specially designed apparatus described in Section (2.8.3). The spectra were then computer fitted assuming Lorentzian-shaped lines and that the recoil free fraction is the same for all iron containing phases. The theory behind the observed patterns has been dealt with in Section 2.8.2.

All isomer shifts are reported relative to natural iron

3.5.1. Mössbauer Results for CCP30

The Mössbauer spectrum of the calcined precursor is shown in Figure 3.14. The precursor was then reduced in hydrogen (30 Torr) and the spectrum was redetermined. The reduction treatment consisted of heating for 24 hours at 553 K, 24 hours at 623 K and 24 hours at 693 K. The resulting spectrum is shown in Figure 3.15. A final spectrum was recorded after further reduction at 723 K for 24 hours (Fig.3.16).

The isomer shifts (IS), quadrupole splitting (QS), line widths (Γ) and the hyperfine field (H) for the various spectral components along with the spectral contributions of each are contained in Table 3.12. All isomer shifts are reported with respect to metallic iron.

The spectrum of the calcined material (Fig.3.14) has been

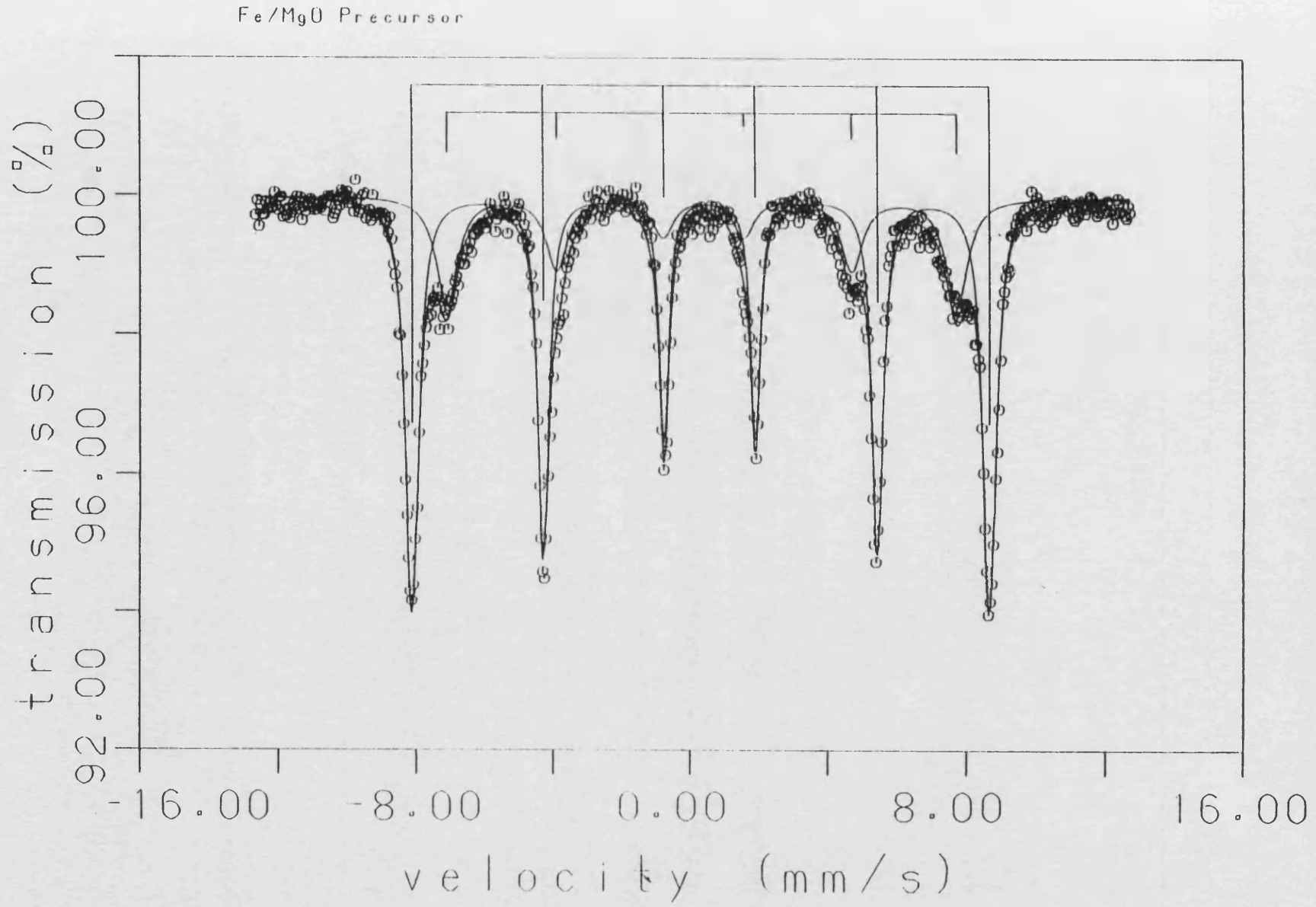

Figure 3.14 Mössbauer spectrum of the precursor CCP30.

Table 3.12 Mössbauer parameters for the spectra obtained from the reduction of CCP30.

		I.S. /mm s^{-1}	Q.S. /mm s^{-1}	Γ /mm s^{-1}	H /kOe	Spectral contribution %
Precursor	α-Fe_2O_3	0.41	0.31	0.27	520	76
	Mg Fe_2O_4	0.35	-0.10	0.71	459	24
Reduced Catalyst	FeO	1.14	0.72	0.52,0.46		48
	Fe_3O_4	0.35		0.43	497	30
		0.70		0.43	464	
	α-Fe	0.05		0.34	333	21
		0.14		0.57		1
Extended Reduction	FeO	1.13	0.75	0.47,0.45		45
	Fe_3O_4	0.36		0.41	499	14
		0.70		0.41	464	
	α-Fe	0.04		0.31	334	39
		0.13		0.57		2

fitted to two overlapping six-line spectra. The major of these accounting for 76 % can be assigned to α-Fe_2O_3, the Mössbauer parameters being in good agreement with the literature (92). The lesser component can be assigned to magnesium ferrite ($MgFe_2O_4$), this is consistent with the findings of Bhinde and Tambe (93).

Reduction of the sample caused dramatic changes in the resulting Mössbauer spectrum (Fig.3.15). On reduction the six-line spectra due to the α-Fe_2O_3 and $MgFe_2O_4$ completely disappear, this is in agreement with the observations of Topsøe et al. (3). Deconvolution of the Mössbauer spectrum of the reduced catalyst indicates that three main phases are present. These are wustite (FeO), magnetite(Fe_3O_4) and α-Fe. The FeO exhibits a doublet with an isomer shift of 0.72 mm s^{-1}, which for the purpose of computer fitting was treated as two singlets with identical widths but dissimilar heights. The magnetite phase produces two superimposed six-line patterns with isomer shifts of 0.35 and 0.70 mm s^{-1} and respective hyperfine fields of 497 and 464 kOe. The α-Fe produces a six-line spectrum with an isomer shift of 0.05 mm s^{-1} and a hyperfine field of 330 kOe. A singlet of isomer shift 0.14 mms^{-1} has also been included in the fit of the Mössbauer spectrum, following the results of Boudart et al. (2). These authors have attributed this singlet to superparamagnetic metallic iron. As the spectral contribution is only 1 % from this component (Table 3.12) and given the uncertainties involved in fitting these complex spectra, this small contribution may be considered to be insignificant.

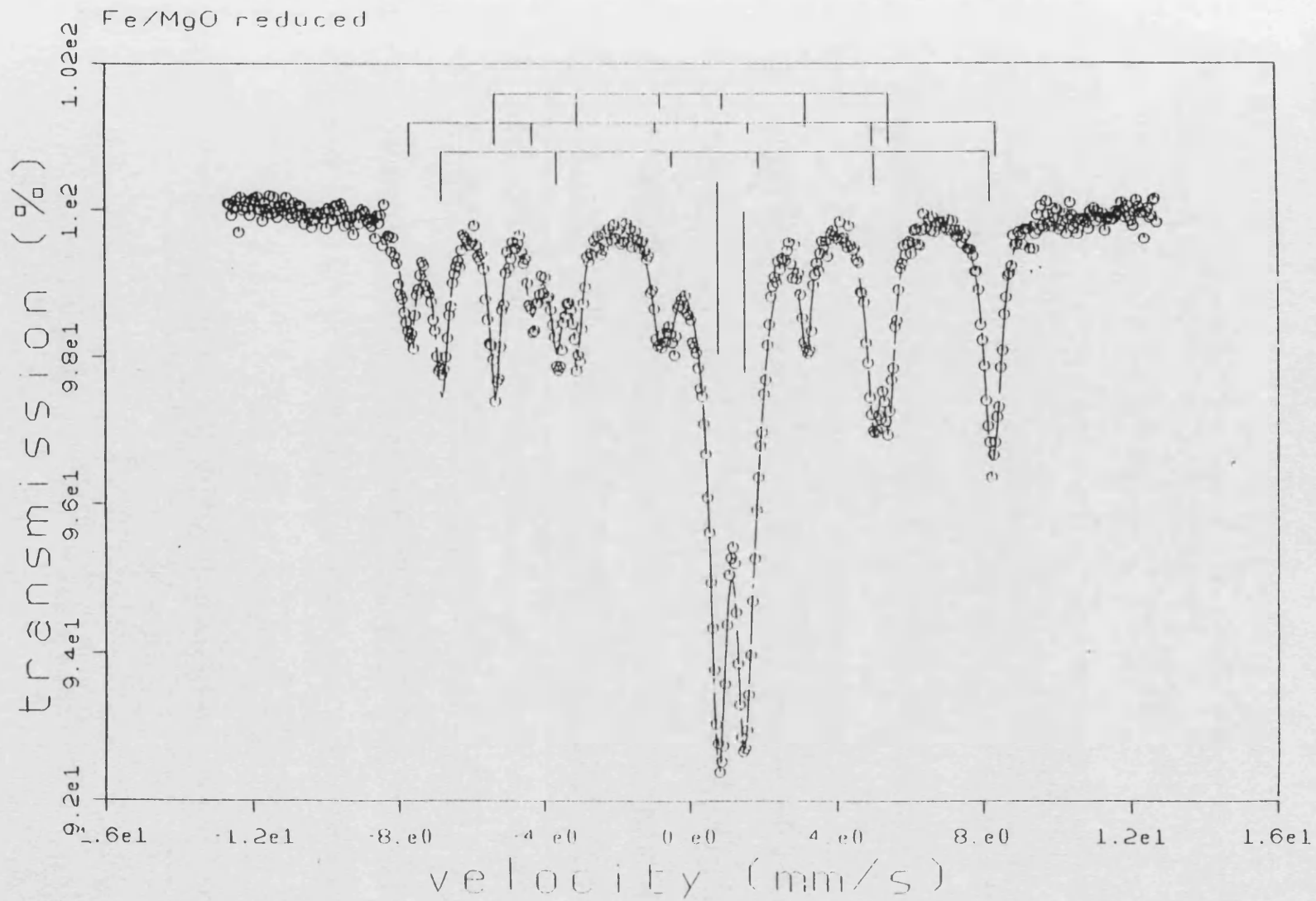

Figure 3.15 Mössbauer spectrum of catalyst CCP30 after reduction at 693 K.

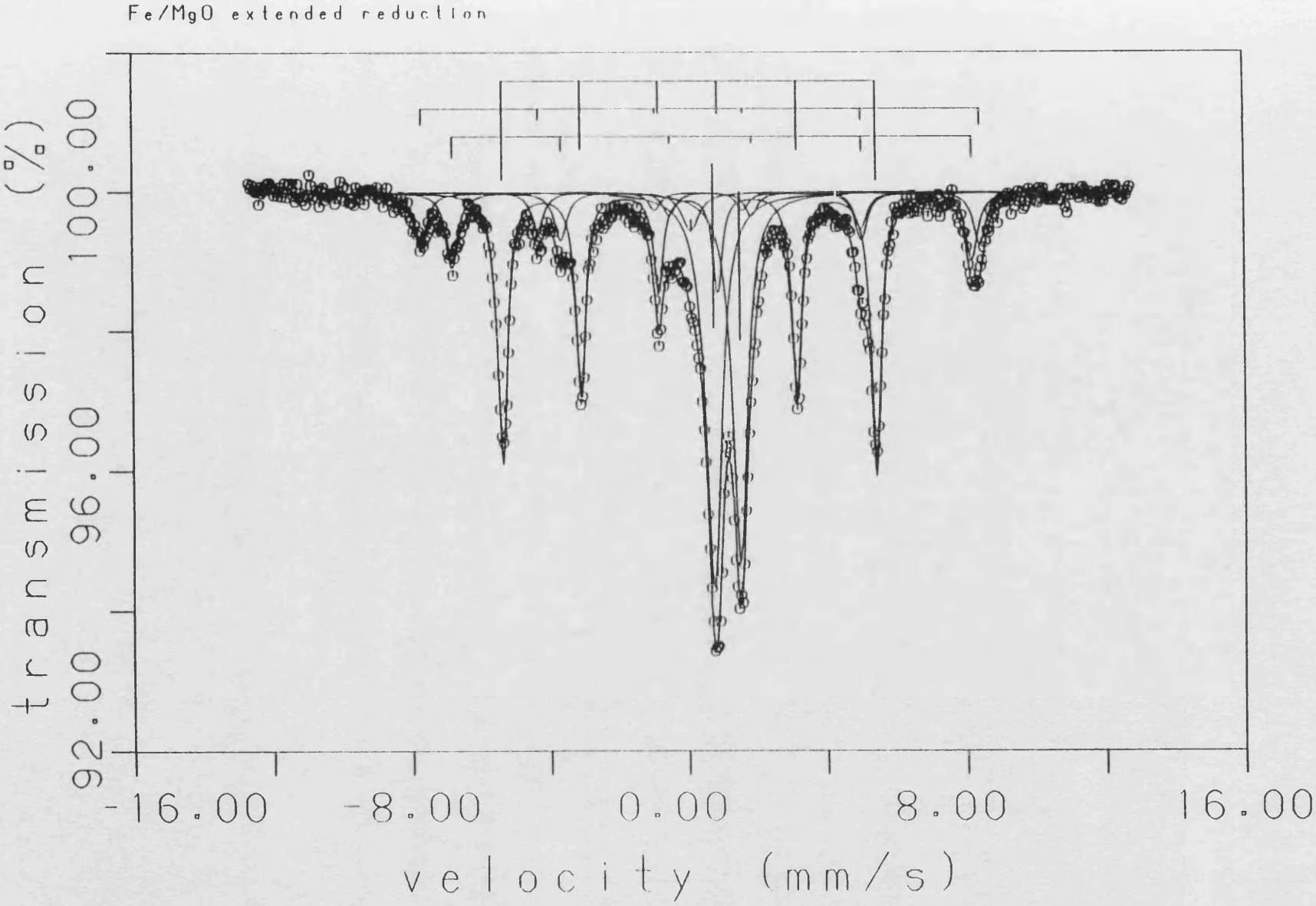

Figure 3.16 Mössbauer spectrum of catalyst CCP30 after reduction at 723 K.

The Mössbauer spectrum obtained after extending the reduction (Fig.3.16) indicates that no new phases are formed. However, deconvolution of the spectrum shows that there is an increase in the amount of α-Fe formed and that this is produced at the expense of the Fe_3O_4 phase , the amount of FeO remaining essentially constant.

3.5.2. Mössbauer Results for the 1 % Fe/MgO Catalyst

This sample was prepared using enriched ^{57}Fe in order that a Fe/MgO system with low iron loading could be studied using Mössbauer spectroscopy. The spectra of the calcined precursor is shown in Figure 3.17.The sample was reduced under identical conditions to sample CCP30, described in Section 3.5.1. The spectra recorded are contained in Figures 3.18 and 3.19. After reduction the sample was exposed to nitrous oxide at ambient temperature and the Mössbauer spectrum recorded (Fig.3.20). Finally the sample was heated in oxygen at 573 K for 6 hours and a final spectrum was recorded (Fig.3.21). Computer fitting and deconvolution of the spectra showed the spectral parameters and proportions of the phases present as recorded in Table 3.13.

The 1 % Fe/MgO precursor exhibited a Mössbauer spectrum which was fitted to two overlapping doublets (Fig. 3.17). This produced a better fit than a single doublet which is the more commonly adopted method (2,3). The notion that the observed doublet is in fact composed of two doublets follows a suggestion made by Dutartre et al. (34). One of the doublets

Table 3.13 Mössbauer parameters for the spectra obtained from the reduction and reoxidation of 1 % Fe/MgO

		I.S. /mm s^{-1}	Q.S. /mm s^{-1}	Γ /mm s^{-1}	H /kOe	Spectral contribution %
Precursor	Fe^{3+}	0.34	0.57	0.41		34
		0.30	1.03	0.65		66
Reduced Catalyst	Fe^{3+}	0.37	0.61	0.47		20
		0.28	1.10	0.73		20
	Fe^{2+}	0.89	1.69	0.77		10
		0.81	0.89	0.86		28
	α-Fe	0.02		0.40	326	21
Extended Reduction	Fe^{3+}	0.42	0.72	0.28		10
		0.32	0.97	0.35		7
	Fe^{2+}	0.91	1.55	0.77		19
		0.87	0.90	0.82		43
	α-Fe	0.02		0.40	327	21
After N_2O Treatment	Fe^{3+}	0.40	0.59	0.50		22
		0.22	1.18	0.71		16
	Fe^{2+}	0.88	1.66	0.64		9
		0.79	0.90	0.85		28
	α-Fe	0.01		0.40	326	25
After O_2 573 K	Fe^{3+}	0.42	0.53	0.60		42
		0.39	1.04	0.79		58

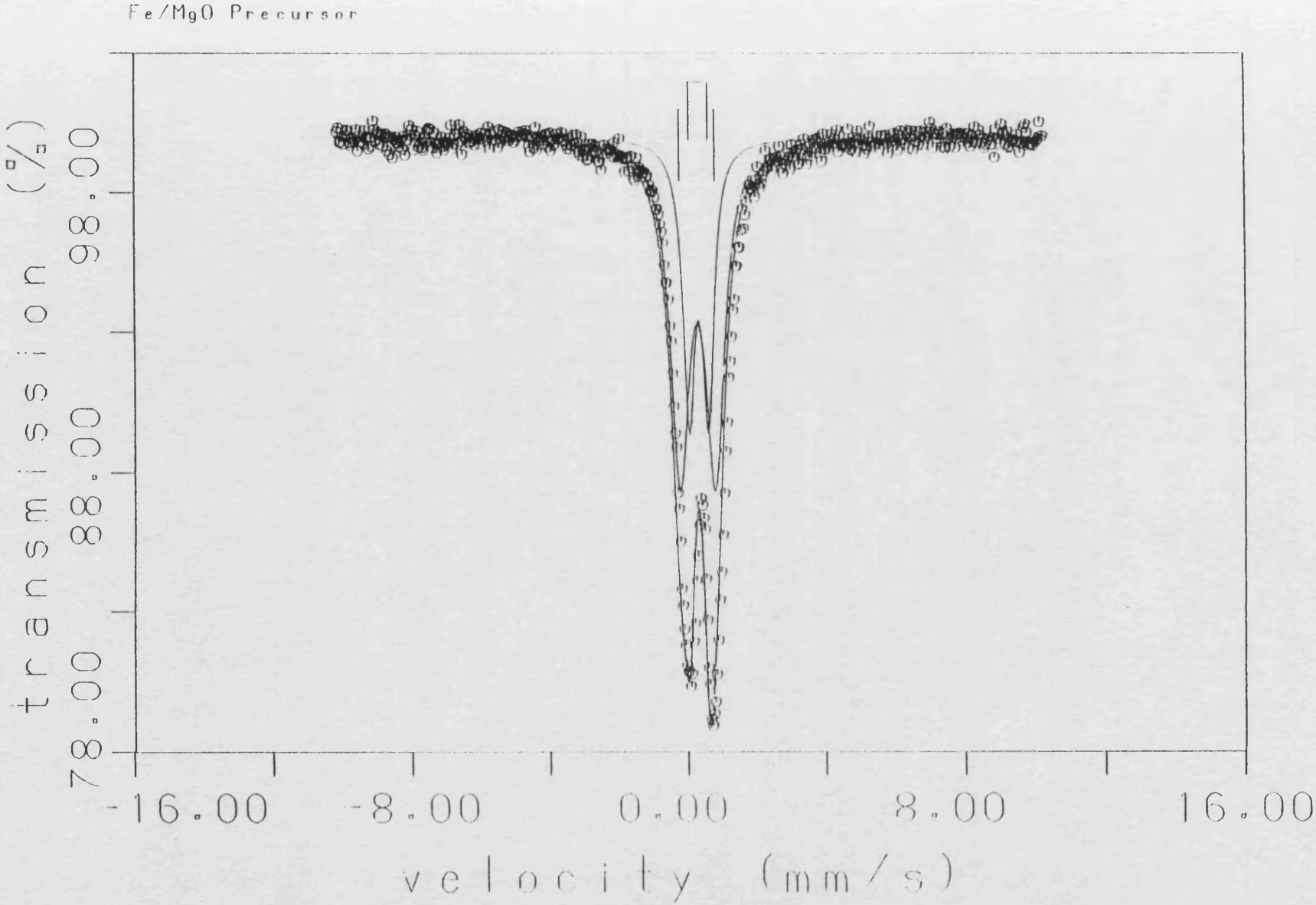

Figure 3.17 Mössbauer spectrum of a 1% Fe/MgO precursor.

can be assigned to γ-FeOOH, but the origin of the other remains unclear. Results from catalysts prepared by an identical method but with higher iron loadings, have indicated the presence of γ-Fe_2O_3 in the catalyst precursors (Section 3.2). The other doublet may be due to small (hence superparamagnetic) particles of γ-Fe_2O_3.

Reduction of the precursor results in a catalyst which exhibits the Mössbauer spectrum in Figure 3.18. As expected, there are important new features. Analysis of the spectrum indicates that some of the original Fe^{3+} species are still present (40 %), but Fe^{2+} and Fe^{0} contributions are now strong. Early workers on this type of system treated the contribution due to Fe^{2+} as one doublet(2,3). In this study the approach of Connell and Dumesic (86) has been adopted, in which the spectral contribution of Fe^{2+} is fitted to two doublets, which together account for a further 38%. The presence of metallic iron (21 %) is clearly characterised by the six-line spectrum with an isomer shift of -0.02 mm s^{-1} and magnetic field of 327 kOe.

Extending the reduction as described previously did not result in an increase in the amount of metallic iron present in the sample. The Mössbauer spectrum (Fig. 3.19) does however show that there is an increased conversion of Fe^{3+} to Fe^{2+}. The spectrum obtained after treatment of the sample with nitrous oxide (Fig. 3.20) still contains α-Fe, Fe^{2+} and Fe^{3+}. Heating the sample in oxygen at 573 K results in the total reoxidation of the sample. The resulting material exhibits a Mössbauer spectrum (Fig. 3.21) similar to that of the precursor.

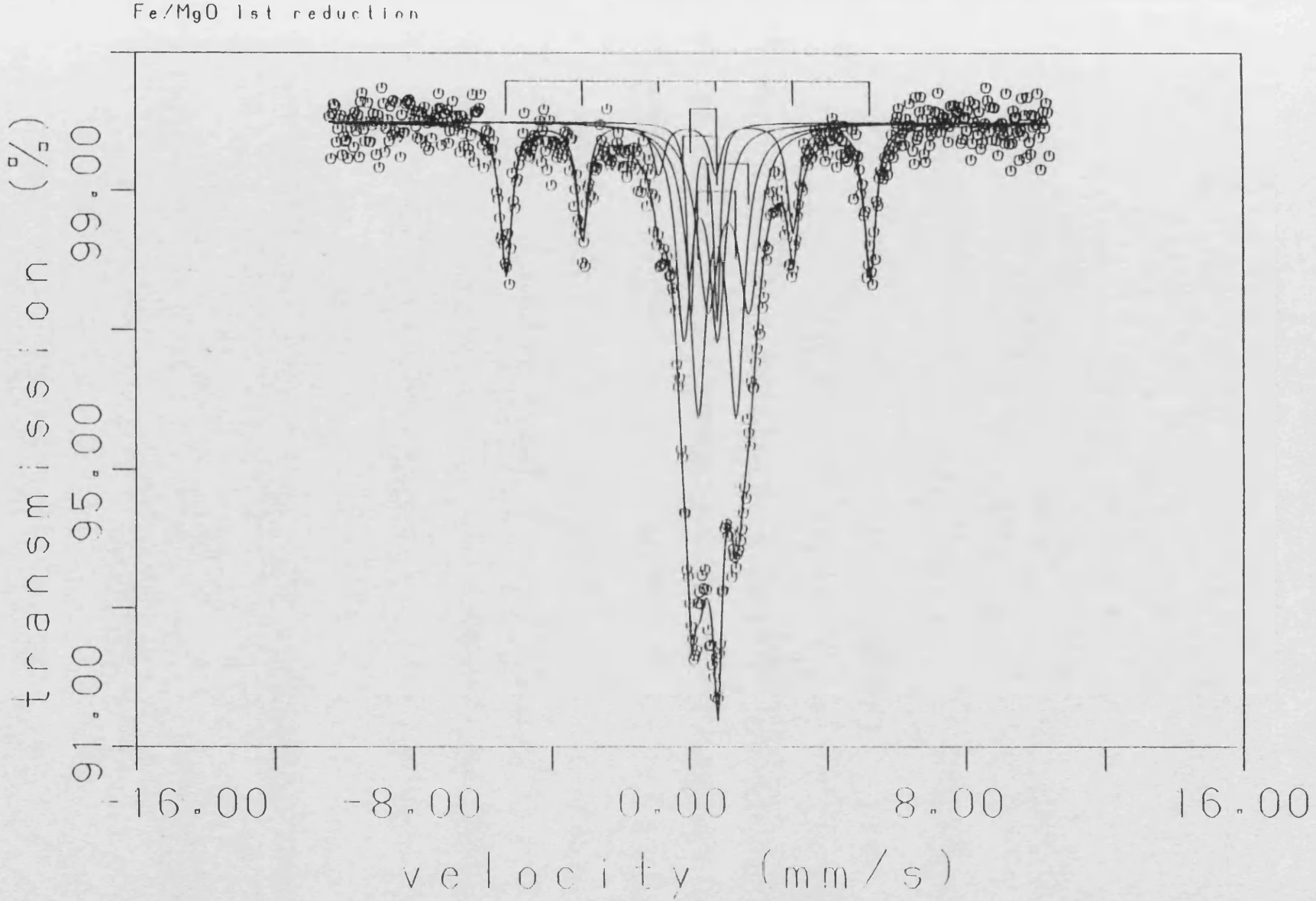

Figure 3.18 Mössbauer spectrum of a 1% Fe/MgO catalyst after reduction at 693 K.

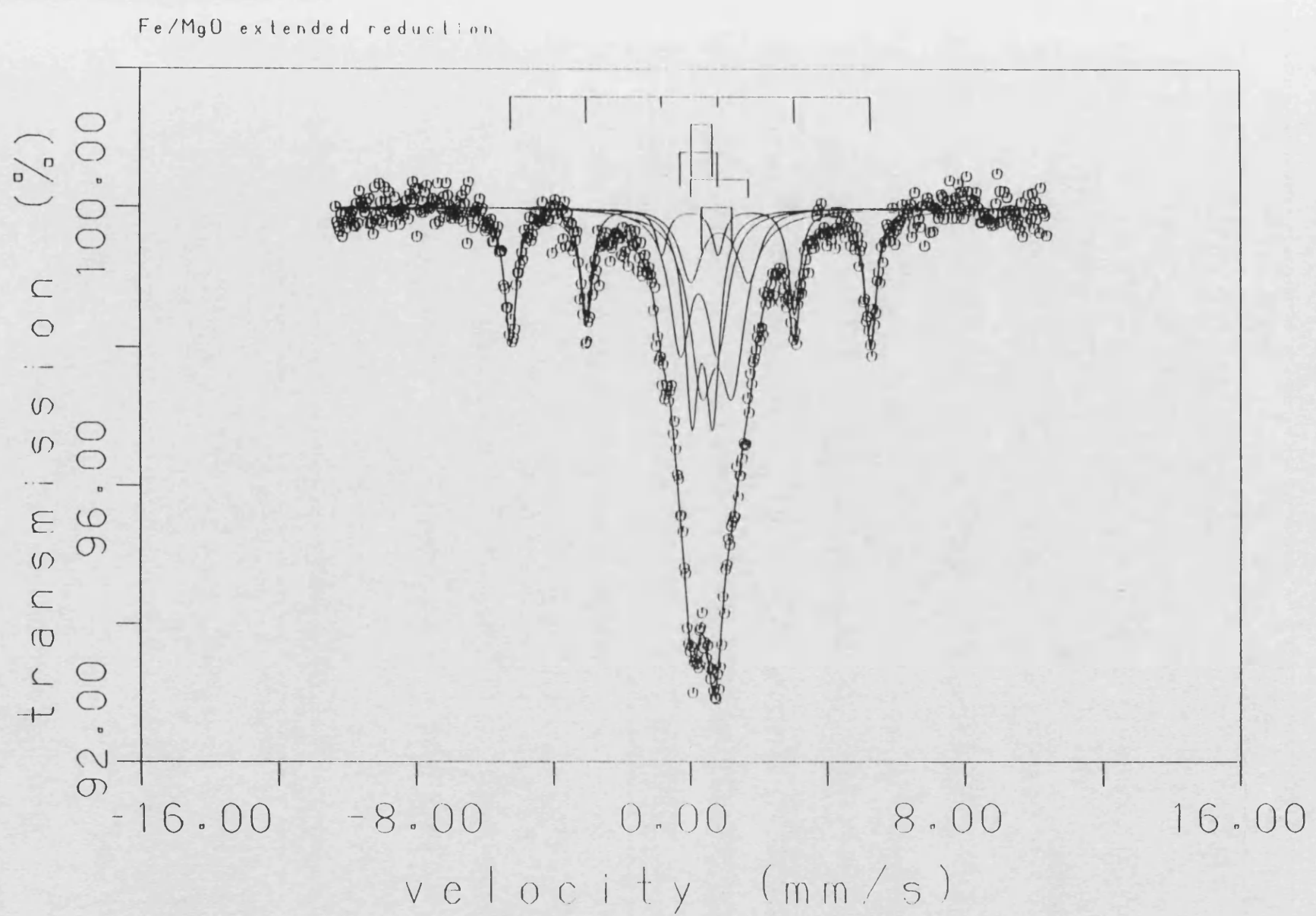

Figure 3.19 Mössbauer spectrum of a 1% Fe/MgO catalyst after reduction at 723 K.

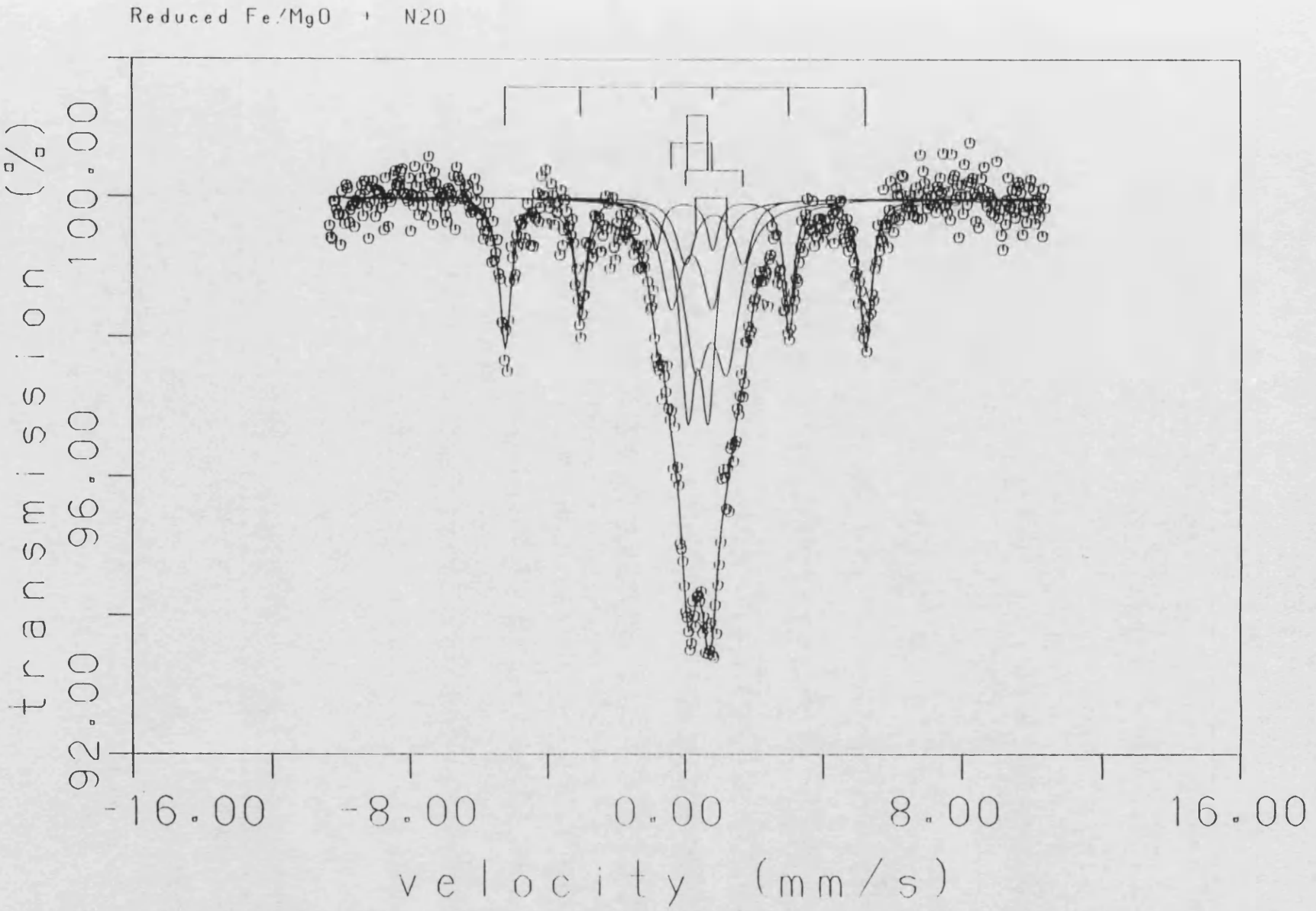

Figure 3.20 Mössbauer spectrum of a 1% Fe/MgO catalyst after reduction at 723 K followed by exposure to N_2O.

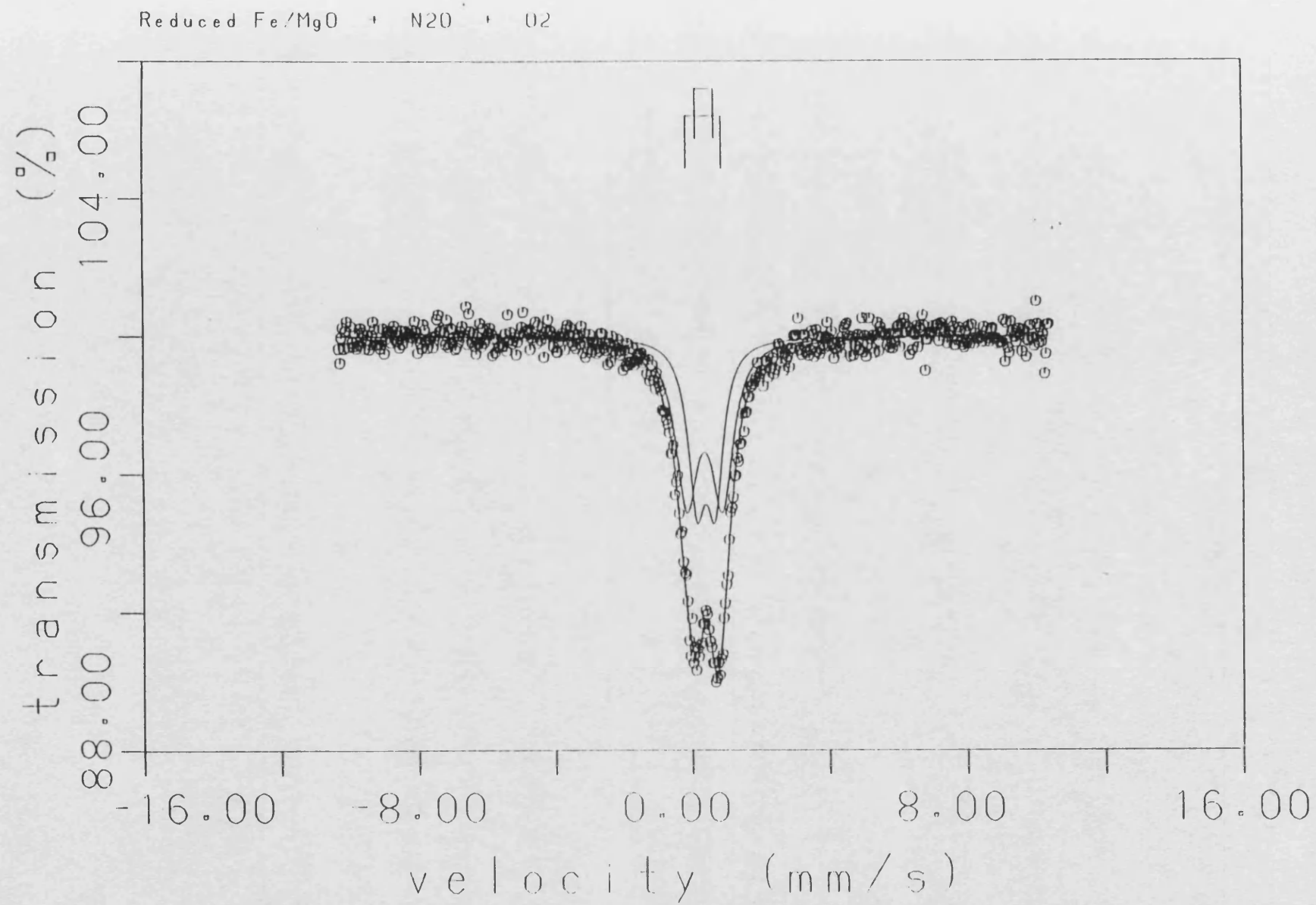

Figure 3.21 Mössbauer spectrum of a 1% Fe/MgO catalyst after reduction at 723 K followed by heating in oxygen at 573 K.

3.6. Infrared Spectroscopy

Infrared spectroscopy is one of the most common tools for the characterisation of heterogeneous catalysts. This section will contain the results from the characterisation of the 5% loaded catalyst CCP5. The characterisation has been achieved by the adsorption of CO and NO in separate studies. An attempt has also been made to investigate the surface reactions which occur when ethanenitrile and propanenitrile are adsorbed onto the surface of the catalyst.

3.6.1. Infrared Study of the Adsorption of Carbon Monoxide on MgO and Fe/MgO Catalysts

Carbon monoxide has been used as a probe molecule in a number of studies with iron catalysts (22, 94-101). There is however some contention as to whether CO is chemisorbed on Fe^{2+} and Fe^{3+} centres and to the position of these bands. The difficulty in determining the positions lies in the fact that they are usually obscured by the gas phase spectrum of CO, which exhibits the typical P and R branches at 2118 and 2175 cm^{-1} respectively. Attempts to evacuate the gaseous CO usually results in the loss of these weakly adsorbed species. In an attempt to overcome these difficulties a low temperature study has been made.

A study has also been made of the adsorption of CO on MgO, this is so bands which are attributable to CO adsorption

on the support can easily be identified when studying the supported iron catalyst.

3.6.1.1. Adsorption of CO on MgO

The adsorption of CO (120 Torr) on a sample of MgO which had been outgassed for 24 h at 693 K produced the spectrum shown in Figure 3.22. The gaseous CO has been evacuated for a period of 5 minutes. The resulting spectrum exhibits strong absorption bands at 1657, 1607, 1519, 1468, 1369 and 1313 cm^{-1}.

3.6.1.2. Adsorption of CO on 5% Fe/MgO

The adsorption of CO has been studied on samples of catalyst CCP5 which have been reduced under the standard conditions described in Section 2.1.3. A study was made of the effect of surface hydrogen on the adsorption of CO as marked differences in the CO spectra were observed when surface hydrogen was present.

All the spectra shown in this section have previously had the infrared spectrum of the catalyst disc prior to the adsorption of CO and the spectrum of gaseous CO subtracted from them using software facilities provided by the data station.

The spectra produced after adsorbing CO (120 Torr) on a sample which had been reduced as described previously and the hydrogen evacuated at 693 K are shown in Figure 3.23. Spectra were recorded after the sample had been exposed to CO for 3 minutes, 1.5 hours and 3 hours and are represented by spectra

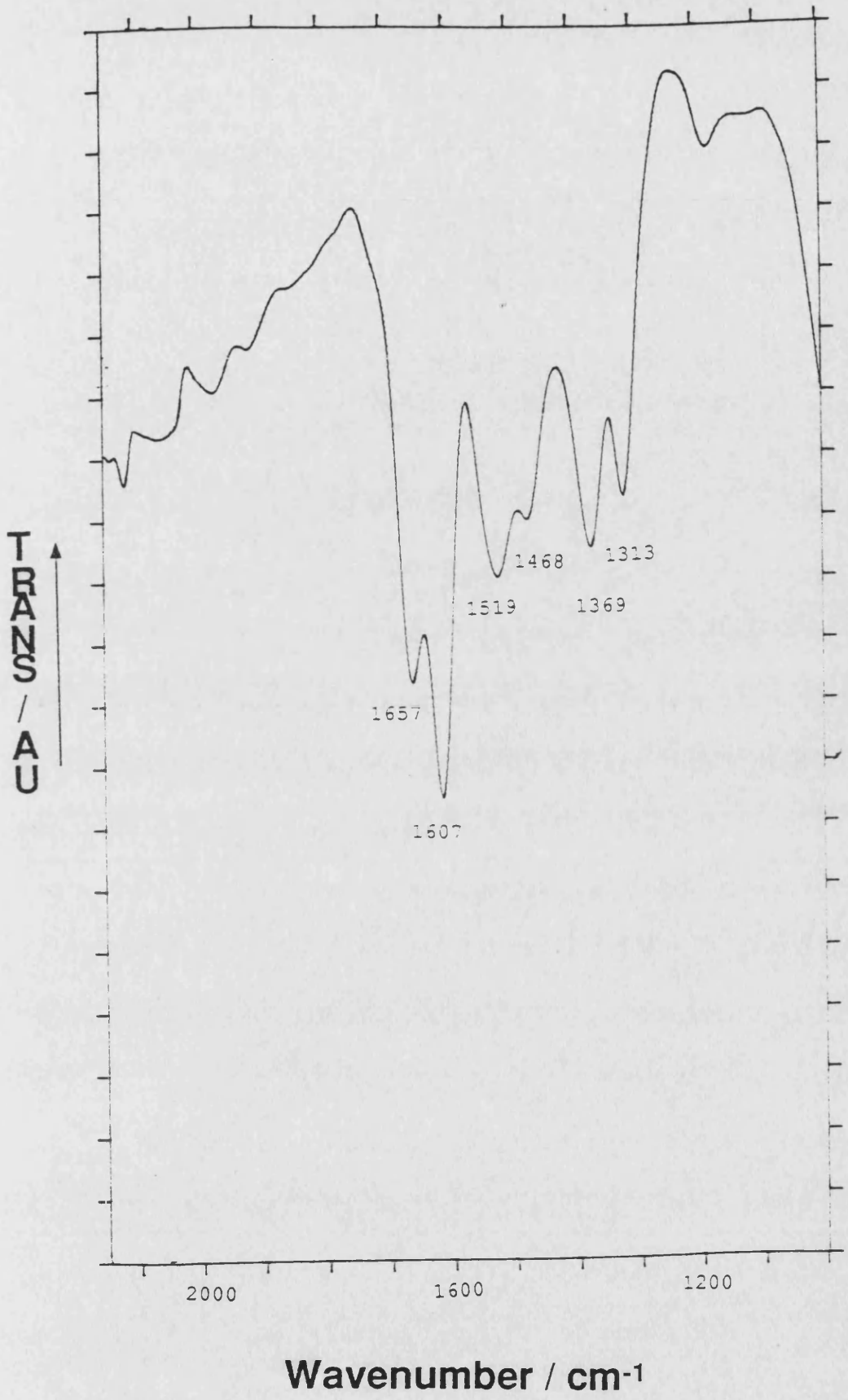

Figure 3.22 Infrared spectrum of CO adsorbed on MgO.

A, B and C respectively. Spectrum A exhibits absorption bands at 2180 (w), 2106 (w), 2023 (s), 1889 () and a shoulder at 1850 cm^{-1} (w). After increased exposure to the CO (spectrum B and C) new bands at 2155 cm^{-1} (w) and 2060 cm^{-1} (w) were visible. The intensity of the band at 1889 cm^{-1} increased markedly and distinct shoulders appeared at 1936 and 1914 cm^{-1}. The band at 1850 cm^{-1} resolved into two separate bands at 1862 and 1850 cm^{-1}.

A second catalyst disc was reduced as described previously but instead of evacuating the hydrogen at 693 K the sample was cooled to beam temperature before evacuation. The sample was then dosed with CO (120 Torr) and spectra recorded after 3 minutes, 1.5 hours and 3 hours, these are shown in Figure 3.24 A, B, and C respectively. The initial spectrum exhibited absorption bands at 2170 (w), 2143 (w), 2110 (w), 2060 (w), 2018 (s), 1920 (m), 1889 (s) and 1855 cm^{-1} (w). On standing in CO, there was a very marked change to produce a strong band at 2057 cm^{-1}, a new but very weak band also appeared at 2085 cm^{-1}. The band at 1889 cm^{-1} became very strong, dominating the spectrum, but bands at 1937, 1920 and 1855 cm^{-1} also became more pronounced. Evacuation of the CO at beam temperature resulted in the loss of the band at 2057 cm^{-1}.

A further catalyst disc was treated as the first sample described above except that when the sample had been allowed to cool to beam temperature (~ 303 K) the sample was exposed to hydrogen for a period of 15 minutes, the hydrogen was then evacuated prior to the adsorption of the CO. The resulting spectra recorded after exposure of 3 minutes, 1.5 hours and 3

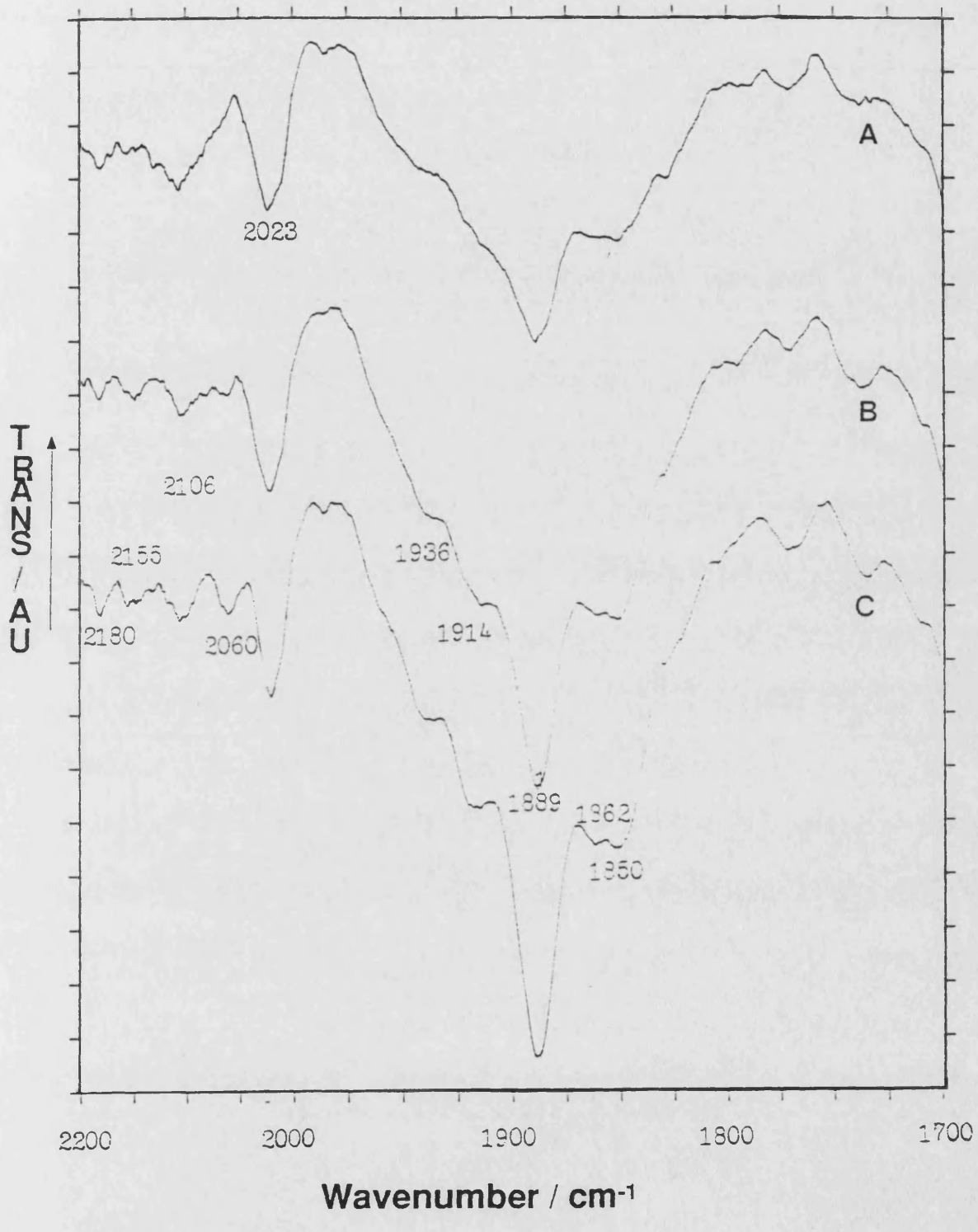

Figure 3.23 Infrared spectrum of CO adsorbed on 5% Fe/MgO which had previously been reduced at 693 K the hydrogen being evacuated at 693 K. CO exposure times A 3 mins, B 1.5 h and C 3 h.

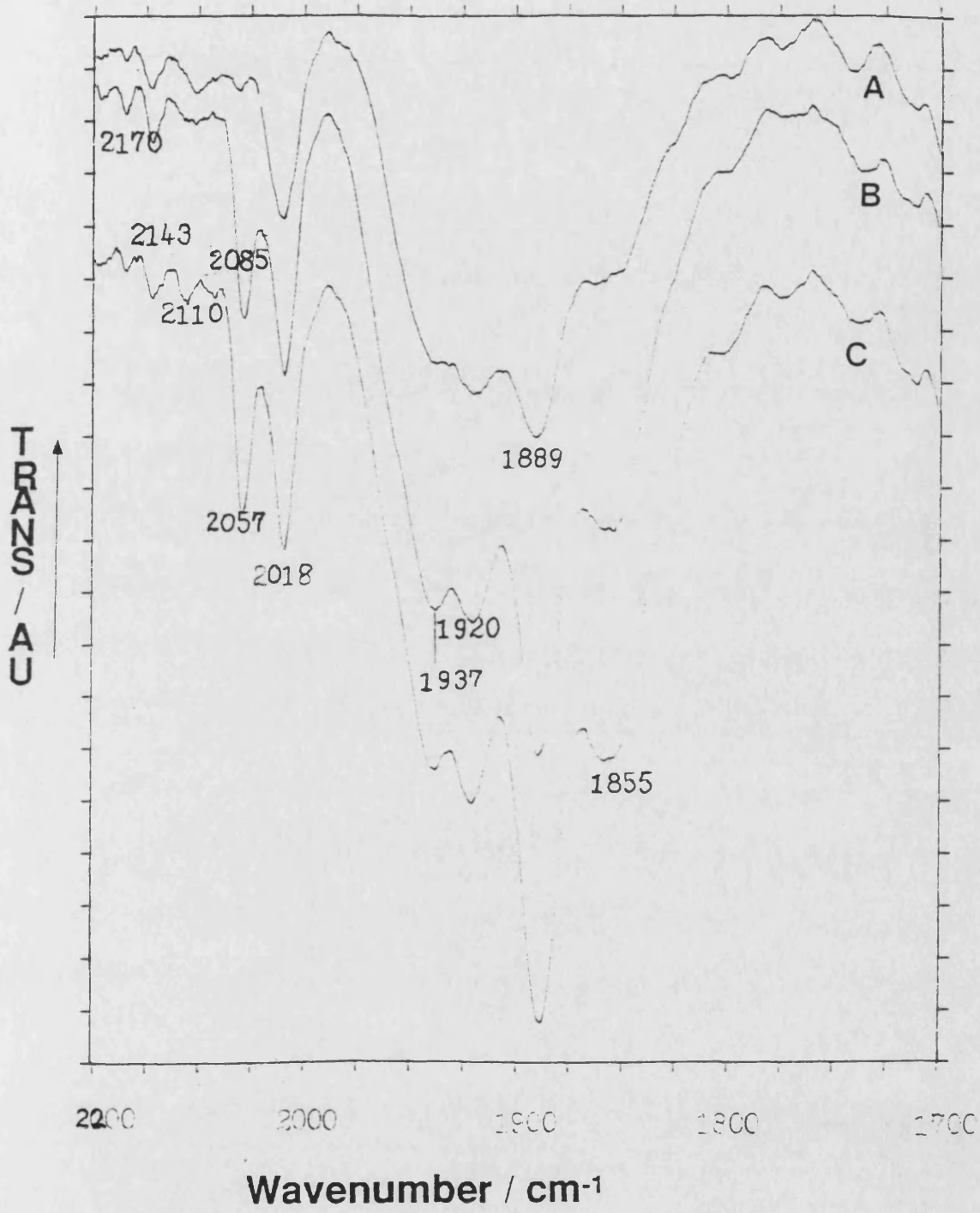

Figure 3.24 Infrared spectrum of CO adsorbed on 5% Fe/MgO which had previously been reduced at 693 K the sample being cooled to beam temperature before the hydrogen was evacuated. CO exposure times A 3mins, B 1.5 h and C 3 h.

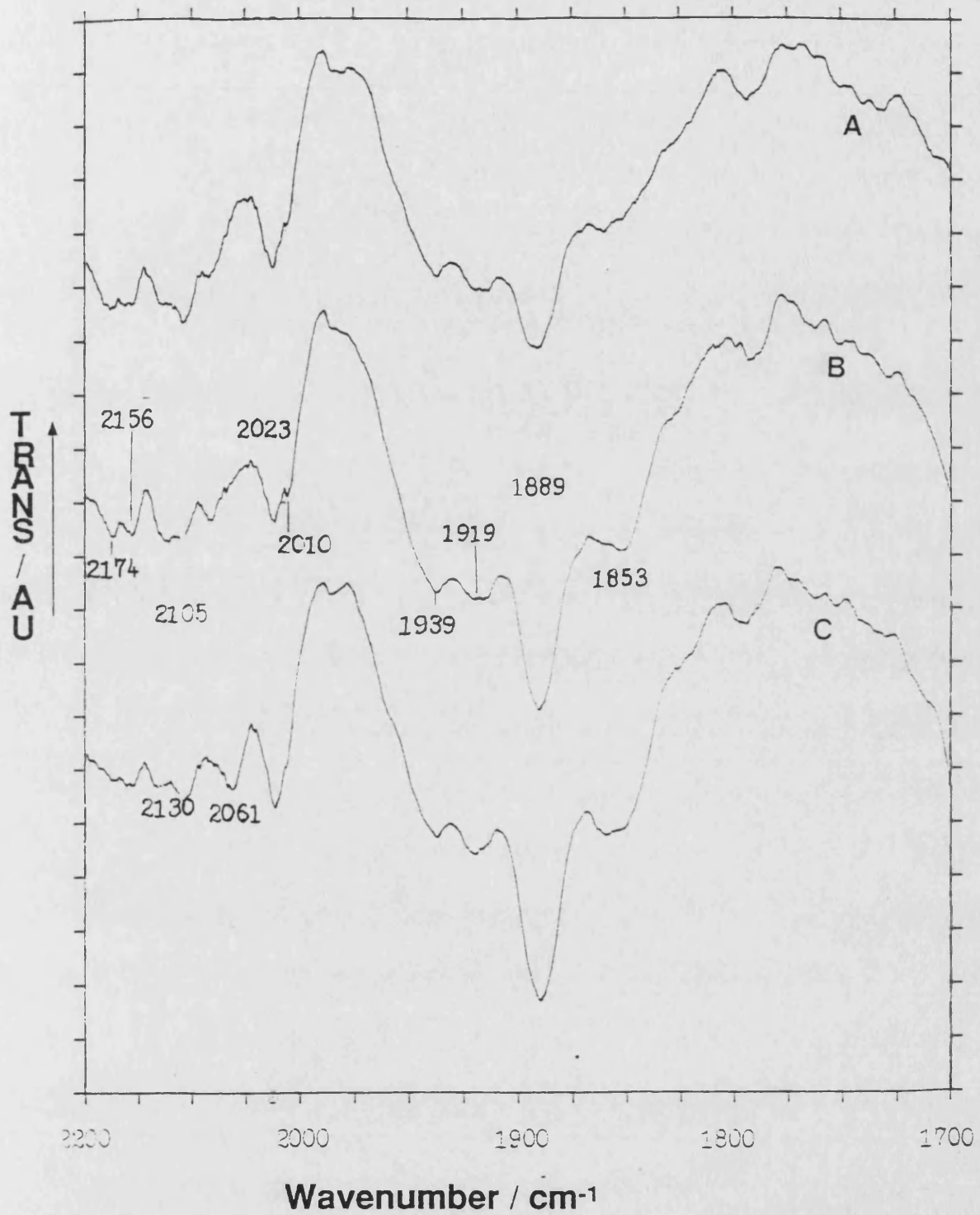

Figure 3.25 Infrared spectrum of CO adsorbed on 5% Fe/MgO which had previously been reduced at 693 K, the hydrogen evacuated at 693 K and the sample exposed to a hydrogen at beam temperature before the the adsorption of CO. CO exposure times A 3mins, B 1.5 h and C 3 h.

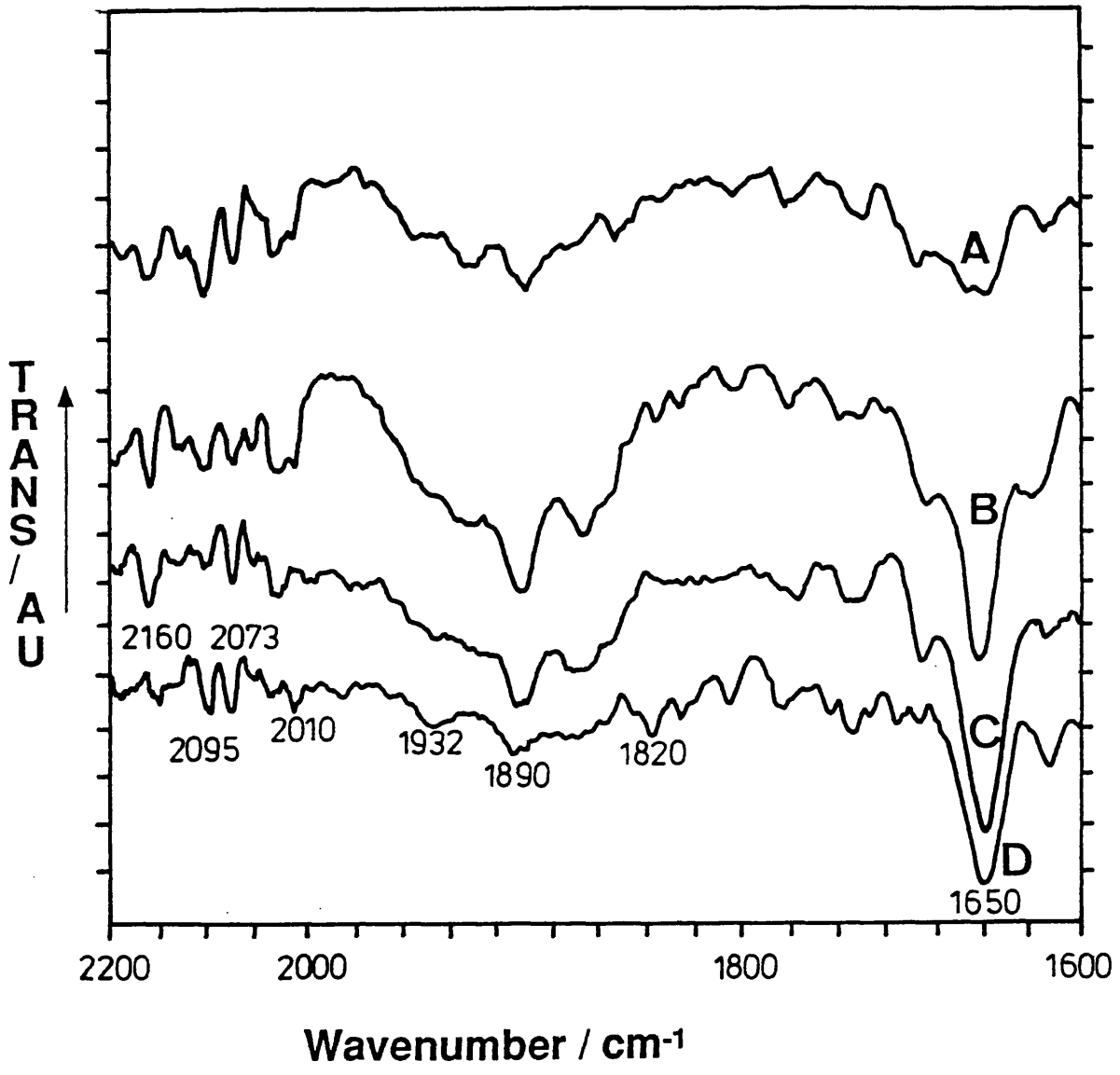

Figure 3.26 Infrared spectra of 5% Fe/MgO after reduction at 623 K A) CO exposure of 3 mins B) CO exposure of 1.5 h C) after evacuation of gaseous CO for 10 mins D) after evacuation for 45 mins

hours are shown in Figure 3.25. After an exposure of 1.5 hours (spectrum B) absorption bands were visible at 2174 (w), 2156 (w), 2130 (w), 2105 (w), 2061 (w), 2023 (m) with a shoulder at 2010, 1939 (w), 1919 (w), 1889 (s) and 1853 cm^{-1} (w).

An attempt was made to determine which bands, if any could be assigned to the adsorption of CO on Fe^{2+} centres. The catalyst sample was given a less vigorous reduction treatment with the aim of increasing the amount of Fe^{2+} in the sample. This reduction treatment consisted of heating the sample in hydrogen (30 Torr) for 24 hours at 553 K followed by 24 hours at 623 K. The hydrogen was evacuated before admitting CO (120 Torr). The spectra recorded are shown in Figure 3.26, spectra A and B correspond to the spectra produced after 3 minutes and 1.5 hours exposure respectively, the spectrum due to gaseous CO has been subtracted from these spectra. Spectra C and D correspond to the spectra recorded after evacuation of the gaseous CO for periods of 10 and 45 minutes respectively. The spectra indicate that most of the bands previously observed with the more rigorously reduced samples are present. However, the bands at 2160, 2095 and 2073 cm^{-1} have increased prominence in the spectra.

3.6.1.3. Low Temperature Adsorption of CO on 5% Fe/MgO

The low temperature studies were made in the low temperature cell described in Section 2.8.3. The catalyst discs were pretreated in the prerequisite manner the sample was then cooled to beam temperature before the CO was admitted after

which the sample was cooled to approximately 130 K before the gaseous CO was evacuated. Unfortunately the spectra obtained suffer from the catalyst still having a considerable amount of CO physisorbed, this has the effect of obscuring some of the bands due to chemisorbed species.

The infrared spectrum obtained from the adsorption of CO on a sample of 5% Fe/MgO which had undergone the standard reduction procedure (up to 693 K) as described in Section 2.1.3 is shown in Figure 3.27 spectrum B. The most prominent band is that at 2078 cm^{-1}, there also appears to be absorptions at 2174, 2124, 2104, 2030, 2010, 1920, 1890 and 1819 cm^{-1}.

The infrared spectrum was obtained in the same manner as described above for a sample of 5% Fe/MgO which had not been reduced but which had been evacuated overnight at 433 K. The infrared spectrum after evacuation of the CO is shown in Figure 3.27 spectrum A, transmission of the infrared beam through this sample was exceptionally low, this resulted in the final spectrum being of rather poor quality. The spectrum does however appear to contain absorption bands at 2225, 2202, 2174, 2125, 2070, and 2042 cm^{-1}.

The content of Fe^{2+} in the sample was again increased by using a less rigorous reduction program which consisted of heating the sample in hydrogen (30 Torr) for 24 hours at 553 K followed by 24 hours at 623 K. The CO was dosed and the spectra recorded using the method described above. The spectra obtained after the CO had been evacuated is shown in Figure 3.28. The spectrum shows very few distinct bands but there appears to be absorption bands at 2130, 2100, 2080, 2050, 2010, 1950, 1884,

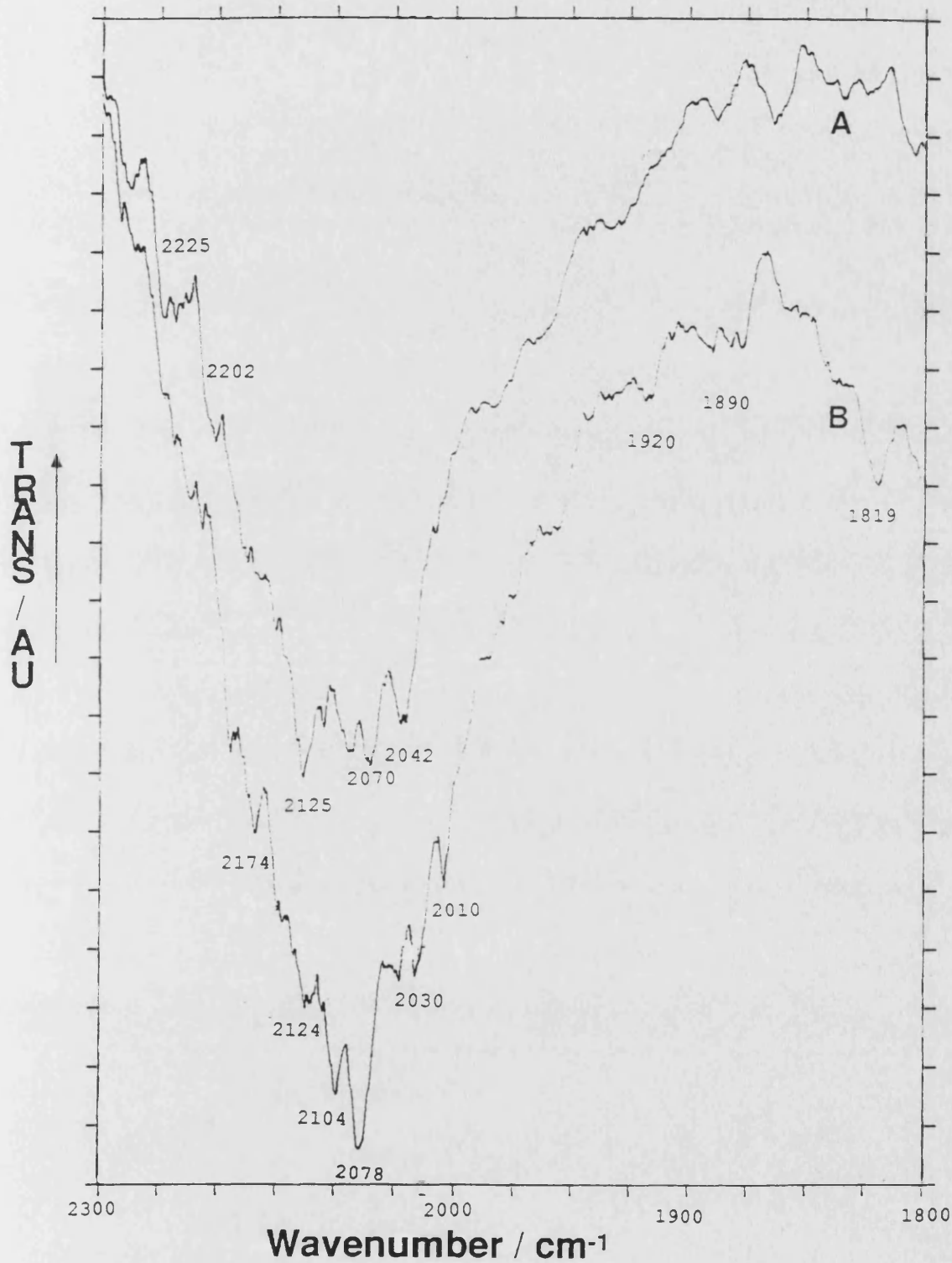

Figure 3.27 Infrared spectrum of CO adsorbed at 130 K
A) unreduced 5% Fe/MgO B) 5% Fe/MgO
reduced at 693 K

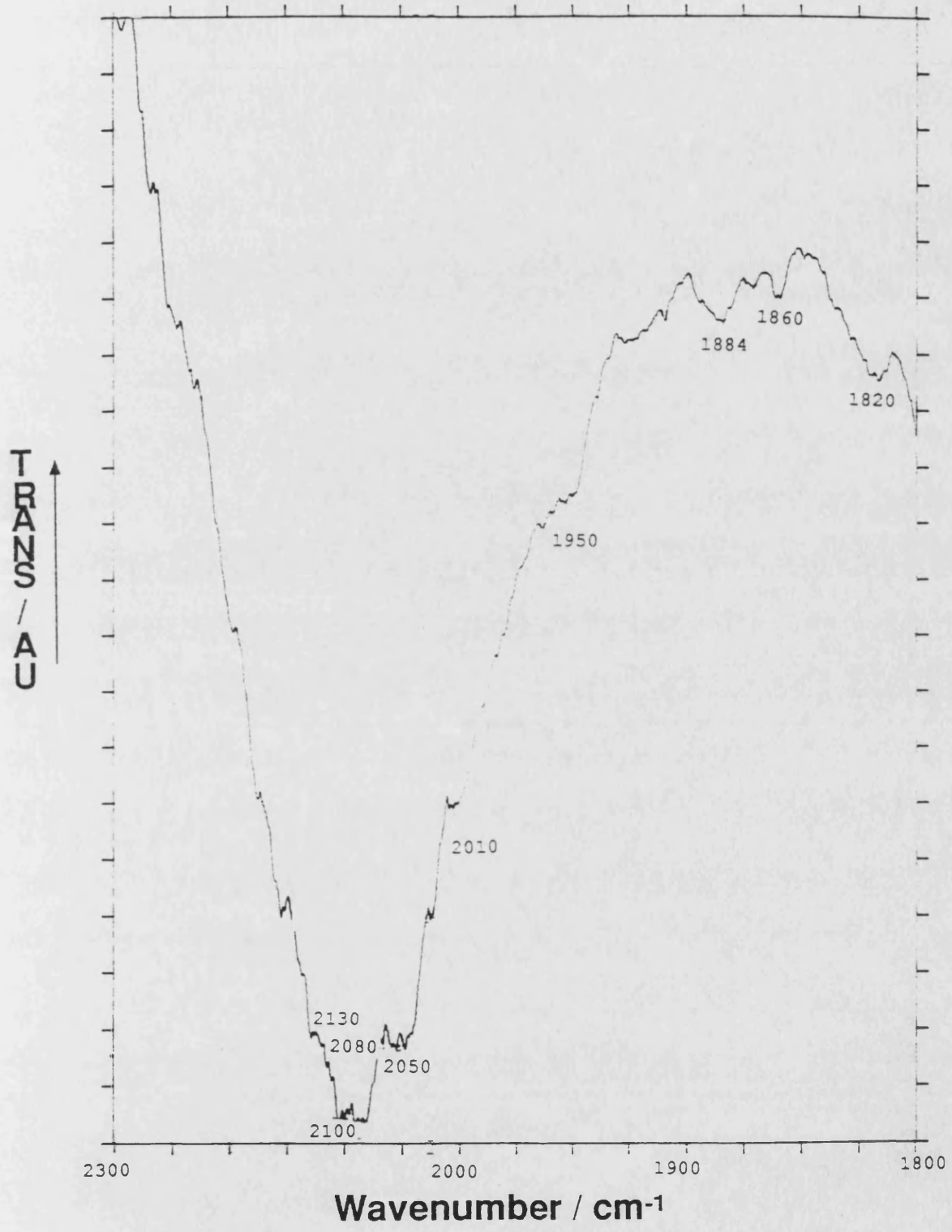

Figure 3.28 Infrared spectrum of CO adsorbed at 130 K on 5% Fe/MgO which had undergone reduction at 623 K

1860 and 1820 cm^{-1}.

3.6.2. Infrared Study of the Adsorption of Nitric Oxide on MgO and Fe/MgO Catalysts

Nitric oxide has been used as a probe molecule in a number of infrared studies with reduced iron catalysts (102-104). There have also been reports concerning the adsorption of NO on haematite (α-Fe_2O_3) (105, 106). The adsorption of NO on haematite is a matter of some contention, as some authors claim NO is not chemisorbed on haematite (107, 108). This section contains the results of an infrared study on the adsorption of NO on an oxidised 5% Fe/MgO catalyst and a catalyst which had been reduced by the standard method.

3.6.2.1. The Adsorption of NO on MgO

The adsorption of NO on MgO has previously been studied at ambient temperature on samples which have undergone outgassing at 1073 K (109, 110). In the present work a MgO disc after an initial degassing period was heated in hydrogen at 693 K for a period of 16 hours. After the evacuation of the gaseous hydrogen NO was admitted to a pressure of 80 Torr. The infrared spectra after a contact time of 40 mins is shown in Figure (3.29). Spectrum A is that obtained prior to the evacuation of the gaseous NO, while spectrum B is the spectrum obtained after the evacuation of the sample for 15 minutes. The two bands at 1902 and 1840 cm^{-1} in spectrum A can be assigned to the gaseous

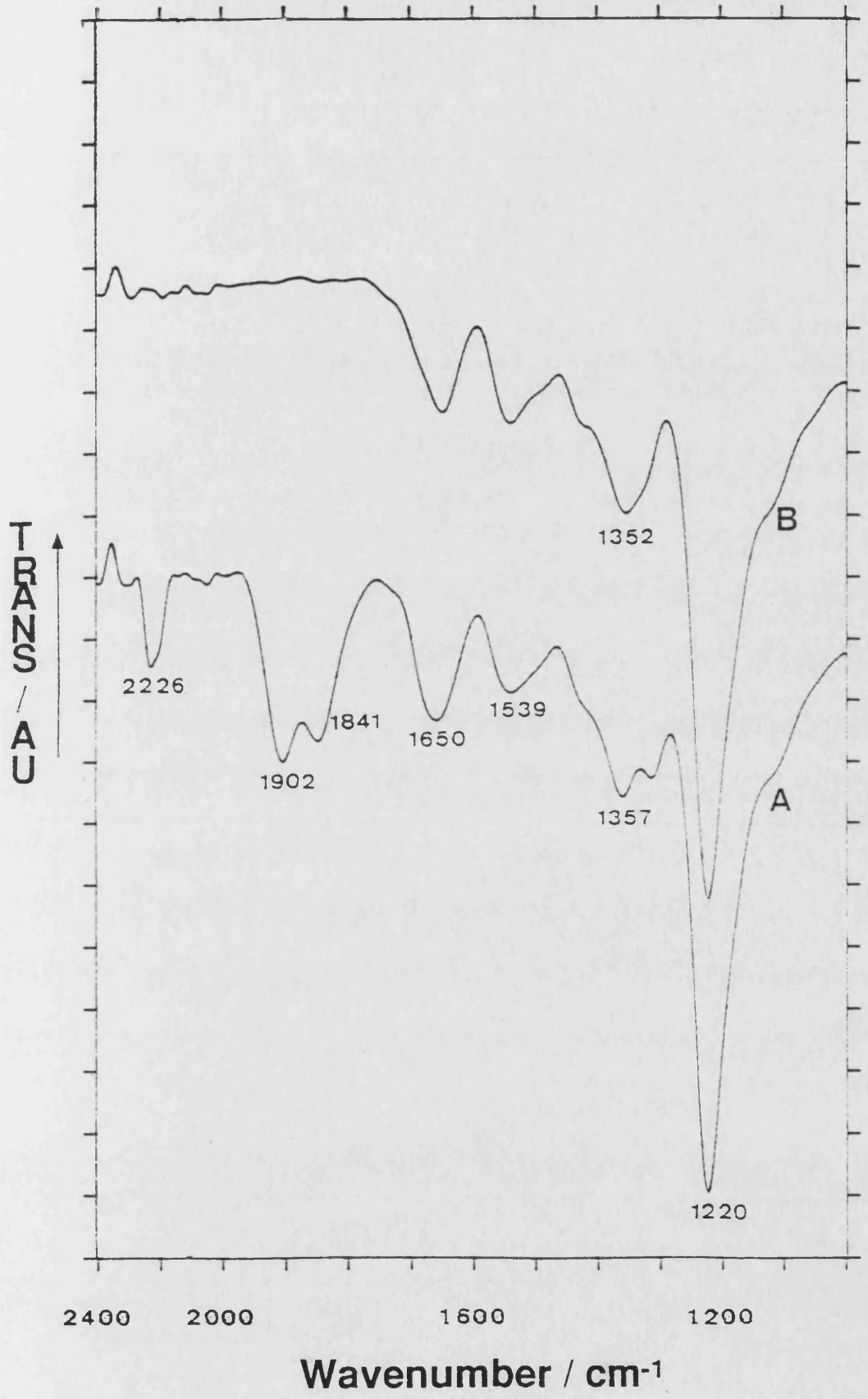

Figure 3.29 Infrared spectrum of NO adsorbed on MgO A) sample including gas phase NO (80 Torr) after 40 mins
B) after evacuation of gaseous NO

NO (111). The band observed at 2226 cm^{-1} in spectrum A is also removed on evacuation of the sample, this band is due to gaseous N_2O (11). The origin of this band will be discussed later.

3.6.2.2. Adsorption of NO on Unreduced 5% Fe/MgO

The adsorption of NO (80 Torr) at ambient temperature on a 5% Fe/MgO disc which had previously been outgassed at 393 K but not reduced resulted in the spectra presented in Fig. 3.30. Spectrum A corresponds to the disc in the presence of gaseous NO. Spectrum B was produced by the subtraction of a spectrum of gaseous NO from that of the disc + gaseous NO, performed using the software facilities provided by the data station. Spectrum C was recorded after the NO had been evacuated for a period of 15 minutes.

A comparison of the spectra produced from the MgO system and those produced from the unreduced Fe/MgO system indicate that the main differences in the two sets of spectra are:

A large increase in the intensity of the band at 1135 cm^{-1} compared with that at 1220 cm^{-1}.

Additional bands are observed in the spectral region 1650-1350 cm^{-1} in the unreduced Fe/MgO system.

Spectrum B of Fig 3.30 exhibits a band at 1860 cm^{-1} which is not observed when pure MgO is the adsorbent.

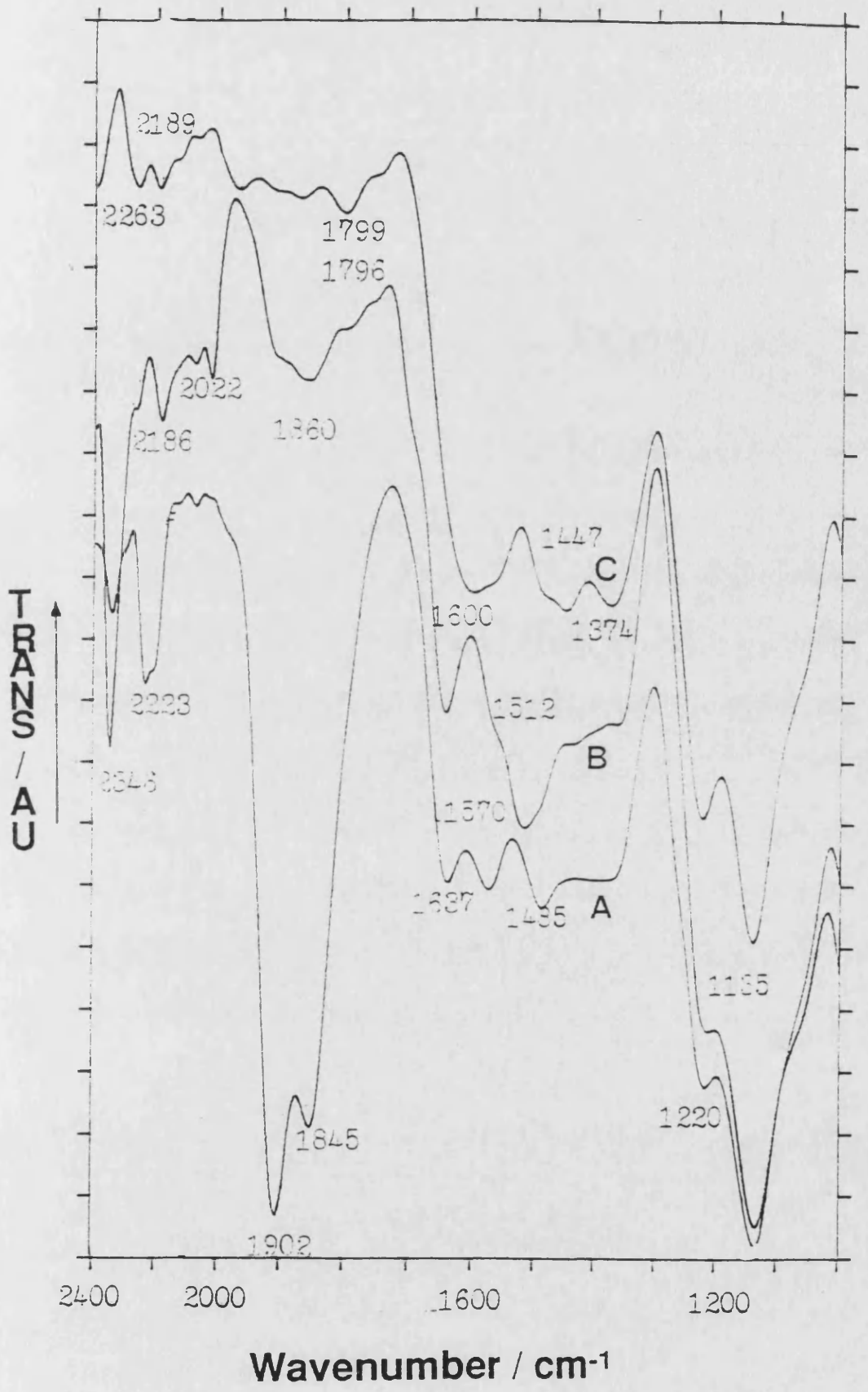

Figure 3.30 Infrared spectrum of NO adsorbed on 5% Fe/MgO A) sample + NO (80 Torr) B) sample after computer subtraction of gaseous NO C) after evacuation of gaseous NO

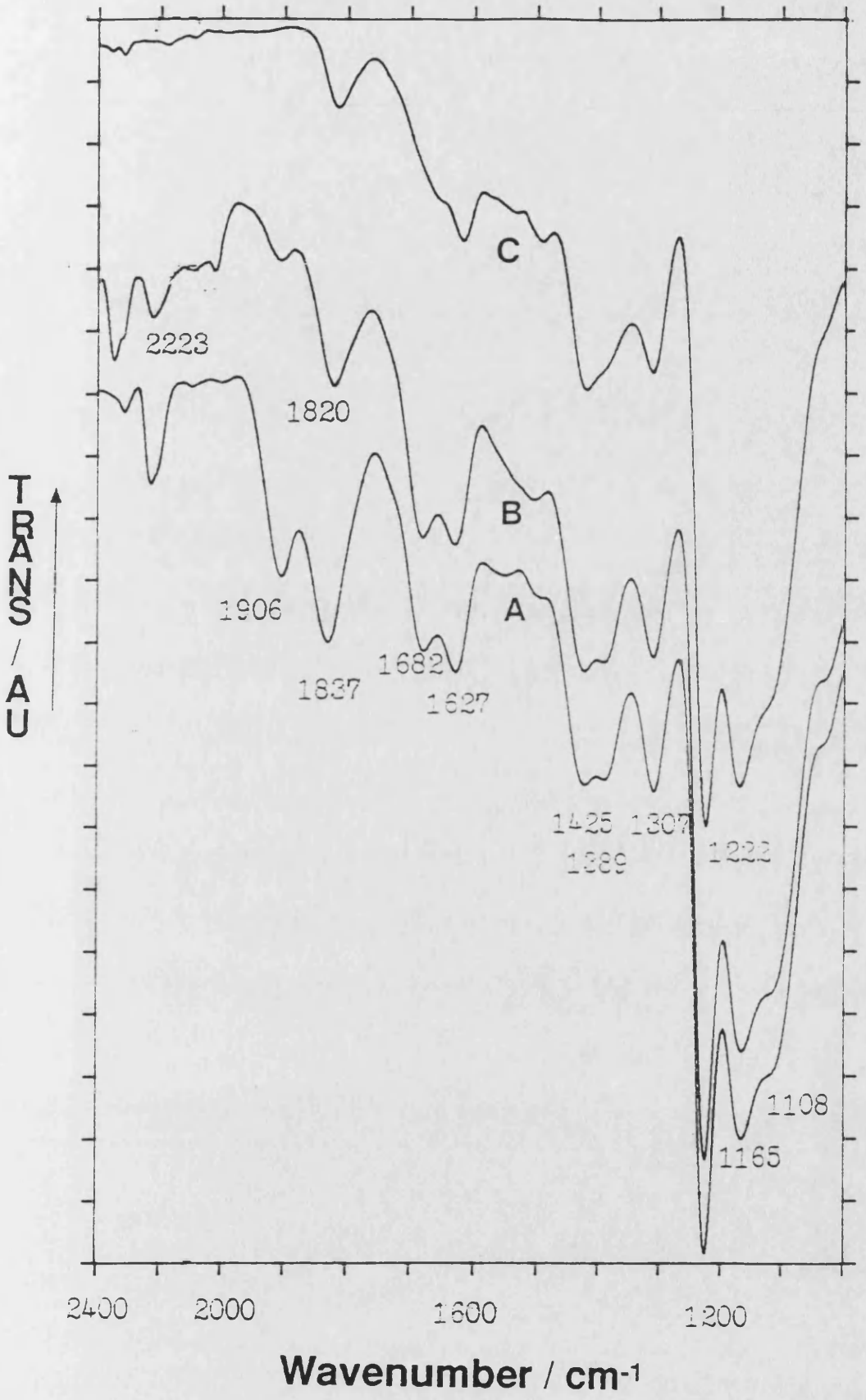

Figure 3.31 Infrared spectrum of NO adsorbed on 5% Fe/MgO which had been reduced at 693 K A) sample + NO (80 Torr) B) sample after computer subtraction of gaseous NO

3.6.2.3. Adsorption of NO on Reduced 5% Fe/MgO

The adsorption of NO on a sample of 5% Fe/MgO which had been reduced using the standard method described in Section 2.1.3, resulted in the spectra shown in Figure 3.31. These spectra exhibit absorption bands due to adsorbed species at 1820 cm^{-1} (m), 1682 cm^{-1} (m), 1627 cm^{-1} (m), 1425 cm^{-1} (m), 1389 cm^{-1} (m), 1307 cm^{-1} (m), 1222 cm^{-1} (vs), 1165 cm^{-1} (s), and a shoulder at 1108 cm^{-1}.

The main differences in the spectra when compared to those produced from the adsorption of NO on pure MgO are:

the production of two new bands at 1820 cm^{-1} and 1307 cm^{-1};

the band observed at 1650 cm^{-1} with MgO now appears to be split to give a doublet with peaks at 1682 cm^{-1} and 1627 cm^{-1};

the band previously observed at 1350 cm^{-1} has been shifted to a higher wavenumber and appears in the form of a doublet with peaks at 1425 cm^{-1} and 1389 cm^{-1};

the band observed at 1135 cm^{-1} when NO is adsorbed on unreduced Fe/MgO now appears to be in the form of a doublet with centres at 1165 cm^{-1} and 1108 cm^{-1}.

3.6.3. Infrared Spectroscopy of Adsorbed Ethanenitrile and Propanenitrile

In order to diagnose the effects of adsorption and reaction it was appropriate first to record the spectrum of free nitrile. Figure 3.32. shows the infrared spectrum of ethanenitrile (CH_3CN). This is a well known spectrum; the

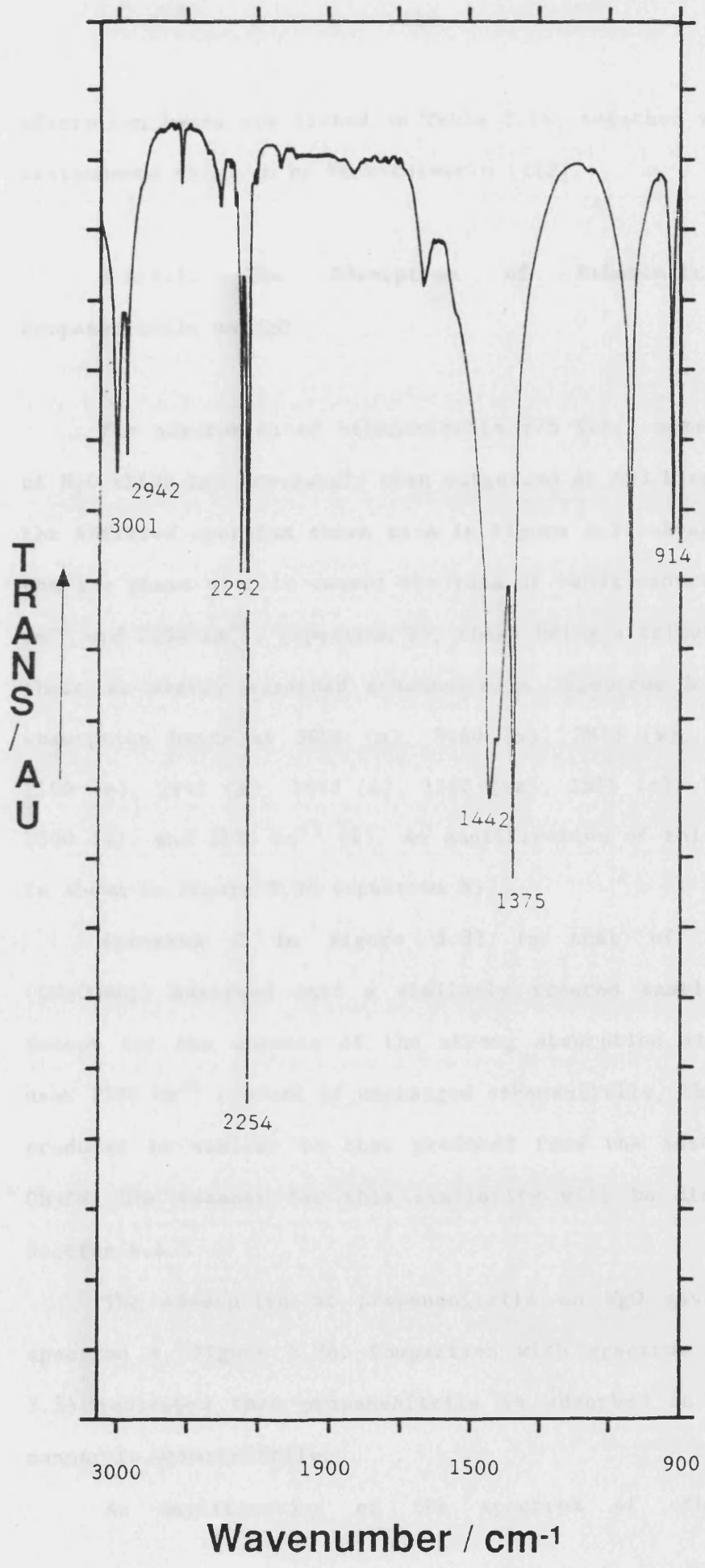

Figure 3.32 Infrared spactrum of ethanenitrile in the liquid phase

Table 3.14 Infrared Bands of Liquid Ethanenitrile and their Assignments

Description	Designation	wavenumber /cm^{-1}
symmetric C-H stretching	ν_1	2942
$C \equiv N$ stretching	ν_2	2254
symmetric CH_3 deformation	ν_3	1375
C-C stretching	ν_4	914
anyisymmetric CH_3 deformation	ν_5	1442
antisymetric C-H stretching	ν_6	3001
$C - C \equiv N$ bending	$\nu_3 + \nu_4$	2292

adsorbed on MgO in the spectral region 4000 - 1600 cm^{-1} is shown in Figure 3.35, spectrum B. The amplification reveals further structure in the spectrum, including weak absorption bands situated at 3361, 3144, and 2354 cm^{-1}. A similar treatment of the spectrum obtained from the adsorption of propanenitrile on MgO is shown in Figure 3.37, spectrum B. The similarities with ethanenitrile on MgO already noted are seen to extend also to the weak absorption bands at 3338 and 3134 cm^{-1}.

3.6.3.2. The adsorption of Ethanenitrile and Propanenitrile on 5% Fe/MgO

Ethanenitrile was adsorbed at its ambient saturated vapour pressure on a 5% Fe/MgO catalyst which had previously undergone the reduction programme described in Section (2.1.3). The resulting spectrum in the region 4000 - 1100 cm^{-1} is shown in Figure 3.34, spectrum A. This spectrum contains very strong absorption bands at 1566, 1451 and 1185 cm^{-1}. Both spectrum A and spectrum B (ethanenitrile on MgO) have undergone identical amplification procedures.

Further amplification is shown in Figure 3.35 where the spectra on Fe/MgO and MgO are again compared. The 5 % Fe/MgO sample (spectrum A) shows most of the absorption bands found with the adsorption on MgO (spectrum B), although they are in general weaker. However, there are some significant bands revealed at 2800 - 2400 cm^{-1} which do not appear in the spectrum of MgO alone. In this region the Fe/MgO system

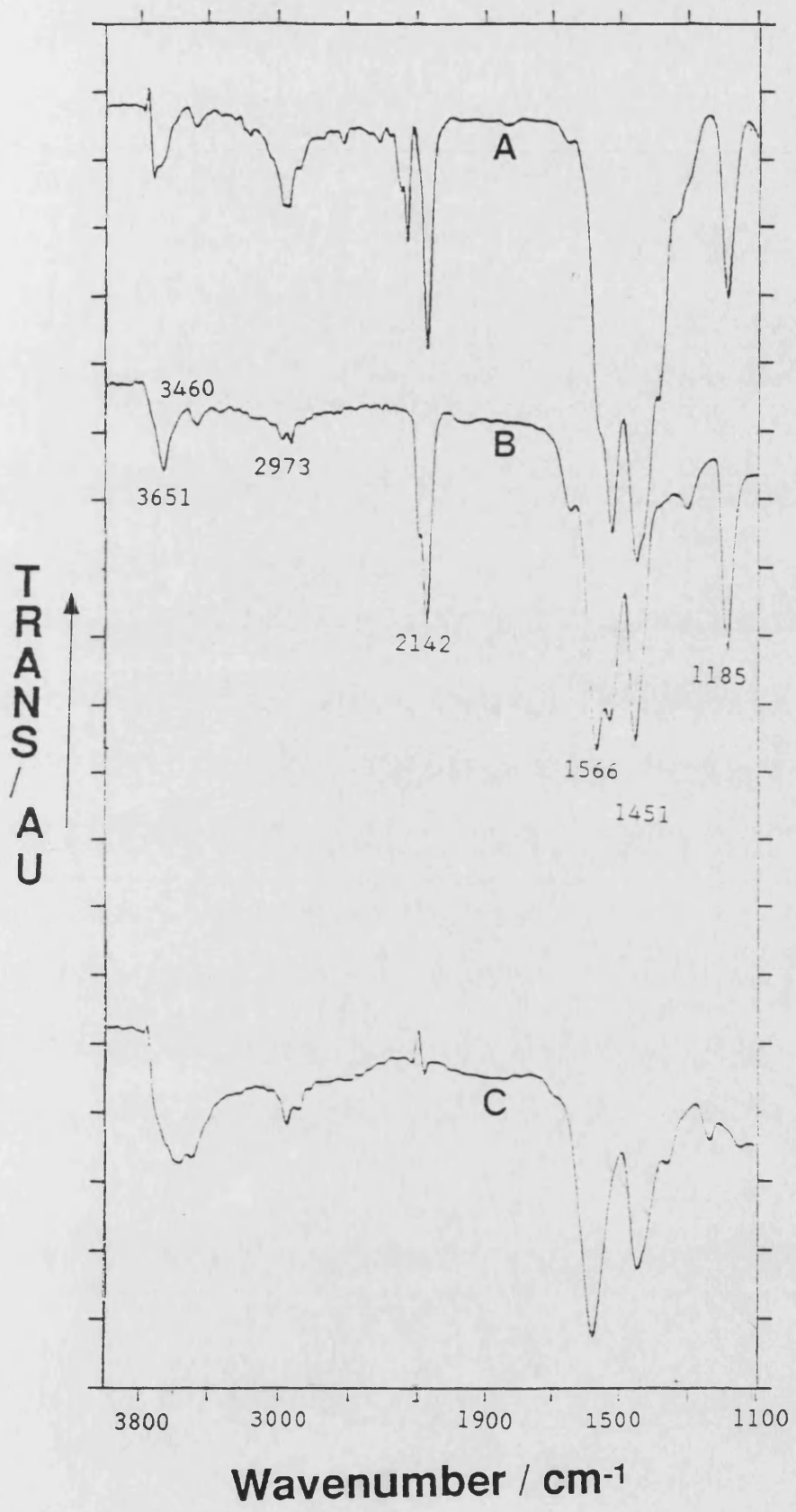

Figure 3.33 A) MgO + gaseous ethane nitrile (75 Torr)
B) MgO after evacuation of gaseous ethanenitrile
C) Ethanamide adsorbed on MgO

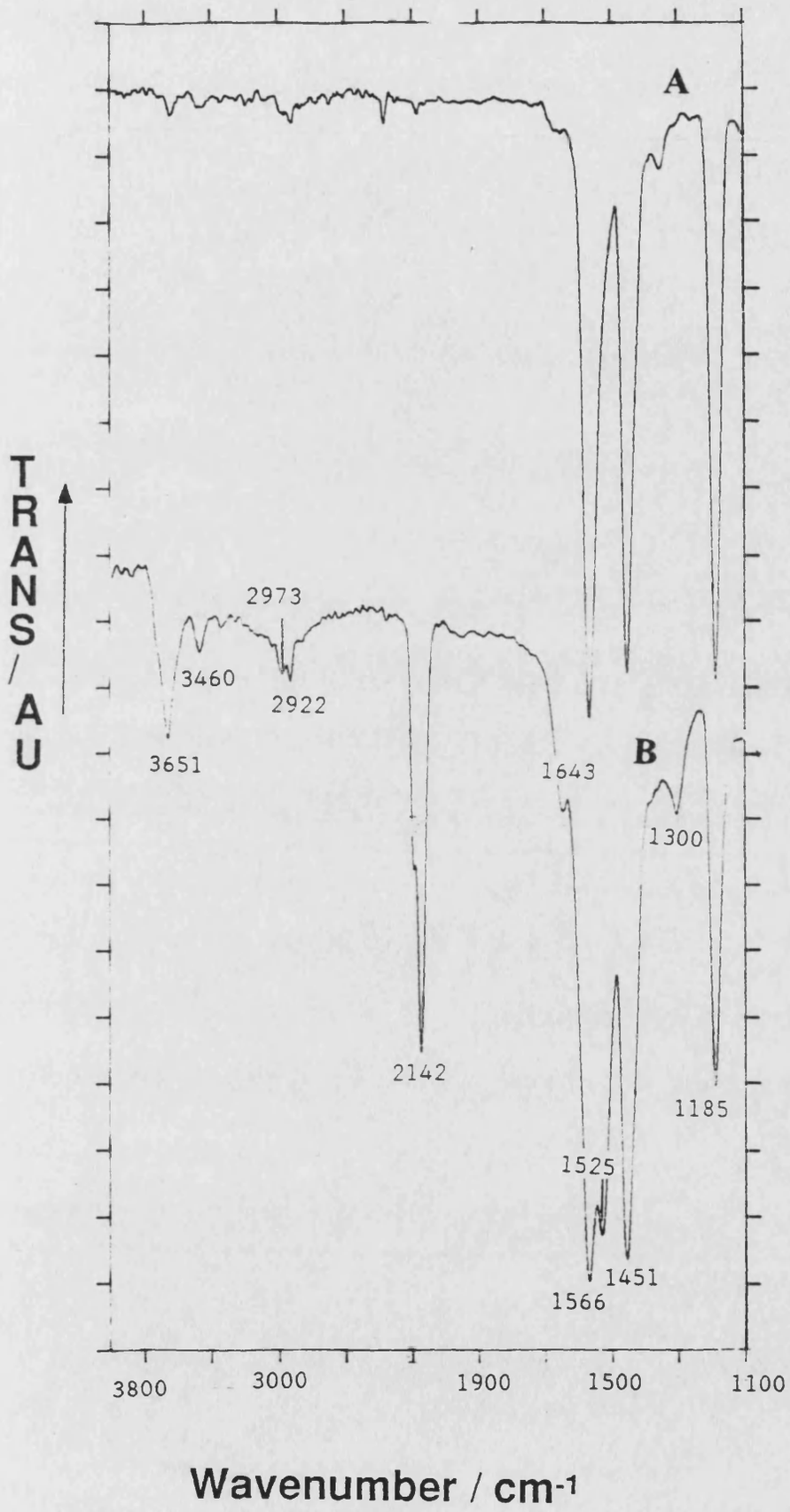

Figure 3.34 Infrared spectrum of ethanenitrile adsorbed on A) 5% Fe/MgO and B) MgO

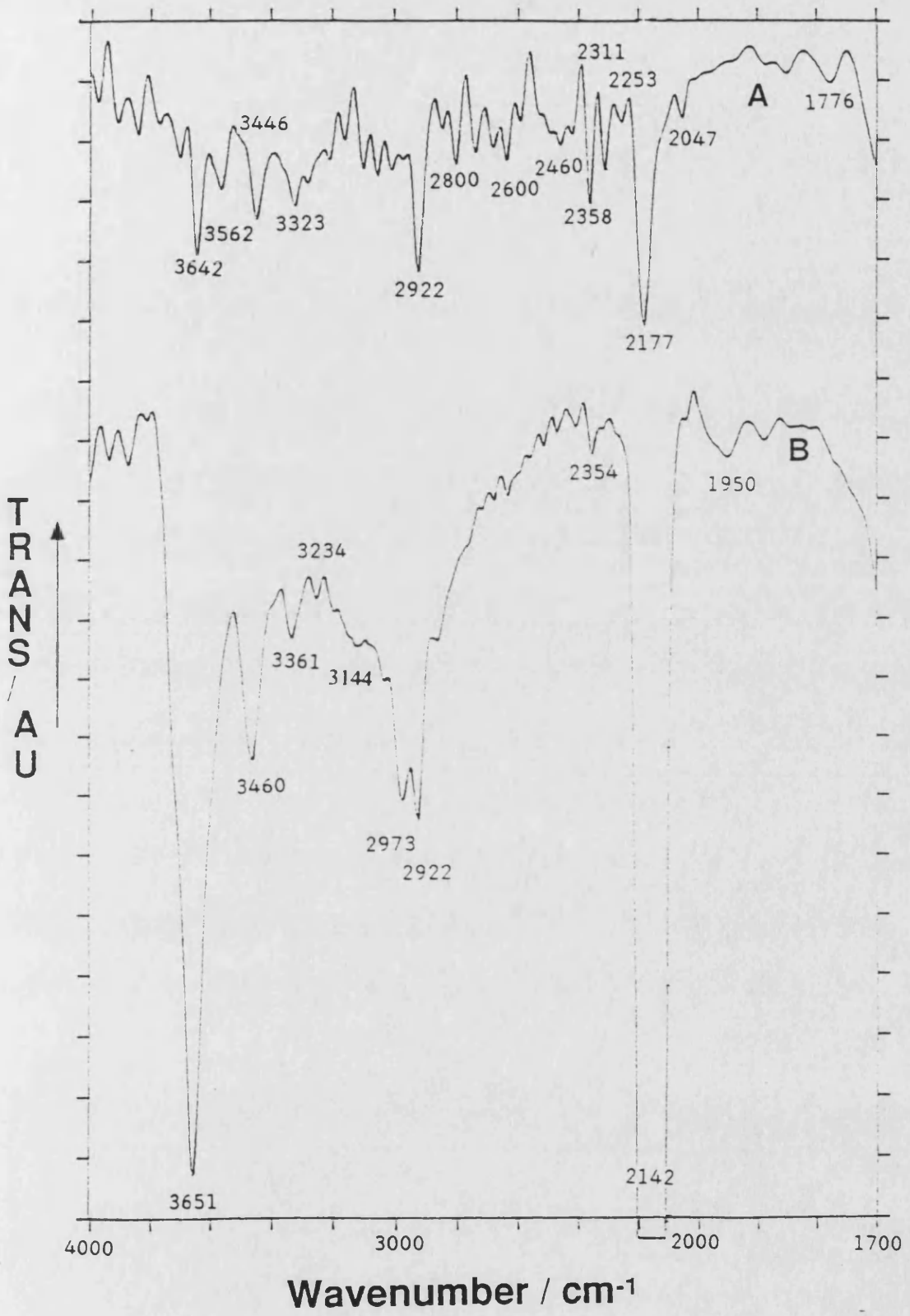

Figure 3.35 Infrared spectrum of ethanenitrile adsorbed on A) 5% Fe/MgO and B) MgO

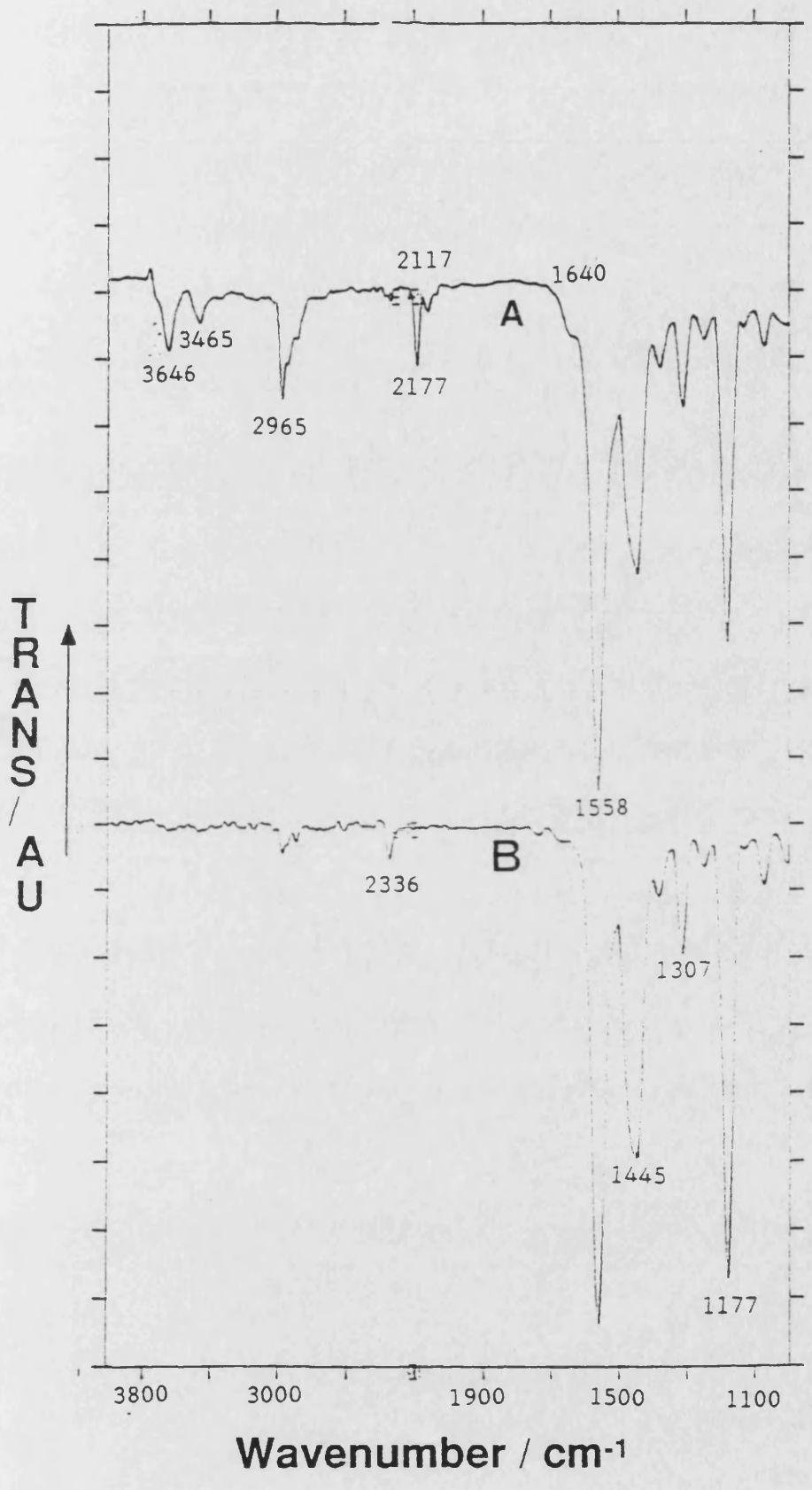

Figure 3.36 Infrared spectrum of propanenitrile adsorbed on A) MgO and B) 5% Fe/MgO

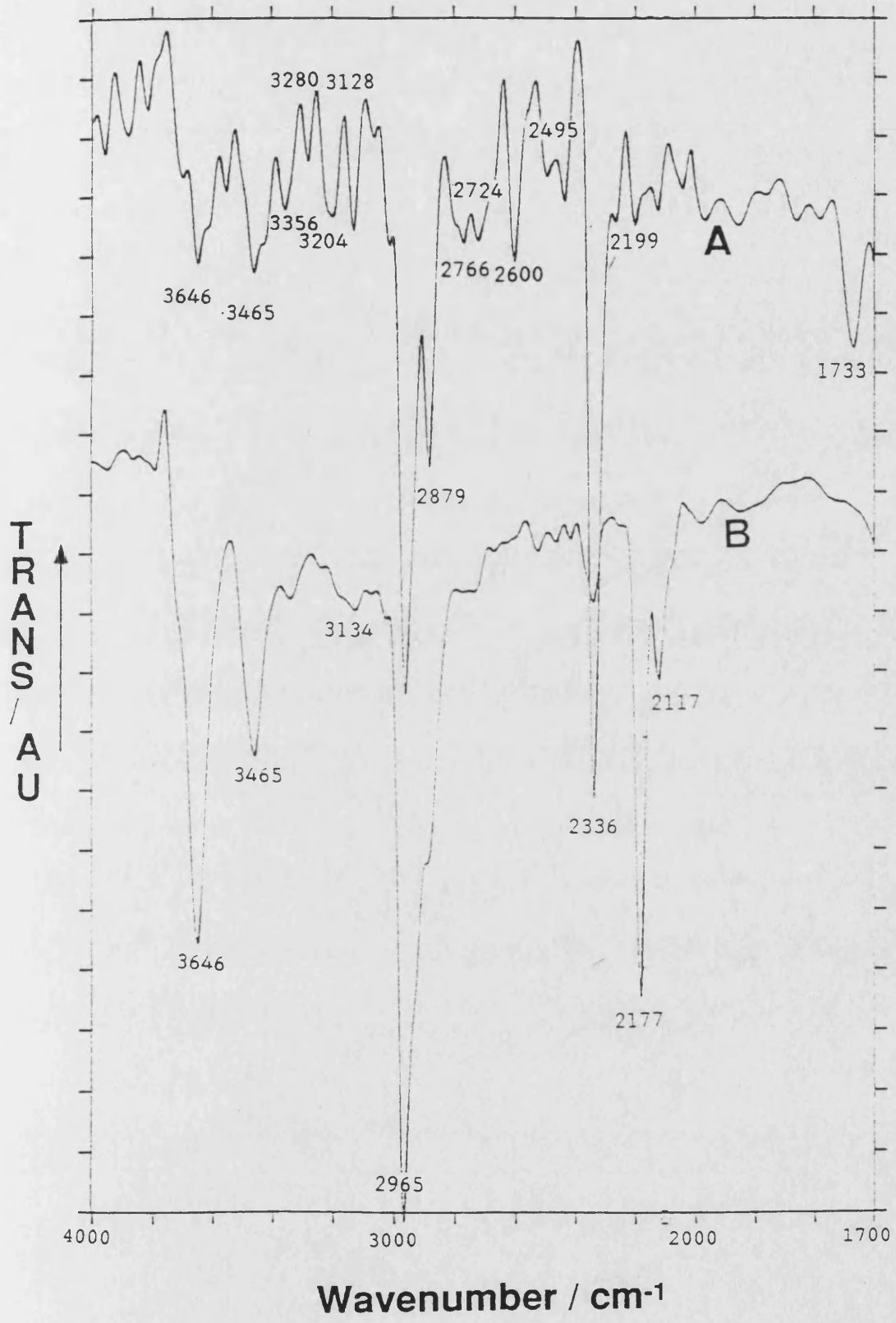

Figure 3.37 Infrared spectrum of propanenitrile adsorbed on A) 5% Fe/MgO and B) MgO

exhibits absorption bands which may be divided into three groups centred at 2800 cm^{-1}, 2636 cm^{-1}, and 2463 cm^{-1}. There is also an additional absorption at 1776 cm^{-1}.

A similar set of absorption bands are produced from the adsorption of propanenitrile on the Fe/MgO catalyst (Fig. 3.36 B and 3.37 A), There are some differences in the position of the bands, but it is very clear in this case that some bands are present with Fe/MgO which are absent with MgO alone, notably those at 2600 and 1733 cm^{-1}.

3.7. Catalytic Hydrogenation of Nitriles

3.7.1. Catalyst Testing using the Flow Reactor

Hydrogenation reactions were carried out using the flow apparatus described in Section 2.9.2.1. The aim of these experiments was to obtain kinetic data on the hydrogenation of ethanenitrile (CH_3CN) using the catalysts prepared in this work. It was not possible to obtain this type of information from the catalyst testing performed in the autoclave reactor.

The experiments performed can be split into three categories; (a) variation of reaction temperature in order to obtain the activation energy, (b) variation of the space velocity in order to obtain values for the rate of reaction and (c) variation of hydrogen and ethanenitrile concentration, independently, to determine the order of reaction with respect to both reactants.

3.7.1.1 Calibration of the Gas-Liquid Chromatograph

The GC was calibrated by injecting known amounts of ethanenitrile, 70% ethylamine in water and diethylamine. After a trial reaction it was noticed that a shoulder appeared on the trailing edge of the hydrogen peak. This was thought to be due to products formed from the hydrogenolysis of the ethanenitrile. The shoulder was found to have a similar retention time to that of ethane and hence was calibrated using ethane. Figures 3.38-3.41 contains the calibration graphs for the reactants and products.

3.7.1.2 Catalyst Testing

The catalysts tested were found to hydrogenate ethanenitrile with a high selectivity to the primary amine, only minor amounts of secondary amine were detected and no tertiary amine. There was however some indication of some hydrogenolysis as mentioned above. The analysis system was not adequate to resolve the hydrogenolysis products from the hydrogen peak with any degree of accuracy, hence this study is limited to measurements on the loss of ethanenitrile and the formation of ethylamine.

A plug flow model has been adopted to represent the flow reactor used. A schematic representation of a plug flow reactor is shown in Fig 3.42. Referring to Figure 3.42 and applying a mass balance to a differential volume of the reactor gives

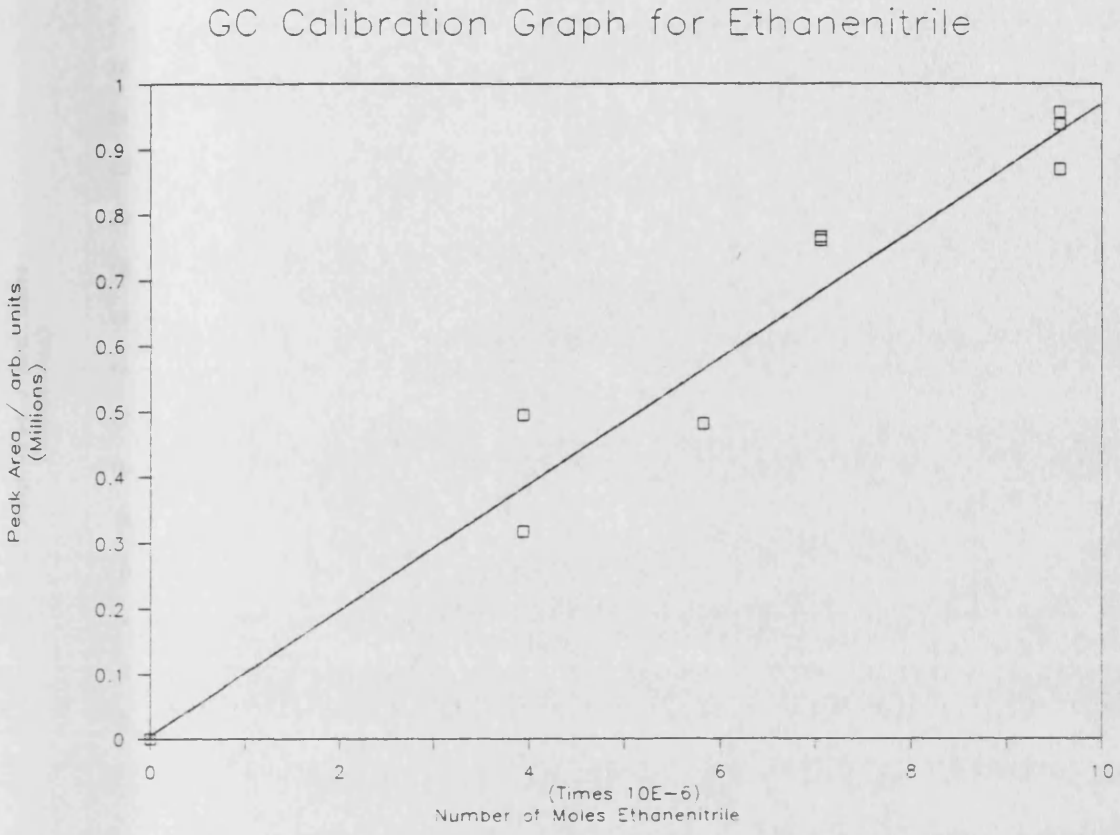

Figure 3.38 Calibration graph for ethanenitrile

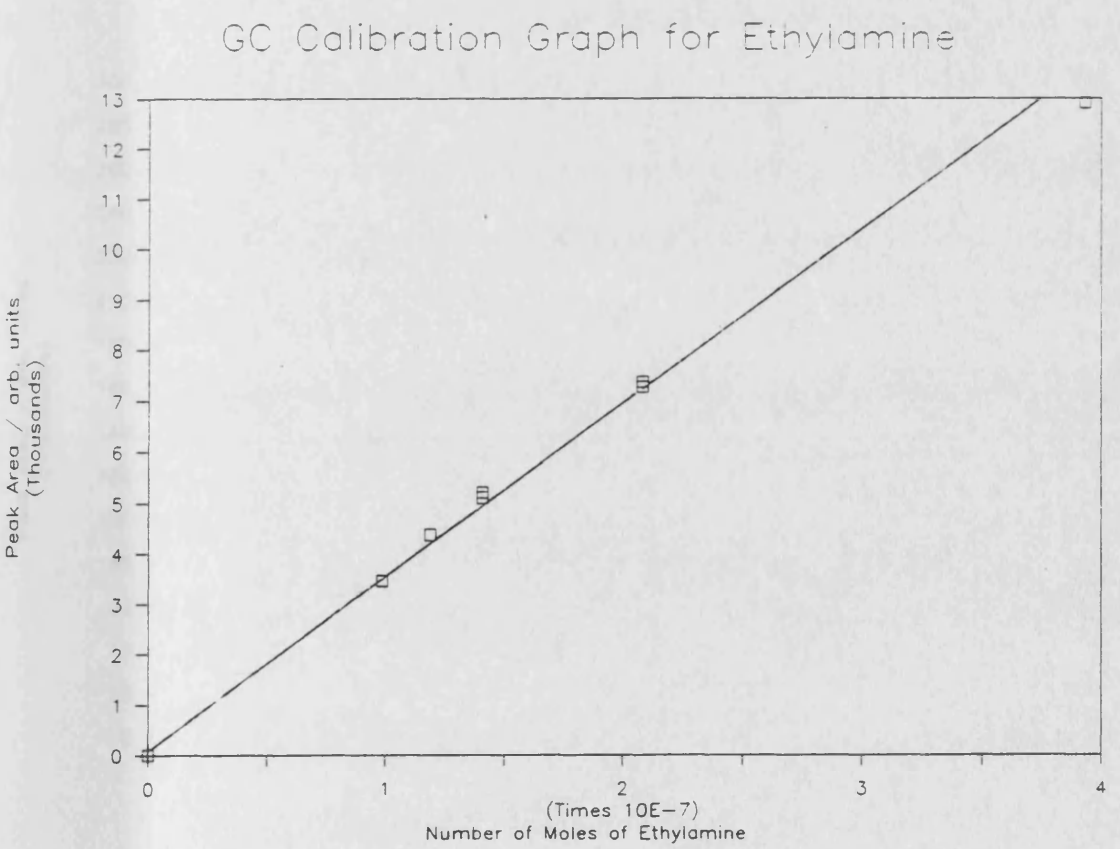

Figure 3.39 Calibration graph for ethylamine

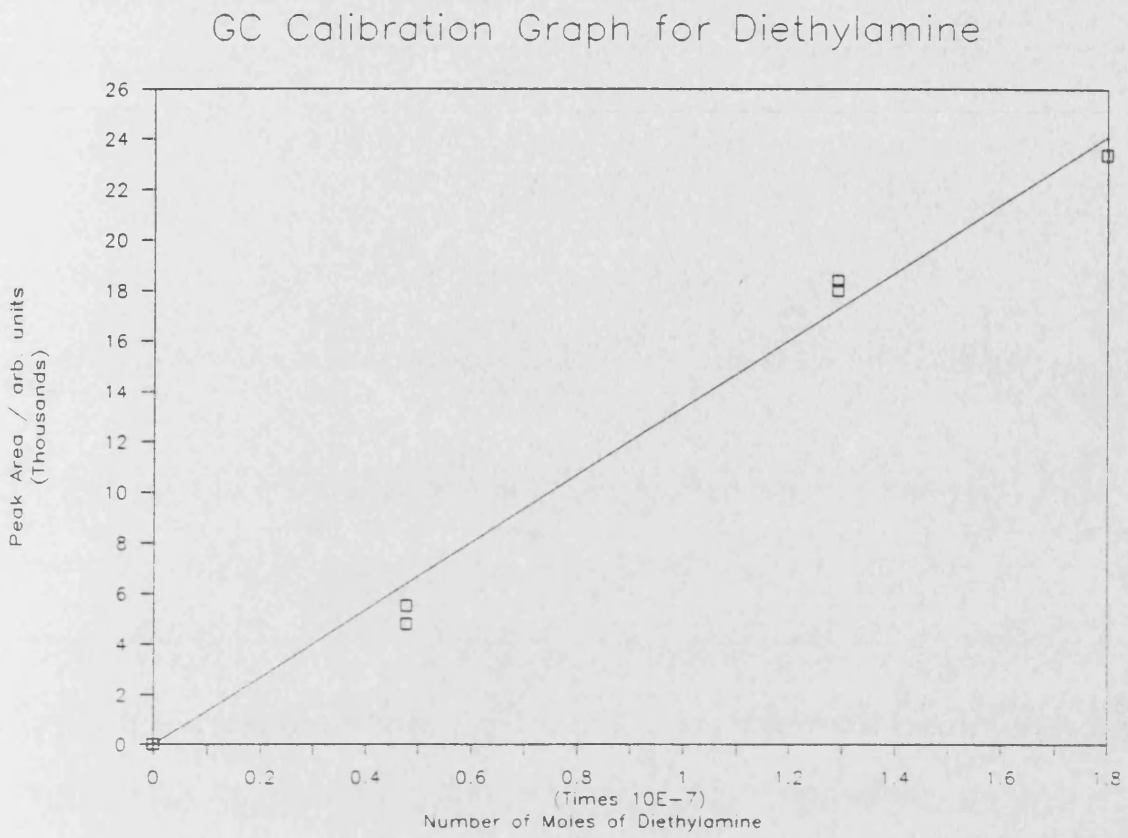

Figure 3.40 Calibration graph for diethylamine

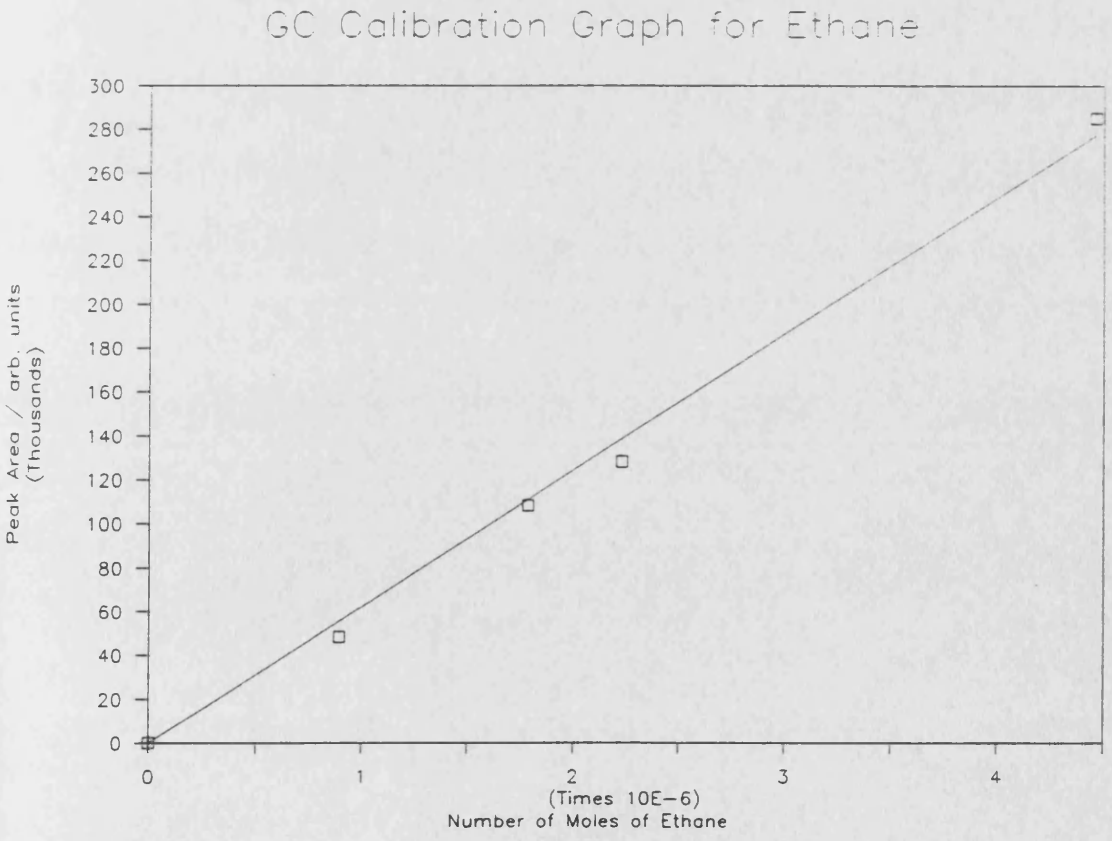

Figure 3.41 Calibration graph for ethane

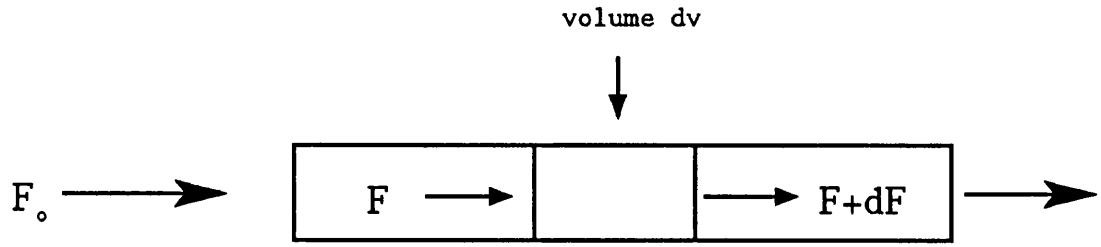

Figure 3.42 Schematic diagram of a plug flow reactor F_o and F are the molar flow rates of reactant entering the reactor, and crossing any plane in the reactor respectively.

$$F = (F + dF) + r\,dV$$

and so

$$r = -\frac{dF}{dV}$$

where r is the reaction rate per unit volume of catalyst.

If F_o is the molar feed rate of the reactant to the reactor, and χ is the fractional conversion, then

$$F = F_o\,(1-\chi)$$

and

$$\frac{dF}{dV} = -F_o\,\frac{d\chi}{dV}$$

so

$$r = F_o\,\frac{d\chi}{dV}$$

The plug flow reactor only gives a direct measurement of rate when conversions are so small that $d\chi$ may be replaced by $\Delta\chi$. This means a very small amount of catalyst, and such a reactor is referred to as a differential reactor. Experimentally, however, very low conversions lead to analytical problems and hence the reactor is operated at higher conversions, that is in the integral mode, where the rate varies with the axial position in the reactor. Here

$$r = F_o\,\frac{d\chi}{dV} = C_o\,\frac{d\chi}{d\tau}$$

hence

$$\int_{x_o}^{x_L} \frac{d\chi}{r} = \frac{V}{F_o} = \frac{\tau}{C_o}$$

and the space time $\tau = V/Q_o$, where C is the reactant concentration and Q_o is the volumetric feed-rate. If there is no volume change during the reaction then

$$r = C_o \frac{d\chi}{d\tau} = - \frac{dC}{d\tau}$$

3.7.1.2.1 Rate of Reaction

The rate of reaction at 508 K was measured for catalysts OH5, OH20, OH30, HT1 and IP30. The results are contained in Table 3.15. obtained by varying the flow rate through the

Table 3.15 rate of reaction for some catalyst tested in the flow reactor.

Catalyst	Rate of Reaction /mol l^{-1} min^{-1}
OH30	0.021
OH20	0.029
OH5	0.0081
IP30	0.0073
HT1	0.013

catalyst bed, typically between 10 ml min^{-1} and 50 ml min^{-1}. The temperature of the gas saturator was maintained at 273 K throughout the experiment. The conversion in mol l^{-1} was obtained by sampling the exit gas from the reactor. The space time (τ) was varied by varying the flow rate of hydrogen through the reactor. The rate was obtained from the gradient of the plot of space time vs conversion shown in Figure 3.43.

3.7.1.2 Temperature Dependence of the Rate of Reaction

The rate of hydrogenation of ethanenitrile was measured

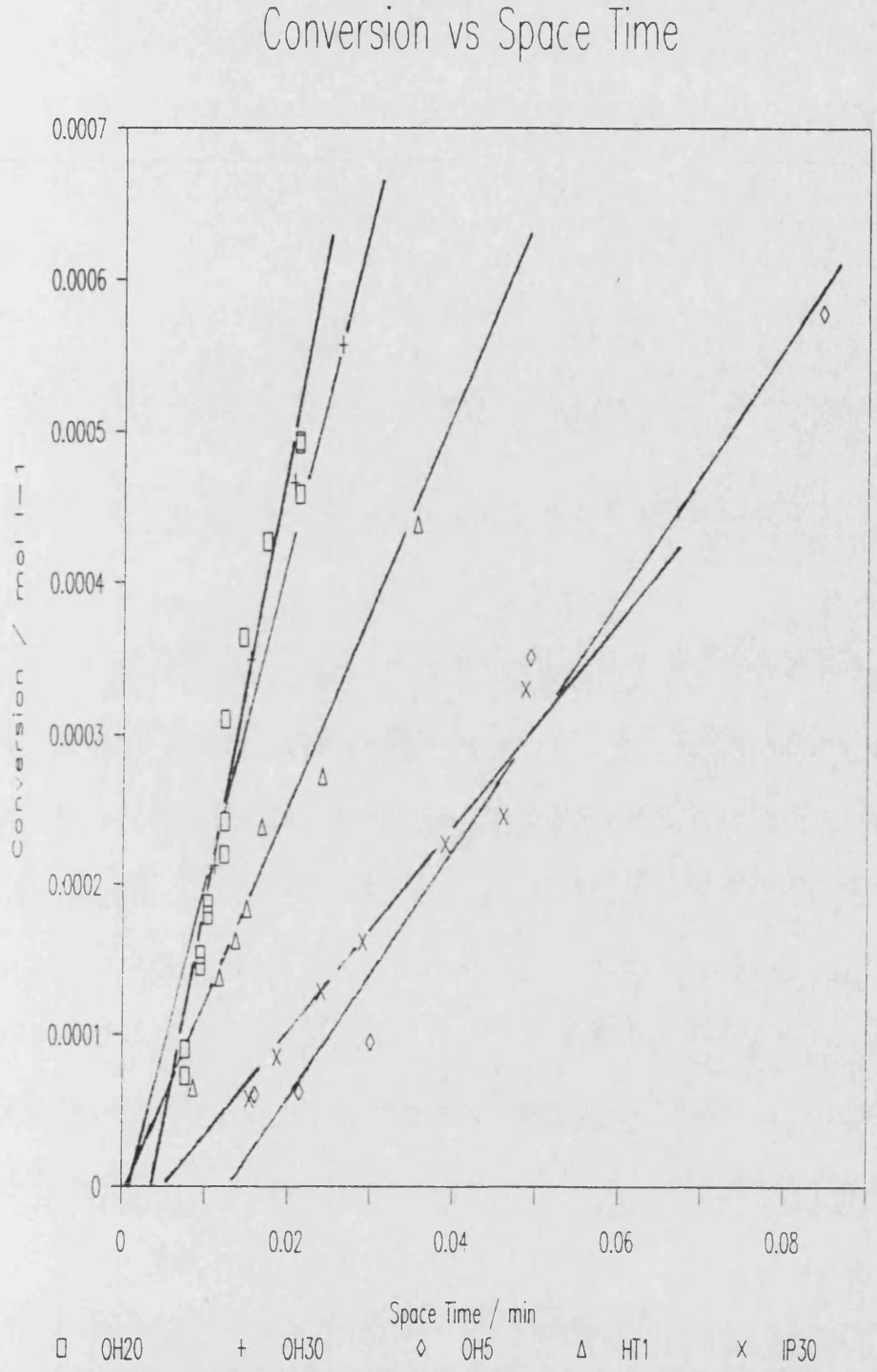

Figure 3.43 Plot of conversion vs space time

on catalysts HT1, OH20 and OH5 in the temperature region 450 K to 530 K. The measurements were made using a hydrogen flow rate of 19.8 ml min^{-1} and with the gas saturator maintained at 273 K.

The activation energy $E^{\#}$ was derived from the Arrhenius equation

$$k = A \exp(-E^{\#}/RT)$$

as the rate constant is proportional to the rate a plot of ln rate vs 1/T will produce a line with a gradient of $-E^{\#}/R$. Plots of this type for catalysts HT1, OH5 and OH20 are shown in Figures 3.44, 3.45 and 3.46 respectively. The non-linear behaviour of the catalysts over the temperature range studied will be discussed in Section 4.5.1. Analysis of the linear regions of the above Figures yields activation energies of 100.8, 58.5 and 58.5 kJ mol^{-1} for catalysts OH5, HT1 and OH20 respectively.

3.7.1.3 Determination of the Order of Reaction for Ethanenitrile and Hydrogen

The concentration of ethanenitrile was varied by varying the temperature of the gas saturator between 273 K and ambient temperature. This resulted in a variation in the ethanenitrile concentration between 1.2×10^{-7}mol l^{-1} and 4.9×10^{-7} mol l^{-1}. The hydrogen flow rate was maintained at 19.7 ml min^{-1} throughout the experiment. The reactor temperatures used for these studies were 458 K in the case of catalyst HT1 and 503 K in the case of catalyst OH5. These temperature were chosen to coincide with the regions of chemical control as indicated by

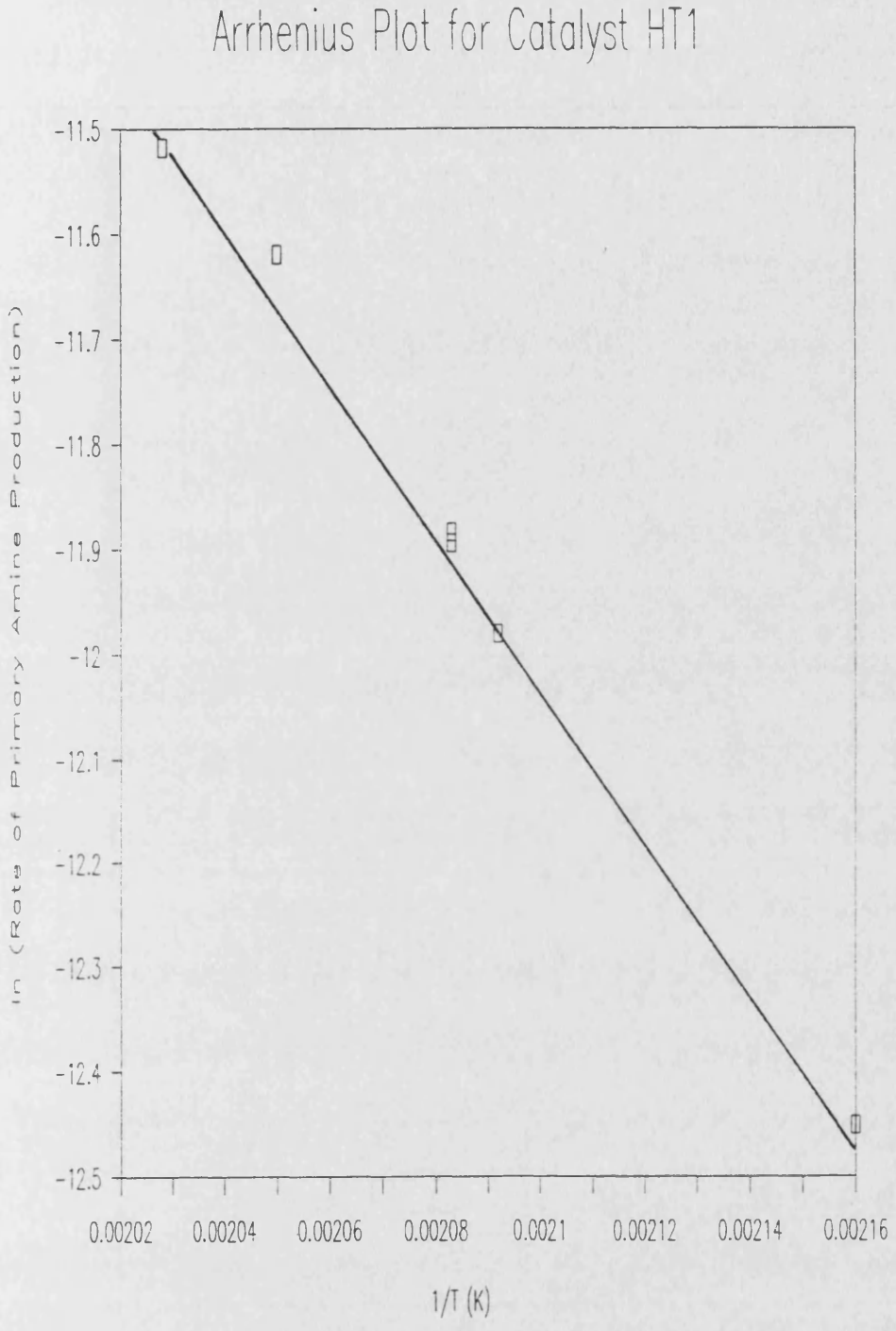

Figure 3.44 Arrhenius plot for ethanenitrile hydrogenation over catalyst HT1

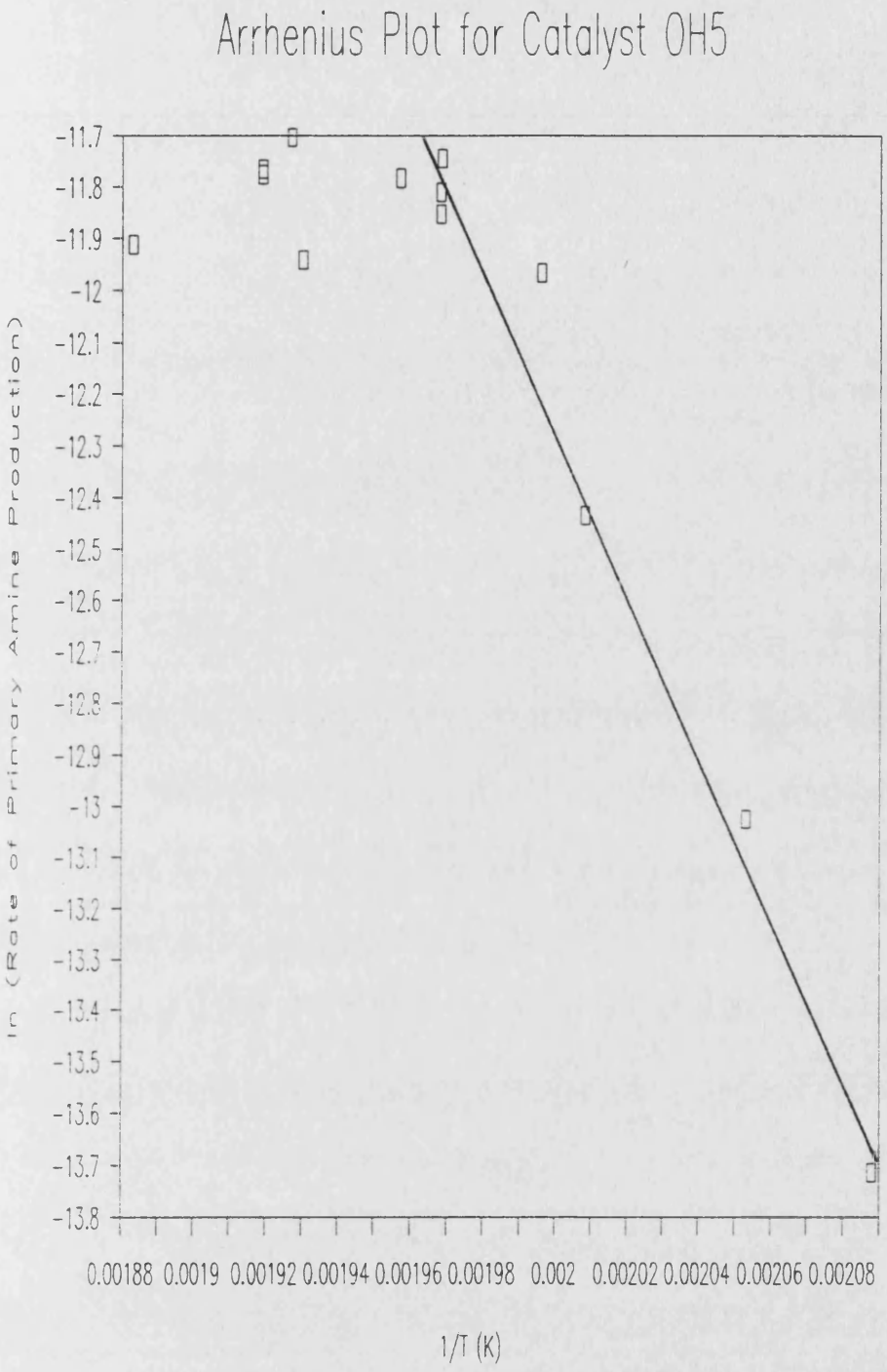

Figure 3.45 Arrhenius plot for ethanenitrile hydrogenation over catalyst OH5

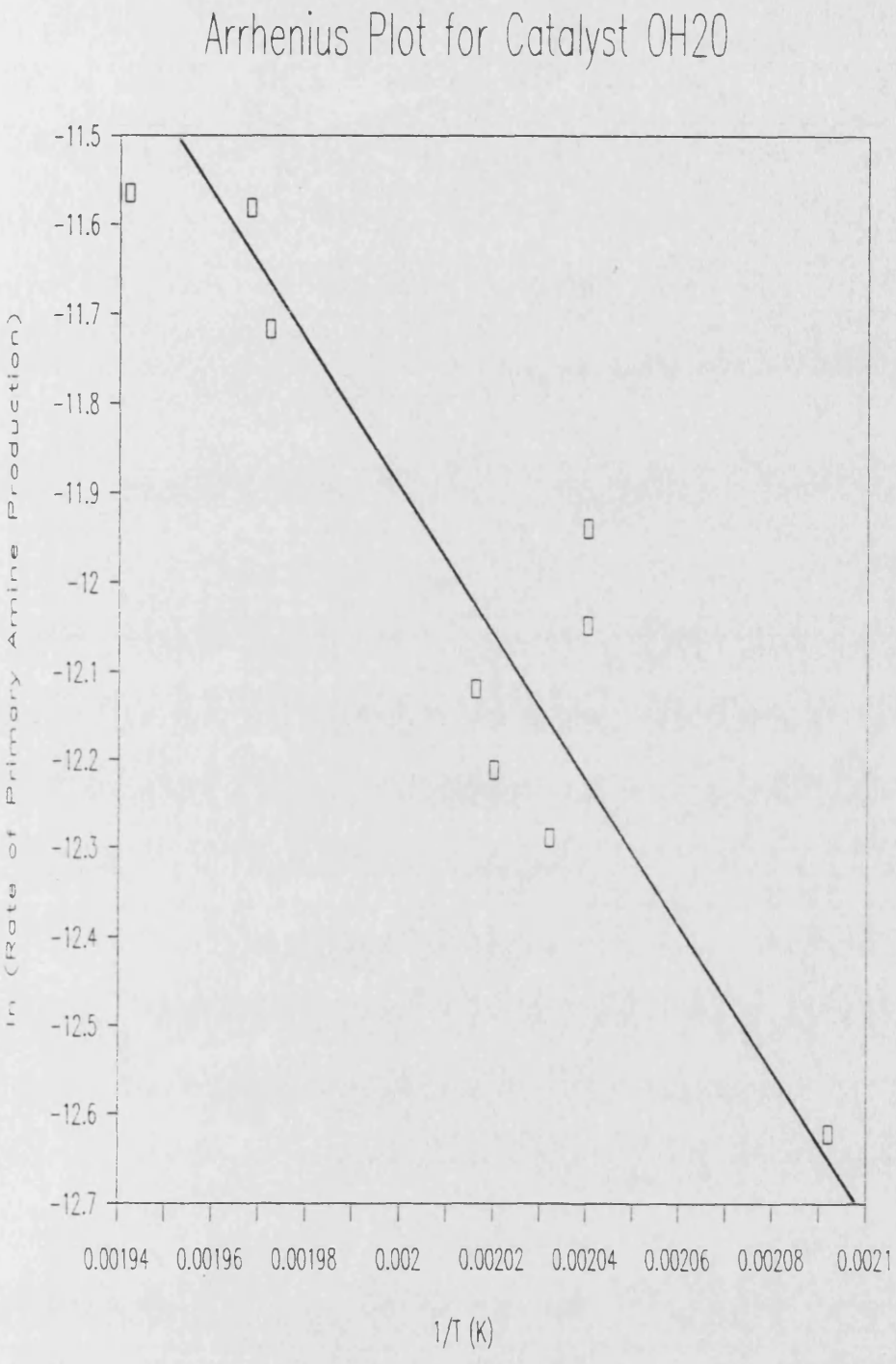

Figure 3.46 Arrhenius plot for ethanenitrile hydrogenation over catalyst OH20

the Arrhenius plots (Figs. 3.44, 3.45)

The order was obtained from a plot of log rate of primary amine production vs log ethanenitrile concentration (Fig. 3.47). The order of reaction with respect to the ethanenitrile concentration for catalysts HT1 and OH5 were determined to be 0.28 ± 0.04 and -0.25 ± 0.08 respectively.

Variation of the hydrogen concentration was achieved by dilution of the hydrogen flowing through the reactor with helium. The rate of reaction was monitored while varying the percentage hydrogen in the reactant gas between 0 and 100 % . The concentration of ethanenitrile was maintained constant throughout. The order of reaction was again determined from plotting log rate of primary amine production vs log hydrogen concentration (Figure 3.48). The order of reaction w.r.t. hydrogen concentration for catalyst HT1 was determined to be 1.9 ± 0.3.

3.7.2. Catalyst Testing Using the High Pressure Autoclave Reactor

The first reaction studied was the hydrogenation of propanenitrile, C_2H_5CN. Propanenitrile was chosen as the preferred model nitrile because it has a simple structure and could be expected to yield a relatively simple range of products on hydrogenation. Ethanenitrile hydrogenation was not studied in this reactor because the primary product ethanamine is gaseous at ambient temperature and pressure, this would have caused additional problems in the analysis of the final product.

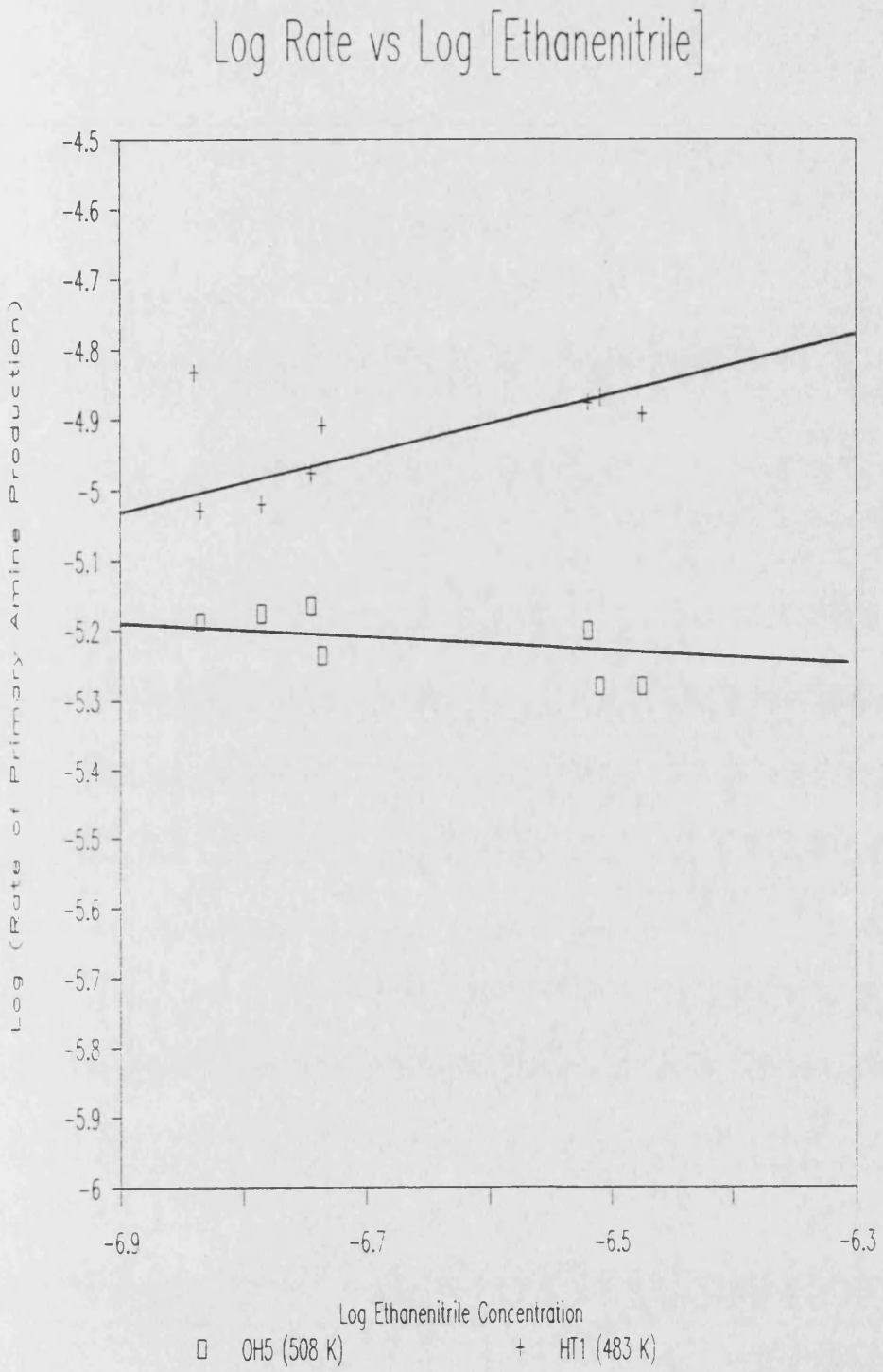

Figure 3.47 Plot of log rate vs log ethanenitrile concentration for catalysts OH5 and HT1

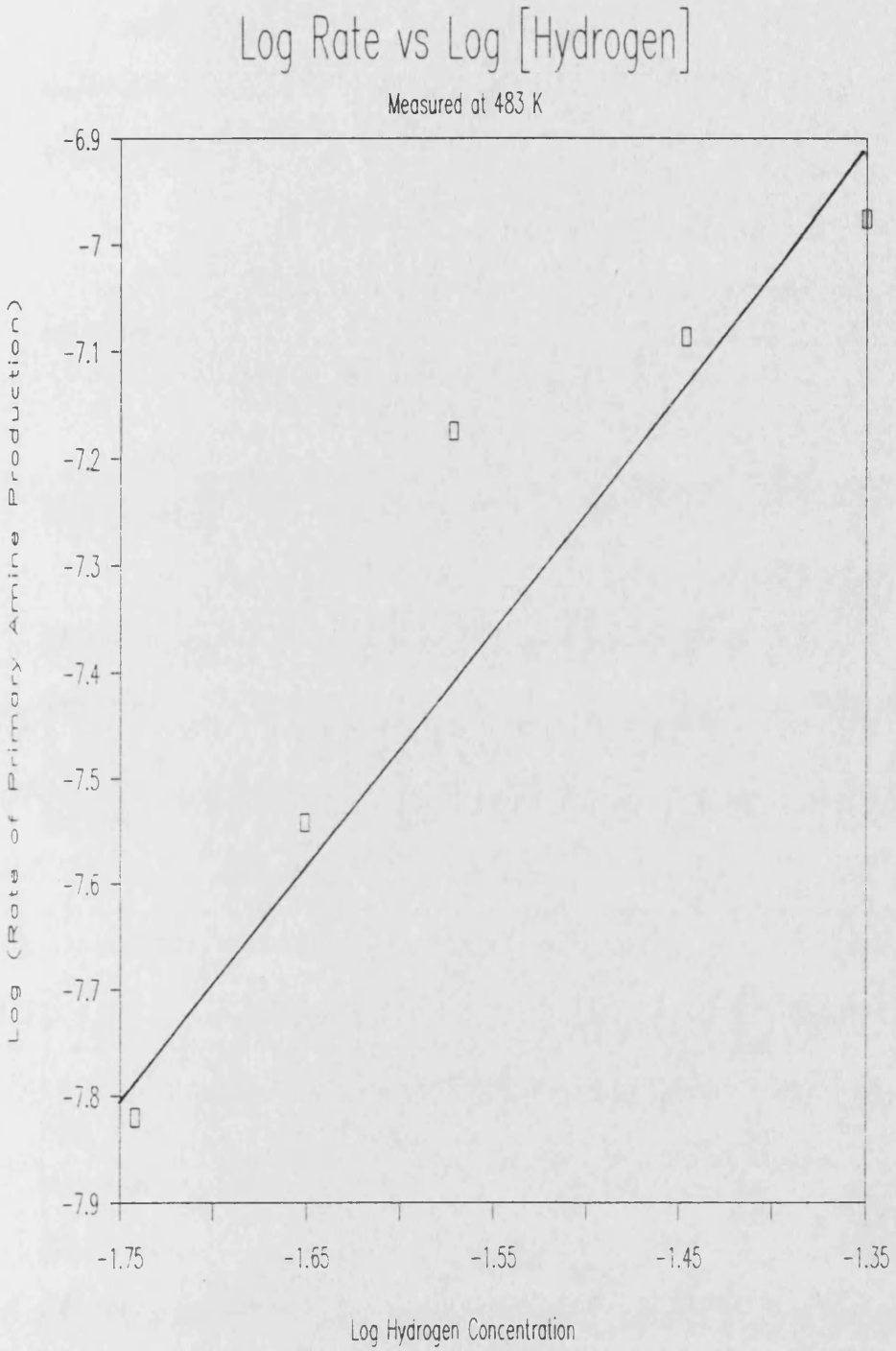

Figure 3.48 Plot of log rate vs log hydrogen concentration for catalyst HT1

At a later stage hexanenitrile and dodecanenitrile were hydrogenated in order to test the effect of the hydrocarbon chain length had on the rate of reaction.

3.7.2.1. Analysis of the Products from the Hydrogenation of Propanenitrile

The GC was calibrated using the operating conditions described in Section 2.9.1.2.

The response factors were calculated from the injection of a standard of known composition. Response factors were calculated for the reactant nitrile and for the primary, secondary, and tertiary amines. The values obtained are given in Table 3.16.

3.7.2.2. Propanenitrile Hydrogenation

All the catalysts prepared in this study were tested in the autoclave reactor, along with a commercial catalyst used for the hydrogenation of ADN. The reaction conditions used for the work were; an initial hydrogen pressure of approximately 420 psig (29 bar), and a reaction temperature of 473 ±5 K.

The procedure was to fill the reactor with hydrogen (200 psig) at ambient temperature. Heating was then commenced and there was an initial increase in the pressure within the reactor due to thermal expansion of the gas, giving a maximum in pressure of approximately 420 psig. The reaction was monitored by noting the fall in hydrogen pressure over a period

Table 3.16 Response factors obtained from the calibration of the GC.

Reaction:	Propanenitrile Hydrogenation
Internal Standard:	N-Propanol
Component	Response Factor
Propanenitrile	1.0055121
N-Propylamine	0.9878313
Di-N-propylamine	0.7772166
Tri-N-propylamine	0.7253016
Reaction:	Hexanenitrile Hydrogenation
Internal Standard:	N-Propanol
Component	Response Factor
Hexanenitrile	0.6547013
N-Hexylamine	0.7004736
Di-N-hexylamine	0.6876987
Tri-N-hexylamine	0.6902533
Reaction:	Dodecanenitrile Hydrogenation
Internal Standard:	Hexanenitrile
Component	Response Factor
Dodecanenitrile	1.0213722
N-Dodecylamine	1.1276627

of up to 20 hours. The reaction was observed to be exothermic resulting in a rise in temperature of approximately 10 K.

The hydrogen uptake curve for catalyst OH20 in the period upto 400 minutes of reaction is shown in Figure 3.49 and is typical of those observed for other catalysts. The rate of reaction was obtained by drawing a tangent to the uptake curve in the pressure region 360-340 psig. The observed hydrogen uptake rates for the catalysts are given in Table 3.17

As indicated above, he hydrogenations were allowed to proceed for approximately. 1200 minutes, after which the product was analysed using GC and the product distribution determined. Results are shown in Table 3.18). It was only possible to charge sufficient hydrogen to the reactor to obtain 50 % reduction of the nitrile. Analysis of the product from the autoclave resulted in the detection of a number of "unknown" products. The two most abundant had retention times of 8.8 mins and 31.2 mins on the GC column. Analysis using GC/MS indicated that these were 1-(n-propylamino)propene $(CH_3CH_2CH_2)NH(CH{=}CHCH_3)$ and 1-(n,n-dipropylamino)propene $(CH_3CH_2CH_2)_2N(CH{=}CHCH_3)$

An attempt was made to analyse the gas phase within the reactor, in order that it might be possible to determine whether any hydrogenolysis of the nitrile had occurred. This was achieved by using a gas syringe to withdraw 100 ml of the gas from the vent line when the reactor had been cooled at the end of the reaction. The gas was then analysed using a GC system designed to analyse low molecular weight hydrocarbons. The result from the reactions using catalysts OH10 and OH30

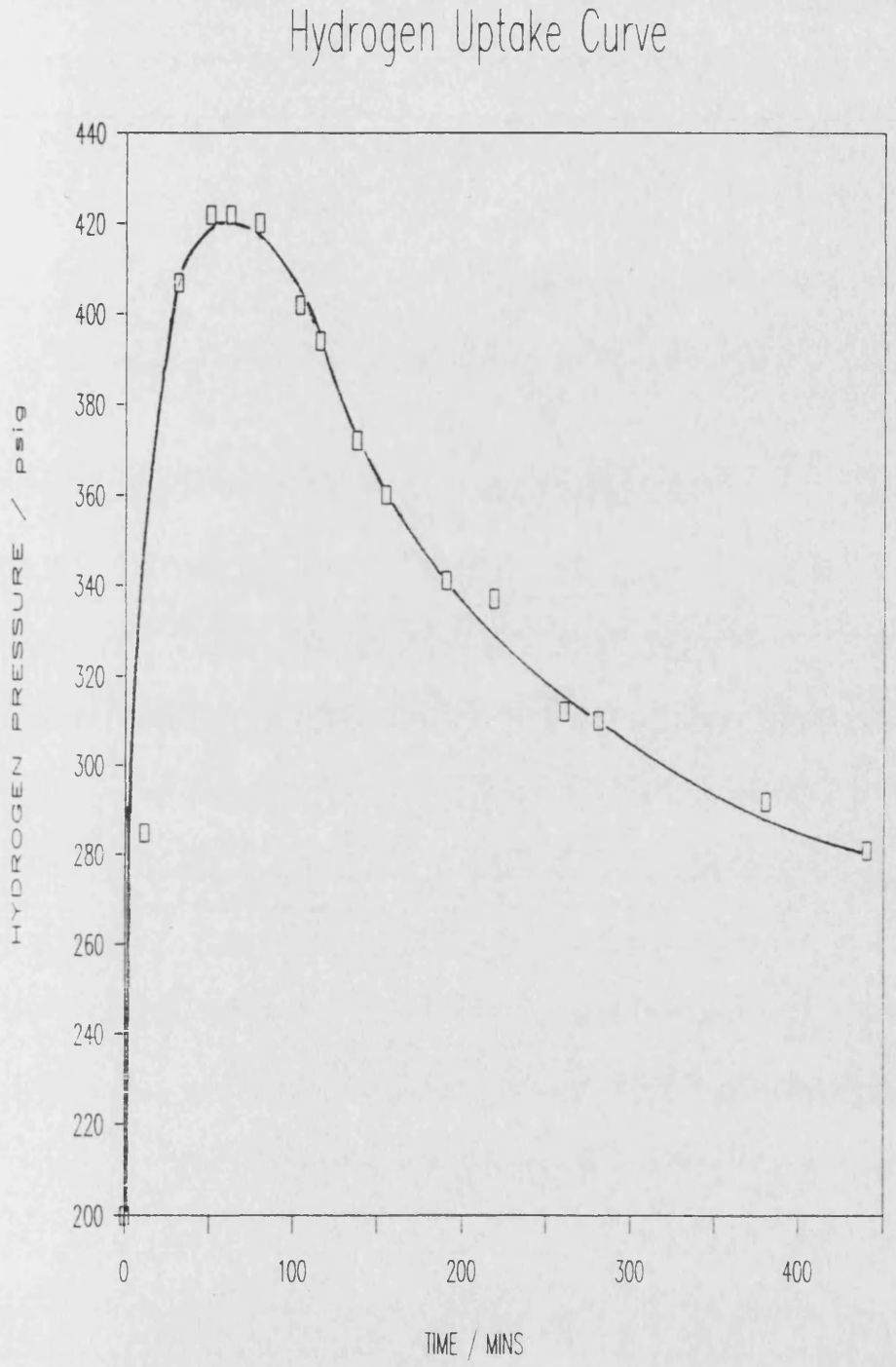

Figure 3.49 Hydrogen uptake curve fot the hydrogenation of propanenitrile using catalyst OH20

of up to 20 hours. The reaction was observed to be exothermic resulting in a rise in temperature of approximately 10 K.

The hydrogen uptake curve for catalyst OH20 in the period upto 400 minutes of reaction is shown in Figure 3.49 and is typical of those observed for other catalysts. The rate of reaction was obtained by drawing a tangent to the uptake curve in the pressure region 360-340 psig. The observed hydrogen uptake rates for the catalysts are given in Table 3.17

As indicated above, he hydrogenations were allowed to proceed for approximately. 1200 minutes, after which the product was analysed using GC and the product distribution determined. Results are shown in Table 3.18). It was only possible to charge sufficient hydrogen to the reactor to obtain 50 % reduction of the nitrile. Analysis of the product from the autoclave resulted in the detection of a number of "unknown" products. The two most abundant had retention times of 8.8 mins and 31.2 mins on the GC column. Analysis using GC/MS indicated that these were 1-(n-propylamino)propene $(CH_3CH_2CH_2)NH(CH{=}CHCH_3)$ and 1-(n,n-dipropylamino)propene $(CH_3CH_2CH_2)_2N(CH{=}CHCH_3)$

An attempt was made to analyse the gas phase within the reactor, in order that it might be possible to determine whether any hydrogenolysis of the nitrile had occurred. This was achieved by using a gas syringe to withdraw 100 ml of the gas from the vent line when the reactor had been cooled at the end of the reaction. The gas was then analysed using a GC system designed to analyse low molecular weight hydrocarbons. The result from the reactions using catalysts OH10 and OH30

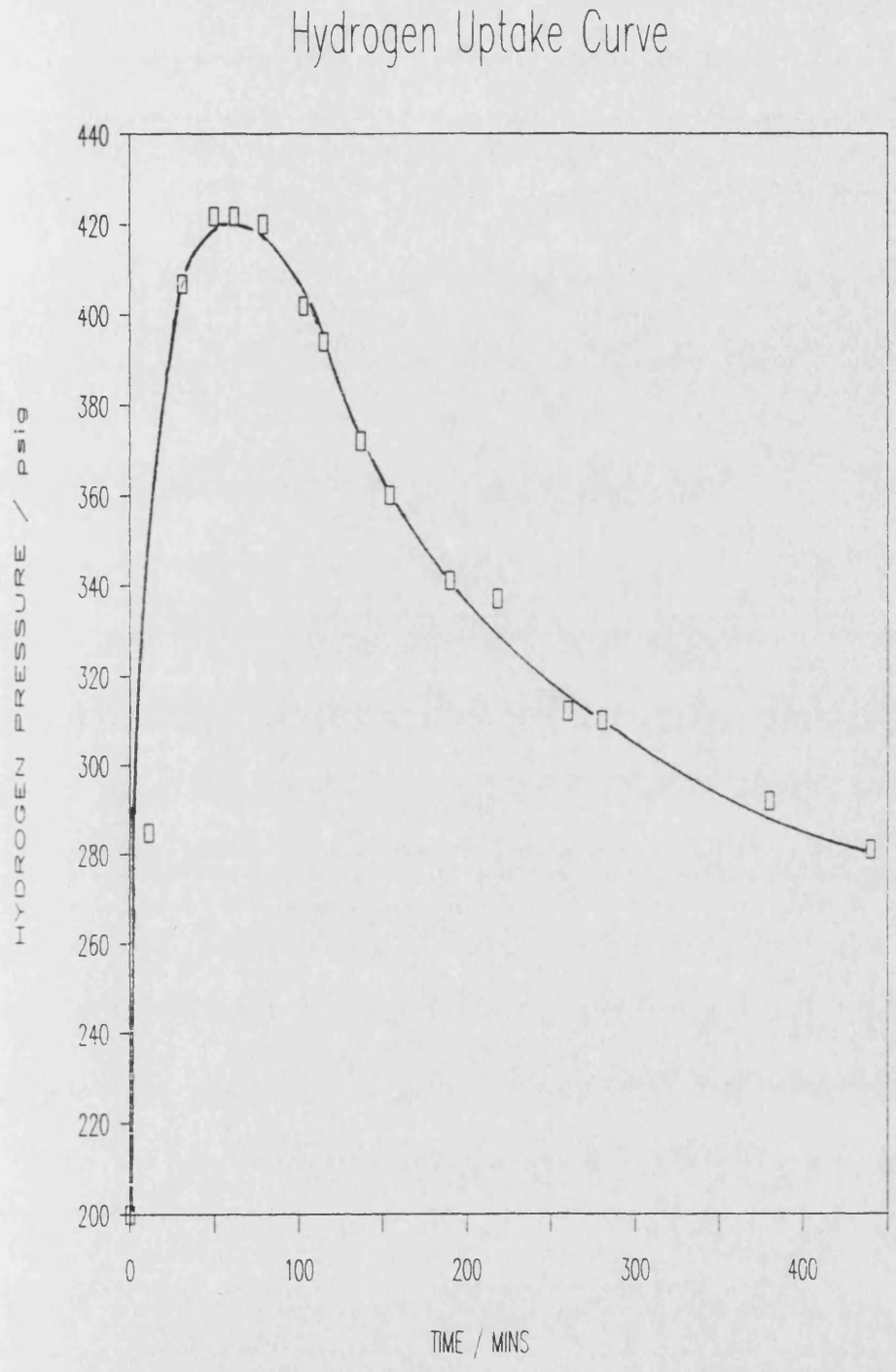

Figure 3.49 Hydrogen uptake curve fot the hydrogenation of propanenitrile using catalyst OH20

Table 3.17 Rates of Propanenitrile Hydrogenation for the Catalysts Tested in the Autoclave Reactor.

Catalyst	Rate of Hydrogen Uptake / psig min^{-1}
CCP5	0.191
CCP10	0.670
CCP20	0.717
CCP30	1.423
OH5	0.455
OH10	3.201
OH20	1.021
OH30	0.651
IP5	0.078
IP10	0.115
IP20	0.155
IP30	0.212
HT1	1.330
Commercial ADN Catalyst	4.577

Table 3.18 Composition of the Products from the Hydrogenation of Propanenitrile in the Autoclave Reactor.

Catalyst	Product Composition %						
	Nitrile	1^{ary} Amine	2^{ary} Amine	3^{ary} Amine	RT 8.8 mins	RT 31.2 mins	Other products
CCP5	88.61	6.73	1.71	0.24	2.43	0.13	0.13
CCP10	77.76	14.75	1.72	0.13	4.93	0.36	0.15
CCP20	85.41	10.04	0.96	0.11	3.17	0.15	0.16
CCP30	50.66	37.47	3.21	0.30	6.70	1.36	0.2
IP5	99.58	0.07	0.11	0.11	0.05	0.05	-
IP10	98.89	0.49	0.22	0.07	0.13	0.10	0.09
IP20	94.9	2.75	0.95	0.08	1.15	0.05	0.11
IP30	91.05	5.04	2.20	0.35	1.35	-	-
OH5	89.74	8.10	0.26	-	1.52	0.18	0.25
OH10	44.05	44.65	1.91	0.03	8.95	-	0.14
OH20	51.92	33.86	2.97	0.02	10.41	0.44	0.16
OH30	56.32	34.80	1.74	0.07	6.38	0.22	0.24
HT1	59.52	34.31	1.02	0.05	4.68	0.12	0.24
Commercial Catalyst	49.44	35.82	7.2	0.63	6.11		
CCP30[b]	86.08	9.14	0.81	0.04	3.74	0.08	0.11

CCP30[b] catalyst ran to low conversion to determine the relationship between conversion and selectivity

indicated that hydrogenolysis accounted for ≈2% of the reacted nitrile. The composition of the gas is given in Table 3.19

3.7.2.4 Hexanenitrile and Dodecanenitrile Hydrogenation

Hexanenitrile and dodecanenitrile were hydrogenated using catalyst CCP30. The reaction conditions used were identical to those used for the hydrogenation of propanenitrile.

The hydrogenation of hexanenitrile and dodecanenitrile resulted in a more exothermic reaction than that observed with propanenitrile. The temperatures with hexanenitrile and dodecanenitrile rose from 473 K to 511 K and 519 K respectively, compared with a rise of only 10 K for propanenitrile. Analysis of the products from the hydrogenation of the higher molecular weight nitriles gave the results shown in Table 3.20

The hydrogen uptake curves are shown in Fig 3.50 where results for propanenitrile with CCP30 are also shown. The rate of hydrogenation of the two heavy nitriles are largely independent of the length of the hydrocarbon chain. The propanenitrile curve exhibits a higher maximum and a more rapid uptake of hydrogen up to 200 min. This is probably due to propanenitrile having a higher vapour pressure than the other two nitriles at the reaction temperature.

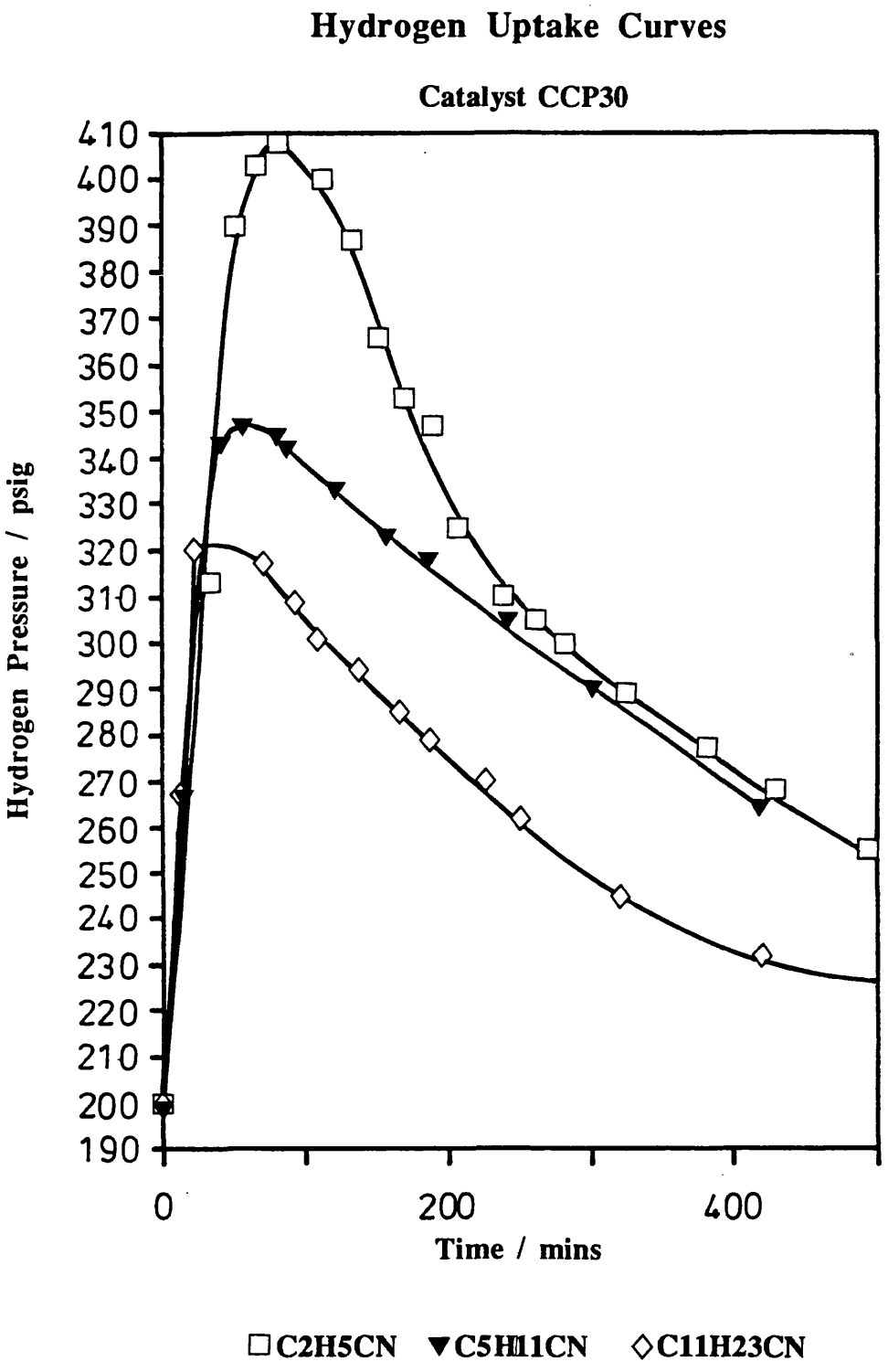

Figure 3.50 Hydrogen uptake curve for the hydrogenation of C3, C6 and C12 nitriles using catalyst CCP30

Table 3.19 Typical composition of the hydrogenolysis products from propanenitrile hydrogenation

Component	%
Methane	2.4
Ethane	10.1
Ethene	1.1
Propane	51.4
Propene	34.2
Butane	0.6

Table 3.20 The Composition of the Products from the Hydrogenation Hexanenitrile and Dodecanenitrile in the Autoclave Reactor.

Reactant Nitrile	Product Composition %						
	Nitrile	1^{ary} Amine	2^{ary} Amine	3^{ary} Amine	RT 1.49 mins	RT 6.27 mins	RT 19.24 mins
Hexanenitrile	26.47	50.75	4.94	0.68	1.12	0.64	14.58
Dodecanenitrile	38.05	58.49					

From GC/MS the products from the hydrogenation of hexanenitrile not calibrated for were

RT 1.49 mins - Products form the hydrogenolysis of the hexanenitrile, mainly hexane and hexene

RT 6.27 mins - Hexanimine ($CH_3(CH_2)_4CH{=}NH$) and Cyclohexylamine

RT 19.24 mins - 1(N-hexylamino)hexene ($CH_3(CH_2)_5)NH(CH{=}CH(CH_2)_3CH_3$)

Chapter 4

Discussion

"Since the measuring device has been constructed by the observer ... we have to remember that what we observe is not nature in itself but nature exposed to our method of questioning.

W. K. Heisenberg 1901-1976

4.1. Analysis of the Starting Precipitates

4.1.1. Analysis of the Carbonate-Coprecipitated Precipitates

In Fig 3.1, diffractograms D and E refer to precipitates obtained in this way. Comparison with diffractogram A, which is that of magnesium hydroxycarbonate, shows that no peaks other than those associated with the magnesium hydroxycarbonate structure are present. Moreover, the precipitate from the solution containing 30% iron gives a weaker X-ray pattern (E) than that from the solution containing 5% iron (D). This further confirms that the peaks observed in D and E are not due to a separate iron containing phase. This implies that the iron must either be present as an amorphous phase or as some crystalline phase with very small particles which would make them undetectable by X-ray diffraction.

The magnesium appears to be in the form of magnesium carbonate hydroxide hydrate (hydromagnesite) $Mg_5(CO_3)_4(OH)_2.4H_2O$ although the presence of dypingite $Mg_5(CO_3)_4(OH)_2.5H_2O$ and magnesium carbonate hydrate cannot be excluded. A comparison of the diffractograms of the materials produced via this method with those of impregnated magnesium hydroxycarbonate (diffractograms B and C in Fig. 3.1) indicates that the materials are very similar

4.1.2. Analysis of the Hydroxide-Coprecipitated Precipitates

The diffractograms (Fig. 3.2) indicate that the iron is present as the iron hydrotalcite, pyroaurite $Mg_6Fe_2CO_3(OH)_{16}.4H_2O$. Compounds of this type were first produced synthetically by Feitknecht (113) and are often referred to as Feitknecht compounds. The excess magnesium present in the materials of lower iron loading takes the form of brucite $Mg(OH)_2$. As the iron content of the precipitate increases so the intensities of the brucite peaks decrease and the intensities of the pyroaurite peaks increase. The carbonate species probably originate from the absorption of carbon dioxide from the atmosphere.

Pyroaurite, sjögrenite (which has the same formula as pyroaurite) and other related minerals have been discussed by Taylor (114). The structures of both pyroaurite and sjögernite are based on brucite-like layers separated by what can be described as an interlayer; one brucite layer and one interlayer make up an elementary layer. The cation sites in the brucite-like layers are occupied by Mg^{2+} and Fe^{3+} ions. Between adjacent brucite layers are the interlayers, these contain all the CO^{3-} ions and H_2O molecules resulting in (Fig. 3.3). The structure of the two minerals pyroaurite and sjögernite differ only in the way the layers stack; pyroaurite exhibits an 3R-polytype as opposed to the 2H-polytype of sjögernite.

4.1.3. Analysis of the Iron-Impregnated Magnesium Hydroxycarbonate

Comparing the diffractograms of the iron-containing material with that of the starting material (diffractogram A in Fig. 3.1) indicates that the addition of Fe^{3+} ions has not resulted in the loss of the magnesium hydroxycarbonate (MHC) structure. There is a change in the intensity of the peak at $2\theta = 15.35$ compared with that at $2\theta = 29.9$, which may be a result of iron being substituted into the MHC lattice. The diffractograms clearly do not correspond to the formation of a Feitknecht compound, in contrast to the report of Topsøe et al. using this method (3). Kock et al. (28) also observed the preservation of the MHC structure when using this method of preparation. The explanation proposed by Kock et al. (28) was that the reactivity of the original MHC support material was low and hence insufficient Mg^{2+} ions were available to form a pyroaurite structure with the Fe^{3+} ions.

4.2 Analysis of the Catalyst Precursors

The diffractograms contained in Figure 3.4 confirm that both the iron and magnesium are present in their oxidised forms in all the precursors. The interesting feature is that the catalyst precursors which originated from a hydrotalcite type structure form on calcination iron in the form of γ-Fe_2O_3, whereas the precursors owing their origin to carbonate coprecipitation or impregnation contain iron in the form of

α-Fe_2O_3. The two forms of the oxide can easily be distinguished from their X-ray diffraction patterns, the presence of α-Fe_2O_3 is characterised by reflections at 2θ values 33° and 24°.

4.3. Reduction of the Catalyst Precursors

In order to understand the problems in reducing iron catalysts it is important to consider the equilibria between Fe_2O_3, Fe_3O_4, FeO and metallic iron. This has been treated by Kock et al. (38). Reduction of Fe_2O_3 to Fe_3O_4 proceeds at a ratio of partial pressures of water and hydrogen of about 10^5, while reduction to metallic iron calls for ratios of 10^{-5} at 300 K to about 0.01 at about 500 K. The ratios indicate that reduction to magnetite can proceed at high water vapour pressures, whereas for the reduction to metallic iron low vapour pressures are required.

Scholten (115), working on promoted ammonia synthesis catalysts has shown that transport of water vapour from the reduction interface to the gas phase can limit the extent of reduction. Since many supported catalysts contain an appreciable pore volume containing often narrow pores, transport of water out of the porous system will proceed slowly. Dalmon (116) made a comparison of the reduction of unsupported iron oxides and magnesia-supported iron oxide catalysts, and his results confirmed that the unsupported system reduced much more rapidly than the magnesia supported catalysts.

The work of Scholten (115) and Dalmon (116) both indicate

that the pore structure of the catalyst is important in governing the reduction of the iron species present. The values obtained for the extent of reduction of the catalysts in this work confirm further that the extent of reduction is to a large extent governed by the pore structure of the catalysts. From the pore size distributions of the catalysts depicted by the bar charts in Figures(3.6-3.12) it is apparent that the catalysts which yield higher extents of reduction tend to have a greater proportion of larger diameter pores. This is because the removal of water vapour is more difficult from narrow pores. Hence it can be concluded that the low rate of reduction for this type of catalyst is determined mainly by the transport of water vapour out of the catalyst particles.

4.4. Analysis of the Catalysts

4.4.1. Nitrogen Adsorption at 77 K

As discussed in Section 2.3.1 it is more common to use the desorption branch of nitrogen isotherms to calculate pore size distributions. In fact all investigators prior to Cranston and Inkley (117) used the desorption branches of nitrogen isotherms for pore structure analysis. They offered as the main criterion of the correctness of their analysis the agreement between the cumulative surface area of the pore walls and the BET surface area. Cranston and Inkley, however, used both the adsorption and desorption branches in their analysis, and found that for most of their adsorbents the adsorption branch gave a

cumulative surface area in better agreement with the BET surface area. This was confirmed by Mikhail et al. (118), who also found their adsorbents contained a large fraction of ink-bottle pores, i.e. pores with a narrow entrance and a wider body.

The better agreement between adsorption branch data and BET-derived areas for the catalysts studied in this work, provided the justification for using the adsorption branch to calculate pore size distributions. This may be taken to indicate that the catalysts contain a significant proportion of ink-bottle type pores.

4.4.2. Determination of Metallic Iron surface Areas and Crystallite sizes

The variation of metallic iron area with respect to iron loading as determined by CO chemisorption is shown in Figure 4.1. The results indicate that the iron area of the catalyst is increased by increasing the iron loading in the range 5 - 30 mol%.

Catalysts originating from the pyroaurite structure , namely OH5 - OH30 and HT1, attain higher iron surface areas than those derived from the impregnation of magnesium carbonate or coprecipitation using ammonium carbonate. However in the catalysts derived from the pyroaurite structure increasing the iron loading in excess of 20 % appears to have a detrimental effect. This may be a result of the pyroaurite structure having a Fe:Mg ratio of 1:3 (i.e. 25 % loading), adding iron in excess

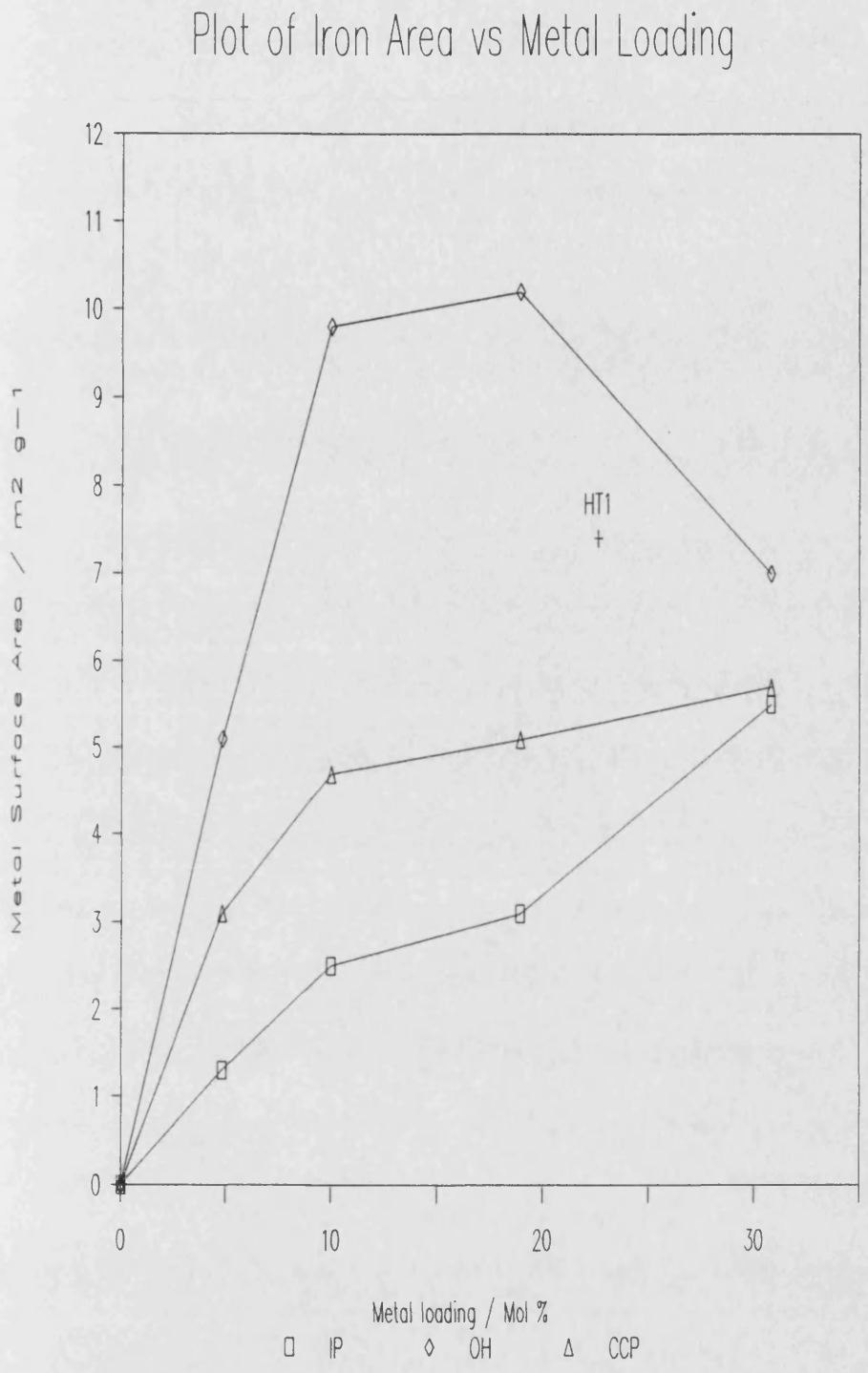

Figure 4.1 Variation of Fe^{0} surface area with iron loading

of this ratio results in the partial loss of this structure. This can be seen in Figure 3.2 as a reduction in intensity of the peaks attributable to pyroaurite in diffractogram E compared to D. From the diffractogram it is not possible to determine what form this additional iron takes although it does appear to result in the formation of larger iron crystallites in the reduced catalyst.

Catalysts produced by the method described by Boudart et al. (2) (IP5 - IP30) were observed to adsorb less CO than those reported by those authors. The discrepancy being greater for catalysts with lower loadings. However the catalysts derived from material prepared by coprecipitation using ammonium hydroxide do exhibit similar CO uptakes over the whole range of loadings to those reported by Boudart et al (2). Comparing catalysts with similar iron contents it can be seen that OH30 and a 40 wt % catalyst prepared by the above authors exhibit CO uptakes of 71.5 and 67 μmol g^{-1} respectively, while catalysts OH5 and a 4.9 wt % exhibited CO uptakes of 50 μmol g^{-1} and 41 μmol g^{-1} respectively.

The use of nitrous oxide decomposition to obtain metallic iron surface areas depends on assumptions as to the depth of oxidation of the iron by the nitrous oxide at 293 K. This is a matter of some uncertainty. The value of 2.5 used in this work gave iron areas which were closely comparable with those obtained from CO chemisorption. Vogler et al.(90) advocated a N_2O : Fe stoichiometry of 4 using a nitrous oxide pressure of 280 Torr compared to a pressure of 20 Torr in this study. The discrepancy may be a result of the depth of oxidation being

pressure dependent. Despite this uncertainty nitrous oxide remains a good probe for the determination of metallic iron areas and for comparisons between catalysts. The main advantage of the N_2O decomposition technique is that it is practically much less demanding than the determination of CO adsorption isotherms. CO chemisorption has the parallel disadvantage that one has to assume a particular stoichiometry for the chemisorption, an Fe:CO ratio of 2:1 was assumed for the data reported in this study. This implies that all the CO is bridge bonded to the iron. Indeed this is not the case as is evident from absorption bands between 2020-2010 cm^{-1} in the infrared spectrum of CO adsorbed on a reduced iron catalyst (Figure 3.23). Further more, any CO Chemisorbed on unreduced iron (e.g. Fe^{2+}) is unlikely to be removed by pumping at 195 K. Supported iron catalysts reduced in H_2 contain a significant proportion of Fe^{2+}, as shown by the Mössbauer results in Section 3.5. Thus the determination of metallic iron surface areas by either N_2O decomposition or CO chemisorption will be subject to uncertainty.

Metallic iron surface areas obtained from X-ray line broadening are significantly lower than those obtained via chemisorption techniques for catalysts with low iron loadings. However the agreement between the techniques improves as the iron loading is increased, reasonable agreement being achieved for catalysts with a 30 % loading. The observed trend is what might have been predicted from the results in Section 3.4.3. These show that the average size of the iron crystallites obtained by chemisorption for 5 % loaded catalysts are in the

region of 4 nm in diameter. This is an average value and hence a substantial portion of the crystallites will be smaller than 3 nm in diameter. This is significant as crystallites smaller than 3 nm in diameter will not be detected by X-rays and hence will not contribute to the line broadening. As the iron loading is increased the portion of iron crystallites which are not detected by the X-rays decreases and hence the surface areas obtained from X-ray line broadening and chemisorption are in better agreement for catalyst with higher loadings. This is borne out by catalysts with low loadings not producing a discernable diffraction pattern due to metallic iron. The surface areas obtained from either CO chemisorption or N_2O decomposition are always likely to be higher than the corresponding result from X-ray line broadening due to adsorption of CO on Fe^{2+} sites, in the case of N_2O decomposition the depth of oxidation may slightly exceed the assumed value and this would also produce iron surface areas which were artificially high.

The above arguments also explain the results in Table 3.11 as to why iron crystallites sizes calculated from chemisorption data differ from those obtained from X-ray line broadening.

4.5. Mössbauer Spectroscopy

The Mössbauer results from the catalyst precursor CCP30 are in agreement with the X.R.D. patterns obtained (Section 3.2), showing that the precursor consists of α-Fe_2O_3 particles

on MgO. The α-Fe_2O_3 particles exhibit a magnetically split six line spectrum as was observed by Graham et al. (92) for a sample of unsupported haematite. This is an unusual observation as supported iron catalysts usually exhibit a two line spectrum similar to that exhibited by the 1 % Fe/MgO precursor in this study. The origin of this two-line spectrum is paramagnetic or superparamagnetic Fe^{3+} (2). According to Kundig et al.(119) a two-line spectrum is observed from α-Fe_2O_3 when the particle size is less than 130 Å and a magnetically split six-line spectrum when the particle size is greater. On this basis, it can be concluded that the majority of the iron oxide particles present in the precursor CCP30 have a size in excess of 130 Å

Care should be taken when examining the Mössbauer spectra of catalyst precursors of this type, since hydroxide precipitated material may contain γ-FeOOH, as observed by Dutartre et al. (34). γ-FeOOH exhibits a two-line spectrum which is only magnetically split at 4.2 K (120). However, there was no evidence for this in CCP30 precursor.

Reduction of the precursor CCP30 resulted first in the formation of magnetite (Fe_3O_4), which exhibits two superimposed six-line spectra. Two six-line spectra are produced because in magnetite sites of tetrahedral coordination are occupied by Fe^{3+} cations and sites of octahedral coordination by equal numbers of Fe^{3+} and Fe^{2+}ions. The first six-line pattern is due to Fe^{3+} occupying tetrahedral sites. The second is due to Fe^{3+} and Fe^{2+} occupying octahedral sites. These ions do not exhibit separate spectra because of the rapid electronic exchange occurring between these ions, and the observed spectrum is thus

an average of those expected for the two ion species.

The formation of Fe_3O_4 in the reduction sequence of supported iron catalysts is interesting. The reduction behaviour of small iron oxide particles observed by other authors (2,3,93) show no sign of the formation of a magnetite phase. The spectra indicate that Fe^{2+} and α-Fe are the only products of reduction. Results obtained from the reduction of a 1 % Fe/MgO catalyst in this study also confirm the absence of an Fe_3O_4 phase in the reduction sequence of small supported Fe^{3+}-containing particles. Counter-evidence to this, however has been supplied by Wielers et al. (22), who studied a 25 % Fe/Al_2O_3 catalyst. They identified a two-line spectrum in the precursor at 300 K as being due to small particles of α-FeOOH. It should be recalled that large-particle α-FeOOH exhibits a six-line spectrum at 300 K (120). On reduction of their precursor Wielers et al. (22) observed the presence of Fe_3O_4 prior to the formation of a Fe^{2+} doublet. Hence there is a precedent for formation of Fe_3O_4 in the present work on CCP30.

The fate of the spinel $MgFe_2O_4$ on reduction is a matter of some controversy, The present work, along with that of Topsøe et al. (3) shows no sign of the $MgFe_2O_4$ in the reduced catalyst. Connell and Dumesic (87) on the other hand, attribute a doublet present in the Mössbauer spectrum obtained after reduction of 0.8% Fe/MgO sample in H_2 at 723 K to Fe^{3+}. They concluded that the large amount of Fe^{3+} that remains after reduction is indicative of the formation of magnesium ferrite. They consider that the formation of this phase renders the Fe^{3+} inert to gas phase reduction. A possible explanation for the

discrepancy in the observations is that Connell and Dumesic (87) ascribe a two-line spectrum to $MgFe_2O_4$. This implies that it is present as small superparamagnetic particles. The observation of a six line spectrum in this study and in that of Topsøe et al.(3) indicates the $MgFe_2O_4$ to be present as larger particles.

Mössbauer spectroscopy has been used to study the reduction of unsupported haematite by Graham et al.(92). The spectra recorded at ambient temperature showed no sign of wustite, FeO, although it has been shown that the reduction of hematite proceeds in a stepwise manner (38):

$$\underset{\text{hematite}}{\alpha\text{-}Fe_2O_3} \longrightarrow \underset{\text{magnetite}}{Fe_3O_4} \longrightarrow \underset{\text{wustite}}{FeO} \longrightarrow \underset{\text{iron}}{\alpha\text{-}Fe}$$

The reason is that wustite is thermodynamically metastable with respect to magnetite and iron at temperatures below 843 K. Hence in low temperature reductions of unsupported α-Fe_2O_3, FeO is not observed. As can be seen from the Mössbauer spectra of both the 1 and 30 % MgO-supported Fe_2O_3, there is clear evidence on reduction for the formation of a Fe^{2+} species. The Fe^{2+} spectral contribution fitted to a single two-line spectrum for the CCP30 sample, as is the more conventional approach . The Fe^{2+} spectral contribution for the 1 % Fe/MgO catalyst fitted better to two doublets, which is in line with the work of Connell and Dumesic (86). The doublet with the smaller isomer shift and quadrupole splitting is termed the inner doublet and has been assigned to Fe^{2+} cations in sites of low coordination. The doublet with the larger isomer shift and quadrupole splitting is termed the outer doublet and assigned

to Fe^{2+} cations in sites of higher coordination. In theory, extending the reduction period should increase the proportional contribution of the outer doublet due to increased migration of Fe^{2+} to form large clusters (2,3). The Mössbauer results do indicate this but the validity of the observation may be questioned in view of the difficulties involved in fitting such complex spectra.

The Mössbauer results show that the treatment of the sample with nitrous oxide results only in a surface oxidation. The α-Fe component is equally as large in the reduced sample as in that obtained after treatment with N_2O. However, heating in oxygen at 573 K resulted in a product which exhibited a Mössbauer spectrum identical to that of the original precursor, confirming that complete oxidation could be obtained under these conditions.

The conclusions to be drawn from the Mössbauer study are that there appear to be two pathways for the reduction of Fe^{3+} supported on MgO and Al_2O_3. Large particles(> 130 Å) appear to be reduced by the following mechanism:

$$\underset{\text{hematite}}{\alpha\text{-}Fe_2O_3} \longrightarrow \underset{\text{magnetite}}{Fe_3O_4} \longrightarrow \underset{\text{wustite}}{FeO} \longrightarrow \underset{\text{iron}}{\alpha\text{-}Fe}$$

Whereas small Fe^{3+} particles appear to reduce so as not to make Fe_3O_4 evident:

$$\underset{\text{hematite}}{\alpha\text{-}Fe_2O_3} \longrightarrow \underset{\text{wustite}}{FeO} \longrightarrow \underset{\text{iron}}{\alpha\text{-}Fe}$$

It is interesting that silica supported catalysts do not stabilise a FeO phase, instead a iron (II) silicate phase is formed (22).

4.6. Infrared Spectroscopy

4.6.1. Carbon Monoxide Chemisorption

4.6.1.1. The Adsorption of CO on MgO

The adsorption of CO on MgO has been the topic of a number of infrared studies (121-124), amongst the most detailed of these is that of Guglielminotti et al. (124). However, the spectra produced in this study are somewhat different from those produced by Guglielminoti et al., the differences are attributable to the different sample pretreatments. Guglielminotti et al used a high outgassing temperature (1073 K), under these conditions the MgO surface is devoid of any surface hydroxyl groups. In this study a lower outgassing temperature of 693 K results in the MgO sample still containing a substantial proportion of surface hydroxyl species, the result is that the polymeric species observed by Guglielminotti are not observed. The spectra produced in this study resemble more those of Smart et al. (121) and Davydov (122), who only observe the formation of carbonate-like species.

The bands shown in Figure 3.22 can be assigned as follows;

the bands situated at 1520 $cm^{-1}$and 1370 cm^{-1} are respectively due to the asymmetric and symmetrical stretching in the unidentate carbonate

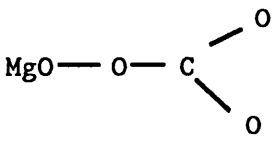

the bands situated at 1657 cm^{-1} and 1313 cm^{-1} are respectively attributable to the C=O stretching frequency and the COO asymmetric stretching of the bidentate carbonate

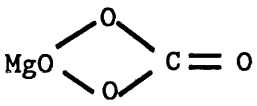

the band at 1468 cm^{-1} is likely to be from the formation of the simple carbonate $MgCO_3$ which exhibits bands at 1450, 1010, 890 and 750 cm^{-1} (125). The origin of the band at 1607 cm^{-1} is not clear possible explanations may be that it is the C=O stretching frequency from a bridge bonded carbonate species. Another plausible explanation is that it is the result of a second bidentate carbonate species, Smart et al (121) have observed two forms of bidentate carbonate on the adsorption of CO on MgO but the C=O stretching frequency observed by these authors was higher than 1607 cm^{-1}

The results show that the adsorption of CO on a sample of MgO which had been previously outgassed at 693 K results in the formation of surface carbonates. These appear to be both of the simple carbonate type with a structure similar to $MgCO_3$ and also of the bidentate type with a structure similar to $MgC_2O_4.2H_2O$.

4.6.1.2. Adsorption of CO on 5% Fe/MgO

A weakening of the C-O bond is observed when CO is

chemisorbed on transition metals as seen by an absorption band at lower wavenumber than that of gaseous CO. When CO is adsorbed on transition metal ions the C-O bond is strengthened as seen by an absorption band at higher wavenumber compared to the gaseous CO. These observations have been explained by the model proposed by Blyholder (88) and has been dealt with in Section 2.8.1.2.

The results of some other workers on the adsorption of CO on iron and iron containing catalysts are summarised in Table 4.1. The results indicate that bands assignable to the adsorption of CO on Fe^0 are found in the region 2020 - 1860 cm^{-1}. Blyholder (126) suggested that different absorption bands in this region can arise from basically the same structure e.g. linear Fe-C-O. This interpretation has now been discarded in favour of that of Nguyen and Sheppard (127) and Eischens (128), in which a band at approximately 2020 cm^{-1} is assigned to linearly bonded CO on Fe^0 and bands in the region 1890 arise from bridge bonded species of the form 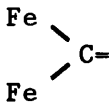 .

The bands observed in this study between 2020 cm^{-1} and 2010 can confidently be assigned to CO which is linearly bonded to Fe^0, likewise the absorption band observed at 1889 cm^{-1} can be assigned to CO bridge bonded to Fe^0.The band observed at 1820 cm^{-1} which is prominent in the low temperature study but appears as only a shoulder in the room temperature study has not been previously reported for iron although bands in this region have been reported when CO is adsorbed on Ni (127) and Co (127).

Table 4.1 Summary of the Positions of Absorption Bands Previously Observed by Other Worker for CO Adsorbed on Iron Catalysts

Catalyst	Fe^{3+}	Fe^{2+}	Fe^{0}	REF	Comments
Fe/SiO_2			1960 cm^{-1} 2020 cm^{-1}	128	Weak band at 2020 cm^{-1} thought to be iron carbonyl or weakly chemisorbed linear CO
10 % Fe/SiO_2			2020 cm^{-1} 1960 cm^{-1} 1886 cm^{-1}	126	1960, 2020 cm^{-1} linear Fe=C=O 1886 cm^{-1} Bridge structure
Unsupported Fe			1950		linear Fe=C=O
5% Fe/MgO	2150 cm^{-1}	2070 cm^{-1}	2020 cm^{-1} 1965 cm^{-1}	99	Band at 2020 cm^{-1} due to CO on small Fe^0 clusters
Fe			1960 cm^{-1}		
FeO		2100 cm^{-1}			
Fe_2O_3	2175 cm^{-1}				
9% Fe/SiO_2			1970 cm^{-1} 2020 cm^{-1} 2040 cm^{-1}	100	2020, 2040 cm^{-1} bands due to linear CO, band at 2040 cm^{-1} from bonding to sites with a larger iron coordination number
5% Fe/SiO_2			1880 cm^{-1}		
Fe/Al_2O_3		2150 cm^{-1}	2030-2050 cm^{-1}	22	Fe^{2+} band removed by evacuation

Changes in intensity of absorption bands in the region 1950 - 1900 cm^{-1} have also been observed by Topsøe et al. (35). They showed that there was an increase in the intensity of the absorption above 1890 cm^{-1} when the iron particle size was reduced from 12.8 nm progressively to 1 nm. A similar variation of intensity is observed in this study when comparing the spectra in Figure 3.23 with those in Figures 3.24 and 3.25. The difference in this study however is not a difference in iron particle size but in surface hydrogen concentration, the spectra in Figures 3.24 and 3.25 are produced from the adsorption of CO on a system which will have a considerably greater surface hydrogen coverage. Therefore it would seem that the amount of hydrogen is at least an equally critical factor in determining the intensity of the absorption bands in this region and not necessarily the particle size directly.

Topsøe et al. (35) also conclude that hydrogen adsorption on small iron particles is an activated process. Although no experimental procedure as to catalyst treatment prior to CO adsorption is stated by Topsøe et al. (35) it would seem plausible that the catalyst containing the smaller iron particles will retain a higher coverage of hydrogen on the surface than those catalysts with larger iron particles.

The absorption band observed in the region 1855 cm^{-1} may arise from an adsorbed species in which the CO is partially dissociated. Kishi and Roberts (129) have shown that CO adsorbed on polycrystalline iron films is adsorbed both molecularly and dissociatively at 295 K. The intensity of the band at 1855 cm^{-1} appears to be linked with that observed

between 2060 - 2057 cm^{-1}, both bands becoming more prominent on increasing the time that the sample has been exposed to the CO. A band at 2057 cm^{-1} has been observed by Wielers et al. (22) and has been attributed to CO adsorbed on a Fe^0 surface which has some carbon contamination arising from the dissociation of other CO molecules. Hence the link between the absorption at 1855 cm^{-1} and that in the region 2057 - 2060 cm^{-1}.

The band at 2057 cm^{-1} is only pronounced if the sample is cooled to room temperature prior to the evacuation of the hydrogen (Figure 3.24). A possible explanation for this may be that the species responsible for the dissociation of the CO is oxidised by high temperature evacuation. This reoxidation can result from interaction with water molecules formed by condensation of hydroxyl groups from the support $Fe^0 + H_2O \longrightarrow Fe^{2+}O + H_2$ Dutartre et al. (34) concluded that high temperature evacuation of magnesia-supported iron particles resulted in reoxidation of the surface.

As can be seen from Table 4.1 there is some disagreement as to the precise location of the CO stretching frequency of CO adsorbed on Fe^{2+} and Fe^{3+} centres. Values for CO adsorbed on Fe^{2+} vary between 2070 cm^{-1} (99) and a value of 2198 cm^{-1} obtained for an Fe^{2+}-exchanged zeolite (130). The problem arises from the adsorption being weak, resulting in the absorption bands being lost by evacuation at ambient temperature. Unfortunately the low temperature adsorptions performed in the present study do not clarify the situation significantly. Comparing spectrum B Figure 3.27 with the

spectrum in Figure 3.28 it can be seen that by using the less vigorous reducing pretreatment of the sample in Figure 3.28 results in a increased intensity of bands in the 2100 - 2170 cm^{-1}. The frequency of the CO adsorbed on Fe^{2+} sites probably depends upon the extent of oxidation of the iron as the surrounding metallic iron will exhibit large electronic effects. This has already been hinted at by Wielers et al. (22) who attribute a absorption band at 2100 cm^{-1} to an "FeO-like" species which they claim is due to CO adsorbed on metallic iron with a low surface oxygen coverage.

The C-O stretching frequency of CO associated with Fe^{3+} centres is probably in excess of 2200 cm^{-1}. The absorptions at 2203 and 2225 cm^{-1} in Figure 3.27 spectrum A may be a result of the adsorption of CO on Fe^{3+} sites. Bianchi et al. (98) have assigned a band at 2205 cm^{-1} to the adsorption of CO on Fe^{3+}.

4.6.2. The Adsorption of Nitric Oxide

4.6.2.1. The Adsorption of NO on MgO

The band at 1650 cm^{-1} is typical of that produced by a bridge bonded NO_3^- group 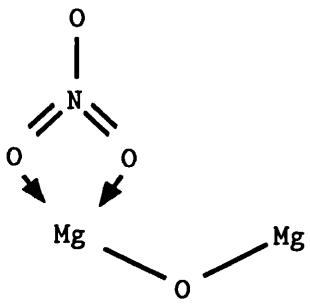

. This has been previously reported by Parkyns to be produced by the adsorption of NO_2 on alumina (131), but this author did not observe bands

in this region when NO was adsorbed. There is some disagreement in the literature as Terenin and Roev (132) have observed a band in the 1660 cm^{-1} region when NO was adsorbed on alumina and other oxides. Rethwisch and Dumesic (133) have also observed a band at 1620 cm^{-1} when NO is adsorbed on a 1% Fe/MgO catalyst, they assign this band to a nitrate band on MgO. The possibility of this band occurring as a result of contamination of the NO appears unlikely as there is no evidence for a band at 1610 cm^{-1} which is characteristic of gaseous NO_2. A possible explanation for the production of this band may be that it is formed from an NO_2^- ion. The formation of a surface NO_2^- species has been previously reported when NO is adsorbed on MgO (109).

There also exists the possibility of covalently bonded nitrato species which may bond to form in such a manner so as to form either a bidentate or monodentate species on the surface. The formation of species of this type has been observed when NO is adsorbed on CaO (134). In line with the assignment of Low and Yang (134) the absorption bands at 1539 and 1310 cm^{-1} may be assigned to a covalent bidentate species, such as that shown 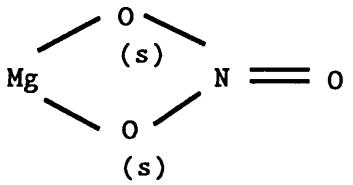 . The shoulder at 1422 cm^{-1} and the absorption band at 1357 cm^{-1} are likely to be due to the monodentate species of the type 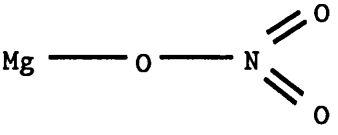 .

The adsorption of NO on highly outgassed MgO has been the

topic of an in depth study by Cerruti et al. (109), in which a complex series of absorption bands were observed due to the formation of the ionic species NO_2^-, NO^- and $N_2O_2^-$ ions. The strong adsorption observed at 1220 cm^{-1} (Figure 3.29) may be attributed to the NO_2^- surface species with the following adsorption geometry 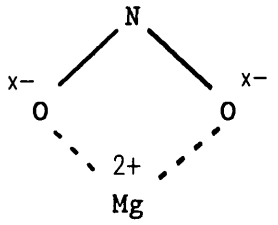

. Cerruti et al. (109) suggested two species of this type existed which they found to be spectroscopically distinguishable. The two species differed only in that different co-ordination sites were involved. They recorded adsorption bands at 1208,1168 and 850 $cm^{-1}$for one species and absorption bands at 1222,1190 and 850 cm^{-1} for the other. Clearly the broad band observed at 1220 cm^{-1} observed in this work may be assigned to these species. Cerruti et al. (109) also suggested the formation of species of the type

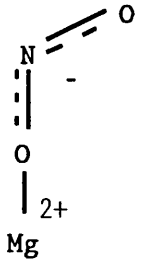

Characterised by a band pair at 1416 and 1145 cm^{-1} and a pair at 1404 and 1120 cm^{-1}. One of the N-O bonds is assigned greater double bond character to explain the higher wave number of one of the bands.

The $N_2O_2^-$ species was characterised by bands at 1384, 1190,1150 and 830 cm^{-1} and a NO^- surface species coordinated to a Mg^{2+} ion by a band at 1160 cm^{-1}. The spectra obtained in this work (Figure 3.29) indicates that all of these species may be

present to some extent.

The following mechanisms were proposed by Cerruti et al. (109) for the formation of these ionic species. The first suggests as the initial step the formation of a paramagnetic species reported by Lunsford (135)

$$NO_{(g)} + O^{2-} \longrightarrow NO_2^{2-} \quad (1)$$

Then

$$NO_{(g)} + NO_2^{2-} \longrightarrow NO_2^- + NO^- \quad (2)$$

or

$$2NO_2^{2-} \longrightarrow NO_2^- + NO^- + O^{2-} \quad (3)$$

Reactions 2 and 3 are followed by the dimerisation of NO^-:

$$2\ NO^- \rightleftharpoons N_2O_2^{2-} \quad (4)$$

The second mechanism proposed is based on the observation made by Tench and Nelson (136) that molecules with electron affinities greater than 0.5 eV are able to extract electrons from about 0,5 % of the surface O^{2-} ions of MgO. Seshadri and Petrakis (137) confirm this point of view and underline that the same process can occur even on incompletely dehydrated surfaces

$$NO_{(g)} + O^{2-} \rightleftharpoons NO^- + O^- \quad (5a)$$

$$NO_{(g)} + O^- \rightleftharpoons NO_2^- \quad (5b)$$

followed by reaction (4).

The former of the two mechanisms seems to be the more likely, especially in view of the low electron affinity of NO (24 meV) (138).

The presence of N_2O in the gas phase may well originate from the surface reaction

$$N_2O_2^{2-} \longrightarrow N_2O_{(g)} + O^{2-} \quad (6)$$

4.6.2.2. The Adsorption of NO on 5% Fe/MgO

A very interesting feature of the spectrum produced from the adsorption of NO on the unreduced Fe/MgO are the absorption bands situated at 1860 and 1135 cm^{-1} in spectrum B of Figure 3.30. These bands can be attributed to the interaction of NO and NO_2^- respectively with Fe^{3+} centres.

First considering the band situated at 1860 cm^{-1}, this band can be assigned to the interaction of NO with Fe^{3+}. This assignment is made in accordance with the observations of Aparico et al. (139) and Busca and Lorenzelli (106) who studied NO adsorption on Fe-Y zeolites and on α-Fe_2O_3 respectively. Busca and Lorenzelli observed that increasing the NO pressure from 5 to 200 Torr resulted in the formation a band at 1860 cm^{-1} along with the simultaneous disappearance of a band at 1595 cm^{-1}. Evacuation of the sample at beam temperature resulted in the disappearance of the band at 1860 cm^{-1} with the simultaneous reappearance of the band at 1595 cm^{-1}. The results from this work are in agreement with the above observation, evacuation of the gas phase NO resulted in the loss of the band at 1860 cm^{-1} (Fig. 3.30 spectrum B) with the simultaneous formation of a band at 1600 cm^{-1} (Fig. 3.30 spectrum C). The band at 1600 cm^{-1} can be assigned to a NO^- species bonded through a highly ionic interaction with surface cationic sites. The bands at 1860 cm^{-1}, whose frequency is somewhat lower than that of gaseous NO (1880 cm^{-1}) can be assigned to slightly

perturbed NO molecules. As a purely coordinative bond giving partially positive NO species, would be expected to increase the stretching frequency, this is likely to come from an adsorbed species where NO acts as both a s donor and a p acceptor. However as this species only appears at high NO pressures with the simultaneous disappearance of the 1600 cm^{-1} band, its identification with slightly perturbed NO molecules formed by interaction of a second NO molecule with a further coordinative site of iron ions already bonded to a NO^- species has been proposed by Busca and Lorenzelli (106) with the following structure 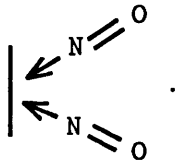 .

The reduction in intensity in the band at 1220 cm^{-1} when NO is adsorbed on the Fe/MgO compared to pure MgO may be a result of two factors. First the Fe/MgO has been pretreated at a much lower temperature than the pure MgO. As a result of this lower thermal treatment the surface will be more highly hydroxylated and hence the MgO will be less basic. Second the observed reduction in the intensity of the band at 1220 cm^{-1} may be a direct result of the addition of the transition metal oxide. Escalona et al. (110) observed a reduction in intensity of the band at 1220 cm^{-1} when Ni^{2+} was added to MgO, in these experiments the pretreatment temperature was identical for both the pure MgO and the Ni/MgO.

The band formed at 1135 cm^{-1} is thought to be the result of a NO_2^- species associated with a Fe^{3+} site. This assignment is in line with that of Escalona et al.(110) who have assigned bands in the region 1250-1125 cm^{-1} to a adsorbed NO_2^- species

when NO is adsorbed on a Ni/MgO solid solution. These authors have proposed the following reactions which explain both the formation of the adsorbed NO_2^- and N_2O in the gas phase:

$$4NO + 2O^{2-} \longrightarrow 2NO_2^- + N_2O_2^{2-} \quad (7)$$

$$N_2O_2^{2-} \longrightarrow N_2O + O^{2-} \quad (8)$$

Note by summation of reactions 7 and 8 the following reaction is obtained:

$$4NO + 2O^{2-} \longrightarrow 2NO_2^- + N_2O \quad (9)$$

The adsorption of NO on a sample of 5% Fe/MgO which has undergone reduction at 693 K as described in Section 2.1.3 exhibited a band at 1820 cm^{-1} (Figure 3.31 spectrum A and B). This band has been observed by a number of other authors (102,103) and has been attributed to NO bonded to Fe^{2+} sites. However the spectra in Figure 3.31 do not exhibit a band in the region of 1750 cm^{-1} which has previously been reported for the adsorption of NO on Fe^0 (102, 104, 108). Poling and Eischens (107) have observed a band at 1750 cm^{-1} but it is their opinion that the band can be accounted for by the following mechanism

$$2\ NO + 2\ Fe_{red} \longrightarrow 2\ FeO_{ads} + N_2 \uparrow$$

followed by

$$NO + FeO_{ads} \longrightarrow Fe\text{-}O\text{-}N\text{=}O$$

the band at 1750 cm^{-1} being attributed to the nitrogen-oxygen stretching frequency of NO chemisorbed on O_{ads}.

The absence of a band at around 1750 cm^{-1} in this work is hardly surprising if the results of other authors are considered. The observations of Bandow et al. (103) made at 77 K show that metallic iron shows some signs of oxidation when contacted with NO. Results presented within this thesis and the results of other workers have shown that N_2O is produced when

NO is adsorbed on MgO, and N_2O is effective as a surface oxidant for metallic iron.

The band previously observed at 1135 cm^{-1} in the case of the unreduced Fe/MgO appears as two bands situated at 1165 and 1108 cm^{-1} in the case of the reduced sample. This is thought to be the result of NO_2^- ions adsorbed on both Fe^{2+} and Fe^{3+} sites. The presence of Fe^{3+} ions in Fe/MgO samples of low iron loading, which have undergone reduction at 693 K has been confirmed by Mössbauer Spectroscopy (Section 3.5).

The use of NO as an infrared probe molecule for studies using Fe/MgO catalysts is limited. The results show that the molecule is not suitable for probing Fe^0 centres due to the formation of N_2O, which results in oxidation of the metallic iron. NO however, is a useful probe for Fe^{2+} and Fe^{3+} centres. The absorption band at 1820 cm^{-1} indicating the presence of Fe^{2+}. This band is easily detectable and resistant to evacuation of the gaseous NO. The strong band at 1135 cm^{-1} appears to be a good indication of the presence of Fe^{3+} sites.

4.6.3. The Adsorption of Ethanenitrile and Propanenitrile

4.6.3.1. The Adsorption of Ethanenitrile and Propanenitrile on MgO

The spectra arising from the adsorption of ethanenitrile and propanenitrile are very similar, as one might expect, therefore only the adsorption of ethanenitrile will be discussed in detail. However the positions and assignments of

the observed bands produced from the adsorption of both ethanenitrile and propanenitrile are contained in Table 4.2.

The adsorption of ethanenitrile on MgO exhibits an infrared spectrum indicating adsorbed species similar to those observed by other authors, when ethanenitrile was adsorbed on zinc oxide (140) and on alumina (141). These authors have observed that on adsorption ethanenitrile undergoes hydrolysis, resulting in the formation of a surface acetamide. The formation of a surface acetamide species on MgO accounts for many of the bands observed when ethanenitrile is adsorbed on MgO (Fig. 3.33 spectrum B) and explains the similarity to the spectrum observed when acetamide is adsorbed (Fig. 3.33 spectrum C). The conclusion to be drawn is that also on MgO there is the formation of an acetamido surface species produced by a hydrolysis type reaction as shown below.

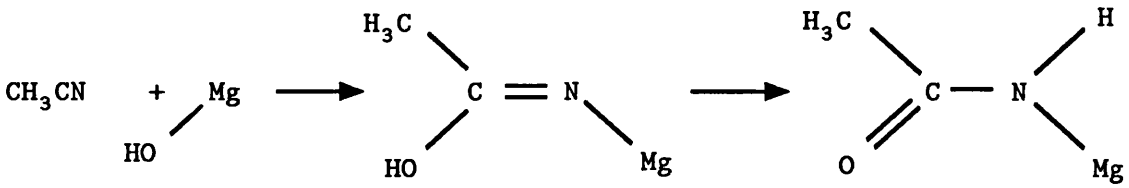

The spectrum of adsorbed ethanenitrile exhibits additional bands at 2185 and 2142 cm^{-1}. These two bands are evidence that heterolytic dissociative adsorption has occurred to give $(CH_2CN)^-$ (140). The band at 2142 cm^{-1} corresponds to the dimer of $(CH_2CN)^-$, the band at 2185 cm^{-1} is attributed to a polymeric form of the $(CH_2CN)^-$ species. The formation of the $(CH_2CN)^-$ ion results in the formation of a new surface hydroxyl group, evident by the absorption band at 3651 cm^{-1}. Significantly less of the corresponding species is produced on

Table 4.2 Assignment of absorption bands produced from the adsorption of ethanenitrile and propanenitrile on MgO

Adsorbed species from		
CH_3CN cm^{-1}	CH_3CH_2CN cm^{-1}	Assignment
3651 (m)	3646 (m)	υ (OH) from new surface hydroxyl formed in the formation of $(CH_2CN)^-$
3460 (w)	3465 (w)	υ (NH) $(RCONH)^-$
2973 (w), 2922 (w)	2965 (m), 2879 (w)	υ (CH_3) $(RCONH)^-$
2354 (vw)	2336 (vw)	υ (CN) nitrile coordinated to Mg^{2+}
	2177 (m)	
2142 (s)	2117 (w)	$(CH_2CN)^-$ dimer
2185 (m)		$(CH_2CN)^-$ polymer
1643 (m)	1640 (w)	free uncoordinated amide on the surface
1566 (vs)	1558 (vs)	υ_a 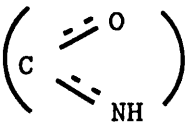
1525 (s)		υ (C—C)
1451 (vs)	1445 (s)	υ_s 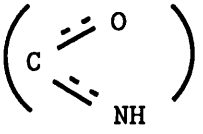
1300 (w)	1307 (m)	δ (CH_3)
1185 (s)	1177 (s)	δ (NH) $(RCONH)^-$

the adsorption of propanenitrile (Fig. 3.36). These observations are consistent with those made by Lavalley et al. (140), who studied the adsorption of ethanenitrile on ZnO.

Figure 3.34 fails to show any absorption bands related to the coordination of ethanenitrile with Mg^{2+} ions. The position of the $C \equiv N$ stretching frequency when ethanenitrile is adsorbed on various metal oxides has been reported as having values of 2315 and 2282 cm^{-1} for ZnO (140), 2328 and 2297 cm^{-1} for Al_2O_3 (142). Results obtained from Mg-substituted NaY zeolites (143) indicate the presence of absorption bands at 2317 and 2293 cm^{-1} for MgY. However, amplification of the spectrum (Fig. 3.35) permits the observation of absorption bands associated with minority surface species. The band observed at 2354 cm^{-1} is probably a result of the coordination of CH_3CN with Mg^{2+} ions.

4.6.3.2. The Adsorption of Ethanenitrile and Propanenitrile on 5 % Fe/MgO

Considering first the information gained from the spectra in Figures 3.34 and 3.36, the main difference between the spectra obtained from MgO and the 5 % Fe/MgO catalyst is that the latter exhibits a significant reduction in the intensity of the absorption bands due to the $(CH_2CN)^-$ both in the form of the dimer and the polymer. The suppression of the ability of MgO to produce heterolytic dissociative adsorption indicates that the iron has the effect of reducing the basic nature of the MgO. This is an important observation because one of the

reasons for choosing MgO as the support material was because of its basic nature.

The interpretation of the spectra due to the adsorption of the nitriles on the Fe/MgO catalyst contained in Figures 3.35 and 3.37 is difficult. There are obviously additional absorption bands produced as a result of the presence of the iron, but these are not easily assigned.

There does not appear to be any information in the literature concerning the adsorption of nitriles on polycrystalline iron catalysts or iron single crystals. However a HREELS study has been made by Friend et al. (144) of ethanenitrile adsorbed on nickel (111). They observed energy losses at 1680-1700 cm^{-1} corresponding to the C-N stretching frequency, and at 2910 cm^{-1} corresponding to the C-H stretching frequency. In a further study by the same group (145) using additional nickel single crystal surfaces the following schematic representation for the bonding of ethanenitrile on flat (111) and (100), stepped 9(111) x (111), and stepped-kinked 7(111) x (310) surfaces has been proposed.

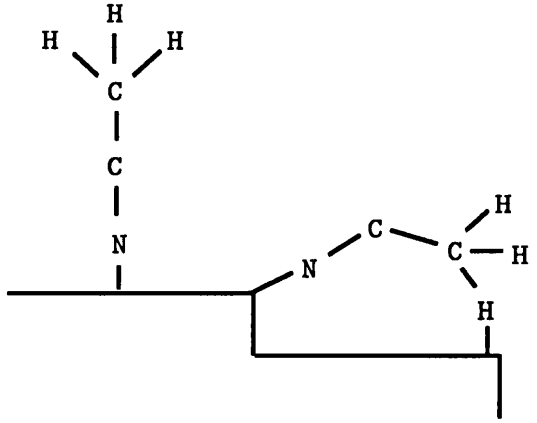

Because of the relatively low energy of the C-N stretch it is proposed that the ethanenitrile molecule is not

coordinated to a single nickel atom, but adsorbed with the nitrogen atom residing over the centre of two or three metal surface atoms.

The absorption bands observed at 1776 cm^{-1} (Fig. 3.35 A) produced on the adsorption of ethanenitrile and 1733 cm^{-1} from propanenitrile (Fig. 3.37 A) could possibly due to the C-N stretching frequency of the adsorbed nitrile. This agrees well with the results of Friend et al. previously described.

The adsorption of HCN on palladium single crystals has been studied by Kordesch et al. (146). They propose that at 300 K HCN is adsorbed in the following manner 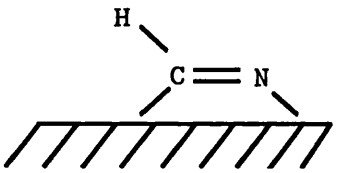 . The HREELS spectra indicate a C-N stretching frequency of 1540 cm^{-1} and a C-H stretching frequency of 3305 cm^{-1}. The adsorption of HCN has also been studied by Anderson and Clark (147) on evaporated films of nickel and tungsten. These authors have proposed the following modes of adsorption exist

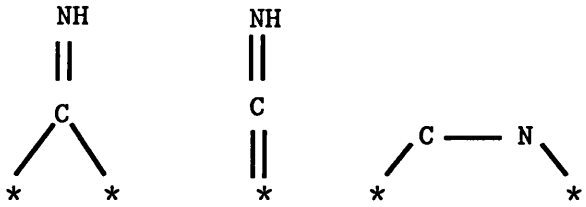

The adsorption of cyanogen (NCCN) has been studied on palladium single crystals (148). Results indicate that adsorption at ambient temperature results in dissociation of the cyanogen producing an adsorbed CN species which produce energy losses at 282 and 1895 cm^{-1}. The loss at 282 cm^{-1} has been assigned to Pd-CN bond while the loss at 1895 cm^{-1} can be assigned to CN stretching. The results on Pd indicate that the

adsorption of nitriles can be dissociative, hence the possibility of adsorbed CN cannot be discarded as a possible mechanism in the adsorption of ethanenitrile and propanenitrile on the iron catalyst used in this study.

The current literature indicates that the adsorption of nitriles on metal surfaces is complex. The complexity is further compounded in the case of Fe/MgO where the iron is present in the form of Fe^{3+}, Fe^{2+}, and Fe^{0}. Hence any attempt to make assignments to the bands observed in addition to those present in pure MgO can at best be made tentatively. The adsorption of the nitriles onto FeO may account for bands observed in the region 2600 cm^{-1} in Figures 3.35 and 3.37.

4.7. Catalyst Testing

4.7.1. Kinetics of Nitrile Hydrogenation

The results obtained from the flow reactor (Section 3.7.1) have shown that the hydrogenation of ethanenitrile is approx. zero order with respect to ethanenitrile concentration and approx. 2^{nd} order w.r.t. hydrogen. The observation of zero order kinetics with respect to ethanenitrile is consistent with this molecule being a strongly adsorbed species. The hydrogenation of the nitrile to the primary amine is a two step process, the imine being the intermediate. In order that the process exhibit zero order kinetics it is necessary for both the nitrile and the imine to be strongly adsorbed at the catalyst surface. This is understandable as both molecules posses a lone pair of electrons on the nitrogen atom. Nitrogen compounds possessing a lone pair of electrons for example pyridine are frequently bound so strongly to catalyst surfaces that they act as catalyst poisons.

The observation of an order of approx. 2 with respect to hydrogen is more difficult to explain. However, the hydrogenation of acetylene over various metals has been shown to exhibit an order significantly greater than one w.r.t. hydrogen (149). It can nevertheless be concluded that hydrogen is only weakly adsorbed on iron compared to the nitrile.

The Arrhenius plots for catalysts OH5, HT1 and OH20 (Fig. 3.44-3.46) are not linear over the whole range of temperatures studied. The Arrhenius plot for catalyst OH5 exhibits a substantial amount of curvature. This nonlinearity is usually a

result of mass transfer limitations (150).

The activation energies for the hydrogenation of ethanenitrile using catalysts OH5, HT1 and OH20 were found to be 100.8, 58.5 and 58.5 kJ mol^{-1} respectively. There is a substantial amount of variation between the catalysts tested, however, the values obtained for catalysts HT1 and OH20 are in reasonable agreement with a value of 52 kJ mol^{-1} quoted by Volf and Pašek (44) for the hydrogenation of lauronitrile catalysed by a cobalt catalyst.

Results from both the flow reactor and the autoclave reactor indicate that there is a relationship between the rate of nitrile hydrogenation and the active area of the catalyst as determined by N_2O decomposition or CO adsorption. Figure 4.2 shows the plot of rate of reaction vs iron surface area using rates obtained from the autoclave reactor. The results indicate that there is an increase in rate with increased metal area but this relationship can not be transferred between catalysts prepared by different methods. Figure 4.3 shows the plot of rate vs active area for catalysts tested using the flow reactor. The plot shows a much more linear variation of rate with active area, which for the limited number of catalysts tested does appear to be independent of the method of production of the catalyst. As has previously been stated the autoclave reactor was not designed to produce accurate rate data. As a result the relationship between rate of hydrogenation and active area may well be linear and independent of the method of production of the catalyst as indicated by the results from the flow reactor.

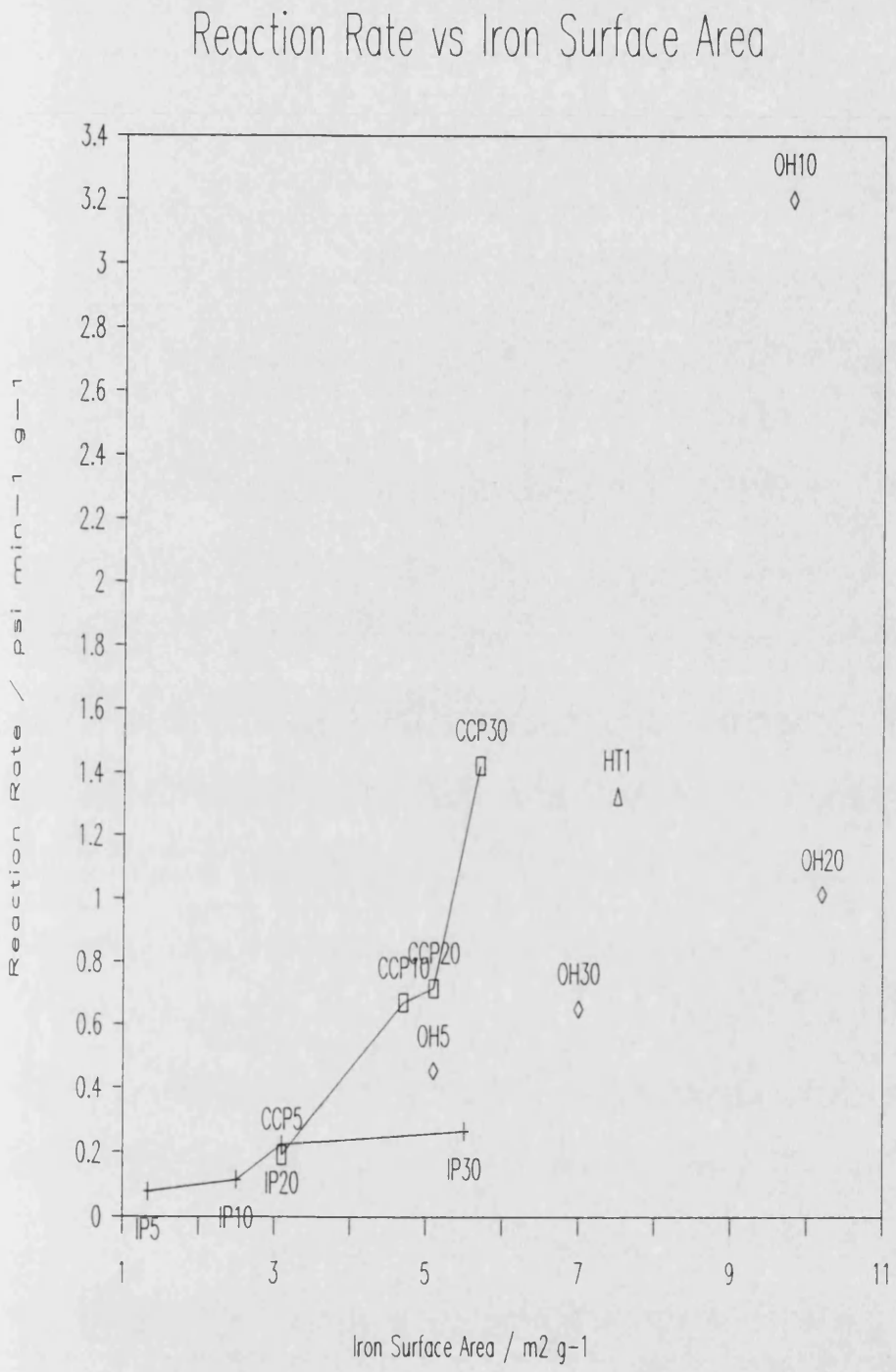

Figure 4.2 Relationship between iron surface area and the rate of propanenitrile hydrogenation (autoclave reactor)

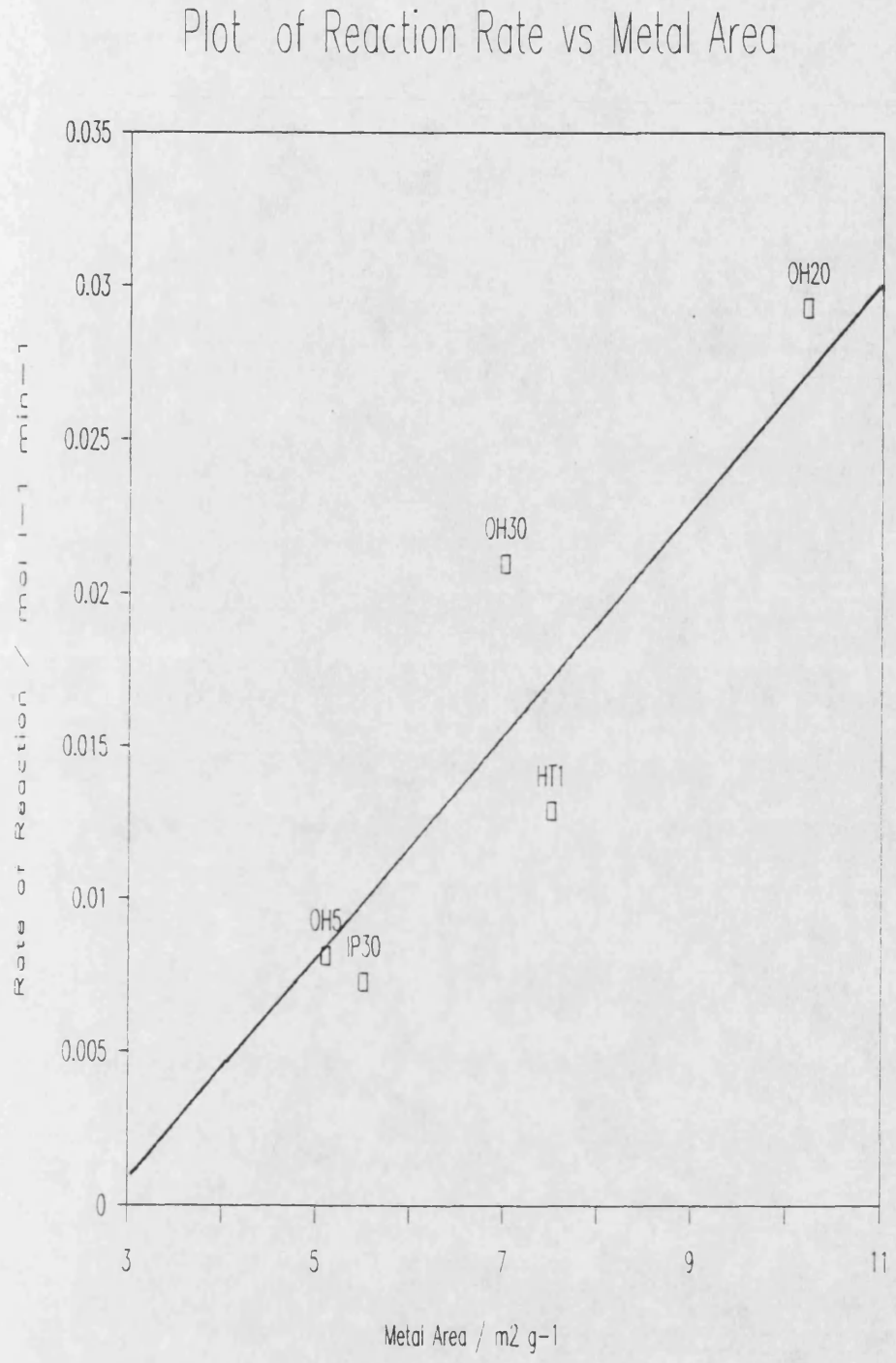

Figure 4.3 Relationship between iron surface area and the rate of ethanenitrile hydrogenation (flow reactor)

4.7.2. Reaction Mechanism and Selectivity

The results clearly confirm that the catalysts prepared in this work are capable of hydrogenating C_2 to C_{12} nitriles. Moreover, reaction over these catalysts is highly selective towards the desired primary amine.

The catalysts show that there is a relationship between both selectivity and rate and between selectivity and conversion. The plot of selectivity vs rate of hydrogen uptake (Fig. 4.4) shows that catalysts which are more active are also more selective. The exception to this is the commercial catalyst which has an exceptionally high rate 4.577 psig min^{-1} for propanenitrile hydrogenation but a selectivity to the primary amine of 70.86 %. This may be a result of this catalyst being unsupported indicating the basic nature of the MgO support may have the effect of suppressing the condensation reaction to form higher amines. Considering only the supported catalysts prepared in this study the relationship between selectivity and rate can be explained by considering how secondary and tertiary amines are formed. The mechanism described in Section 1.6.1 shows that these are formed from the reaction of the imine RCH=NH with either a primary or secondary amine. If the catalyst is more active then the imine is more likely to undergo hydrogenation and less likely to undergo a condensation reaction to form a secondary or tertiary amine.

The plot of selectivity vs conversion (Fig. 4.5) shows that at increased conversion the selectivity to the primary amine is also increased. This observation was confirmed by

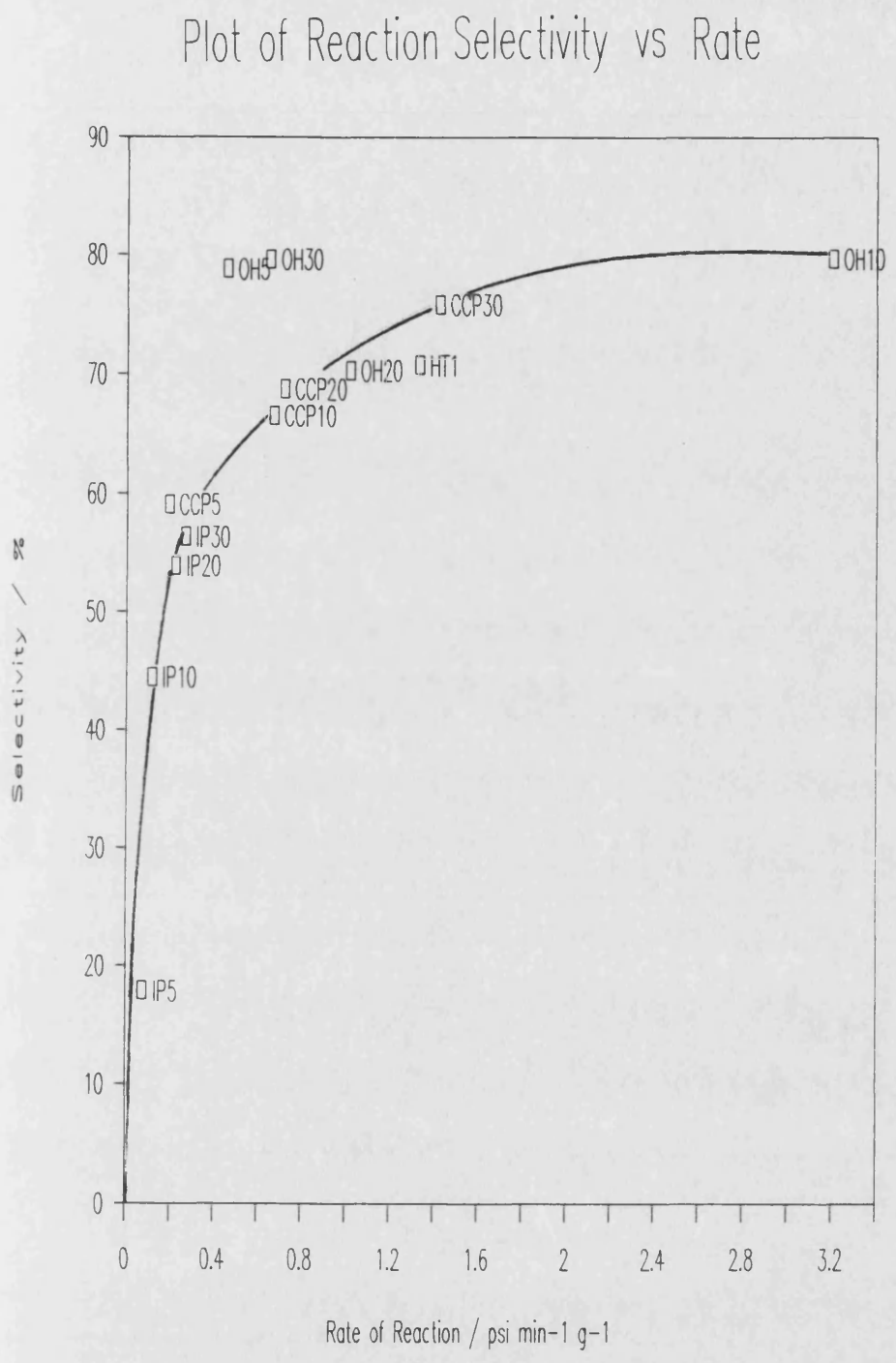

Figure 4.4 Plot of selectivity vs rate of propanenitrile hydrogenation

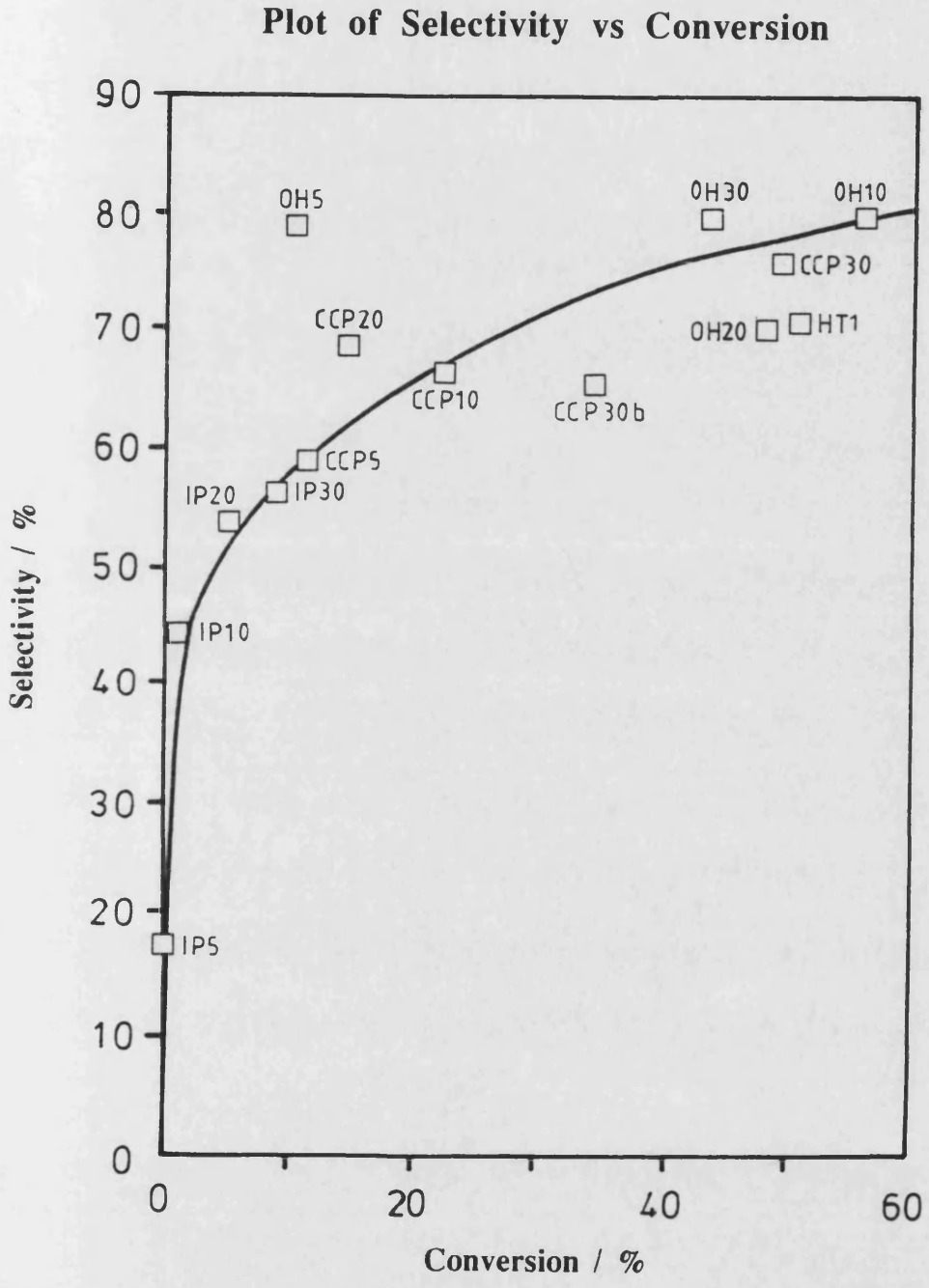

Figure 4.5 Plot of selectivity vs conversion for the hydrogenation of propanenitrile

running catalyst CCP30 to two different conversions, at 13.92 % conversion the selectivity was 65.6 % while at 49.34 % conversion the selectivity was 75.9%. A possible explanation for this is that at lower conversions there is a higher concentration of nitrile, hence there is greater competition between the nitrile and the imine for the active sites. Therefore the imine is more likely to undergo a condensation reaction to form a secondary or tertiary amine. This would require the condensation reaction to take place at a different site to the hydrogenation reaction. This relationship between conversion and selectivity is backed-up by the work of Braun et al. (48), who observed that the content of secondary amines increases with the nitrile concentration in hydrogenations carried out in a solvent.

As described in Section 1.6.1 two mechanisms have been advanced for the production of secondary and tertiary amines. At this point only the formation of the secondary amine will be considered but the same applies to tertiary amines. The 1-aminodialkylamine can lose ammonia to yield an alkylidenalkylamine and then undergo hydrogenation as shown by mechanism 1 below, or undergo hydrogenolysis as shown in

$$\underset{\underset{NH_2}{|}}{RCH\text{-}NH\text{-}CH_2R} \xrightarrow{-NH_3} RCH{=}N\text{-}CH_2R \xrightarrow{+H_2} RCH_2NHCH_2R \qquad (1)$$

mechanism 2

$$\underset{\underset{NH_2}{|}}{RCH\text{-}NH\text{-}CH_2R} \xrightarrow{+H_2} RCH_2NHCH_2R + NH_3 \qquad (2)$$

The presence of 1-(n-propylaminopropene $(CH_3CH_2CH_2)NH(CH{=}CHCH_3)$ and 1-(n,n-dipropylamino)propene

$(CH_3CH_2CH_2)_2N(CH{=}CHCH_3)$ from the hydrogenation of propanenitrile and hexanimine $(CH_3(CH_2)_4CH{=}NH$ and 1-(n-hexylamino)hexene $(CH_3(CH_2)_5)NH(CH{=}CH(CH_2)_3CH_3)$ from the hydrogenation of hexanenitrile show that mechanism 1 is the preferred reaction pathway.

Chapter 5

Conclusions

"The great tragedy of science - the slaying of a beautiful hypothesis by an ugly fact".

T. H. Huxley 1825-1895

5.1 Conclusions

Various methods of preparing iron-magnesia catalysts have been studied. The results show that catalysts possessing the highest active metal areas originate from a starting precipitate having the pyroaurite structure.

Reduction of the iron in Fe/MgO catalysts is difficult, volumetric/gravimetric measurements along with Mössbauer spectroscopy and infrared spectroscopy have shown that not all the iron is reduced to metallic iron by heating in hydrogen at 693 K. The iron oxide phases produced during reduction of the catalyst precursors appears to be dependent upon the size of the iron oxide particles. Large particles reduce in the following manner

$$\underset{\text{hematite}}{\alpha\text{-}Fe_2O_3} \longrightarrow \underset{\text{magnetite}}{Fe_3O_4} \longrightarrow \underset{\text{wustite}}{FeO} \longrightarrow \underset{\text{iron}}{\alpha\text{-}Fe}$$

whereas small particles reduce without any evidence for the formation of an magnetite phase

$$\underset{\text{hematite}}{\alpha\text{-}Fe_2O_3} \longrightarrow \underset{\text{wustite}}{FeO} \longrightarrow \underset{\text{iron}}{\alpha\text{-}Fe}$$

Nitrous oxide decomposition has proved to be a useful technique in the determination of metallic iron surface areas. There is still some doubt as to the depth of oxidation by the nitrous oxide. However, using a N_2O:Fe ratio of 2.5:1 has produced results which are in good agreement with those obtained from CO adsorption isotherms. The main advantage of N_2O decomposition as compared to CO adsorption for the determination of Fe^0 areas is that the technique is

experimentally less taxing.

The infrared study has shown CO to be useful in the identifying Fe^0 sites although the uncertainty still remains concerning the adsorption of CO on iron in higher oxidation states. The use of nitric oxide as a probe molecule is limited especially when MgO is the support material. This is because reactions occur on the MgO resulting in the formation of nitrous oxide, which has been shown to be active as a surface oxidant for metallic iron. However,nitric oxide is useful for probing the presence of Fe^{2+} and Fe^{3+} sites.

The catalysts prepared have shown that they fulfil one of the primary aims in that they are capable of hydrogenating nitriles with a high selectivity to primary amines. Some of the supported catalysts exhibited selectivity to the primary amine up to 12 % higher than the commercial catalyst. The origin of this increased selectivity may be a result of the basic nature of the MgO support, but further work would be required to confirm this. None of the supported catalysts produced were as active as the commercial catalyst for the hydrogenation of propanenitrile. The hydrogenations carried out using hexanenitrile and dodecylnitrile have shown that increasing the size of the nitrile molecules has not effected the rate of hydrogenation significantly. This indicates that most of the iron is still accessible to the larger reactant molecules, this bodes well for experiments using adiponitrile as the reactant.

5.2. Future work

On the grounds of their increased selectivity to the primary amine in the hydrogenation of propanenitrile the supported catalysts probably merit testing on apparatus which is capable of hydrogenating adiponitrile to 1,6-hexamethylenediamine.

There exists the possibility of tailoring the pore structure of the support (151) so as to give better access to the reactant in the liquid phase if this should prove necessary.

The effect of the support could be investigated by preparing a number of catalysts with different supports, in this way it may be possible to say whether or not the increased selectivity observed in this study is a result of the basic nature of the MgO support.

References

1. UK Patent 1317464, 1973.

2. Boudart, M., Delbouille, A., Dumesic, J.A., Khammouma, S., and Topsøe, H., J. Catal. 37, 486 (1975).

3. Topsøe, H., Dumesic, J.A., Derouane, E.G., Claussen, B.S., Mørup, S., Villadsen, and Topsøe, N., Studies in surface science and catalysis vol. 3, p. 365, Eds. Delmon, Grange, Jacobs, and Poncelet, Elsevier Amsterdam 1979.

4. Coluccia, S. and Tench, A.J., Proc. 7th Intern. Congr. Catalysis p. 1154, Elsevier, Amsterdam, 1981.

5. Tanaka, Y., Imizu, Y., Hattori, H. and Tanabe, K., Proc. 7th Intern. Congr. Catalysis p. 1254, Elsevier, Amsterdam, 1981.

6. Ito, T., Yoshioka, M. and Tokuda, T. J. Chem. Soc. Faraday I, 79, 2277 (1983).

7. Hagedorn, F., Gelbke, H.P., in Ullmanns Enzyklopädie der technischen Chemie, Band 17, Verlag Chemie, Weinheim, 1979, p. 333-337.

8. Perman, E.P., Proc. Roy. Soc. 76, 167 (1905)

9. Boudart, M., Catal. Rev.-Sci. Eng. 23(1&2), 1 (1981).

10. Axelrod, L., Catal. Rev.-Sci. Eng. 23(4), 53 (1981).

11. Nielsen, A., Catal. Rev.-Sci. Eng. 23(1&2), 17 (1981).

12. Flory, P.J., J. Am. Chem. Soc. 58, 1877 (1936)

13. Ponec, V., Catal. Rev.-Sci. Eng. 18(1), 151 (1978).

14. Anderson, R.B., Catal. Rev.-Sci. Eng. 21(1), 53 (1980).

15. Newsome, D.S., Catal. Rev.-Sci. Eng. 21(2), 275 (1980).

16. Phadhe, M.D., and Ko, E.I., J. Catal. 100, 503 (1986).

17. Santos, J., Phillips, J., and Dumesic, J.A., J. Catal. 81, 147 (1983).

18. Santos, J. and Dumesic, J.A., Studies in surface science and catalysis, vol 11 p.43 Eds Imelik et al. Elsevier 1982.

19. Rodríguez-Reinoso, F., Rodrríguez-Ramos, I., Guerrero-Ruiz, A. and López-González Appl. Catal. 21, 251 (1986).

20. Jung, H-J., Walker, P.l., and Vannice M.A., J. Catal. 75, 416 (1982).

21. Segawa, K.I., Chen, Y., Kubsh, J.E., Delgass, W.N., Dumesic, J.A., and Hall, K., J. Catal. 76, 112 (1982).

22. Wielers, A.F.H., Kock, A.J.H.M., Hop, C.E.C.A., and Geus, J.W., J. Catal. 117, 1 (1989).

23. Inui, T., Nagata, H., Matsuda, H., Kuroda, T., Yoshikawa, M., Takeghuchi, T., and Miyamoto, A., Appl. Catal. 24, 257 (1986).

24. Schay, Z., Lázár, K., mink, J., and Guczi, L., J. Catal. 87, 179 (1984).

25. Yuen, S., Chen, Y., Kubsh, J.E., Dumesic, J.A., Topsøe, N., and Topsøe, H., J. Phys. Chem. 86, 3022 (1982).

26. Artyukh, Yu.N., Lunev, N.K., and Rusov, M.T., Kinet. Katal. 13(3), 741 (1972).

27. Ren-Yuan, T., Su, Z., Chengyu, W., Dongbai, L., and Liwu, L., J. Catal. 106, 440 (1987)

28. Kock, A.J.H.M., Fortuin, H.M., and Geus, J.W., J. Catal. 96, 261 (1985).

29. Perrichon, V., Turlier, P., Barrault, J., Forquy, C., and Menezo, J.C., Appl. Catal. 1, 169 (1981).

30. Nahon, N., Perrichon, V., Turlier, P., and Bussière, P., React. Kinet. Catal. Lett. 11(3), 281 (1979).

31. Dumesic, J.A., Topsøe, H., Kammouma, S., and Boudart, M., J. Catal. 37, 503 (1975).

32. Dumesic, J.A., Topsøe, H., and Boudart, M., J. Catal. 37, 513 (1975).

33. Dutartre, R., Primet, M.,and Martin, G.A., React. Kinet. Catal. Lett. 3(3), 249 (1975).

34. Dutartre, R., Bussière, P., Dalmon, J.A., and Martin, G.A., J. Catal. 59, 382 (1979).

35. Topsøe, H., Topsøe, N., Bohlbro, H., and Dumesic, J.A., Proc. 7^{th} Intern. Congr. Catal. Tokyo 1980, Elsevier Amsterdam.

36. McDonald, M.A., Storm, D.A., and Boudart, M., J. Catal. 102, 286 (1986).

37. Geus, J.W. Appl. Catal., 25, 313 (1986).

38. Kock, A.J.H.M., "The Characterization of Iron Catalysts" Thesis University of Utrecht (1985).

39. Vink, T.J., Gijzeman, O.L.J. and Geus, J.W., Surf. Sci. 150, 14 (1985).

40. Emmett, P.H. and Brunauer, S.J., Amer. Chem. Soc. 56, 35 (1934)

41. Huang, Y.Y., and Anderson, J.R., J. Catal. 40, 143 (1975).

42. Bond, G., and Stone, F.S., unpublished work.

43. U.S. Pat. 2,484,042

44. Volf, J., and Pašek, J., Studies in surface science and catalysis, vol 27, p.105 Ed. Červeny, Elsevier 1986.

45. Paal, C., and Gerum, J., Chem. Ber., 42, 1553 (1909).

46.. Rupe, H., and Hodel, R., Helv. Chem. Acta., 6, 865 (1923).

47. Mignonac, G., C.R. Hebd. Seances Acad. Sci., 171, 114 (1923)

48. Braun, J., Blessing, G., and Zobel, F., Chem. Ber., 36, 1988 (1923).

49. Winans, Ch.F., and Adkins, H., J. Am. Chem. Soc., 54, 306 (1932).

50. Juday, R., and Adkins, H., J. Am. Chem. Soc., 77, 4559 (1955).

51. Rylander, P.N., Catalytic Hydrogenation in Organic Synthesis, Academic Press, New York, 1979, pp.138-140.

52. Lazaris, A.J., Zilberman, E.N., Lumitcheva, E.V., and Vedin, A.M., Zh. Prikl. Khim., 38, 1097 (1965).

53. Greenfield, H., Ind. Eng. Chem. Prod. Res. Develop., 6, 142 (1967).

54. Private Communication from Wheeler, E.L., Uniroyal Chemical Division of Uniroyal Inc. to Greenfield, H.

55. Baiker, A., and Kijenski, J., Catal. Rev.-Eng. 27(4), 653 (1985).

56. Hill, J.W., and Carothers, W.H., J. Am. Chem. Soc., 55, 5023 (1933).

57. Brit. Pat. 567,525

58. Brit. Pat. 1,336,865 1973.

59. Rennison, A.J., Ph. D Thesis University of Bath 1988.

60. Lockyer, D.M., Ph. D Thesis University of Bath 1988.

61. Gregg, S.J. and Sing, K.S.W., "Adsorption, Surface Area and Porosity", Academic Press London (1967).

62. Innes, W.B., Anal. Chem. 29, 1069 (1957).

63. Barrett, E.P., Joyner, L.G., and Halenda, P.P., J. Am. Chem. Soc. 73, 373 (1951).

64. Brunauer, S., Mikhail, R.SH., and Bodor, E.E., J. Coll. Int. Sci. 24, 451 (1967).

65. Emmett, P.H., and Harkness, R.W.J., J. Am. Chem. Soc. 57, 1631 (1935).

66. Emmett, P.H., and Brunauer, S., J. Am. Soc. 57, 1754 (1935).

67. Emmett, P.H., and Brunauer, S., J. Am. Soc. 59, 310 (1937).

68. Emmett, P.H., and Brunauer, S., J. Am. Soc. 59, 1553

(1937).

69. Brunauer, S., and Emmett, P.H., J. Am. Soc. 62, 1732 (1940).

70. Subramanyam, K., and Rao, M.R.A., J. Res. Inst. Catal. Hokkaido Univ 18 (3), 115 (1970).

71. Westrik, R., and Zwietering, P., Proc. Kon. Ned. Akad. Wetensch. Ser. B56, 492 (1953).

72. Jung, H.J., Vannice, M.A., Mulay, L.N., Stanfield, R.M., and Delgass, W.N., J.Catal. 76, 208 (1982).

73. Bianchi, D., Borcar, S., Teule-Gay, F., and Bennett, C.O., J. Catal. 82, 442 (1983).

74. Evans, J.W., Wainwright, M.S., Bridgewater, A.J., and Young,D.J., Appl. Cat. 7, 75 (1983).

75. Scholten, J.J.F., and Konvalinka, J.A., Trans. Faraday Soc. 65, 2465 (1969).

76. Chinchen, G.C., Hay, C.M., Vandervell, H.D., and Waugh, K.C., J. Catal. 103, 79 (1989).

77. Keating, D.T., and Warren, B.E. Rev. Sci. Instr. 23, 519 (1952).

78. Alexander, L., J. Appl. Phys. 21, 216 (1950).

79. Scherrer, P., Gött. Nachr. 2, 98 (1918).

80. Stokes, A.R., and Wilson, A.J.C., Proc. Phys. Soc. (London) 56, 174 (1974).

81. Dumond, W.M., and Kirkpatrick, H.A., Phys. Rev. 37, 136 (1931).

82. Rachinger, W.A., J. Sci. Instr. 25, 254 (1948).

83. Schoening, F.R.L., Acta Cryst. 18, 975 (1965).

84. Jones, F.W. Proc. Roy. Soc. (London), 166A, 16 (1938).

85. Rochester, C.H., and Topham, S.A., J.Chem. Soc. Faraday Trans I 75, 872 (1979).

86. Connell, G., and Dumesic, J.A., J. Catal. 101, 103 (1986).

87. Connell, G., and Dumesic, J.A., J. Catal. 102, 216 (1986).

88. Blyholder, G., J. Phys. Chem. 68, 2772 (1964).

89. Scholten, J.J.F., Studies in surface science and catalysis vol. 3 p.685 Eds Delmon, B., Grange, P., Jacobs, P., and Poncelet, G., Elsevier Amsterdam 1979.

90. Vogler, G.L., Jiang, X.Z., Dumesic, J.A. and Madon, R.J., J. Catal. 89, 116 (1984).

91. Private Communication from ICI Billingham to Bond, G.

92. Graham, M.J., Channing, D.A., Swallow, G.A., and Jones, R.D., J. Mat. Sci. 10, 1175 (1975).

93. Bhinde, V.R., and Tambe, B.R., J. Mat. Sci. 4, 955 (1969).

94. Blyholder, G., J. Chem. Phys. 44, 3134 (1966)

95. Blyholder, G., and Tanaka, M., J. Phys. Chem. 76, 3180 (1972).

96. Heal, M.J., Leisegang, E.C., and Torrington, R.G., J. Catal. 51, 314 (1978).

97. Perrichon, V., Primet, M., Nahon, N., and Turlier, P., C. R. Acad. Sc. Paris, t. 289 Série C 149 (1979).

98. Bianchi, D., Batis-Landoulsi, H., Bennett, C.O., Pajonk, G.M., Vergnon, P., and Teichner, S.J., Bulletin de la Société Chimique de France No 9-10, I-345 (1981).

99. Benzinger, J.B., and Larson, L.R., J. Catal. 77, 550 (1982).

100. Jorgensen, N., and Rochester, C.H., Appl. Catal. 25, 69 (1986).

101. Johnston, C., Jorgensen, N., and Rochester, C.H., J. Chem. Soc. Faraday Trans. I 84, 309 (1988).

102. King, D.L. and Peri, J.B., J. Catal. 78, 104 (1983).

103. Bandow, H., Onishi, T. and Tamaru, K., Chem. Lett. p83, (1978).

104. Johnston, C., Jorgensen, N. and Rochester, C.H., J. Chem. Soc., Faraday Trans. I 84, 2001 (1988).

105. Glazneva, G.V., Davydov, A.A., Sazonova, I.S., Shchekochikhin, Yu. M. and Keier, N.P., React. Kinet. Catal. Lett. 9, 131 (1978).

106. Busca, G. and Lorenzelli, V., J. Catal. 72, 303 (1981).

107. Poling, G.W. and Eischens, R.P., J. Electrochem. Soc. 113, 218 (1966).

108. Yuen, S., Chen, Y., Kubsh, J.E. and Dumesic, J.A., J. Phys. Chem. 86, 3022 (1982).

109. Cerruti, L., Modone, E., Guglielminotti, E., Borello, E., J. Chem. Soc. Faraday Trans. I 70, 729 (1974).

110. Escalona, E., Giuseppe, P. and Zecchina, A., J. Chem. Soc. Faraday Trans. I 81, 1283 (1985).

111. Nakamoto, K., "Infrared Spectra of Inorganic and Coordination Compounds" 3rd ed., Wiley, New York 1978.

112. Venkateswarlu, P. J. Phys. Chem., 19, 293 (1951).

113. Feitknecht, W., Z. angew. Chem., 49, 24 (1936).

114. Taylor, H.F.W., Miner. Mag., 39, 377 (1973).

115. Scholten, J.J.F. "Chemisorption of Nitrogen on Iron Catalysts in connection with Ammonia Synthesis." Thesis Technological University Delft (1959).

116. Dalmon, J.A., Proceedings 7^{th} Intern. Congr. Catal. Tokyo 1980, p. 259, Elsevier, Amsterdam (1981).

117. Cranston, R.W. and Inkley, F.A., Advances in Catalysis, 9, 143 (1957).

118. Brunauer, S., Mikhail, R.S. and Bodor, E.E., J. Coll. Int. Sci. 25, 353 (1967).

119. Kundig, W., Bommel, H., Constabaris, G. and Lindquist, R.H., Phys. Rev. 142, 327 (1966).

120. Rossiter, M.J. and Hodgson, A.E.M. J. Inorg. Nucl. Chem. 27, 63 (1965).

121. Smart, R.St.C., Slager, T., Little, L.H. and Greenler, R.G., J. Phys. Chem., 77, 1019 (1973).

122. Davydov, A.A., Rubene, N.A., and Budneva, A.A., Kinet. Katal., 19, 776 (19780.

123. Zecchina, A., Spoto, G., Coluccia, S., and Guglielminotti, E., J. Chem. Soc. Faraday Trans. I, 80, 1875 (1984).

124. Guglielminotti, E., Coluccia, S., Garrone, E., Cerruti, L., and Zecchina, A., J. Chem. Soc. Faraday Trans. I 75, 96 (1979).

125. The Sadtler Standard Spectra

126. Blyholder, G., and Neff, L.D., J. Phys. Chem., 66, 1464 (1962).

127. Sheppard, N. and Nguyen, T.T., Advances in infrared and Raman spectroscopy Vol. 5, p. 67, Heyden and son, London, (1978).

128. Eischens, R.P., and Pilskin, W.A., Adv. Catal. 10, 1 (1958).

129. Kishi, K., and Roberts, M.W., J. Chem. Soc. Faraday Trans. I 71, 1715 (1975).

130. Angell, C.L. and Schaffer, P.C., J. Phys. Chem. 70, 1413 (1966).

131. Parkyns, N.D., Proc. 5^{th} Inter. Congr. Catal. p. 255-266 Elsevier (1973).

132. Terenin, A.N., and Roev, L.M., Spectrochim. Acta 15, 274, 946 (1959).

133. Rethwisch, D.G. and Dumesic, J.A., J. Phys. Chem., 90, 1625 (1986).

134. Low, M.J.D., and Yang, R.T., J. Catal. 34, 479 (1974).

135. Lunsford, J.H., J. Chem. Phys., 46, 4347 (1967).

136. Tench, A.J. and Nelson, R.L., Trans. Faraday Soc., 63, 2254 (1967).

137. Seshadri, K.S. and Petrakis, L., J. Phys. Chem., 74, 1317 (1970).

138. Siegel, M.W., Celotta, R.J., Hall, J.L., Levine, J. and Bennett, R.A., Phys. Rev., 6, 607 (1972).

139. Aparicio, L.M., Hall, W.K., Fang, S.M., Ulla, M.A., Millman, W.S. and Dumesic, J.A., J. Catal. 108, 233 (1987).

140. Lavalley, J.C. and Gain, C. C. R. Acad. Sc. Paris, t. 288 Série C p. 177-179.

141. Knozinger, H., Krietenbrink, H., Muller, H.D. and Schulz, W., Proc. 6th Inter. Congr. Catal. London. 1, 183 (1976).

142. Knozinger, H. and Krietenbrink, H., J. Chem. Soc. Faraday Trans. I 71, 2421 (1975).

143. Angell, C.L. and Howell, M.V., J. Phys. Chem. 75, 2551 (1969).

144. Friend, C.M., Muetterties, E.L. and Gland, J.L., J. Phys. Chem., 85, 3256 (1981).

145. Friend, C.M., Stein, J. and Muetterties, E.L., J. Am. Chem. Soc. 103, 767 (1981).

146. Kordesch, M.E., Stenzel, W. and Conrad, H., Surf. Sci. 175, L687 (1986).

147. Anderson, J.R. and Clark, N.J., J. Catal. 6, 20 (1966).

148. Kordesch, M.E., Stenzel, W. and Conrad, H., Surf. Sci. 186, 601 (1987).

149. Bond, G.C., "Catalysis by Metals" Academic Press London 1962.

150. Anderson, J.R. and Pratt, K.C., "Introduction to Characterisation and Testing of Catalysts" Academic Press Inc. 1985.

151. Marcelin, G., Vogel, R.F. and Kehl, W.L., Preparation of Catalysts III p. 169, Elsevier, Amsterdam, 1983.